MANY-BODY INTERACTIONS AND SPIN-SPLITTING OF THE ELECTRONIC STRUCTURE IN WSE2 AND EUO

Jonathon M. Riley

A Thesis Submitted for the Degree of PhD
at the
University of St Andrews

2017

Identifiers to use to cite or link to this thesis:

DOI: https://doi.org/10.17630/10023-15707
http://hdl.handle.net/10023/15707

Many-Body Interactions and Spin-Splitting of the Electronic Structure in WSe_2 and EuO

Author:
Jonathon M. Riley

Supervisors:
Dr. Phil D. King
Dr. Moritz Hoesch

University of
St Andrews

A thesis submitted in fulfillment of the requirements

for the degree of Doctor of Philosophy in Physics

at the

University of St Andrews

July 1, 2017

Declaration of Authorship

1. Candidate's declarations: I, **Jonathon M. Riley**, hereby certify that this thesis, which is approximately **38,000** words in length, has been written by me, and that it is the record of work carried out by me, or principally by myself in collaboration with others as acknowledged, and that it has not been submitted in any previous application for a higher degree. I was admitted as a research student in **01/09/13** and as a candidate for the degree of Doctor of Philosophy in Physics completed by **31/08/17**; the higher study for which this is a record was carried out in the University of St Andrews between **01/09/13** and **01/07/17**.

Date .... signature of candidate ....

2. Supervisor's declarations:
I hereby certify that the candidate has fulfilled the conditions of the Resolution and Regulations appropriate for the degree of Doctor of Philosophy in Physics in the University of St Andrews and that the candidate is qualified to submit this thesis in application for that degree.

Date .... signature of supervisor ....

3. Permission for publication:(to be signed by both candidate and supervisor)
In submitting this thesis to the University of St Andrews I understand that I am giving permission for it to be made available for use in accordance with the regulations of the University Library for the time being in force, subject to any copyright vested in the work not being affected thereby. I also understand that the title and the abstract will be published, and that the title and the abstract will be published, and that a copy of the work may be made and supplied to any bona fide library or research worker, that my thesis will be electronically accessible for personal or research use unless exempt by award of an embargo as requested below, and that the library has the right to migrate my thesis into new electronic forms as required to ensure continued access to the thesis. I have obtained any third-party copyright permissions that may be required in order to allow such access and migration, or have requested the appropriate embargo below.

The following is an agreed request by candidate and supervisor regarding the publication of this thesis:

PRINTED COPY
Embargo on all of print copy for a period of 2 years on the following ground: publication would preclude future publication

ELECTRONIC COPY
Embargo on all of electronic copy for a period of 2 years on the following ground: publication would preclude future publication

Date .... signature of candidate ....

Date .... signature of supervisor ....

"The more you find out about the world, the more opportunities there are to laugh at it."

-Bill Nye, The Science Guy

Special Dedication to:

Grace Hatt, my family & friends,

and to the members of the King Group

for all their support and help,
without which none of this work would have been possible.

Abstract

The ability to create and control spin-polarised electronic states in solids is vital for realising all-electrical manipulation of spins for the next generation of electronic devices. Such devices are likely to rely upon the injection of a spin-current into a semiconducting material whereupon the current is manipulated for the transfer of data. Two such materials that have been proposed for spin injection and manipulation are EuO, a ferromagnetic semiconductor, and WSe_2, a member of the layered transition metal dichalcogenides, respectively. By directly probing the electronic band structure using angle-resolved photoemission spectroscopy, ARPES, and its spin-resolved analogue, SARPES, a "hidden" spin-polarisaion is observed in bulk WSe_2 due to the local breaking of inversion symmetry that locks the spin to the valley- and layer-pseudospins. By chemical gating, the layer-degeneracy is broken which induces a spin-splitting of the valence bands and the formation of a 2DEG. Increasing the carrier density of the 2DEG is shown to result in a lowering of the chemical potential, providing direct spectroscopic evidence for many body effects due to electron-electron interactions. Whereas WSe_2 hosts spin-polarised states due to local inversion-symmetry breaking, ferromagnetism induces spin-polarised valence and conduction band states in Gd-doped EuO that break time-reversal symmetry. Using ARPES, the full 3D dispersion of the conduction bands is observed for the first time and the temperature dependence of the spin-split conduction band is analysed. By varying the Gd concentration, the carrier density is varied, revealing two kinds of satellite features due to electron-phonon and electron-plasmon interactions in the low temperature phase. Thus, despite differences in dimensionality, structure and symmetries, both materials show evidence of electron interactions which are directly measurable by ARPES and are seen to host spin-split electronic states that can be manipulated via external conditions.

Publications

The research presented in this thesis has directly led to the following publications:

1. **Orbital Texture and Temperature Dependence of the 3D Fermi Surface of Gd-doped EuO**
   J.M. Riley, L. Duffy, M. Watson, L. Bawden, K. Volckaert, T. Hesjedal, M. Hoesch, P.D.C. King
   in preparation (2017).

2. **Doping-Induced Crossover from Lattice to Plasmonic Polarons of a Spin-Polarised Electron Gas in the Ferromagnetic Semiconductor EuO**
   J.M. Riley, F. Caruso, C. Verdi, L. Duffy, M. Watson, L. Bawden, K. Volckaert, T. Hesjedal, M. Hoesch, F. Giustino, P.D.C. King
   in preparation (2017).

3. **Negative Electronic Compressibility and Tuneable Spin Splitting in WSe$_2$**
   J.M. Riley, W. Meevasana, L. Bawden, M. Asakawa, T. Takayama, T. Eknapakul, T.K. Kim, M. Hoesch, S.-K. Mo, H. Takagi, T. Sasagawa, M.S. Bahramy, and P.D.C. King
   Nature Nanotechnology **10**, 1043 (2015).

4. **Direct Observation of Spin-Polarised Bulk Bands in an Inversion-Symmetric Semiconductor**
   J.M. Riley, F. Mazzola, M. Dendzik, M. Michiardi, T. Takayama, L. Bawden, C. Granerød, M. Leandersson, T. Balasubramanian, M. Hoesch, T. K. Kim, H. Takagi, W. Meevasana, Ph. Hofmann, M. S. Bahramy, J.W. Wells, and P.D.C. King
   Nature Physics **10**, 835 (2014).

Research conducted during the study of this degree, but which did not directly contribute to the work discussed in this thesis, has resulted in the following publications:

1. **Maximal Rashba-like Spin Splitting via Kinetic Energy-Driven Inversion Symmetry Breaking**
   V. Sunko, H. Rosner, P. Kushwaha, S. Khim, F. Mazzola, L. Bawden, O. J. Clark, J. M. Riley, D. Kasinathan, M.W. Haverkort, T.K. Kim, M. Hoesch, J. Fujii, I. Vobornik, A.P. Mackenzie, and P.D.C. King
   submitted (2017).

2. **Ubiquitous formation of type-II bulk Dirac cones and topological surface states from a single orbital manifold in transition-metal dichalcogenides**
   M. S. Bahramy, O. J. Clark, B.-J. Yang, J. Feng, L. Bawden, J.M. Riley, I. Marković, F. Mazzola, V. Sunko, D. Biswas, S. Cooil, M. Jorge, J. W. Wells, M. Leandersson, T. Balasubramanian, J. Fujii, I. Vobornik, J. Rault, T. K. Kim, M. Hoesch, G. Balakrishnan, K. Okawa, M. Asakawa, T. Sasagawa, T. Eknapakul, W. Meevasana and P.D.C. King.
   submitted, arXiv:1702.08177 (2017)

3. **Narrow-band anisotropic electronic structure of ReS$_2$**
   D. Biswas, A.M. Ganose, R. Yano, J.M. Riley, L. Bawden, O. J. Clark, J. Feng, L. Collins-Mcintyre, W. Meevasana, T. K. Kim, M. Hoesch, J. E. Rault, T. Sasagawa, D.O. Scanlon, and P.D.C. King
   submitted, arXiv:1703.04725 (2017).

4. **Multiband One-Dimensional Electronic Structure and Spectroscopic Signature of Tomonoga-Luttinger Liquid Behavior in K$_2$Cr$_3$As$_3$**
   M.D. Watson, Y.Feng, C.W. Nicholson, C. Monney, J.M. Riley, H.Iwasawa, K. Refson, V. Sacksteder, D.T. Adroja, J. Zhao, and M. Hoesch
   Phys. Rev. Lett. **118**, 097002 (2017).

5. **Spin and Valley Control of Free Carriers in Single-Layer WS$_2$**
   S. Ulstrup, A.G. Čabo, D. Biswas, J.M. Riley, M. Dendzik, C.E. Sanders, M. Bianchi, C. Cacho, D. Matselyukh, R. T. Chapman, E. Springate, P.D.C. King, J.A. Miwa, and P. Hofmann
   Phys. Rev. B **95**, 041405(R), (2017).

6. **Ultrafast Band Structure Control of a Two-Dimensional Heterostructure**
   S. Ulstrup, A.G. Čabo, J.A. Miwa, J.M. Riley, S.S. Grønborg, J.C. Johannsen, C. Cacho, O. Alexander, R.T. Chapman, E. Springate, M. Bianchi, M. Dendzik, J.V. Lauritsen, P.D.C. King, and Ph. Hofmann
   ACS Nano **10**, 6315 (2016).

7. **Spin-Valley Locking in the Normal State of a Transition-Metal Dichalcogenide Superconductor**
   L. Bawden, S.P. Cooil, F. Mazzola, J.M. Riley, L.J. Collins-McIntyre, V. Sunko, K.W.B. Hunvik, M. Leandersson, C.M. Polley, T. Balasubramanian, T.K. Kim, M. Hoesch, J.W. Wells, G. Balakrishnan, M.S. Bahramy, and P.D.C. King
   Nature Comms. **7**, 11711 (2016).

8. **Nearly-Free Electrons in a 5d Delafossite Oxide Metal**
   P. Kushwaha, V. Sunko, P.J.W. Moll, L. Bawden, J.M. Riley, N. Nandi, H. Rosner, M.P. Schmidt, F. Arnold, E. Hassinger, T.K. Kim, M. Hoesch, A.P. Mackenzie, P.D.C. King
   Science Advances **1**, e1500692 (2015)

9. **Hierarchical Spin-Orbital Polarisation of a Giant Rashba System**
   L. Bawden, J.M. Riley, C.H. Kim, R. Sankar, E.J. Monkman, D.E. Shai, H.I. Wei, E. Lochocki, J.W. Wells, W. Meevasana, T.K. Kim, M. Hoesch, Y. Ohtsubo, P. Le Fèvre, C.J. Fennie, K.M. Shen, F.C. Chou, and P.D.C. King
   Science Advances **1**, e1500495 (2015).

10. **Observation of Ultrafast Free Carrier Dynamics in Single Layer MoS$_2$**
    A.G. Čabo, J.A. Miwa, S.S. Grønborg, J.M. Riley, J.C. Johannsen, C. Cacho,

O. Alexander, R. T. Chapman, E. Springate, M. Grioni, J. V. Lauritsen, P.D.C. King, Ph. Hofmann, and S. Ulstrup

Nano Lett. **15**, 5883 (2015).

Acknowledgements

The work presented here was completed with help from the following persons:
P.D.C King, M. Hoesch and T. Hesjedal for supervision of project; L. Bawden, O. Clark, F. Mazzola, M. Watson, M. Dendzik, M. Michiardi, W. Meevasana, T. Eknapakul, L. Duffy, C. Granerd, and K. Vlockaert for assistance in acquiring beamtime data; T.K. Kim, M. Leandersson, T. Balasubramanian, and S.-K. Mo for maintenance of beamlines; M.S. Bahramy, F. Giustino, F. Caruso, and C. Verdi, for theory collaboration; M. Asakawa, T. Takayama, H. Takagi and T. Sasagawa for single-crystal samples; R. Held, Ph. Hofmann, and J.W. Wells for useful discussions.

Contents

List of Figures

Chapter 1

Motivation

This year marks the 70th anniversary of the first successful demonstration of the transistor, by William Shockley, John Bardeen and Walter Brattain at Bell Labs in Murray Hill. This device, which uses electric potentials to manipulate a barrier allowing or retarding the flow of current across a semiconductor, is the workhorse of many modern electronic devices. Since its creation in 1947, efforts to increase efficiency and reduce its size have been non-stop. Just 6 years after its invention, the first transistor computer had been built, replacing the numerous vacuum tubes of former computers with 92 transistors, each of which were the size of one's hand. By 1971, the first computer processor, Intel 4004, had been developed utilising 2,300 transistors, each smaller than the width of a human hair at only $\sim$10 microns. Fast-forward to the present and the processors of modern mobile phones contain upwards of 2 billion transistors, with each being roughly 20 nm, comparable to the size of a virus and approaching the quantum mechanical scale of some electronic behaviour, such as quantum tunnelling which leads to current leakage and a breakdown of efficiency.

Thus, it is generally accepted that the current design of transistors is reaching its physical limitations due to heat dissipation issues as the result of further miniaturisation [1]. To overcome this obstacle, researchers are attempting to create devices that utilise another fundamental property of electrons to transfer information: spin [2]. It is believed that these spin-transistors would improve energy efficiency and produce more powerful processors. But spin is not the only possible route to more efficient devices currently being investigated. For example, it has been proposed that the valley-pseudospin, i.e. the degree of freedom associated with electronic states that are degenerate in energy but separated in k-space, could also be utilised to process information. The search for suitable materials for use in these next generation materials and, more importantly, a deeper understanding of the underlying physics that these materials embody motivate the work presented in this thesis.

1.1 Spintronics

Spin is already used to store data in hard drives by fixing the alignment of spins in magnetic domains along a specific axis, but until recently, a spin analogue of the transistor has remained elusive and is still far from ready for mass production [3]. The use of spin instead of charge adds considerable complexity to the function of these devices. Like it's traditional charge analogue, the spin transistor, depicted in Fig. 1.1 requires a metallic contact for the injection of current into a semiconducting medium which is transferred to a drain contact; however, unlike a charge based device, the injected current must be highly spin-polarised, requiring contacts that are also half-metals. This requirement causes a problem as the potential barrier at a metal-semiconductor interface results in unwanted effects that reduce the purity of the injected spin current, especially if the interface is not atomically flat. Furthermore, once injection of a high-purity spin current is achieved, electric field gating must be used to not only retard or allow the flow of current through the semiconducting material, but also to control the alignment of the current's spin. If the orientation of the spins are left unperturbed, they are "read" by the drain current, but if they are aligned anti-parallel with the spins of the magnetic contact, a current is not passed through.

This specialised device thus requires two different kinds of materials: 1) a ferromagnetic contact capable of high-purity spin injection and 2) a semiconducting

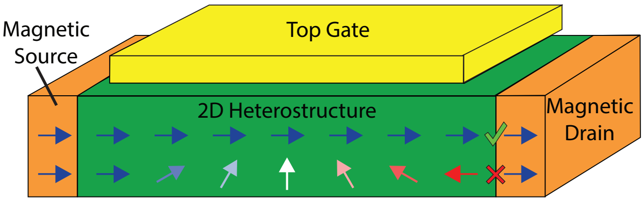

FIGURE 1.1: Spin analogue of the traditional charge transistor. Ferromagnetic, metallic contacts inject a highly spin-polarised current into an intermediate 2D medium. Through application of a voltage across the field gate, the orientation of the spin current is either altered or left unperturbed such that it is either blocked by or flows through the drain contact.

material with spin-polarised conduction states that can be controlled and manipulated. One possible candidate for the contact material is EuO, which is a ferromagnetic semiconductor. Although uncommon, such ferromagnetic semiconductors possess strongly spin-polarised charge carriers (>90% for EuO), while avoiding the issues associated with a metal-semiconducting barrier, theoretically allowing for high-purity spin currents. It has also been proposed that one family of 2D semiconductors, the transition metal dichalcogenides (TMDCs), could be suitable to fulfil the material requirements for a spin-transistor or other spin-based device [4–6]. The semiconducting TMDCs are ideal candidates for integration into spintronic devices as their layered honeycomb crystal structure is similar to graphene, the original candidate for spin- and valleytronic devices, and have already been integrated in traditional field effect transistors [7–9].

Despite the possibility of realising a spin-transistor using these two materials, little research has been done on understanding the underlying electronic structure of the individual materials or how the band structure is affected by external conditions similar to those that might be experienced in a spintronic device, i.e. gating and/or doping. Here an investigation of some of these issues is addressed through direct measurement of the band structure using angle-resolved photoemission spectroscopy.

1.2 Outline of thesis

This thesis will begin with a discussion of the theory of electronic band structure in Chapter 2, which will serve as the foundation for experimental results discussed later. Armed with an understanding of band structure, in Chapter 3 the main experimental technique for directly measuring the electronic structure, angle-resolved photoemission spectroscopy (ARPES), will be reviewed. Along with ARPES, an overview of molecular beam epitaxy (MBE), a method for growing thin film crystalline samples, and some material characterisation techniques will be given. Several ultra-high vacuum setups across the world combine ARPES and MBE capabilities, however the addition of a synchrotron-based light source is less common, limited to less than a handful of places. Therefore, Chapter 4 is dedicated to a summary of the experimental setup of the I05 high resolution (HR) ARPES endstation at Diamond Light Source, where the majority of this work was performed, including a description of the required modifications to the MBE system necessary to allow growth of oxide films.

In the remaining chapters, experimental investigations of the electronic structure of single crystal WSe_2 and EuO thin films are presented. In Chapter 5, spin- and angle-resolved photoemission spectroscopy measurements on single crystal WSe_2 are used to analyse the bulk electronic structure, through which dimensionality effects are shown to give rise to hidden spin-polarised states. In Chapter 6, chemical gating of WSe_2 is used to break the layer degeneracy of the valence band states. This provides an alternative method to analyse the effects of electrically gating these materials, in a manner compatible with ARPES, which is seen to give rise to a surprisingly pronounced effect of many-body interactions. Chapter 7 switches focus, discussing the known properties of EuO and demonstrating the method for growing high quality thin films using the MBE at Diamond Light Source. In Chapter 8, the first measurement of the full 3D dispersion of the conduction band states of $Eu_{1-x}Gd_xO$ is presented before discussing the effects of temperature on the band structure and magnetic properties. In Chapter 9, the presence of many-body effects well below the Curie temperature is analysed, including the first observation of plasmonic polarons. Finally, future work investigating these materials individually, as well as the possibility of a TMDC/EuO heterostructure, is discussed in Chapter 10.

Through the results presented here, the electronic structures of these two materials are investigated and, despite large differences between the two, it is shown that both embody a valley degree of freedom where spin-split states reside that can be manipulated by external conditions and, additionally, present many-body effects from electron interactions. The research discussed in this thesis suggests a need for further study of the electronic structure of these materials and their response to external factors before a fully-functioning spin-based device, incorporating either or both of these materials, can be constructed.

Chapter 2

Introduction to Electronic Structure

The behaviour of crystalline solids, from typical transport properties to novel forms of superconductivity, is the result of electronic structure. There is a wide array of factors that determines how electrons move through a crystal lattice and countless variations for material properties. Since the start of the 20th century, scientists have worked to develop a theory that describes the allowed electronic energies and momenta (states) which determine these properties. Here, a brief introduction to some of the theories developed to explain electronic behaviour will be given, starting with the most basic approach, the free Fermi gas, before discussing more complicated models. This is followed by a discussion of how material composition, such as atomic constituents and crystal structure, effects electron interactions and preserves or breaks time-reversal and inversion symmetries, thus altering electronic behaviour. This introduction will serve to set the foundation for future discussions on experimental results presented here.

2.1 Constructing Bands

The branch of condensed matter physics focused on electronic phenomena and band structure is based around a single Hamiltonian:

$$\hat{H} = \sum_{l} \frac{\hat{P}_l^2}{2M_l} + \frac{1}{2} \sum_{l \neq l'} \frac{q_l q_{l'}}{|\hat{R}_l - \hat{R}_{l'}|}, \tag{2.1}$$

where $\hat{P}_l$, M_l, q_l and $\hat{R}_l$ are the momentum operator, mass, charge and position operator of the l^{th} electron, respectively. As opposed to classical systems, where the addition of a single electron involves the addition of little information to encode its exact properties, the required information to describe quantum systems scales exponentially to account for all possible configurations the system could be in. Because of the exponential scaling, solving Eq. 3.1 becomes too computationally expensive after only a handful of particles, far fewer than the 10^{23} particles of typical solid systems. To overcome this issue, various approximation schemes have been devised to reduce the complexity of the system into a more manageable problem. The simplest model for electrons in a solid medium is the free Fermi gas, which assumes these electrons do not interact with each other or the nuclei of the lattice. Although this model is oversimple and unphysical, it does a surprisingly good job of predicting some basic physical properties of many materials [10]. By adding in the presence of the crystal lattice, through inclusion of a periodic potential, further insight is gained into the origin of insulating behaviour. Finally, by using atomic wave functions in the tight-binding approach, a computationally feasible model is produced that predicts the electronic structure of valence and conduction electrons.

2.1.1 Free Fermi Gas

The free Fermi gas model is by far the simplest model for explaining electronic behaviour, where the system is represented as a cloud of electrons moving in a box and the only condition, apart from boundary constraints, dictating their properties is the Pauli exclusion principle [10, 11]. This model is a specific example of the more general single electron model, which attempts to solve the Hamiltonian

$$\hat{H}\Psi(\vec{r}_1...\vec{r}_N) = \sum_{l=1}^{N}\left(\frac{-\hbar^2\nabla^2}{2m} + U(\vec{r}_l)\right)\Psi(\vec{r}_1...\vec{r}_N) = \varepsilon\Psi(\vec{r}_1...\vec{r}_N), \tag{2.2}$$

where m is the electron mass, $\vec{r}_l$ is the position vector of the l^{th} electron in the N electron system, which interacts with an external potential, U, but not the other electrons. Solutions to this equation for many particle systems are the product of single-particle eignfunctions of Eq. 2.2 and therefore one only needs to solve for single-particle systems.

For the free Fermi gas in a box of volume L^3, one neglects any external potential, $U(\vec{r}_l) = 0$, and applies boundary conditions such that the system is identical under translations of integer multiples of L along the axis directions, i.e. for a one-electron system $\Psi(x_1 + L, y_1, z_1) = \Psi(x_1, y_1, z_1)$, as well as translations along the other axes. Single-particle solutions to this are plane waves of the form $\psi_{\vec{k}} = \sqrt{A}^{-1} e^{i\vec{k}\cdot\vec{r}}$, where the A term is used to normalise the wavefunction and $\vec{k} = \frac{2\pi}{L}(l_x, l_y, l_z)$, shown in Fig 2.1a. The eigenvalue, or eigen energies, are of the form $\varepsilon_{\vec{k}} = \hbar^2 k^2/2m$ [11]. As mentioned, the groundstate of an N electron system is the product of N single-particle wavefunctions, with the only constraint being that the Pauli exclusion principle is upheld. Therefore, in building up the groundstate, one places electrons in states with the lowest value of $|\vec{k}|$ and, because $\epsilon_{\vec{k}} \propto k^2$, additional electrons are added in consecutive shells with increasing radii. Thus one can visualise the groundstate of an N electron system as a

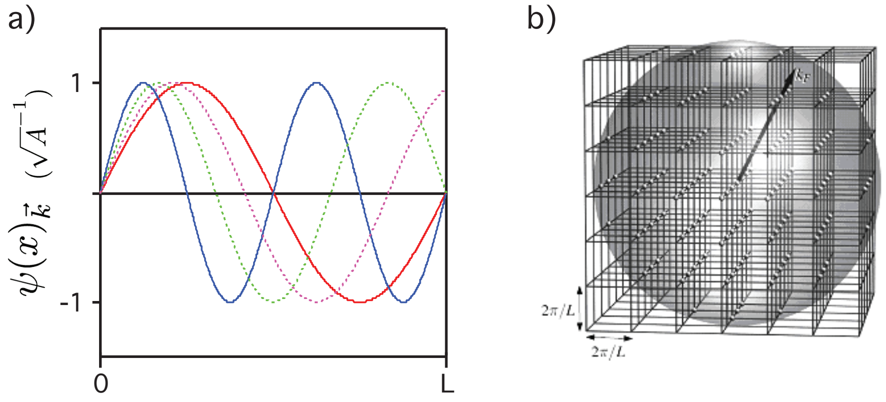

FIGURE 2.1: Visualisation of a free Fermi gas. a) Eigenfunctions (solid lines) for a 1-D box with side length L satisfy boundary conditions of $\psi(0) = \psi(L) = 0$ and repeat without discontinuity for a box of size nL, while functions that are not eigenfunctions (dashed lines) either do not repeat smoothly or satisfy boundary conditions. b) Placing N electrons into the groundstate for a free Fermi gas produces consecutive shells with radius $2k\pi/L$ where k is an integer. Reproduced from Ref. [10].

sphere, or Fermi sphere, of electrons with a radius given by the Fermi wavevector, k_F, Fig. 2.1b. All electronic states contained within the Fermi sphere have energy less than or equal to the Fermi energy, $E_F = \hbar^2 k_F^2/2m$, and an occupation probability of 1, while all states above the Fermi level have an occupation number of 0, for a system at T=0K.

Typically, it is the electrons that sit at the Fermi surface that dictate the physical attributes of a material, such as electrical conductivity or specific heat, and therefore it is typical to refer only to the states at the Fermi level. This is because, in order to move from the ground state to an excited state, electrons must move from an occupied to an unoccupied state. The electrons well below the Fermi level are surrounded by occupied states and therefore would need a large change in energy/momentum to be excited into an unoccupied state, Fig. 2.2a, such as through photoexcitation by a light source or scattering by another electron with sufficiently high energy [12]. On the other hand, there is an abundance of electrons near the Fermi surface and unoccupied states just above it, so only a small amount of energy/momentum transfer is required, Fig. 2.2b.

At T=0K, the Fermi level represents a discontinuity in the occupation probability, where below the Fermi energy all states are occupied and no occupied

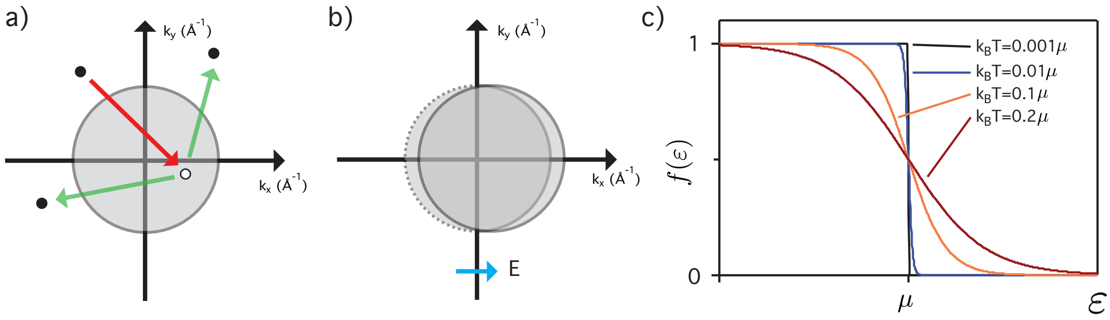

FIGURE 2.2: Excitations from the groundstate of a free Fermi gas. a) Scattering from a high energy electron can excite an electron in the Fermi gas into an excited state, leaving behind an unoccupied state (hole). b) An external electric field causes a rigid shift of the Fermi surface in the direction of the applied field. c) Thermal excitations cause the discontinuity of the Fermi function at T=0K to be smoothed out as the occupation probability above the Fermi level becomes non-zero.

states have an energy greater than this. However, at higher temperatures, thermal excitations promote a small number of electrons just below the Fermi level to just above it, Fig 2.2c. The temperature dependent occupation probability, or Fermi function, has the form:

$$f(\varepsilon) = \frac{1}{e^{\beta(\varepsilon-\mu)} + 1}, \tag{2.3}$$

where $\beta^{-1} = k_B T$, k_B is Boltzmann's constant and μ is the chemical potential, i.e. the energy required to add a single electron to the system.

Although the free Fermi gas is a relatively simple model, it is still capable of predicting the specific heat and electrical conductivity for many metals [10]. However, the model is inadequate in explaining a large range of more complicated questions. For instance, the predicted Hall coefficient is independent of temperature or strength of a magnetic field, which is untrue in most cases [11], and while the order of magnitude is right for most metals, the sign can be wrong. This model also does not answer the questions: what determines the number of conduction electrons and why are some materials non-metallic?

2.1.2 Non-interacting Electrons in a Periodic Potential

The most logical extension of the free Fermi gas model is to turn on the electronic interactions with the nuclei by treating them as an external potential $U(\vec{r})$. Although Eq. 2.2 is still intractable for general potentials, a straightforward solution can be found for periodic potentials which obey $U(\vec{r}+\vec{R}) = U(\vec{r})$, as proposed by Bloch in 1928. The condition of a periodic potential makes intuitive sense as a crystal lattice without impurities can be represented by a unit cell that forms the fundamental building block of a crystal when repeatedly translated along a finite set of primitive lattice vectors and therefore electrons moving in one of these blocks should behave identically to those moving in any other such block.

In one-dimension, it can be shown that a single-particle solution to Eq. 2.2 for a periodic potential with periodicity a is given by:

$$\psi(x) = \frac{e^{ikx}u(x)}{\sqrt{N}} \qquad \text{where } u(x) \equiv \frac{1}{\sqrt{a}}\sum_K u_K e^{iKx}, \tag{2.4}$$

$N = L/a$ is the number of unit cells, $K = 2\pi l/a$ is the reciprocal lattice vector and l is an integer. In other words, a single particle moving in a periodic potential has a wavefunction that is the product of the plane wave solution, e^{ikx}, from the free Fermi gas, and a periodic modulation $u(x)$ with the same periodicity as the potential. However, because of the periodic nature of both the plane wave solution and external potential, solutions with wave number $k+K$ and $k+K'$ are identical, Fig. 2.3, i.e. they satisfy Bloch's theorem. Therefore, it is common convention to

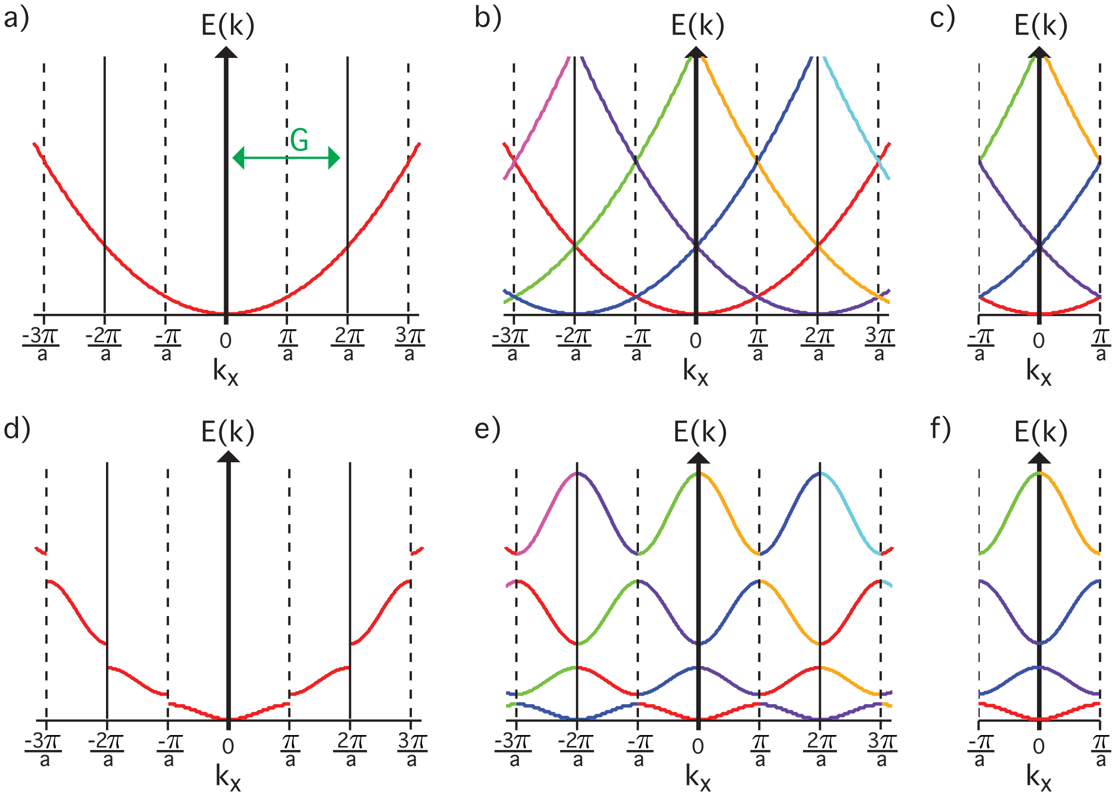

FIGURE 2.3: Free Fermi gas and periodic potential band structures. The band dispersion for a free Fermi gas in the a) extended zone, b) repeated zone and c) reduced zone schemes are parabolic. d-f) Same as in a-c except the addition of a periodic potential opens up band gaps at zone edges.

take only $k = 2\pi m/L$ where $k \in [-2\pi/a, 2\pi/a]$ as this set of k, called the *first Brillouin zone*, encompasses all wave numbers necessary to describe a complete set of solutions. From Fig. 2.3, it is clear where the term electronic "band" structure derives, as when viewed in the repeated or reduced zone schemes, the allowed electronic momenta, k, and energies, ϵ_k, trace out stacks of crossing bands.

In the case of the free Fermi gas, the momentum dispersion of the allowed electronic states is parabolic, with infinite repetitions equally separated in k-space due to the restrictions placed on the translation of the system, as illustrated in Fig. 2.3a-c. One notes that at the zone boundaries, the bands cross and become degenerate. As such these states should be considered a superposition of the two bands [13], which take the form:

$$\begin{aligned} \psi_+ &\sim \left(e^{iGx/2} + e^{-iGx/2}\right) \sim \cos \pi \frac{x}{a} \\ \psi_- &\sim \left(e^{iGx/2} - e^{-iGx/2}\right) \sim \sin \pi \frac{x}{a}, \end{aligned} \tag{2.5}$$

where G is the reciprocal lattice vector that separates the parabolic bands in k-space. The probability density is given by $\psi_+^*\psi_+ \sim \cos^2(\pi x/a)$ and $\psi_-^*\psi_- \sim \sin^2(\pi x/a)$ which have maxima and minima, respectively, located at the zone boundaries. The inclusion of even a small periodic potential, which is centred around the zone edges, induces an energy difference to develop between the ψ_+ (high probability density around charged lattice sites) and ψ_- (high probability density between lattice sites). This asymmetry breaks the energy degeneracy at the zone boundaries and opens up energy gaps which are proportional to the magnitude of the potential [14].

Extending Bloch's theorem to three dimensions is a trivial problem. For a Bravais lattice $\vec{R}$ with reciprocal lattice vectors $\vec{K}$, the three-dimensional periodic

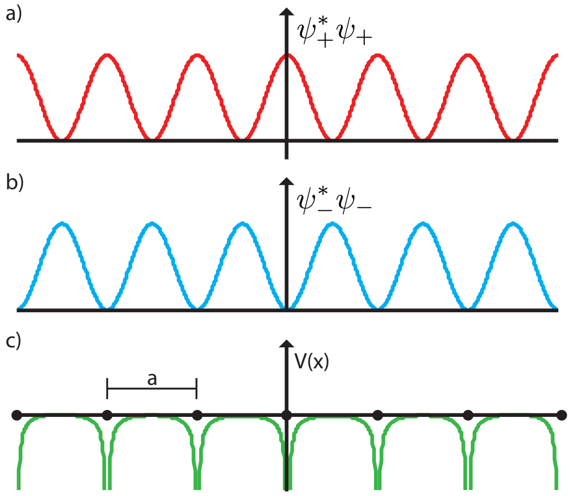

FIGURE 2.4: Probability density of the superimposed wavefunctions at the zone boundaries. a) The ψ_+ state has a probability density that is peaked at the edges of the Brillouin zone, while b) the ψ_- state is peaked between the lattice sites. The inclusion of a periodic potential from the lattice drives the formation of band gaps due to the energy costs associated with the different probability densities. Adapted from Ref. [13].

potential $U(\vec{r})$ is composed of Fourier components $e^{i\vec{K}\cdot\vec{R}}$. Therefore the 3D equivalent of Eq. 2.4, is given by

$$\psi_{\vec{k}}(\vec{r}) = \frac{e^{i\vec{k}\cdot\vec{r}}u_{\vec{k}}(\vec{r})}{\sqrt{N}}, \tag{2.6}$$

where N is now the number of lattice points and $u_{\vec{k}}(\vec{r})$ is periodic on the Bravais lattice. Solutions of this kind satisfy Bloch's theorem, that single-particle wavefunctions are indifferent, apart from a possible phase factor, to a translation of the lattice vector:

$$\psi_{\vec{k}}(\vec{r}+\vec{R}) = e^{i\vec{k}\cdot\vec{R}}\psi_{\vec{k}}(\vec{r}). \tag{2.7}$$

The inclusion of a periodic potential, as proposed by Bloch, into the Sommerfeld model of a free Fermi gas helped to explain the differing electrical behaviour of metals, semiconductors and insulators. The energy gaps that develop at the Brillouin zone boundaries represent an energy barrier, which prevents the flow of current. In metallic systems, such as copper, the number of electrons places the Fermi level within the bandwidth of a partially filled band, with all lower bands completely filled. Upon application of an electric field, like that created by the potential of a battery, there is a multitude of unoccupied states available for the conduction electrons to be excited into. However, in insulators and semiconductors, like silicon, all states of a given band are completely filled, such that the Fermi level resides within the band gap and thus there are no unoccupied states available to shift electrons into. Although this new theory solved some fundamental problems regarding material properties, there arose a new problem: what effect does the strength of the periodic potential have on the resultant electronic behaviour?

2.1.3 Tight Binding Model

If one considers the strength of the periodic potential that arises from the crystal lattice as a spectrum, the nearly-free electron model, i.e. very weak potential, and the tight binding model, i.e. very strong potential, are at opposite ends. Because the core electrons strongly screen the nuclei of the lattice, the dynamics of conduction electrons can be reasonably approximated using the nearly free electron model. On the other end of the spectrum, there is the tight binding model where the potential of the lattice is so large that the electrons are strongly bound to the atomic sites. As such, it makes sense that the electronic wave functions should retain some of their atomic character and mimic bonding and anti-bonding orbitals. This can be visualised by imagining a lattice of atoms with a lattice spacing on the order of microns instead of Ångströms. The spatial extent of the orbital wavefunctions of these atoms are relatively small, on the order of Ångströms, and well localised around the nucleus. By reducing the lattice constant of this artificial array, eventually a point is reached at which the wavefunctions of some atomic orbitals overlap and some electrons are able to move freely throughout the lattice, while others are still localised around the nuclei.

Again, the aim is to solve Eq. 2.2 with $U(\vec{r})$ being the periodic potential from the lattice and therefore any solution should satisfy Bloch's theorem. Whereas before solutions of a single wavefunction were considered, here solutions will be a linear combination of the atomic orbitals and therefore it is necessary to choose the proper basis set. A convenient choice is the orthonormal set of orbitals defined by the Wannier functions [11]:

$$\phi_j(\vec{r}) = \frac{1}{\sqrt{N}} \sum_{R_i}^{N} e^{i\vec{k}\cdot\vec{R}_i} \gamma_j(\vec{r} - \vec{R}), \tag{2.8}$$

where N is the number of lattice sites (needed to normalise the Bloch state), $\vec{R}_i$ is the position of the i^{th} atom in the unit cell and γ_j is the j^{th} atomic wave function. The eigenfunctions of the crystal are linear combinations of Wannier functions, such that:

$$\psi_j(\vec{r}) = \sum_{j'}^{n} b_{jj'} \phi_{j'}(\vec{r}), \tag{2.9}$$

where n is the number of atomic wave functions. To determine these constants, one must solve:

$$0 = \sum_{j'} b_{jj'} \left\langle \phi_{j''} | \hat{H} - \varepsilon | \phi_{j'} \right\rangle \tag{2.10}$$

$$\Rightarrow 0 = \sum_{j'} b_{jj'} (H_{j''j'} - \varepsilon_{j'} S_{j''j'}), \tag{2.11}$$

where

$$H_{jj'} \equiv \left\langle \phi_j | \hat{H} | \phi_{j'} \right\rangle \tag{2.12}$$

$$S_{jj'} \equiv \langle \phi_j | \phi_{j'} \rangle , \tag{2.13}$$

with $H_{jj'}$ and $S_{jj'}$ representing the transfer and overlap parameters of the orbital wavefunctions, respectively, as illustrated in Fig. 2.5. The solution to this gives n eigenvalues, $E(\vec{k})$, for every value of $\vec{k}$, each of which dictates the dispersion of a single band, the sum of which constitutes the band structure of a given material [15]. It is straightforward to envision how this scheme produces complex band dispersions. In the case of the spherical atomic wave functions, i.e. s-orbitals, one would expect isotropic band dispersion, but for highly-directional

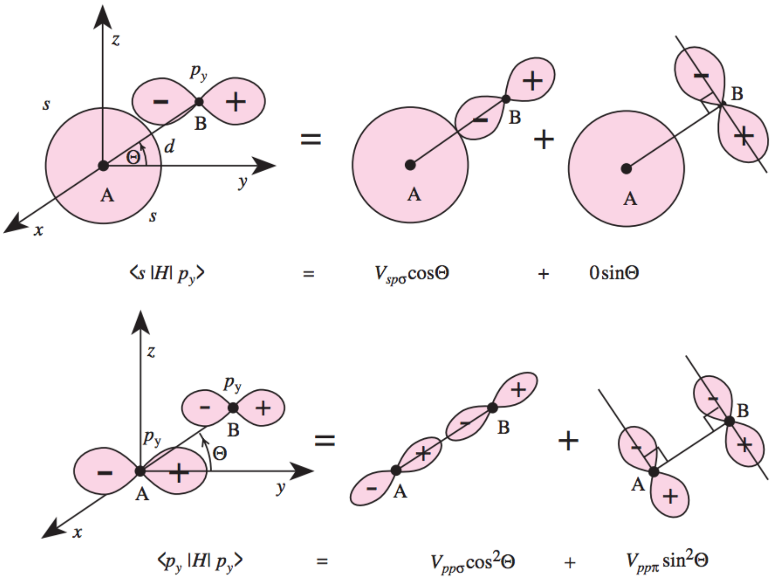

FIGURE 2.5: Projection of the overlap parameter in the tight-biding method. Overlap of the s and p_y orbitals (top) is only non-zero with the p_y aligned along the vector $\vec{d}$ joining the two atoms, while the overlap between two p_y orbitals (bottom) has a contribution from alignment parallel and perpendicular to $\vec{d}$. Reproduced from Ref. [15].

orbitals such, as the p and d orbitals, dispersion along a preferential axis can occur.

Additionally, it can be shown that when one considers a single spherical atomic wavefunction, i.e. an s orbital, the energy of tightly bound electrons is given by the energy of the original atomic orbital, a constant correction from interactions and a hopping term that depends on $\vec{k}$. This hopping term is related to the size of the overlap integral and dictates the velocity at which electrons move from site to site [10]. Also the bandwidth, the difference in the maximum and minimum energies of $\varepsilon_{\vec{k}}$, is proportional to the size of the overlap integral where a small overlap, i.e. localised orbitals, results in narrow bands. In the limit of no overlap, the bandwidth vanishes and the band becomes n-fold degenerate [11]. The tightly held core electrons are typically well described by a dispersionless band, but, as will be seen later in the case of EuO, some valence bands can be localised around the atomic sites resulting in near-dispersionless band structures.

One advantage of the tight binding model is that it drastically reduces the computational expense down to a small number of overlap parameters. Furthermore, by projecting the atomic wavefunctions onto the resultant band structure, one can resolve the orbital character of the electronic structure. Thus far, the tight binding model is the first instance, discussed here, where the chemical composition of the lattice has been considered as this defines the basis of orbital wavefunctions considered when constructing the eigenfunctions.

2.1.4 Density Functional Theory

An alternative method for calculating electronic structure is density functional theory (DFT) [16]. This method is founded on the principle that the electron ground state density $\rho(\vec{r})$ uniquely identifies the potential acting on the electrons, which determines the groundstate wavefunction (first Hohenberg-Kohn theorem). Thus the groundstate wavefunction can be obtained by the minimisation of the total energy. The total energy is a function of the electron density, which is itself a function of only $\vec{r}$ (second Hohenberg-Kohn theorem). Like the tight-binding method, DFT solutions are expressed as linear combinations of a complete set of basis functions. In principle the set of basis functions is infinite, making the exact solution computationally impossible, but an approximation can be made using a limited number of wavefunctions corresponding to a subset of the atomic orbitals. Several commercial packages have been developed using DFT to calculate the electronic structures of materials, here the WIEN2k code [17] was used by collaborators, which typically reproduces measured band structures for weakly interacting systems accurately, except for the well known underestimation of the band gap and bandwidths [18]. Next, an overview of how the lattice structure and chemical makeup of the lattice further affects the resultant band structure will be given.

2.2 Spin-Orbit Coupling

Up until this point, all electrons have been treated on equal footing, except when making considerations for the Pauli exclusion principle, as the non-relativistic

Schrödinger's equation disregards their spin. It was previously shown how the application of an electric potential, in this case from a periodic lattice, dramatically affects the electronic structure. However, if instead of an electric field, a magnetic field is applied to the system, one cannot treat the dynamics of electrons with different spins the same and a relativistic approach is required. Including electric, ϕ, and magnetic, $\vec{A}$, potentials into the relativistic Dirac equation gives:

$$(H - e\phi)^2 = (c\vec{p} - \varepsilon\vec{A})^2 + m^2c^4, \tag{2.14}$$

where $\varepsilon = -e$ is the electron charge. In small to moderate magnetic fields, the resulting Hamiltonian reduces to:

$$\hat{H}\psi = \frac{-\hbar}{2m}\nabla^2\psi - \vec{\mu} \cdot \vec{B}\psi = (E + e\phi)\psi, \tag{2.15}$$

where $\vec{\mu} = e\vec{L}/2mc$ is effectively the magnetic moment due to the electron's orbital angular momentum. This term gives rise to the famous Zeeman effect where degenerate electronic states are shifted in energy, $\Delta E = \pm\mu B_0/2$, when a magnetic field, $\vec{B}$ is applied; however, one should note that electronic spin was not included in this derivation.

If the spin of an electron is included, one finds that additional corrections to the electronic energy levels can occur due to an "internal Zeeman effect" that arises between the electron spin magnetic moment and the orbital angular momentum of the electron in what is called spin-orbit coupling. Even in the absence of an external magnetic field, an electron processing around a charged nucleus, like those of a periodic lattice, will experience the nucleus' electric field as a magnetic field in the electron's rest frame. The inclusion of electronic spin into the Dirac equation gives:

$$\begin{aligned}\Bigg(\frac{1}{2m}(\vec{p} - \frac{\varepsilon}{c}\vec{A})^2 + \varepsilon\phi - \frac{\varepsilon\hbar}{2mc}\vec{\sigma} \cdot \vec{B} \\ + i\frac{\varepsilon\hbar}{4m^2c^2}\vec{E} \cdot \vec{p} - \frac{\varepsilon\hbar}{4m^2c^2}\vec{\sigma} \cdot (\vec{E} \times \vec{p})\Bigg)\psi = W\psi,\end{aligned} \tag{2.16}$$

where $W + m^2c^4$ is the total energy. The first two terms on the left-hand side are equivalent to those in the Shrödinger's equation, Eq. 2.15. The third term corresponds to the interaction energy $-\vec{\mu} \cdot \vec{B}$ of the magnetic dipole, whose moment is described by the operator $\vec{\mu} = \frac{\varepsilon \hbar}{2mc}\vec{\sigma}$. The fourth term is a relativistic correction to the energy and does not have a classical analogy. The fifth term describes the spin-orbit coupling [19].

Although, Eq. 2.16 appears to be extremely complicated, certain physical situations allow one to simplify some terms. By considering the motion of electrons around the nuclei of the periodic lattice, one can approximate the environment to the presence of a centrally symmetric electrical field, which can be written as:

$$\vec{E} = -\frac{1}{\varepsilon}\frac{\vec{r}}{r}\frac{dV}{dr}. \tag{2.17}$$

This approximation allows one to write the change in energy resulting from interactions of the spin with the magnetic field that the electron experiences as:

$$\begin{aligned} E_{SO} &= -\frac{\varepsilon \hbar}{4m^2c^2}\vec{\sigma} \cdot (\vec{E} \times \vec{p}) = \frac{\varepsilon}{2m^2c^2}\vec{s} \cdot \left(-\frac{1}{\varepsilon}\frac{\vec{r}}{r}\frac{dV}{dr} \times \vec{p}\right) \\ &= \frac{1}{2m^2c^2}\frac{1}{r}\frac{dV}{dr}(\vec{s} \cdot \vec{l}) \end{aligned} \tag{2.18}$$

where $\vec{s} = \hbar\vec{\sigma}/2$. One notes that for a given potential, flipping the direction of the electron's spin, i.e. $\vec{s} \rightarrow -\vec{s}$, changes the sign of the energy change. This suggests that states with their spin aligned parallel and anti-parallel to the orbit will have energy shifts in opposite directions. These energy shifts induce a spin-orbit splitting that lifts the two-fold degeneracy of the bands introduced from the non-relativistic Schrödinger picture, which ignored spin. This is the case in free-atoms and gives rise to the fine structure factor first seen in the hydrogen energy spectra, but as will be seen next section, this is not always the case in crystalline solids.

2.3 Importance of Global Symmetries

In free atoms, the lifting of the energy degeneracy for electronic states with the same orbital wavefunction but opposite spins is possible due to a lack of crystal symmetry. However, in certain solids, symmetries can forbid such splittings from occurring. One such symmetry is that of time-reversal (TR) symmetry, which holds for non-magentic materials and requires spin-degeneracy at certain high symmetry points of the Brillouin zone. One fundamental principle, Kramer's theorem, states that for every energy eigenstate of a time-reversal symmetric system with half-integer total spin, such as an electron, there is at least one more eigenstate with the same energy such that degeneracy is preserved between a state $\psi(r, s)$ and its complex conjugate $\psi^*(r, s)$ where the latter is obtained by a reversal of both wave vector and electronic spin. In other words, this requires that for any state $\vec{k}$ in the Brillouin zone, there exists a second state $-\vec{k}$ such that:

$$E(\vec{k}, \uparrow) = E(-\vec{k}, \downarrow). \tag{2.19}$$

Along with time-reversal symmetry, another fundamental symmetry is that of inversion-symmetry. If the unit cell of a material is invariant under the transformation $\vec{r} \rightarrow -\vec{r}$, such as the simple cubic lattice of sodium or iron, the material preserves inversion symmetry. The transformation of $\vec{r} \rightarrow -\vec{r}$ in real space is analogous to the transformation of $\vec{k} \rightarrow -\vec{k}$ in reciprocal space and therefore inversion symmetry requires:

$$E(\vec{k}, \uparrow) = E(-\vec{k}, \uparrow) \tag{2.20}$$

for every state in the Brillouin zone. The simultaneous presence of both time-reversal and inversion symmetry therefore requires $E(\vec{k}, \uparrow) = E(-\vec{k}, \uparrow) = E(\vec{k}, \downarrow) = E(-\vec{k}, \downarrow)$ and therefore all states in the Brillouin zone will be spin-degenerate.

Clearly, the chemical composition and the crystal structure is of utmost importance to the electronic structure of materials. For instance, in solid sodium, one finds a material which is both non-magnetic and crystallises in the body-centred cubic structure, so both time-reversal and inversion symmetry are preserved. However, if the sodium atoms are replaced with iron, the crystal structure is the same (other than a change in the lattice spacings), but, in iron and other magnetic materials, interactions between unpaired electrons give rise to long-range ordering of the electronic spins that lowers the system's total energy. This preferred orientation (majority-spin) results in a separation in energy for electronic states

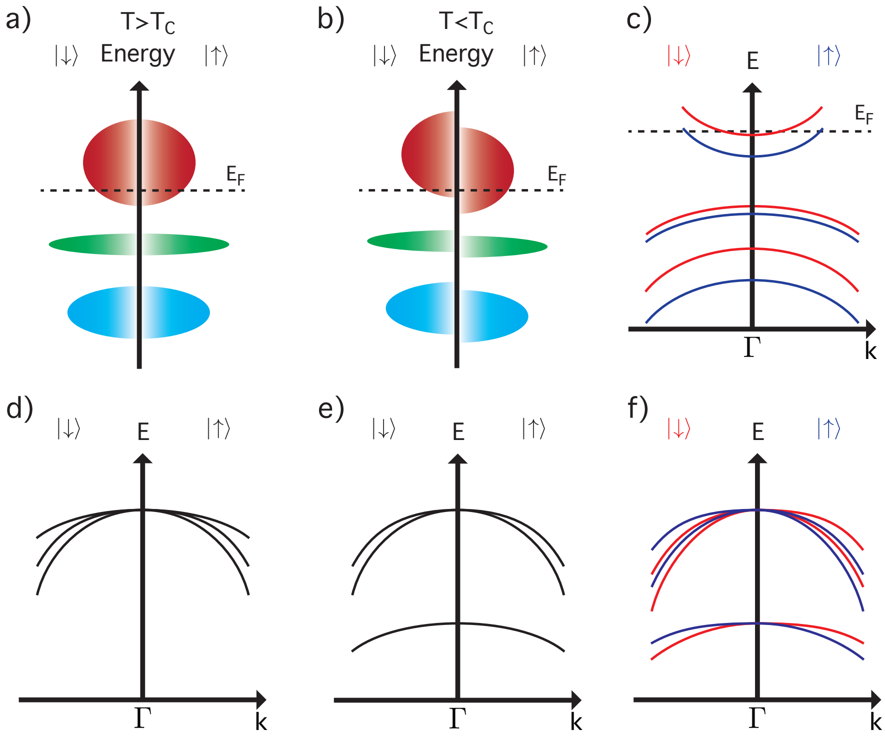

FIGURE 2.6: Effects of breaking global symmetries on electronic structure. a) Above the Curie temperature, ferromagnetic materials have equal populations of spin-up and spin-down states, but below T_C a ferromagnetic transition occurs that induces an exchange splitting which separates states for opposite spins in energy. c) This shift in energy creates an imbalance in spin populations that breaks time-reversal symmetry. d) The electronic states from 3 p-bands in a non-magnetic material without spin-orbit coupling are degenerate in energy at Γ and spin-degenerate everywhere in the Brillouin zone. e) In materials with heavy elements, spin-orbit coupling can cause the p-bands to split in energy, but not break the spin-degeneracy. f) However, if the crystal lattice lacks a centre of inversion, the spin-up and spin-down states will shift in energy, lifting the spin-degeneracy everywhere except Γ and other time-reversal points, without changing the population of spin-up and spin-down states. d-f) Adapted from Ref. [19].

at $\vec{k}$ with opposite spins, known as an exchange splitting, and an asymmetry in the population of electronic spins (i.e. more up-spins than down-spins) develops. This spin-population imbalance breaks time-reversal symmetry as for a state at $\vec{k}$ with majority-spin there is no corresponding state at $\vec{k}$ with spin-minority, Fig. 5.11c.

Returning to the case of a non-magnetic material, one can examine how a different choice of material and crystal structure can result in alternative modifications to the band structure. At the zone centre (Γ) of a Brillouin zone with cubic symmetry, a tight-binding toy-model of atomic p wavefunctions can be visualised as in Fig. 5.11d. In the case of light atoms, where spin-orbit interactions can be ignored, degeneracy occurs at Γ for the three p-bands, each of which is two-fold spin-degenerate. However, if the lattice is constructed of heavy atoms, like those of the transition metals, spin-orbit interactions are likely to be too large to ignore. In this case, a splitting of the $p_{3/2}$ and $p_{1/2}$ bands occurs, as seen in Fig. 5.11e, but spin-degeneracy is expected for each band. Lastly, if the crystal lattice is altered in such a way that breaks inversion symmetry, the spin-degeneracy will be lifted, except at certain high symmetry points where time-reversal symmetry enforces $E(\vec{k}, \uparrow) = E(-\vec{k}, \downarrow)$, such as at Γ. Although the spin-degeneracy of each band has been removed and therefore a spin-polarisation exists along each band, except at these TR points, summing the global spin-populations will reveal no preferred direction as time-reversal symmetry has not been broken and therefore every spin-up state has a corresponding spin-down state at opposite $\vec{k}$.

As has just been demonstrated, some of the electronic behaviour of solids can be determined by completely ignoring the crystal lattice and treating the electrons as a non-interacting gas. However, in order to explain physical properties, such as why some materials are insulators and others metals, the free Fermi gas is inadequate. By including the periodic potential of the crystal lattice, Bloch wavefunctions were shown to present a computationally tractable solution for calculating electronic band structures. Furthermore, by building such solutions using linear combinations of atomic wavefunctions, band structures that account for the localisation of valence electrons and delocalisation of conduction electrons can be calculated. Finally, how spin interacts with electron motions through the lattice ions was discussed, as well as how the chemical composition and underlying crystal structure can further manipulate the band structure. Armed with an understanding of the fundamentals of electronic structure, an overview of the experimental techniques developed to directly measure the band structure of single crystals and thin film samples will now be presented, before discussing one method used for the synthesis of the latter type of materials.

Chapter 3

Experimental Techniques

Countless experimental techniques have been developed to garner information regarding important features of the electronic structure of crystalline materials. For instance, optical absorption spectroscopy can be used to indirectly measure the size of a semiconductor's band gap by probing materials with light to excite electrons into unoccupied states above the Fermi level. Here, a powerful method for measuring the occupied states of semiconducting and metallic samples will be presented. Then a discussion of one method for the growth of thin film materials suitable for measurement using this technique and the associated techniques used to characterise the films will be provided. This will complete the theoretical foundation necessary for the experimental investigations presented in Chapters 5-9.

3.1 Angle-resolved photoemission spectroscopy

Angle-resolved photoemission spectroscopy (ARPES) is a tool to directly observe the electronic structure of a solid by use of the photoelectric effect. This technique uses high-energy ($h\nu$ on the order of tens to hundreds of eV), monochromatic light to overcome an electron's binding energy, E_B, and the material's work function, ϕ, in order to eject photoelectrons into vacuum which are then detected, Fig. 3.1. During the photoemission process, both energy and momentum must be conserved and thus:

$$\begin{aligned} E_{kin} &= h\nu - \phi - E_B, \\ \mathbf{k}_f &= \mathbf{k}_{h\nu} + \mathbf{k}_i, \end{aligned} \tag{3.1}$$

where E_{kin} is the kinetic energy of the photoelectron and $\mathbf{k}_f, \mathbf{k}_i, \mathbf{k}_{h\nu}$ are the momentum of the electron in vacuum, in the solid and the absorbed photon, respectively [20]. Because the momentum of the photon is relatively low in this energy range, it can be neglected such that $\mathbf{k}_f$-$\mathbf{k}_i$=0 (or $\mathbf{k}_f$-$\mathbf{k}_i$=$\mathbf{G}$ through a translation by the reciprocal lattice vector) [21], allowing for details of the initial state of the electron to be recovered from the photoemitted electron. The transition from an N-electron system to an (N-1)-electron system plus a photoelectron is governed

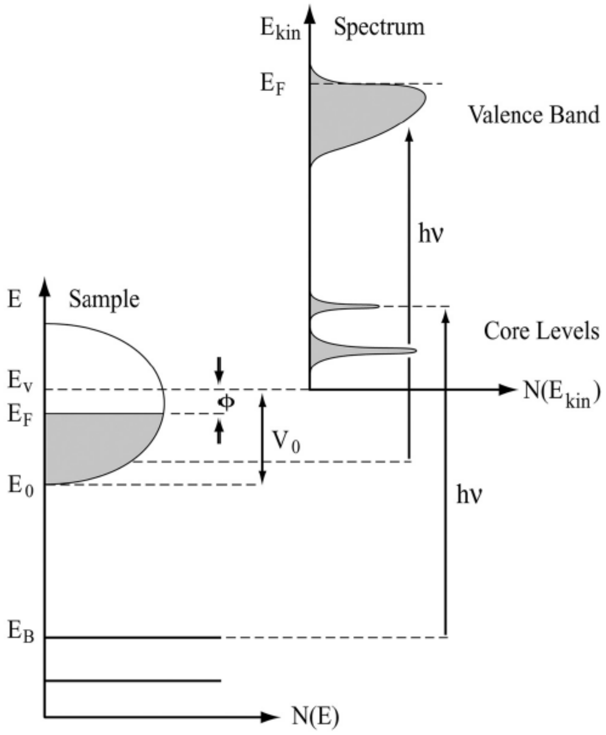

FIGURE 3.1: Energetics of the photoemission process. Electrons with binding energy, E_B, in the single-crystal material are excited by photons with energy $h\nu$, into vacuum. The kinetic energy of the photoemitted electrons, E_{kin}, is given by E_{kin}=$h\nu$ -ϕ-E_B, where ϕ is the material's work function. Adapted from [20].

by Fermi's Golden Rule which can be written as:

$$\omega_{if} = \frac{2\pi}{\hbar} | \langle \Psi_f | H_{PE} | \Psi_i \rangle |^2 \delta(\epsilon_f - \epsilon_i - h\nu) \delta(\boldsymbol{k}_f - \boldsymbol{k}_i - \boldsymbol{k}_{h\nu}) \tag{3.2}$$

where $|\Psi_{i/f}\rangle$ are the initial and final states, respectively, and H_{PE} describes the interaction with the photon, which can be written as $H_{PE} = e/(m_e c)\mathbf{A} \cdot \mathbf{p}$, assuming the electromagnetic vector potential, $\mathbf{A}$, does not change over atomic distances, although, this does not hold at surfaces.

The process of absorption/excitation, travelling to the surface and emission of the electron from the crystal are most accurately described as a single transition; however, this requires a complex model and a simpler *three-step model* is often employed [21]. The details of this model are intricate and the reader is referred to a comprehensive review article by Damascelli [21]. The key feature is that by assuming electron escape times are much shorter than the response time of the system, interactions between the photoelectron and the (N-1)-electron system can be ignored. This is called the *sudden approximation* and allows for the photoemission intensity to be written as:

$$I(\mathbf{k}, E_{lin}) = \frac{2\pi}{\hbar} \sum_{fi} |M_{\mathbf{k},f,i}|^2 \sum_s |c_{s,i}|^2 \delta(E_{kin} + \epsilon_s^{N-1} - \epsilon_s^N - h\nu), \tag{3.3}$$

where ϵ_s^N and ϵ_s^{N-1} are the energy of the eigenstate s of the N- and (N-1)-electron system, respectively, $|M_{\mathbf{k},f,i}|^2 = | \langle \psi_{\mathbf{k},f} | H_{PE} | \psi_{\mathbf{k},i} \rangle |^2$ is the single-electron photoemission matrix element describing the probability of a bound electron going from state $|\psi_{\mathbf{k},i}\rangle$ in the sample to the final state in vacuum $|\psi_{\mathbf{k},f}\rangle$ and $|c_{s,i}|^2$ is the probability that the removal of the electron from state i will leave the (N-1)-electron system in the excited state s [21]. Often one writes $A = \sum_s |c_{s,i}|^2$ and calls A the spectral function. Photoemission intensity is only observed for (N-1)-electron excited states, $\Psi_{f,s}$, that have non-zero overlap with the (N-1)-electron groundstate,

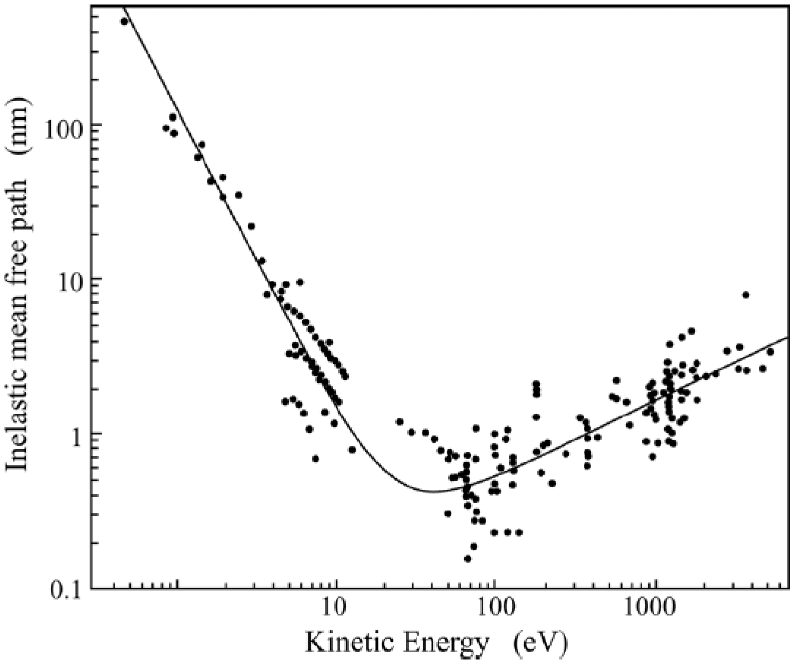

FIGURE 3.2: Universal curve for the inelastic-mean-free-path (IMFP) of an electron. A minimum in IMFP is reached at ~40eV, making ARPES measurements at photon energies close to this the most surface sensitive. Adapted from [21].

Ψ_i, such that:

$$\begin{aligned} A(\mathbf{k}, E) &= \sum_s |\langle \Psi_{f,s}(N-1) | \Psi_i(N-1) \rangle|^2 \\ &= \sum_s |\langle N-1, s | c_{\mathbf{k}} | N \rangle|^2 , \end{aligned}$$

where $c_{\mathbf{k}}$ is the electron annihilation operator [20]. The spectral function is intimately tied to the single-particle Green's function, $G(\mathbf{k}_1, \mathbf{k}_2, E)$, which describes the probability that an electron in state $\mathbf{k}_1$ will be in state $\mathbf{k}_2$ after a scattering process with energy transfer E has occurred. Thus, measurement of the angular and energy dependent photoemission current yields direct observation of the N-electron groundstate. The single-electron photoemission matrix element $|M_{\mathbf{k},f,i}|^2$, which is related to the experimental geometry and orbitals of the initial state, also produces attenuation of the photoemission current and will be discussed in greater detail in Ch. 8.

The second part of the three-step model is the transport of the photoelectron to the surface. During this process, the electron undergoes elastic and inelastic scattering, the latter of which results in a loss of kinetic energy by the photoelectron to exciting secondary electrons, plasmons and phonons [20]. These losses limit the escape depth, d, of the electrons such that the intensity of the emitted electrons is given by:

$$I(d) = I_0 e^{\frac{-d}{\lambda}} \tag{3.4}$$

where I_0 is proportional to the number of the excited electrons and λ is the inelastic-mean-free-path, which has an energy dependence roughly described by the "universal curve," shown in Fig. 3.2. The energies used in ARPES measurements generally limits the probing depth to a few Ångström and thus extremely well-ordered, atomically-flat and clean surfaces are required.

The third process in the three-step model is the escape of the electron from the surface. The abrupt change at the material surface breaks translational symmetry and thus the perpendicular momentum $\mathbf{k}_\perp$ is not conserved, making it not a good quantum number. On the otherhand, translational symmetry is preserved in the in-plane directions and therefore the parallel momentum is well conserved [20]. One can write the in-plane and out-of-plane momenta as:

$$\begin{aligned} \mathbf{k}_\parallel &= \sqrt{2mE_k/\hbar^2}\sin\theta \\ \mathbf{k}_\perp &= \sqrt{2m/\hbar^2(E_k\cos^2\theta + V_0)}, \end{aligned} \tag{3.5}$$

where the free electron final state approximation is used to describe the out-of-plane momentum. V_0 is the inner potential corresponding to the energy of the bottom of the valence band relative to the vacuum level [21]. The inner potential is related to the depth of the potential well of the "particle-in-a-box" picture of the free electron and varies from material to material. In order to determine the value of V_0, one can vary the photon energy of the probing light and construct the $\mathrm{k}_\perp$ dispersion, thereby deducing the value of V_0 from the repeated appearance of band features in adjacent Brillouin zones. Additionally, the finite escape depth

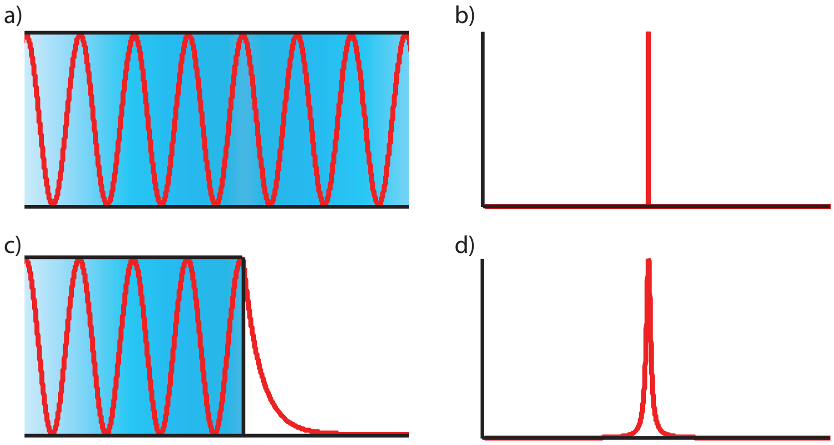

FIGURE 3.3: Crystal momentum as a quantum number. a) The translational symmetry of the in-plane crystal lattice conserves the in-plane crystal momentum, b) with the Fourier transform of an electron's wavefunction given by a δ function at k_0. c) On the other hand, the breaking of translational symmetry at the vacuum interface does not conserve the crystal momentum perpendicular to the sample surface, as d) the Fourier transform of the electron's wavefunction is given by a distribution of $k_\perp$ values.

λ of the photoelectrons introduces an intrinsic uncertainty in the momentum of electrons perpendicular to the crystal surface. Within the material ($z < 0$), the wavefunction of an emitted photoelectron can be approximated by:

$$\psi(z) = \frac{1}{\sqrt{\lambda}} e^{ik_{z0}z} e^{z/2\lambda}, \tag{3.6}$$

where k_{z0} is the out-of-plane momentum of the photoelectron [22]. The squared modulus of the Fourier transform $|\phi(k_z)|^2$ of Eq. 3.6 is proportional to:

$$|\phi(k_z)|^2 \propto \frac{1}{2\pi\lambda} \frac{1}{(k_z - k_{z0})^2 + (1/2\lambda)^2}, \tag{3.7}$$

which implies the uncertainty of k$_z$ is given by a Lorentz function with full width at half maximum of $1/\lambda$. Thus, although ARPES measurements taken using a given photon energy will be centred on a specific value of $k_z = k_{z,0}$, a finite range of k_z values will be simultaneously probed, with an intensity attenuation given by $|\phi(k_z)|^2$.

Once the photoelectrons have escaped the crystal surface, they are separated

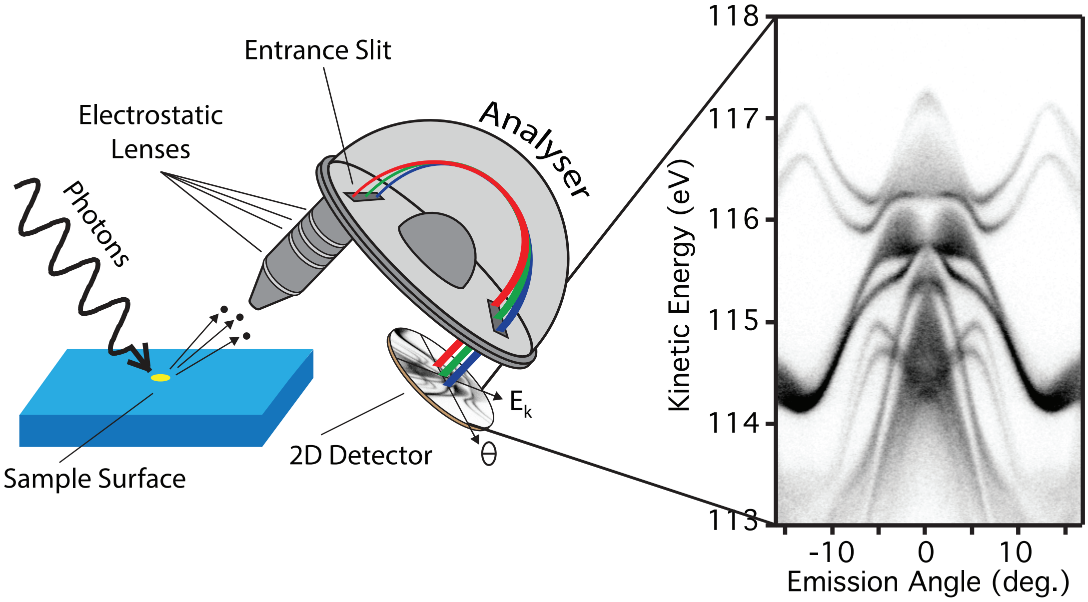

FIGURE 3.4: Cartoon of ARPES setup. Photons incident on the sample surface cause the photoemission of electrons through the photoelectric effect. These electrons are focused and separated by their angular and energy distributions using electrostatic lenses and a hemispherical analyser before being projected onto a 2D-CCD (example data is of WSe_2 data taken at Diamond Light Source).

by their emission angle (horizontal axis of Fig. 3.4) using electrostatic lens elements and focused into a hemispherical electron analyser (HEA) that is comprised of two charged hemispheres that bend the electrons onto a 2D-CCD array. By applying precise voltages to these hemispheres, the electron distribution is separated out by kinetic energy (vertical axis). Using Eq. 3.1 and 3.5, the electron distribution can then be put onto binding energy and momentum, $\mathbf{k}_{\parallel}$, scales, respectively [20]. Only a finite kinetic energy range can be detected on the CCD at one time, but by altering the voltages applied to the analyser, one can sweep across energy ranges to probe a wider range of the band structure in a single measurement. While this technique has revolutionised condensed matter physics with its ability to directly measure the electronic structure, it is not without its difficulties and limitations.

3.1.1 Light sources

ARPES measurements require monochromatic light sources in order to achieve the highest energy and momentum resolution. Most laboratory based setups use gas discharge lamps (typically He) for a light source that has well known atomic spectral lines that can be separated out using a monochromator. This, however, only allows for measurements at a few photon energies and thus little information about the band structure in the $\mathrm{k}_{\perp}$ direction can be gained. This is problematic for samples whose band structures have significant out-of-plane dispersion, as well as making it difficult to disentangle bulk 3D electronic structure from 2D surface states. Additionally, the photon energy produced using traditional He lamps is relatively low, $h\nu$=21.2 eV, which typically covers only a small area of the Brillouin zone, except for structures with large lattice spacings and therefore small Brillouin zones. The limited range of $k_{\|}$ probed in a single ARPES measurement at this low photon energy requires the sample's orientation to be greatly altered to map the full Brillouin zone, which can cause problems for sample manipulators that have restricted motions.

To overcome this issue, synchrotron radiation can be used whereby a stored beam of electrons pass through an undulator, which creates a precise magnetic field, causing the electron to oscillate and radiate light of particular polarisation (linear horizontal, linear vertical, etc.) that is highly peaked at a certain frequency. By filtering the radiated light using a grating monochromator, one can select the desired photon energy with a high degree of resolving power, R [21]. In this way, the photon energy can be varied and the $\mathrm{k}_{\perp}$ dispersion can be measured. Energy and momentum resolution are given by:

$$\begin{aligned} \mathrm{R} &= \mathrm{E}/\Delta\mathrm{E}_m \\ \Delta\mathbf{k}_{\|} &\simeq \sqrt{2mE_k/\hbar^2}\cdot\cos\theta\cdot\Delta\theta, \end{aligned} \tag{3.8}$$

where ΔE_m is the energy resolution of the monochromator. Therefore decreasing the photon energy improves the in-plane momentum resolution. Energy resolutions of 1-2meV and angular resolutions of 0.2° have been achieved at synchrotrons using photon energies of 20eV [21].

3.1.2 Spin-ARPES

Another useful advancement in ARPES technology is the ability to resolve the spin of the photoelectrons. Spin- and angle-resolved photoemission spectroscopy (SARPES) combines the use of a spin polarimeter (such as a Mott-polarimeter) [23] with a HEA, described above. This type of polarimeter uses Mott scattering to deflect the trajectories of electrons based off their spin and, by measuring the energy distribution of the deflected electrons, one can measure the spin-polarisation of the band structure. An electron that passes through the electric field of a high-Z nucleus will experience a magnetic field in its own reference frame. Because the electron has spin angular momentum, the force from the magnetic field will deflect the electron differently depending on the orientation of it's spin [24, 25]. This is very similar to the spin-orbit coupling effect discussed previously, except the electrons considered here move through a vacuum and are not bound within a periodic lattice. The potential scattering curves are skewed depending on the electron's spin, introducing asymmetries in the left/right scattering probabilities:

$$A = \frac{I_L - I_R}{I_L + I_R} \tag{3.9}$$

where I_L and I_R are the currents detected in the left and right channels of the Mott polairmeter. The Sherman function (S_{eff}) is a measure of detector efficiency and relates this asymmetry to the actual polarisation of the photoelectrons, P_e, according to:

$$A = S_{eff} P_e. \tag{3.10}$$

At the typical photon energy used for SARPES measurements, the cross sections for such scattering events are extremely low and therefore the electrons are accelerated up to 25keV before being scattered. Still, Mott-polarimeters are extremely inefficient compared to spin-integrated measurements [23]. Another tradeoff of this form of spectroscopy is that traditional spin polarimeters effectively operate as single-channel detectors and therefore one loses the ability to acquire the 2D grid of angle and energy distribution of initial states [26], although 2D spin-detectors have been developed in recent years.

3.1.3 Sample Preparation

As mentioned, ARPES requires atomically-flat surfaces that are free from contaminants. There are three methods to acquire such a clean surface: sputtering and annealing, in-situ cleaving, and in-situ growth. The first relies upon using inert gases with large kinetic energy to bombard atoms on the surface (which have been exposed to atmospheric pressures and have become oxidised, absorbed with CO_2, hydrogen, water, etc.) and remove them. Then the sample is heated and cooled to produce a crystalline structure with a clean surface. In-situ cleaving is an especially useful method for highly-layered materials such as the transition-metal dichalcogenides. Weak interlayer bonding allows one to break off part of the sample, using a post adhered to the surface, revealing a layer of the clean, bulk crystal. This technique is the one utilised in Chapters 5-6 for the preparation and measurement of WSe_2 single crystals.

In-situ growth of thin films also allows for clean surfaces to be achieved and transferred in vacuum for ARPES measurements. One such growth technique is discussed next in relation to work at Diamond Light Source where such a growth system has been attached to the I05 HR-ARPES endstation, capable of producing Gd-doped EuO films, the subject of Chapters 7-9, with a growth rate of approximately one monolayer every two minutes.

Once a clean surface has been achieved, measurements can begin; however, there is a limited lifetime which varies from sample to sample (between hours to days) because the imperfect vacuum (ideally 10^{-10}-10^{-11} mbar) in the chamber only slows the surface degradation, it does not completely stop it. Additionally, in synchrotron-based ARPES experiments, the high intensity photon flux of the light source can damage the surface of delicate materials, but in some cases the high powered beam can also be used to preserve the surface by providing enough energy to remove weakly-bonded contaminants.

3.2 Molecular beam epitaxy

As mentioned, one method for preparing samples suitable for ARPES measurements is molecular beam epitaxy (MBE), whereby thin film samples are grown on single crystal substrates using one or more molecular or elemental sources, allowing for precise control of the films' stoichiometry. Here, the basic principles for developing MBE growth recipes will be described, as well as the various characterisation techniques associated with determining the quality and composition of films grown using this method.

3.2.1 Basic principles

Molecular beam epitaxy allows for the layer-by-layer growth of thin films at a rate on the order of 5Å/min. For such controlled growth, ultra pure (99.9% purity minimum) source material is required to reduce the presence of contaminants that act as impurity sites in the resultant crystal structure. The source material is placed in specially designed crucibles, typically made of pyrolitic boron nitride (PBN), aluminate (Al_2O_3), tantalum or molybdenum, which are chemically stable to extremely high temperatures, can be made with low impurities, and are chosen to prevent alloying with the source material at high temperatures. These crucibles are then heated in effusion cells, typically using filaments also made of tantalum or molybdenum, until the source material sublimates, releasing a small vapour pressure of atoms, see Fig. 3.5. To obtain high-purity films, the mean free path of the emitted atoms needs to be longer than the distance to the target substrate and

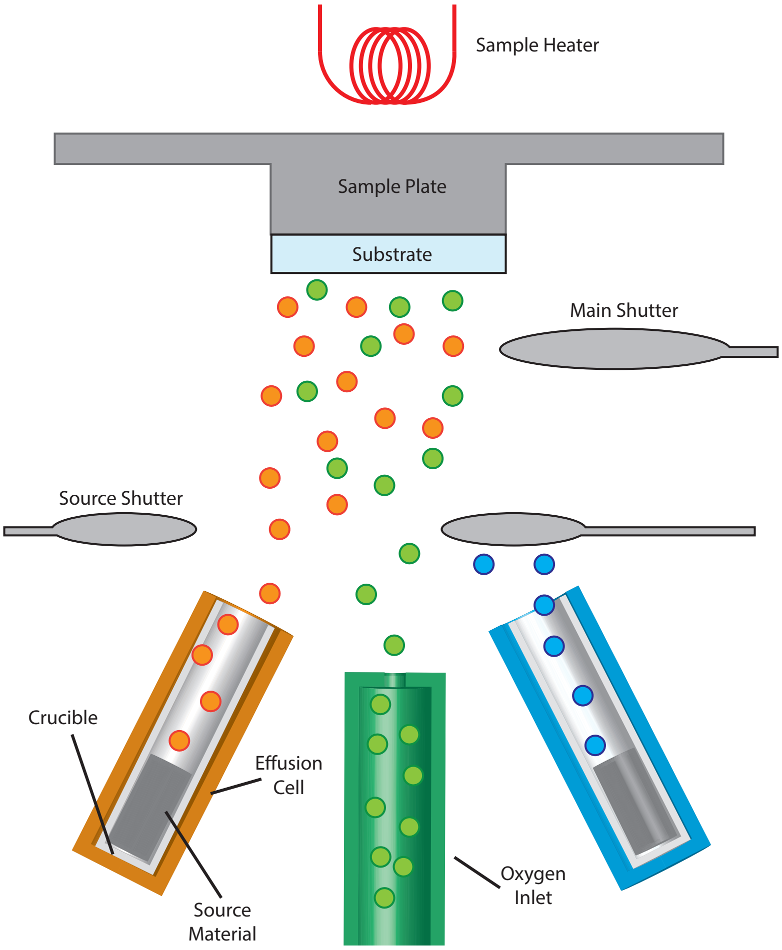

FIGURE 3.5: Cartoon of molecular beam epitaxy setup. A single-crystal substrate is suspended upside-down and the backside of the sample plate is heated with a filament. High-purity source material inside crucibles is heated with effusion cells, producing highly directional fluxes of atoms. Additionally, for oxide MBE systems, an oxygen inlet is required. Magnetic shutters above the sources and below the substrate can be opened and closed to allow or prevent the exposure of the substrate to some or all of the fluxes.

therefore the chamber pressure must be reduced significantly. Typically, ultra-high vacuum pumping is implemented to reach the pressure requirements which are on the order of 10^{-9}mbar or better. The high temperatures of the effusion cells also usually dictates water cooling or a cryoshield being used to prevent the effusion cells from breaking and to reduce the release of contaminants from the chamber walls which can outgas when heated. A specific example of one setup is described in the next chapter and can be viewed in Fig. 4.1

The crucibles and effusion cells are designed such that the emitted atoms are highly directional and form a beam of material that is aimed towards the sample stage where a polished single-crystal substrate is placed. In many MBE systems, this substrate sits upside-down on a rotatable platform that can also be heated to a desired temperature, using standard UHV methods such as tungsten filaments or silicon-carbide disks, Fig. 3.6a. Because typical MBE systems have multiple sources, the alignment of effusion cells is crucial to provide a large area of approximately uniform distribution of evaporated material with sufficient overlap between all sources. However, the slight angling of the effusion cells gives a small gradient of flux across the target area and therefore sample rotation is typically implemented to improve sample homogeneity. Magnetic shutters with opening/closing durations significantly shorter than deposition times are used to shield the substrate from unwanted fluxes while exposing it to only the desired source material. The ability to shutter the individual atomic fluxes allows for the sources to be kept at a constant temperature during growth cycles and therefore at well-defined flux rates.

In order to calibrate the fluxes, two pieces of equipment can be used: a quartz

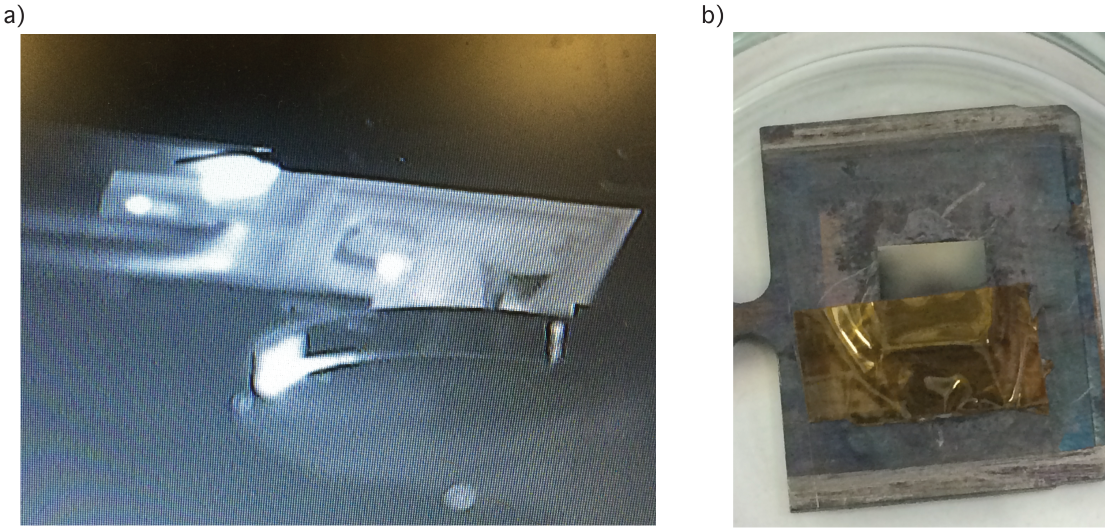

FIGURE 3.6: Molecular beam epitaxy sample orientation and flux calibration. a) Thermal image of heated 3x3mm substrate on posted sample plate, with main shutter closed. b) Exposing part of a substrate to an atomic flux produces a step-edge, measurable by AFM, which can be used to determine deposition rate.

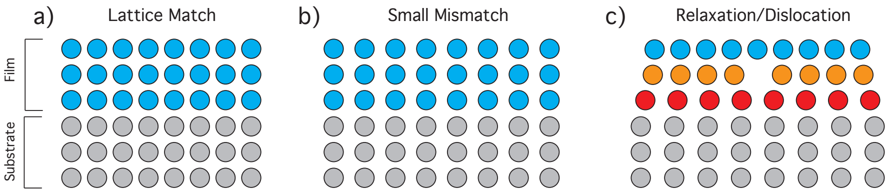

FIGURE 3.7: Lattice mismatch effects on film growth. a) Perfect match between substrate and film lattice constants results in unstrained growth while b) a small mismatch can induce strain into grown film. However, if the mismatch is too great c) the film can relax back into a lattice constant closer to the unstrained film, introducing abrupt dislocations and vacancies.

crystal microbalance or a beam flux monitor. The former uses changes in the resonance frequency of a quartz crystal to determine the amount of deposited material on its surface over a period of time and, by knowing the density of the evaporated material, a deposition rate can be determined. A beam flux monitor, on the other hand, is essentially an ion gauge which is placed in the path of the source flux and by measuring the change in the pressure with the source shutter open and closed, one can determine an effective partial pressure from the source material. This presents a complication, as one either needs to relate the pressure to an ionisation probability that differs between materials (and is not known for every element) or relate the pressure to a deposition rate. The latter can be performed by evaporating material onto a substrate that is partially covered with Teflon tape, which is UHV compliant, see Fig. 3.6, and by measuring the step-edge that develops upon removal of the tape using atomic force microscopy (AFM). Once a known deposition rate of each desired material is known a film can be grown by opening and closing the relevant shutters to correspond with the correct ratio of deposited materials.

High quality films with low impurity concentrations can be grown using this method because the moderate temperatures of the heated source materials provides a low growth rate where the incoming atoms have energies only slightly higher than their equilibrium lattice energies. In other words, incoming atoms incident on the substrate surface have enough energy to make small movements along the surface to find the appropriate lattice position that leads to the lowest energy crystal structure and the deposition rate is low enough that the atoms can settle into place before another layer is deposited overtop, preventing the presence of significant vacancies. The choice of substrate is of utmost importance for films with single domains and the lattice spacing is usually matched as close as possible to the in-plane lattice constant of the material to be grown. Although introducing a small mis-match in the lattice constants of the film and substrate can induce epitaxial strain in the resultant films, Fig. 3.7b, this can reduce the quality of films as relaxations occur which introduce vacancies and dislocations in the crystal structure, Fig. 3.7c.

In addition to the presence of dislocations and vacancies, the growth mode drastically effects the quality of the film and the surface homogeneity [27]. There are three main growth mechanisms, which are effected by substrate temperature, deposition rate and surface energy, as shown in Fig. 3.8. In the ideal case of layer-by-layer (Frank-van der Merwe) growth, subsequent monolayers are formed only after the completion of the underlying layer. By precisely timing the closing of shutters, one can achieve atomically flat surfaces. Volmer-Weber growth is characterised by the formation of 3D islands which increase in both height and width

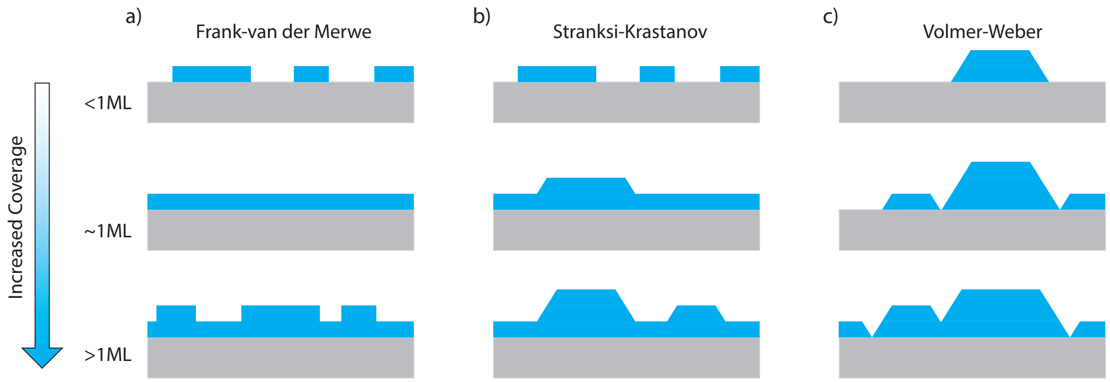

FIGURE 3.8: MBE growth modes. a) Layer-by-layer (Frank-van der Merwe) growth provides high quality thin films as additional layers are only started after the completion of the underlying monolayer. b) Stranksi-Krastanov growth is characterised by the formation of 3D islands which form on top of a "wetting" layer, while c) Volmer-Weber growth produces rough surfaces as complete monolayers are formed only when the boundaries of 3D islands join together.

as deposition of material is increased until eventually the islands form a sheet. Stranski-Krastanov growth is a hybrid of the previous two mechanisms, in which 3D islands form on top of a "wetting" layer. Next, an overview of some key techniques used to characterise the film quality and composition will be presented.

3.3 In-Situ Characterisation

Epitaxial growth of high quality films through MBE is dependent upon a large range of parameters: substrate material, substrate temperature, source flux ratios, growth rate, and chamber pressure, to name a few. This presents a huge parameter space to explore when developing a new growth recipe, even for simple mono and binary systems. Thankfully, there is a range of in-situ techniques that can be used to determine sample quality and composition that allow for increased sample throughput and near real-time analysis of growth parameters. Below is a discussion of three techniques which are essential for such determination.

3.3.1 Reflection High Energy Electron Diffraction

Arguably the most important film characterisation technique, reflection high energy electron diffraction (RHEED) allows for real-time analysis of a film's surface structure and quality during growth. Unlike most other forms of electron diffraction, a typical RHEED setup uses a very shallow angle of deflection ($\sim 5^\circ$) which restricts diffraction to only the surface layers of the film. Usually diffraction in bulk materials is the result of interference effects of the 3D crystal structure, but because only the surface layers contribute to diffraction in RHEED, one is only concerned with the surface lattice given by [28]:

$$\vec{R}_n = n_1\vec{a} + n_2\vec{b} \tag{3.11}$$

where $\vec{a}/\vec{b}$ are the real-space lattice vectors. The corresponding surface reciprocal lattice vectors are given by:

$$\vec{a}^{*} = 2\pi \frac{\vec{b} \times \hat{z}}{\vec{a} \cdot (\hat{b} \times \hat{z})}$$
$$\vec{b}^{*} = 2\pi \frac{\vec{a} \times \hat{z}}{\vec{b} \cdot (\hat{a} \times \hat{z})},$$

where $\hat{z}$ is the unit vector perpendicular to the sample surface. Because of the surface sensitivity of RHEED, there is no diffraction condition in the direction perpendicular to the sample surface and thus diffraction is observed when:

$$\vec{S}_{\|} = \vec{k}_{f,\|} - \vec{k}_{i,\|} = \vec{B}_m \tag{3.12}$$

where $\vec{S}_{\|}=h\vec{a}^{*} + k\vec{b}^{*}$ gives the in-plane lattice sites, $\vec{k}_{f/i,\|}$ are the scattered and incident wavevectors, respectively, and $\vec{B}_m=m_1\vec{a}^{*} + m_2\vec{b}^{*}$, is the spacing of the RHEED pattern. Therefore, for films with near perfect surfaces, the resulting diffraction pattern on the fluorescent screen is not a set of sharp points, as in 3D diffraction, but a series of long thin rods. The spacing of these RHEED streaks is related to the in-plane lattice constant by:

$$a = \frac{2\pi}{\theta K}, \tag{3.13}$$

where θ is the angle between two RHEED streaks and K is the distance between the RHEED screen and sample. Because one does not generally know K or θ, it is generally easier to determine the in-plane lattice constant of a grown film, a_{film}, relative to that of the underlying substrate, a_{sub}, using:

$$\frac{d_{film}}{d_{sub}} = \frac{a_{sub}}{a_{film}}, \tag{3.14}$$

where $d_{film/sub}$ is the spacing of RHEED streaks for the film and substrate, respectively.

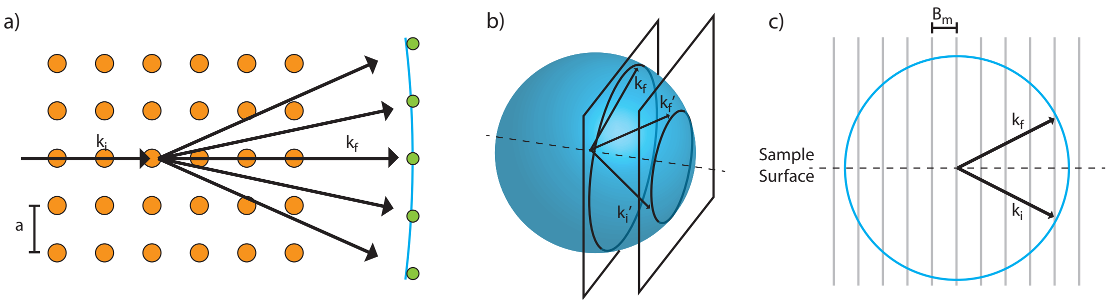

FIGURE 3.9: Reflection diffraction of high energy electrons. a) High energy grazing incident electrons with wavefector k_i are diffracted off the surface layers of a crystalline material with a wavevector k_f onto a fluorescent screen (green dots). b) The scattering events that conserve momentum and energy form a Ewald's sphere. Planes cutting through the sphere, normal to the sample surface (dashed line) trace out circles. c) Each of these planes contributes to the RHEED streaks where the intersection of the reciprocal lattice rods, spaced by B_m, and the Ewald sphere satisfy the diffraction conditions.

RHEED is a vital characterisation technique because it not only allows one to determine the in-plane lattice constant, but also gives information about surface quality and growth rate, all of which can be observed during growth along different crystallographic orientations utilising a rotating sample stage. The intensity and uniformity of the RHEED streaks is directly related to the flatness of the sample surface, as depicted in Fig. 3.10. For atomically flat surfaces, free from dislocations and defects, the RHEED streaks will be sharp and uniform with maximal intensity. However, as atoms are added to the surface, the surface becomes rougher, i.e. no longer atomically flat, and the streaks lose intensity as a single high-intensity region forms along the rods. For epitaxial growth, minimal intensity is reached when half of the film surface is covered as further addition of atoms fills in the vacancies in the current surface layer and eventually a complete layer is formed which leads to a peak in the oscillatory intensity function. This periodic fluctuation in the intensity of the streaks, known as RHEED oscillations, can be used to determine the deposition/growth rate of films and is extremely useful for timing the opening and closing of shutters when growing heterostructures. However, if the growth is not epitaxial, intensity oscillations

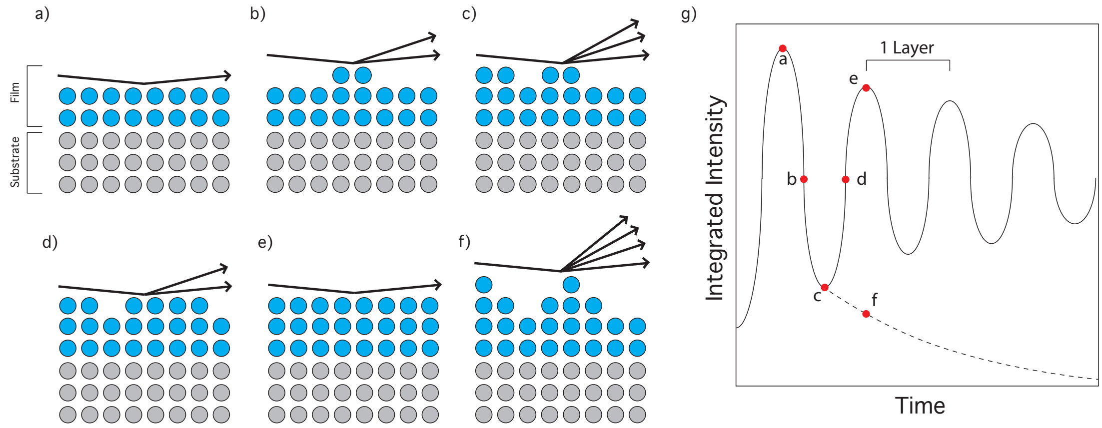

FIGURE 3.10: Surface coverage vs. RHEED intensity. a-e) For epitaxial growth, increasing surface coverage produces g) oscillatory behaviour in the integrated intensity of RHEED streaks whereas f) growth of 3D islands produces diffraction spots and reduces streak intensity.

do not occur as an atomically flat surface fails to form. For films with near pristine crystal structure, inelastic scattering gives rise to additional lines of intensity, Kikuchi lines, directed at angles relative to the vertical RHEED streaks [28]. Thus RHEED is an excellent tool for observing film growth and surface quality, as rough surfaces, which can also develop past a critical film thickness, will not produce RHEED patterns with uniform streaks, but have an intensity profile that is peaked at the position corresponding to 3D diffraction.

Additionally, RHEED guns use electrostatic fields to deflect the electron beam which allows for fine-tuning of alignment. This also allows one to track the beam across the film's surface to determine the uniformity of the surface quality. For large films, temperature gradients can develop across the substrate depending on the methods used for fixing the substrate to its holder. Also, differences in chemical composition due to inhomogeneity in beam fluxes and growth conditions can occur given the larger surface area. For small films, such as the 3x3mm samples that were produced in Chapter 7-9, growth conditions tend to have a smaller effect on inhomogeneity. As mentioned, because of the surface sensitivity of ARPES, atomically flat surfaces free of dislocations are needed and using RHEED such pre-requisites can be tested for.

3.3.2 Low Energy Electron Diffraction

Another method for determining surface structure in single-crystal materials is low energy electron diffraction (LEED), but unlike RHEED which uses grazing incidence diffraction, LEED uses a collimated beam of electrons normal to the surface which are elastically scattered back onto a fluorescent screen. Similar to ARPES, the electrons incident on the sample will lose kinetic energy due to inelastic scattering and therefore the inelastic mean free path of the electrons limits the depth to which the crystal structure can be probed. The mean free path for electrons is at its minimum in the energy range typically used for LEED (20-200eV), meaning that only the first few atomic layers are probed. The surface sensitivity of LEED is useful in determining the surface structure, including surface reconstructions and adsorbate patterns.

Like a RHEED setup, a LEED unit consists of an electron gun and fluorescent screen, Fig. 3.11a; however, with LEED, a set of electrostatic grids is used to filter out inelastically scattered electrons and the electron gun, screen and grids form a single unit. The electron beam is represented as a plane wave with a wavelength given by the de Broglie relation:

$$\lambda = \frac{h}{\sqrt{2mE_k}} \tag{3.15}$$

and will constructively interfere when backscattered if the Laue condition is met:

$$\begin{aligned} \vec{k} - \vec{k}_0 &= \vec{G}_{hkl} \\ \vec{G}_{hkl} &= h\vec{a}^* + k\vec{b}^* + l\vec{c}^* \end{aligned} \tag{3.16}$$

where $\vec{G}_{hkl}$ is a reciprocal lattice vector given by $\vec{a}^*, \vec{b}^*$ & $\vec{c}^*$, $\vec{k}_0 = 2\pi/\lambda$ is the incoming wave vector and $\vec{k}$ is the scattered wave vector. Because only elastically scattered electrons are considered, the wave vector is unchanged, i.e. $|\vec{k}_0| = |\vec{k}|$. Just like in the RHEED, the surface sensitivity relaxes diffraction conditions in the direction perpendicular to the surface and therefore diffraction occurs when:

$$\vec{k}^{||} - \vec{k}_0^{||} = h\vec{a}^* + k\vec{b}^*, \tag{3.17}$$

where the surface reciprocal lattice vectors are given by:

$$\vec{a}^* = 2\pi \frac{\vec{b} \times \hat{z}}{\vec{a} \cdot (\hat{b} \times \hat{z})}$$
$$\vec{b}^* = 2\pi \frac{\vec{a} \times \hat{z}}{\vec{b} \cdot (\hat{a} \times \hat{z})}$$

where $\hat{z}$ is the unit vector normal to the surface, as in RHEED. The LEED pattern that results from a well ordered pattern will be symmetric around the incident beam spot (i.e. $h = k = 0$). Because the wavelength is inversely proportional to $\sqrt{E_k}$, where $E_K \propto V$, increasing the voltage of the electron gun decreases the spacing between spots, i.e. more will appear on the screen. Similarly, because the wavelength is also inversely proportional to the lattice spacing, increasing the lattice spacing will also decrease the spacing of peaks in the diffraction pattern.

Using LEED for characterising a film's surface, one has the ability to detect surface reconstructions or superstructures, which can be induced by heating/annealing, adsorbate coverage or altering other growth parameters. In these cases, the surface structure cannot be fully described by a single set of primitive lattice vectors, Fig. 3.11c,d and these additional sets of lattice vectors, often larger than the underlying lattice, result in "extra" spots in the LEED pattern. One complication with using LEED is that the size of the electron beam, ~1mm, is significantly larger than typical domain sizes. If these domain sizes are larger than the coherence length of the probing electrons, the LEED pattern will be the sum of the patterns from all measured domains. Therefore, if two rotated domains are rotationally symmetric, for instance, rotating the honeycomb lattice by 60°, the LEED pattern will be indistinguishable from the pattern of a single domain. On the

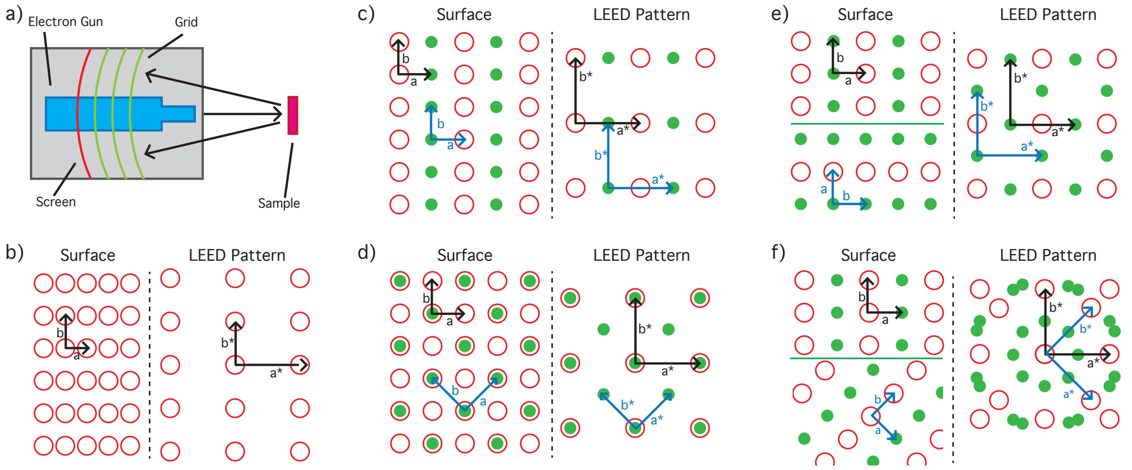

FIGURE 3.11: Surface structure effects on LEED pattern. a) Cartoon of a typical LEED setup. b) Lattice vectors of a simple surface structure with anisotropic lattice spacing. Stretching of lattice in $\vec{b}$ direction in real spacing creates LEED pattern with stretched $\vec{a}$ lattice vector. c) (2x1) superstructure (vertical strips) results in extra spots along the horizontal direction. d) Sub-monolayer deposition can form a (2x2) structure onto of a substrate, producing extra spots with smaller $\vec{a}^*$ and $\vec{b}^*$ reciprocal lattice vectors. e) Measurement of (2x1) and (1x2) superstructures, i.e. 90° rotated domains, results in a rotation of LEED pattern with significant overlap, while f) an arbitrary rotation produces several extra spots and "rings" start to form.

other hand, if an arbitrary rotation exists between the domains, the LEED pattern will consist of multiple reproductions of the patterns corresponding to the individual domains but with rotations equal to the rotation of the domains, Fig. 3.11f. In extreme cases, with multiple rotated domains, rings of intensity form as diffraction patterns are reproduced at several rotated orientations. However, given that MBE samples are often at least 1-10mm across, a translational stage can be used to move the electron beam around the sample surface to determine the sample homogeneity and assess the presence of rotational domains.

3.3.3 X-ray Photoelectron Spectroscopy

While RHEED and LEED are useful in determining the surface structure of films grown using MBE, in most cases they are unable to determine the chemical composition of films. The final in-situ characterisation technique, X-ray photoelectron spectroscopy (XPS), that will be discussed, is capable of determining the chemical composition and atomic valence of thin films and single crystals. This technique is very similar to ARPES, except that high energy X-rays are used, often generated using the atomic spectral K-α emission lines of magnesium (1253.7eV) or aluminium (1486.7 eV) in lab setups.

As discussed previously, the increase in photon energy, as well as the angular acceptance of the analyser and Debye-Waller effects, reduce the angular resolution and therefore XPS is a momentum-integrated technique, and will provide only energy specific information here. However, the increase in photon energy greatly increases the electron escape depth, up to several atomic layers, as well as the binding energy range available for probing. The higher photon energy is important in the determination of chemical composition, including dopant concentration, as the core levels of tightly bound electrons have specific binding energies, typically between 10's to several 100's of eV. For many of these core levels, these energies typically do not vary greatly (smaller than 100meV shifts) depending on chemical environment; however, in some materials like those containing the transition metals, which change valence state (i.e. $Eu^{2+} \rightarrow Eu^{3+}$), or silicon oxides, which have different bonding structures, Fig. 3.12a, some of these levels

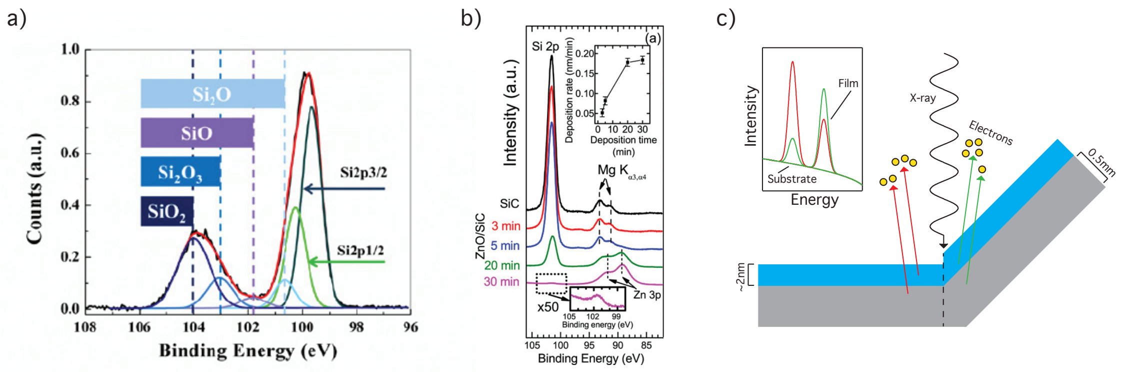

FIGURE 3.12: Chemical composition and thickness determination with XPS. a) XPS on core levels reveals a variety of chemical compositions within a silicon sample from surface oxidation, reproduced from [29]. b) XPS spectra taken after consecutive depositions can be used to determine the deposition rate through analysis of relative peak intensities, reproduced from [30]. c) Rotation of a thin (few monolayer) film in XPS increases path of photoemitted electrons through films by a factor of $1/\cos\theta$, allowing the film thickness to be determined from the decrease/increase in substrate/film core level intensities.

can have observable shifts on the order of eV. Additionally, by measuring the relative intensities of core levels of different elements and using the corresponding photoemission cross-sections, one can determine the relative composition. This is useful when one is varying the concentration of a substitutional dopant, provided that the dopant and host materials have core levels with well-separated binding energies and large cross-sections.

The increase in electron escape depth from using high energy photons can also be used in determining the thickness of thin films. If the deposition rate of the thin film growth is sufficiently low, one can grow monolayers, or sub-monolayers, controllably. By measuring the XPS spectrum of samples grown with increasing coverage, under the same growth conditions, and observing the relative decrease (increase) in the intensity of core levels associated with the substrate (film), one can estimate the deposition rate of the film, Fig. 3.12b. This is possible because the electron escape depth for typical XPS photon energies is on the order of several atomic layers, and therefore the substrate core levels are measurable, even after a few layers of film growth. Alternatively, one can determine the film thickness by depositing a few layers of material onto the substrate and measuring the XPS spectrum in normal emission and at various rotations, which has the effect of increasing the amount of film the electrons must pass through before reaching vacuum, Fig. 3.12c. In the work that will be presented in Chapter 7, these methods will be used to determine film thicknesses, along with an explanation of how XPS can be used to determine the oxidation state of europium in EuO films.

3.4 Ex-Situ Characterisation

Thus far, only experimental techniques that can be performed at the I05-endstation under constant ultra-high vacuum via in-situ transfer have been discussed. One reason for the in-situ transfer is to preserve the surface quality as exposure to atmospheric conditions can change the chemical composition of samples, such as oxidise the surface layers of Si wafers, or introduce contaminants. Prevention of such sample degradation is vital for accurate characterisation of thin films by surface sensitive techniques; however, as will be discussed next, experimental methods that measure bulk properties can be used that do not typically require the preservation of surface layers. The ex-situ characterisation methods discussed here are aimed at determining the bulk magnetic character of thin films presented in Chapter 7.

3.4.1 Superconducting Quantum Interference Device

The superconducting quantum interference device (SQUID) consists of two superconductors separated by a thin insulating layer to form two parallel Josephson junctions. These Josephson junctions, theorised by Brian David Josephson in 1962, can experience tunnelling of Cooper pairs of electrons through the insulating layer. The Cooper pairs on either side of the junction can be represented by wavefunctions and the Josephson junctions will behave differently depending on the nature of the applied bias voltage. In a DC Josephson junction, a current across the junction is proportional to the phase difference of the wavefunctions in the absence of an applied voltage, while an AC Josephson junction will oscillate with a characteristic frequency proportional to the applied voltage. One of the main observations from the theory of Josephson junctions is that the magnetic flux threading the loop is quantised in units of $\Phi_0 = \pi\hbar/e$.

A DC SQUID magnetometer utilises two DC Josephson junctions to observe small changes in external magnetic fields, such as those created by magnetic samples. In the absence of an external field, the current across the two Josephson junctions is identical, but when a small magnetic field is introduced, a screening current, I_S, flows to create a magnetic field that cancels the external magnetic field. Because the magnetic flux must be quantised in units of Φ_0, if the external field is larger than $\Phi_0/2$, it becomes energetically favourable to increase it to Φ_0 and the screening current is reversed in direction. The external field that threads the magnetometer is generated by a current induced via a pickup coil, Fig. 3.13a. By moving the pickup coil relative to the magnetic sample, the flux that threads the pickup changes and this fluctuation is detected as a change in the voltage across the Josephson junctions.

SQUIDs can be used for a range of purposes in characterising the magnetic properties of thin films and single crystals. These devices use cryogenic cooling to allow the temperature dependence of the magnetic moment of samples to be measured in a range typically from ~5K to 300K and sometimes even to higher temperatures with small heating elements. External magnetic fields can also be applied, typically of a few Tesla, which allows for magnetic moment vs temperature (MvT) scans to be performed in either a zero-field cooled (ZFC) or field cooled (FC) method. In the latter, an external field is applied upon cooling through the magnetic transition to measure the extent of anisotropy, i.e. domains with moments aligned in different directions. These MvT scans allow the Curie temperature, the point at which the transition from paramagnetic to ferromagnetic ordering occurs, to be determined. The onset of ferromagnetic ordering is observed as a sudden increase in the magnitude of the magnetic moment, Fig. 3.13b, and as the temperature approaches T=0K, in ferromagnetic materials, the magnetisation reaches a saturated value that can be related to the magnetic moment per atom if the film thickness is known.

In addition to temperature dependent measurements, magnetic hysteresis loops can be built by measuring the magnetic moment while varying the applied magnetic field (MvH scans) at a constant temperature. These measurements determine a material's ability to retain its ferromagnetically ordered state under application of an external field directed anti-parallel to the aligned spins, Fig. 3.13c. Initially, the external field is ramped up from 0T to a specified value well above the saturated magnetisation, step $0 \rightarrow 1$, which aligns all domains in the sample. The magnetic field is then ramped down to 0T (step $1 \rightarrow 2$) and beyond until saturation is achieved in the opposite direction (step $2 \rightarrow 4$). At step 2, one finds that

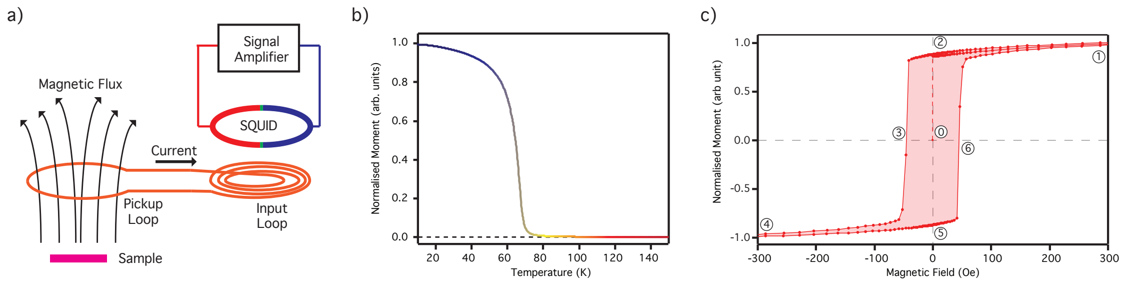

FIGURE 3.13: Bulk magnetic measurements using SQUIDs. a) Magnetic flux from sample threads pickup loop, which induces a circulating current. The input loop produces a magnetic field that threads the SQUID, such that changes in the flux through the pickup loop are measurable. b) By varying the temperature in a fixed field, the transition to a ferromagnet can be observed, while c) varying the field at constant temperature provides information on the magnetic hysteresis. See text for explanation of numbering.

once aligned, the domains will remain ordered even without the presence of an external field, while at some point (step 3) a non-zero field is needed to disorder enough domains for the sample to have no net moment. Upon saturation of the magnetisation in the opposite direction, the field is returned to its positively saturated moment (step $4 \rightarrow 5 \rightarrow 6 \rightarrow 1$), exhibiting the same, but opposite retained magnetisation at zero applied field. The width of the hysteresis loops is related to the amount of energy needed to reverse the magnetic field of the sample; wide loops are favourable for materials where the moment needs to be stable against temperature and other perturbations, like those in magnetic memory units, while narrow loops are favourable in transformers where low energy dissipation is desirable for the fields created from AC circuits.

3.4.2 X-Ray Absorption Spectroscopy and X-Ray Magnetic Circular Dichroism

One advantage of using a SQUID to measure the magnetic properties of a material is the ease of use and high throughput of samples. Because only a vacuum of a few mbar is needed, samples can be introduced into the system, measured and removed in a matter of a few hours. While a vast amount of information about the bulk magnetic characteristics of thin films can be gained using SQUID, the properties of individual elements cannot be resolved. However, two additional techniques can be used to understand the magnetic behaviour specific to each element in a compound: X-ray absorption spectroscopy and X-ray magnetic circular dichroism.

X-ray absorption spectroscopy (XAS) is similar to X-ray photoelectron spectroscopy in that high energy X-rays (keV to a few 10keV) are used to examine the electronic structure of crystalline materials, except instead of analysing emitted photoelectrons, the absorption spectrum is measured. X-rays incident on a material will either be: 1) elastically scattered; 2) absorbed by electrons producing either a photoelectron (as in XPS) or fluorescent X-rays as excited electrons return to their ground state (XAS); or 3) be transmitted through the material. The intensity of the transmitted X-rays follows a predictable relation:

$$\ln\left(\frac{I_O}{I}\right) = \mu x, \tag{3.18}$$

where x is the sample thickness and μ is the linear absorption coefficient, which depends on the density of the material and the elemental composition. In the case of XAS, high energy X-rays are absorbed, exciting an electron from the core level into the unoccupied conduction band states according to specific transition rules (i.e. only transitions between states whose total angular momentum differ by one are allowed). Thus by measuring the intensity of the transmitted X-rays, and therefore the absorption coefficient of the X-rays which drastically increases at allowed transitions, one can determine the energy of transitions into unoccupied states. These steep increases in absorption are denoted as K-, L-, and M-edges, depending on the core level principal quantum number, i.e. $1s$ level is a K-edge, while the $2s$ and $2p$ electrons are L-edges. Just as in XPS, XAS spectra can be used to determine the chemical concentration by analysing the relative intensity of absorption edges, as well as atomic valence and density of states of the unoccupied states.

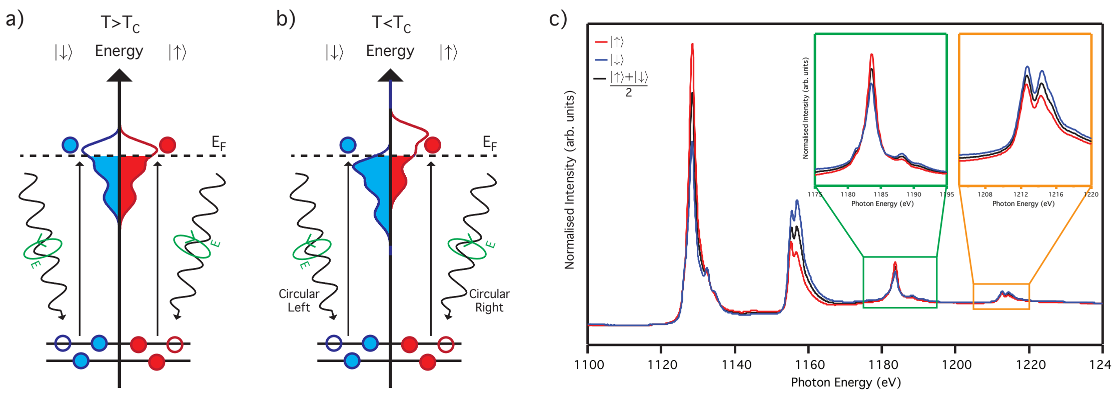

FIGURE 3.14: Observing chemical specific magnetic moments using XMCD/XAS. a) A peak in the absorption spectra is observed when photon energies sufficient to promote electrons from core levels to above the Fermi level. For a paramagnet, when probed with circularly polarised light, the spectra look identical, but for b) a ferromagnet, the density of spin-up and spin-down states above the Fermi level differ and thus the spectra will differ as circular left/right polarised light couples to spin-down/up electrons, respectively. c) An example XMCD spectra of Eu$_{1-x}$Gd$_x$O shows alternating intensity for similar core level pairs (at 1128eV/1156eV and 1184eV/1214eV), as is typical for ferromagnets.

Linearly polarised light interacts equally with spin-up and spin-down electrons as both transitions result in no change in the magnetic quantum number, $\Delta m = 0$, Fig. 3.14a, while excitation with circularly left and right polarised light is only allowed for transitions with $\Delta m = 1$ and $\Delta m = -1$ and thus interact only with spin-down and spin-up electrons, respectively, Fig. 3.14b. X-ray magnetic circular dichroism (XMCD) exploits the difference in these transition strengths to reveal element specific magnetic properties. Initially, a magnetic field is applied to the sample and an XAS spectrum is taken, revealing the chemical specific absorption edges energies. For a paramagnetic material, if this spectrum is repeated using both circularly right and left polarised light, no measurable difference in the two spectra will occur as there are an equal number of spin-up and spin-down electrons. However, if the material is ferromagnetic, there will be an imbalance in the density of spin-up and spin-down states just above the Fermi level and, since photoexcitation forbids spin-flips, a difference is measured in the absorption spectra for the two light polarisations, Fig. 3.14c. By varying the sample temperature, similar to the MvT SQUID measurements, the degree of dichroism as a function of temperature can be measured. In materials with multiple magnetic elements, such measurements focused on absorption edges corresponding to different elements allow one to determine any chemical specific magnetic properties and if the moments of the two kinds of atoms align ferro- or anti-ferromagnetically. Additionally, by varying the applied magnetic field, as in the MvH SQUID measurements, at a given photon energy and fixed temperature, one can build element specific hysteresis loops by measuring the dichroism of each elements absorption edge.

This concludes the experimental techniques foundation necessary to understand the experimental results discussed later. An overview of how the electronic structure of crystalline materials can be directly observed using ARPES and how high-quality thin film samples with finely-tuned stoichiometry can be grown using MBE was presented. Additionally, various techniques used for characterising the surface structure, quality and chemical composition of these thin films have been described, as well as the bulk and element-specific magnetic properties.

Chapter 4

MBE/ARPES at Diamond Light Source's I05 Beamline

Thus far, an overview of the theory of electronic structure in crystalline solids and an experimental technique used to directly measure these band structures has been presented, as well as one method used to grow thin film samples which could be measured using ARPES. However, up until this point, there has been no discussion of experimental apparatus that combines ARPES and MBE, and that reflects the relative rareness of such systems. Single crystal samples, such as those grown via chemical vapour deposition, constitute the vast majority of ARPES studies, but the ability to measure the band structure of tailor-made or ultra-thin (i.e. monolayer, bilayer, etc.) samples presents intriguing possibilities to manufacture specific electronic behaviour. Add to this an ability to measure the full electronic structure using synchrotron radiation, without samples leaving UHV, and the number of such systems drops to just a handful scattered across the globe. One such system is the I05 beamline at Diamond Light Source (DLS) in Oxfordshire, UK, where much of the following work was performed. Here a brief overview of the ARPES and MBE systems on the I05 endstation and some obstacles that were overcome in preparing the system for growth of oxide thin films is given.

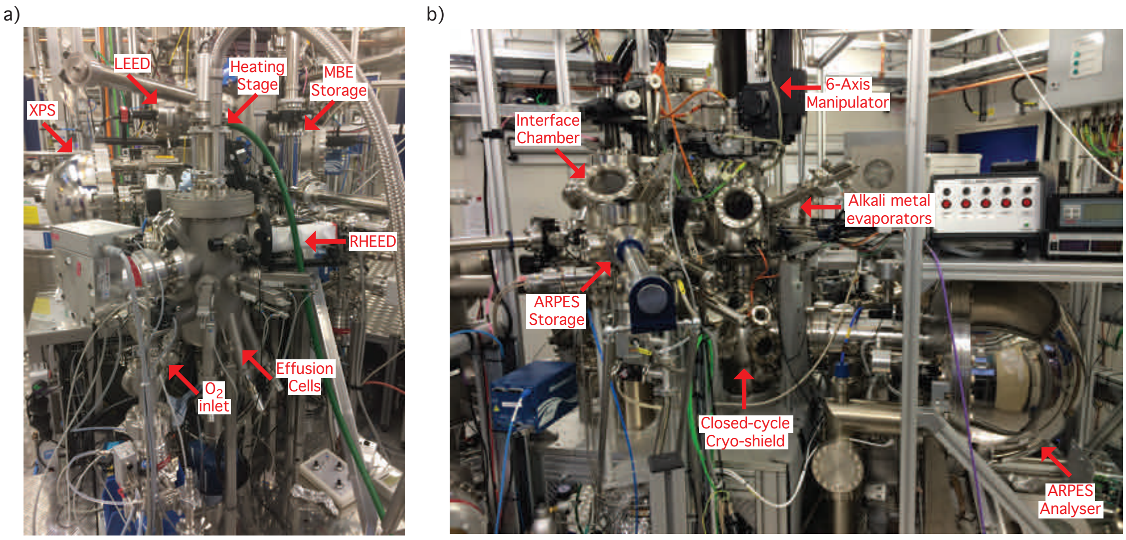

FIGURE 4.1: Setup of the ultra-high vacuum chambers on the I05-beamline endstation. a) Thin film samples produced in the growth chamber can be monitored during growth using RHEED and, after transfer to the preparation chamber, through an intermediate storage chamber, further in-situ characterisation with LEED and XPS can be performed. b) Additional, in-situ transfers provide access to HR-ARPES facilities for electronic structure characterisation.

4.1 General Chamber Setup

The I05 endstation, Fig. 4.1, at DLS consists of 5 main UHV chambers: growth, preparation, interface, upper and lower chambers. Broadly speaking, the growth chamber is the main MBE chamber where sample growth was performed; the preparation chamber contains the majority of in-situ characterisation equipment as well as few-layer and sub-monolayer growth capabilities; the interface chamber is used for single-crystal sample storage and interface preparation with sputtering and annealing capabilities; the upper and lower chambers constitute the ARPES chambers in which single-crystal sample cleaving, low-temperature LEED and alkali metal deposition are performed (upper chamber) with measurements taking place in the lower chamber. Here, a detailed look at the experimental setup of the high-resolution (HR) ARPES endstation and the mu-MBE system is given.

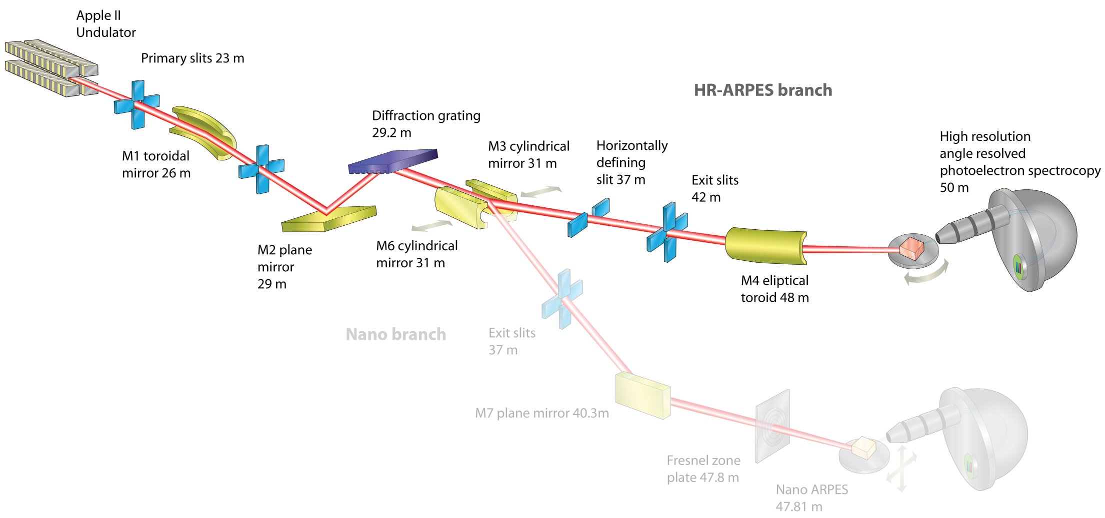

FIGURE 4.2: Detailed schematic of the I05-beamline optics. Electronic vibrations induced by the undulator produce photons of a tuneable wavelength and polarisation which are focused and filtered to deliver a beam spot of $\sim$50x50μm with energy resolution of better than 2meV for the core range of hν=18-80eV. Reproduced from Ref. [31].

4.1.1 HR-ARPES

The I05-beamline, at which the majority of the measurements to be discussed later where acquired, is depicted in Fig. 4.2. The Apple II undulator is capable of providing 10^{15}photons/s in a range of $h\nu$=18-240eV. Additionally, linear horizontal, linear vertical and circularly polarised light can be produced over the entire range, providing an ability to measure the full 3D electronic structure over multiple Brillouin zones, as well as resolving orbital character by comparison of polarisation dependence. The collimated plane grating monochromator (cPGM) provides excellent energy resolution, with a resolving power of R $>$20000.

The HR-ARPES endstation at DLS consists of a Scienta R4000 hemispherical electron analyser with a ±15° multiplexing lens and a 6-axis manipulator. The ability to rotate or translate samples into a large range of orientations and the reproducibility of the manipulator positions, using optical encoders, allows for reliable sample measurement and accurate repositioning after contraction/expansion of the manipulator upon cooling/heating. Upon cryogenic cooling with liquid helium, temperatures as low as 6K can be easily stabilised. This has been aided by the recent addition of a closed-cycle helium cyro-shield that has also improved the base pressure of the lower/measurement chamber to $\sim$1e-10mbar or better, providing excellent measurement conditions and sample lifetimes [32].

4.1.2 MBE and Characterisation

The growth chamber of the mu-MBE, built by Createc, Fig. 4.1a, is based around larger production sized instruments, having been scaled down to accommodate substates with a maximum size of 10x10mm instead of standard 3" wafers. Despite its miniature size, the mu-MBE has the capability of hosting 8 effusion cells (although one is used for an oxygen inlet, discussed below) and magnetic shutters, allowing for a wide-range of source materials and sample stoichiometries to be grown. Additionally, the diminutive size allows for the disassembly and thorough cleaning/etching of the main growth chamber to be performed in standard fume hoods with minimal effort. In principle, this allows for the chamber to be switched from the growth of one family of materials to another (such as chalcognide to oxide) without introducing contamination into subsequent films, a process which is typically unfeasible or impossible in other systems.

Contained within the growth chamber is a cryo-shield, shown in Fig. 4.3, which, when filled with liquid nitrogen, provides adequate cooling to the effusion cells, even when run up to 1300°C, as well as additional vacuum pumping. Source flux calibration is performed using a Bayard-Alpert gauge as a beam-flux monitor, which can be translated horizontally in and out of the direct path of the sources allowing the local pressure of each source to be measured accurately. Real-time growth quality can be monitored using a RHEED gun and fluorescent screen, while a rotating, heated sample stage allows for crystallinity to be analysed along any crystallographic direction and for a wide range of substrate temperatures to be reached (20°C-900°C). The MBE chamber vacuum is established

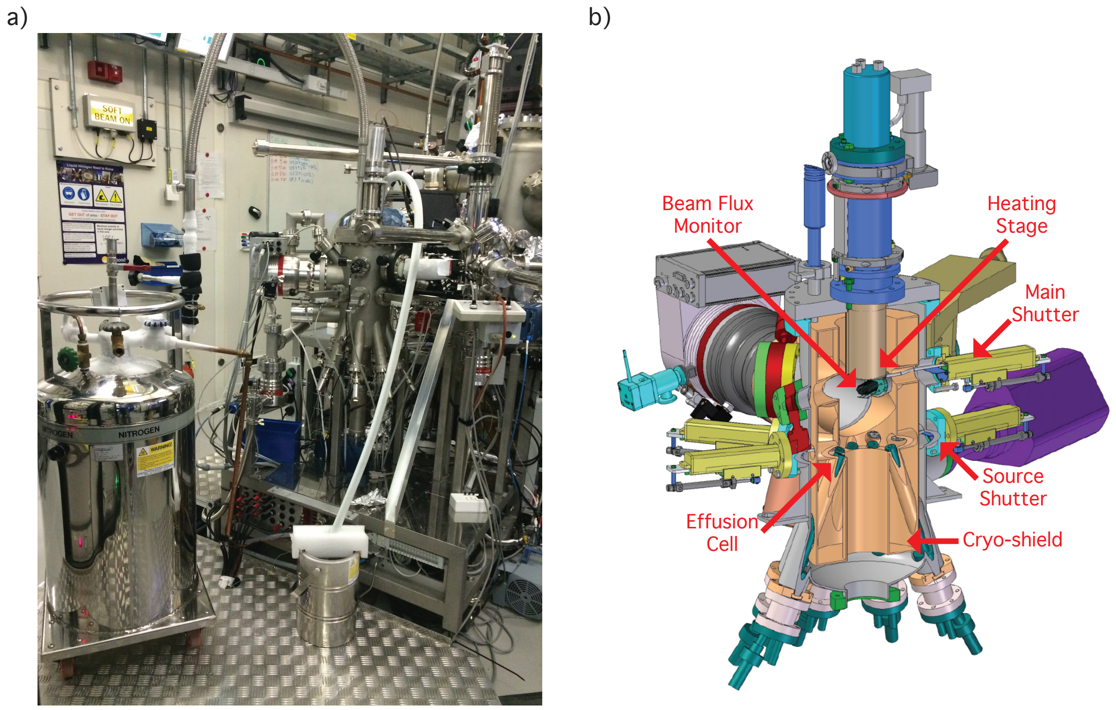

FIGURE 4.3: Setup of the mu-MBE system on the I05-beamline endstation. a) Liquid nitrogen fills the internal cryo-shield of the mu-MBE, providing cooling to the effusion cells and additional vacuum pumping. b) The Createc oxide mu-MBE consists of 7 effusion cells, with magnetic shutters, plus molecular oxygen inlet, a rotating heating stage and RHEED capabilities. Reproduced from Ref. [33].

with two turbomolecular pumps, backed by a membrane pump, providing a base pressure below 1x10^{-10} mbar [33].

4.2 Working with Reactive Sources

One of the benefits of growing samples using MBE is the ability to control and tailor the chemical composition of the samples in a layer-by-layer fashion. This allows for a vast array of complex structures to be grown, from fine-tuning of doping concentration to heterostructures of different materials. Another option is to grow materials which are unstable in normal atmospheric conditions, such as those that would typically oxidise out of vacuum. One such group of materials is the rare-earth metals, such as europium and gadolinium, which were used in the work to be discussed later.

Europium, and to a lesser extent gadolinium, is extremely reactive to oxygen, as Eu metal is its least stable form. Solid Eu is typically stored under oil to prevent the near-irreversible oxidation to its most stable form, Eu_2O_3. This presents two main issue when working with an MBE system: installation of the source material into an effusion cell and preservation of the source material during all subsequent maintenance. To overcome these obstacles, the following procedures were implemented:

- Eu source material, originally stored under oil, was cleaned of all contaminant by the supplier, MaTeck, as suitable for use in ultra-high vacuum
- Clean Eu source material was placed into an Al_2O_3 crucible before being packed in argon and sealed
- Prior to installation, the growth chamber was vented using an overpressure of argon, after which the sealed crucible was opened inside the argon atmosphere of the chamber and placed into the effusion cell
- Eu and Gd sources were outgassed for at least one week at 400°C to remove any water contamination and minimise hydrogen contamination
- Eu and Gd sources were kept at 300°C to reduce re-adsorption of hydrogen
- All subsequent venting of the growth chamber was performed using an argon overpressure

Adhering to these precautionary steps allowed for clean, unoxidised europium and gadolinium to be evaporated from the effusion cells for the growth of $Eu_{1-x}Gd_xO$ thin films in a background pressure $\sim$2x10^{-9} mbar, when these source materials were at growth temperature.

4.3 Converting to a Molecular Oxygen MBE

In oxide MBEs there are three methods commonly used to provide the necessary oxygen flux: 1) supplying a flow of ozone (O_3); 2) cracking molecular O_2

using a plasma sources to produce O^{2-} ions; or 3) using molecular O_2. The former method is extremely resource intensive as special ozone production systems must be built and, because ozone is a contact explosive, it is unsuitable to use ozone in systems with cryo-cooling, such as the cryo-shield on the mu-MBE. While plasma sources are less expensive and are suitable for use with cryogenics, it is still technically challenging to operate a plasma source, such as the one that was initially installed on I05's mu-MBE. One advantage of using a highly reactive material is the ability to use molecular oxygen without sacrificing film quality or reducing growth rates.

As mentioned, Eu and Gd are readily oxidised by molecular oxygen. As such, the plasma source was removed from the mu-MBE and a pin-hole inlet nozzle connected to a molecular oxygen source was installed. Additionally, a gas purifier and piezo leak valve were installed prior to the O_2 nozzle to provide fine-regulation of clean O_2 into the growth chamber. Unfortunately, due to the pin-hole nature of the inlet nozzle, the resultant flow of O_2 was highly directional, with an incident area smaller than that of the effusion cells. This presented an issue, as the motion of the heating stage shifts the sample position as it is rotated azimuthally, moving the sample surface in and out of areas where Eu/Gd and

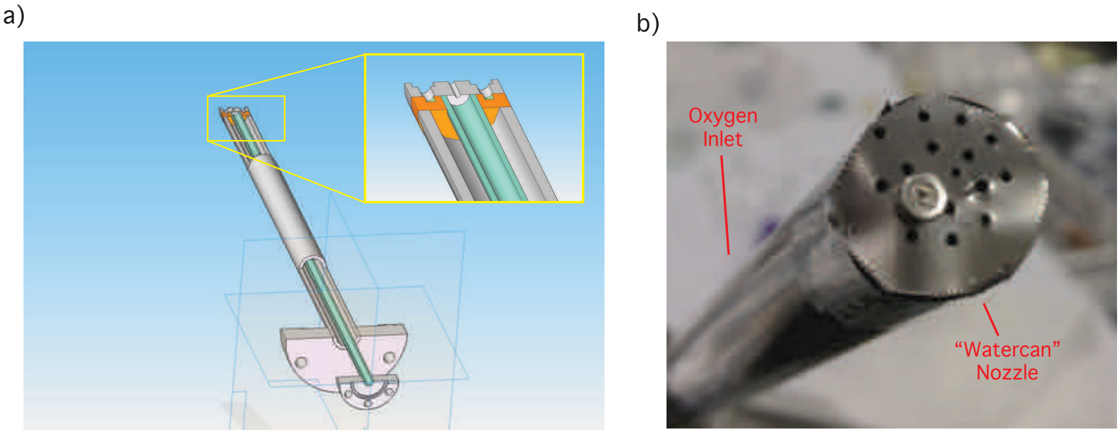

FIGURE 4.4: Modification to oxygen inlet. a) A cut-view of the oxygen inlet nozzle shows the highly-directional nature of oxygen flow, requiring b) a "watercan" or "leaky-bucket" diffuser to be fixed to the end, allowing a dispersed molecular oxygen source.

O_2 fluxes were thought to overlap. In order to overcome this issue, a "watercan"-shaped gas diffuser device was fabricated and attached to the in-vacuum side of the inlet nozzle, Fig. 4.4b, providing a more evenly dispersed flow of O_2.

4.4 Down-to-Earth Samples

As previously discussed, ARPES uses high-energy photons incident on a crystalline surface to emit electrons, leaving the material surface positively charged. In metallic systems, this charge imbalance is not able to accumulate as the sample is connected to ground through the sample plate. However, in insulating and semiconducting samples, an inability to move electrons through the material's bulk to the surface allows for charge accumulation to occur. This presents a particular issue for ARPES measurements as the local electric fields that build at the sample surface can distort the electrons' trajectories as they travel into the analyser cone and the binding energies of the electrons inside the sample are

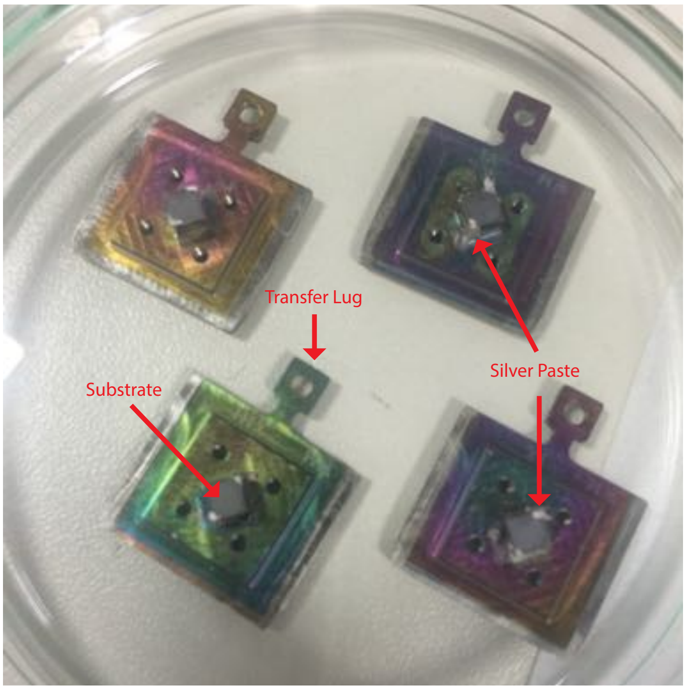

FIGURE 4.5: Application of conductive silver paste to the substrate surface provides excellent grounding for subsequent thin film growth, allowing samples to be measured using LEED, XPS and ARPES. Plate discolouration is the result of varying thicknesses of Eu, Gd, Si and interstitials deposited on the surface.

increased as more energy is needed to overcome the additional electrostatic potential.

Grounding the surface of the insulating crystalline substrates to the sample plates provides sufficient electrical contact to earth when a thin film is grown overtop. Therefore, the following procedure was developed to provide adequate grounding:

1. Cleaned single-crystal substrates were attached to the sample plates using PELCO high-temperature carbon paste, a suspension of carbon flakes in an inorganic silicate aqueous solution, and cured for two hours at 93°C
2. Highly conductive silver paste, also from PELCO, was applied to the sides of two corners of the sample plate posts before being painted up the edge and over the surface of the substrate in a small region near the corners
3. The silver paste was cured for two hours at 93°C and a further two hours at 200°C to improve structural strength and conductivity at cryogenic temperatures

Substrates prepared in this manner, Fig. 4.5, have excellent conductive properties, as seen by a lack of charging effects under X-ray and synchrotron radiation sources, to be discussed later. Additionally, the limited application of silver paste to just the corners allows for RHEED analysis of film growth to be performed along high symmetry directions with azimuthal range greater than 90 degrees, which is more than adequate for the cubic structure of EuO. This concludes the theoretical foundation of electronic structure and experimental techniques used in the investigations performed here. In the next two chapters, the electronic structure of single-crystal WSe_2 samples will be analysed before switching focus to Gd-doped EuO thin films grown using MBE for the remaining three chapters.

Chapter 5

Bulk Bandstructure of WSe_2

As mentioned, the electronic structure determines most of the transport and thermodynamic properties of a material. The underlying crystal lattice governs the band structure and is dictated by the unit cell's symmetries and chemical composition. As such, a brief overview will be given of recent studies on mono- and few-layer films of the transition metal dichalcogenides (TMDCs), a family of 2D materials, that revealed the effects of the layered crystal structure on the electronic structure. Following this introduction, a study of the bulk electronic structure of WSe_2, a semiconducting member of the TMDCs, single crystals using ARPES will be presented. This chapter will focus on the implications of the layered nature of WSe_2 on its band structure, which gives rise to unexpected features that are revealed using spin-ARPES.

5.1 Background information

The discovery of graphene and the novel phenomena exemplified by its band structure has led to a rise in the study of two-dimensional materials. Monolayer graphene forms in the honey-comb lattice, constructed by a single sheet of carbon atoms on a two-site triangular lattice as shown in Fig. 5.1, which preserves inversion symmetry and, being non-magnetic, upholds time-reversal symmetry. The unique electronic structure of this material embodies massless Dirac fermions [34–37], which form linear, gapless dispersions at the corners of the hexagonal Brillouin zone. Although graphene displays a wide range of novel physics, like the quantum Hall effect [38–40], and excellent transport properties, the zero-bandgap limits graphene's application to electronic devices which require semiconducting materials with a small, but finite band-gap to retard the flow of charge except when a gate-voltage is applied. It was also seen that bilayer graphene is also a zero-gap semiconductor, but if the inversion symmetry between the two layers is broken a finite gap develops [41–43]. This non-zero bandgap can be controlled, but it was found that the opening of a bandgap diminishes the high conductivity of pristine graphene.

5.1.1 Moving beyond Graphene

Although these properties present limitations for implementing graphene into new devices, the intense study of this material opened up research to a wide range of 2D materials that have been shown to host a number of novel phenomena. One such family of materials is the transition metal dichalcogenides (TMDCs) that form in the MX_2 stoichiometry, where M is a transition metal and X is a chalcogen. Like graphene, these materials form a two-site triangular lattice

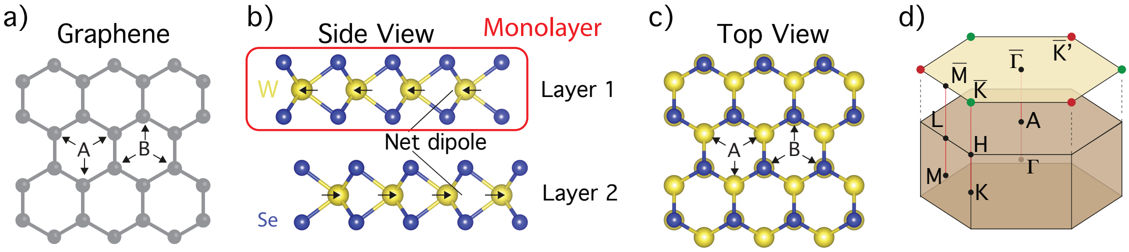

FIGURE 5.1: Crystal structure of 2H-WSe_2. a) Graphene is formed by single sheets of carbon atoms that sit on either an A- and B-site, arranged in the honeycomb, hexagonal lattice. b) Side view of the monolayer and 2H structure of WSe_2 shows a W-plane with Se-planes positioned above and below. In the 2H structure, a 180° rotation exists between the two monolayers of the unit cell. c) Top view of the structure reveals similar structure as graphene. d) Surface and bulk Brillouin zone for monolayer and bulk WSe_2.

structure, except instead of having carbon atoms at both the A- and B-sites, a transition metal atom sits at the A-site and two chalcogens reside at the B-sites, positioned above and below the W-plane. This configuration results in a net dipole directed along the W-planes, Fig. 5.1b. Generally speaking, the particular choice of transition metal dictates the crystal symmetry as well as the position of the Fermi level, and therefore the overall electronic behaviour of the material. For example, Group VI elements (Mo or W) are semiconductors which tend to form in the 2H, shown in Fig. 5.1b, or 3R structures, and Group V are metals/semimetals [44].

In the following discussion, the focus will be on the semiconducting Group VI TMDCs and results on WSe_2 will be presented thereafter. Although these measurements are performed on a single member of this large family of materials, the phenomena exhibited by WSe_2 is believed to apply to all members of this family, which is partially supported by additional studies, conducted after this investigation was performed, that are beyond the scope of this thesis.

5.1.2 Spin-Valley Coupling

As with graphene, there are electronic states near the Fermi level at the zone corners of the hexagonal Brillouin zone in TMDCs, but, as can be clearly seen in Fig. 5.1b, monolayer TMDCs lacks a centre of inversion that induces a gap in the states analogous to the Dirac points of graphene, producing a local minimum (maximum) in the conduction (valence) band, Fig. 5.2a,b. These local minima/maxima are referred to as valleys and because there is a choice between states in the valleys at k (K) and $-k$ (K′), due to the two-site basis of the unit cell, one can discuss the electronic structure in terms of a valley-pseudospin, in an analogue to the electronic spin. However, unlike graphene, the presence of heavy transition metals increases the effects of spin-orbit interactions that further modifies the band structure at these valleys. The combination of broken inversion symmetry in the monolayer and spin-orbit interactions cause the in-plane electric

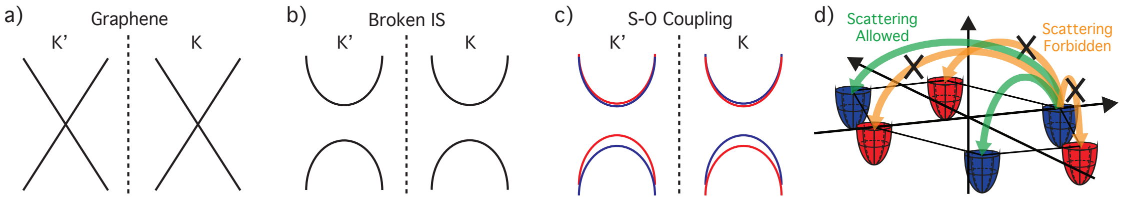

FIGURE 5.2: From Graphene to TMDC. At opposite corners of the Brillouin zone, a) Dirac cones are present for pristine graphene. If b) inversion-symmetry (IS) is broken, such as in the unit cell of monolayer TMDCs or by gating in bi-layer graphene, a finite gap opens. Additionally, c) spin-degeneracy is lifted when spin-orbit coupling is included, coupling the spin and valley-pseudospin. d) Spin-valley coupling reduces the probability of backscattering events which require spin-flips. d) adapted from Ref. [46].

field from the monolayer's net dipole to induce a massive Zeeman-like splitting, that has been estimated to be equivalent to a magnetic field of $\sim 10^2 - 10^3$T [45], which switches sign at K and K', Fig. 5.2c.

Although the overall spin-up and spin-down populations remain equal, preserving the non-magnetic nature of the material, the breaking of spin-degeneracy results in spin-polarisation of electronic states with a reversal of spin between conjugate valleys. For the valence bands near the zone corners, this splitting reaches ~500meV in WSe$_2$. The distinction between spins in a particular valley is an embodiment of the coupling of the spin and valley-pseudospins, as the spin of an electron is determined directly from which valley/state it is in. This spin-valley coupling has been predicted to play a vital role in reducing back-scattering in these materials as scattering from a state of k to $-k$, Fig. 5.2d, requires either a reversal of spin or a significant change in energy associated with the splitting of the upper and lower valence band [46].

5.1.3 Mono and bi-layer TMDC Experimental Studies

The presence of such spin-valley coupling in monolayer TMDCs grants an interesting opportunity to experimentally observe and manipulate the spin and valley degrees of freedom, making them ideal candidates for spin- and valley-tronic devices. One method of detecting the coupling of spin and valley-pseudospins is through photoexcitation experiments, such as those performed by Zeng *et al.* [47], Mak *et al.* [48] and Cao *et al.* [49]. Using linearly and circularly polarised light, electrons in valence states just below the Fermi level are excited into unoccupied conduction bands. Subsequently, these electrons become de-excited through the emission of photons, which were seen to have the same polarisation as the excitation light. Because optical selection rules for monolayer MoS_2 dictate that circularly-right (-left) polarised light can only photoexcite states at K (K′), the presence of asymmetries in the resultant luminescence spectra from excitation with the different polarisations indicates spin-polarisations within the different valleys, as shown in Fig. 5.3a.

In addition to circular luminescence measurements on monolayer MoS_2, bilayer samples were investigated, but unlike the monolayer samples, no polarisation was measured in the resultant luminescence spectra, Fig. 5.3b. Unlike freestanding graphene, only certain forms of TMDCs have a centre of inversion. In the 2H structure of MoS_2 (and WSe_2), the unit cell is formed by two monolayers of MoS_2 with a 180° rotation between each layer, Fig. 5.1b. This rotation establishes a centre of inversion and therefore, as a result of the combination of both time-reversal and inversion-symmetries, all states must be spin-degenerate. In the bilayer configuration, valley-dependent selection rules no longer apply, and thus the asymmetry in the circular luminescence spectrum is suppressed.

5.1.4 Thickness dependence of band structure

It is clear from circular photoexcitation measurements that the number of layers in TMDCs and the stacking of each layer has a dramatic effect on the band structure. Not only does the number of layers preserve/break inversion symmetry, i.e. even or odd number of layers, respectively, giving rise to the presence of spin-degenerate or spin-polarised states at zone corners, respectively, but there are additional thickness-dependent band reconstructions. Calculations,

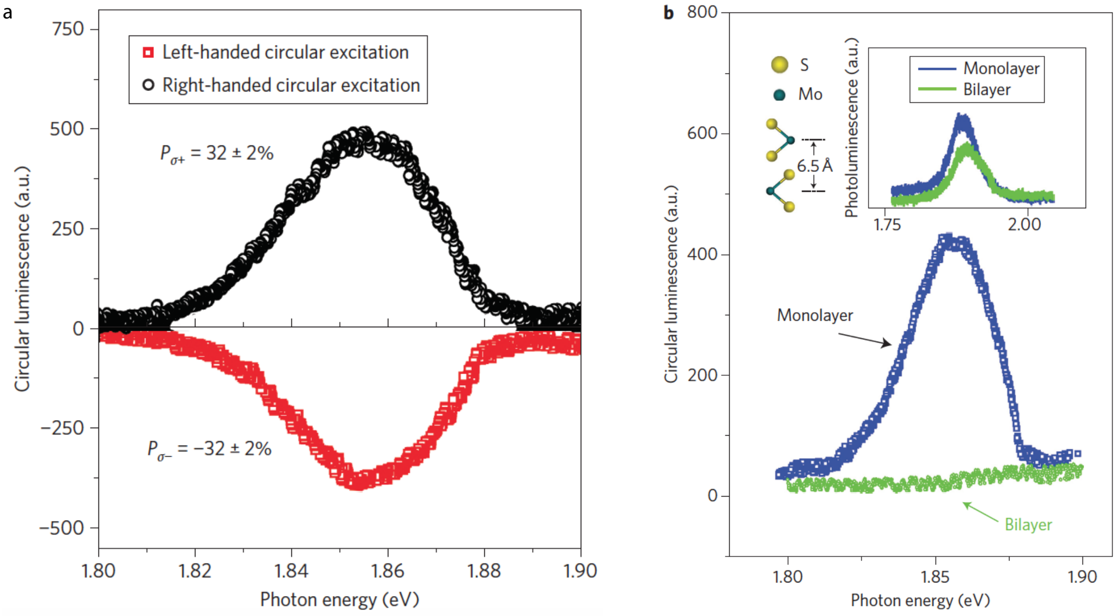

FIGURE 5.3: Circular luminescence on few-layer MoS_2. a) Photoexcitation using left- and right-handed circularly polarised light reveals a polarisation, with the same handedness, in the resultant luminescence spectra, indicating a valley-dependent spin-polaristion in monolayer MoS_2. c) Similar measurements on bi-layer MoS_2 exhibit no circular luminescence due to the restoration of inversion-symmetry. Adapted from Ref. [47].

presented by Zeng *et al.* [50], of the band structure of mono-, bi-, tri- and quad-layer films of WSe_2 and WS_2 predicted that the degree of energy splitting of these bands is the result of extreme spin-orbit coupling effects. When spin-orbit coupling is ignored, *ab initio* calculations predict that the addition of a monolayer to atomically thin films adds an almost degenerate band at K, with minor energy shifts due to interlayer hopping, Fig. 5.4a-d. However, when spin-orbit interactions are taken into consideration, the calculations show that for the mono- to quadlayer films, as well as the bulk, only two bands exist just below the VBM, with an almost constant energy splitting of ∼0.44eV in WS_2 and ∼0.47eV in WSe_2, Fig 5.4e-h, which matches experimental data [47]. Theoretical predictions [51, 52] and experimental measurements [53] on bulk MoS_2 reveals that the splitting of the valence bands is drastically reduced, as a result of the reduced spin-orbit interaction strength from the substitution of W with Mo. Thus the particular choice of transition metal modifies the degree of the energy splitting between opposite

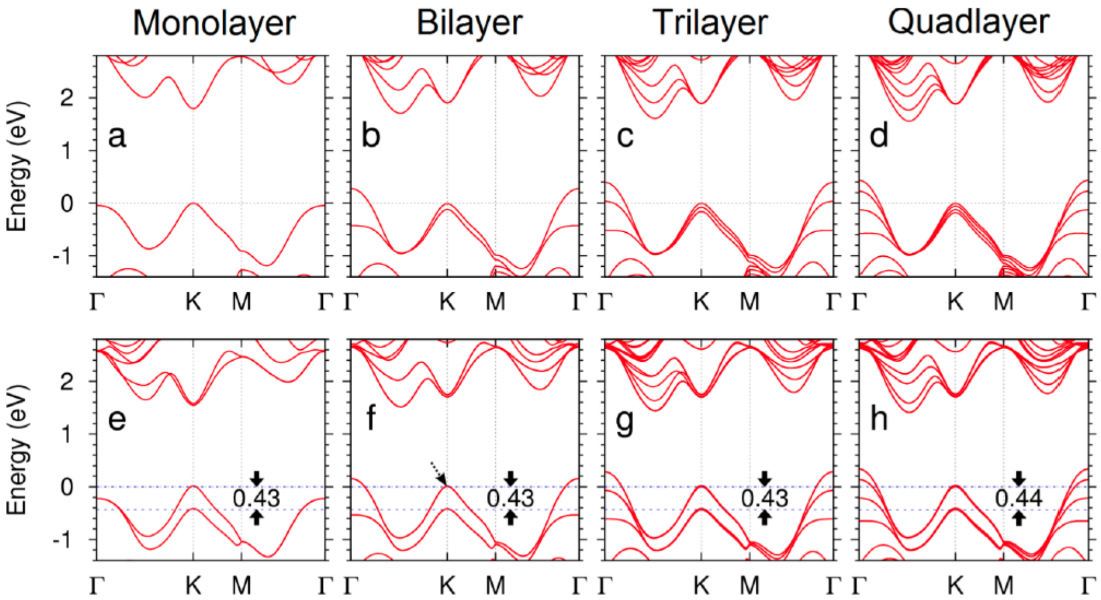

FIGURE 5.4: Band structure of few-layer WS_2. a-d) Ignoring spin-orbit interactions, additional layers result in stacks of valence bands at K which are non-degenerate in energy. e-h) Inclusion of spin-orbit coupling, produces two sets of bands with almost fixed energy splitting. A transition from direct to indirect band gap develops in both cases when shifting from the mono to bi-layer. Adapted from Ref. [50].

spins at a given k, where WX_2 compounds can be thought of as the stronger spin-orbit coupling cousins of the MoX_2 materials.

While the splitting of the valence bands at K is relatively independent of material thickness, other features of the band structure experience significant reconstruction when moving from a monolayer film to a bulk crystal. In the monolayer samples, the valence band maximum and conduction band minimum both sit at K/K′, resulting in a direct bandgap. However, with the addition of even a single layer, the valence band maximum shifts to the zone centre, Γ, while the conduction band minimum shifts to a position partway between Γ and K/K′. The combination of these simultaneous shifts results in a transition to an indirect bandgap semiconductor [51–59]. As a result of the change to an indirect semiconductor, one not only sees the shift in wavelength of the peak photoluminescence intensity, but also a huge decrease in the intensity of photoluminence [50, 54]. Studies showed that the photoluminence intensity increased almost 3-4 orders of magnitude when the sample was thinned down from a bulk crystal to that of a monolayer, and almost 2 orders during the bilayer transition. Interestingly, the second-harmonic generation also showed an increase from bulk to monolayer, but only for odd-number layered samples, while zero intensity was observed for all even-number layered samples, as a result of the restoration of the centre of inversion in integer multiples of the bi-layer unit cell. These results highlight the intricate effects of spin-orbit coupling and also the effect of broken inversion symmetry, which becomes more relevant in the thin films and has its largest effect in the monolayer.

5.2 Bulk Electronic Structure

Like graphene, monolayer to few-layer samples of TMDCs can be produced using the "Scotch-tape" method, where adhesive tape is used to lift off thin samples from bulk single crystals. However, the homogeneity of these exfoliated samples is such that monolayer and thicker domains are clustered in neighbouring regions and the domain sizes are on the order of microns [47]. Alternatively, thin TMDC films can be grown using methods like MBE; however, such samples typically have domains with rotations in multiples of 60° and small domain sizes. The small domain sizes relative to the beam spot of typical ARPES systems presents an issue for studying the electronic structure of isolated monolayers, while measurement of rotated domains prevents separate analysis of states at K and K′ as a real space rotation of 60° produces an overlap of these states in k-space. Fortunately, high-quality, single crystal samples with large domain sizes can be produced that allow for in-situ cleavage and measurement of the bulk electronic structure using synchrotron radiation.

5.2.1 Quasi-2D and 3D states

The present investigation of such single crystal samples of WSe_2 begins with a summary of the bulk electronic structure [60]. Initial measurements confirm the

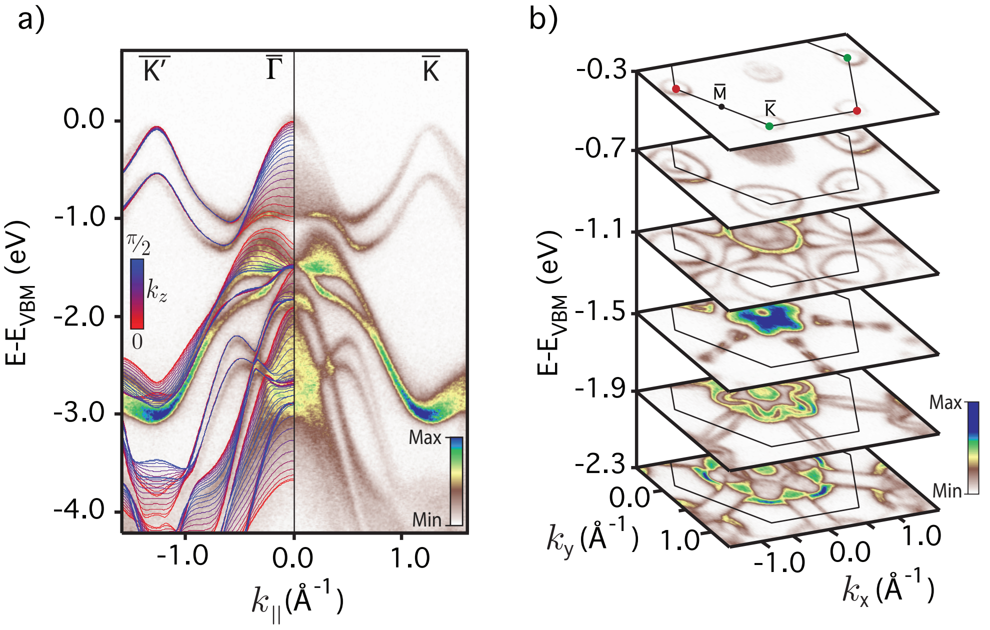

FIGURE 5.5: Electronic structure of bulk WSe$_2$. a) ARPES measurement ($h\nu$=125eV, T=30K) of electronic structure along $\overline{\mathrm{K}'}$-$\overline{\Gamma}$-$\overline{\mathrm{K}}$, with DFT calculations for a range of k_z values. b) Iso-energy contours throughout the in-plane Brillouin zone reveal sharply-defined features toward zone edges, indicative of 2D electronic states, and poorly-defined features near zone centre, indicating 3D states.

semiconductor nature of the material, Fig. 5.5a, indicated by the lack of electronic states crossing the Fermi level, which sits in the bandgap. While the valence band maxima at $\overline{\Gamma}$ and $\overline{\mathrm{K}}/\overline{\mathrm{K}'}$ are almost degenerate, it is possible to resolve that the global maximum is located at the bulk Γ point. Excellent agreement with density functional theory (DFT) calculations, performed by Dr. Saeed Bahramy, is seen when overlaid on ARPES measurements. These calculations highlight the presence of two-dimensional electronic states with negligible dispersion in the k_z direction around the zone corners at low binding energies, as indicated by the degeneracy of bands at different values of k_z. By comparison, states near the zone centre have considerable k_z dispersion, as well as in-plane dispersion, indicating three-dimensional electronic states.

By rotating the sample relative to normal emission, one can collect ARPES measurement across the Brillouin zone and, by taking constant energy cuts, construct contours of the in-plane electronic structure, Fig. 5.5b. Performing such measurements, one observes almost circular hole-like pockets centred around the zone corners, formed by the lowest binding energy valence bands near $\overline{\mathrm{K}}$. As one moves to higher binding energies, these circular rings become triangularly warped until they merge into bone-like shapes along the $\overline{\Gamma}$-$\overline{\mathrm{M}}$ direction. Such measurements reveal sharply-resolved features around the zone edges, indicating 2D states, and the broad features near the zone centre, corresponding to 3D states.

One additional method used to confirm the quasi-2D and 3D nature of the electronic states, and therefore that such measurements are probing the bulk band structure, was probing the material using different photon energies, which alters the value of k_z measured, as indicated by Eq. 3.5. At the zone corners and midway between corners, i.e. $\overline{\mathrm{M}}$, one indeed finds little dispersion in the out-of-plane direction, Fig. 5.6a,b, with excellent agreement to DFT calculations. However, at the zone centre, considerable out-of-plane dispersion is observed, as seen by the feature with a bandwidtch of ~4eV. Additionally, one finds quasi-2D states at $\overline{\Gamma}$, similar to the features at $\overline{\mathrm{K}}$ and $\overline{\mathrm{M}}$. The presence of highly dispersive states in

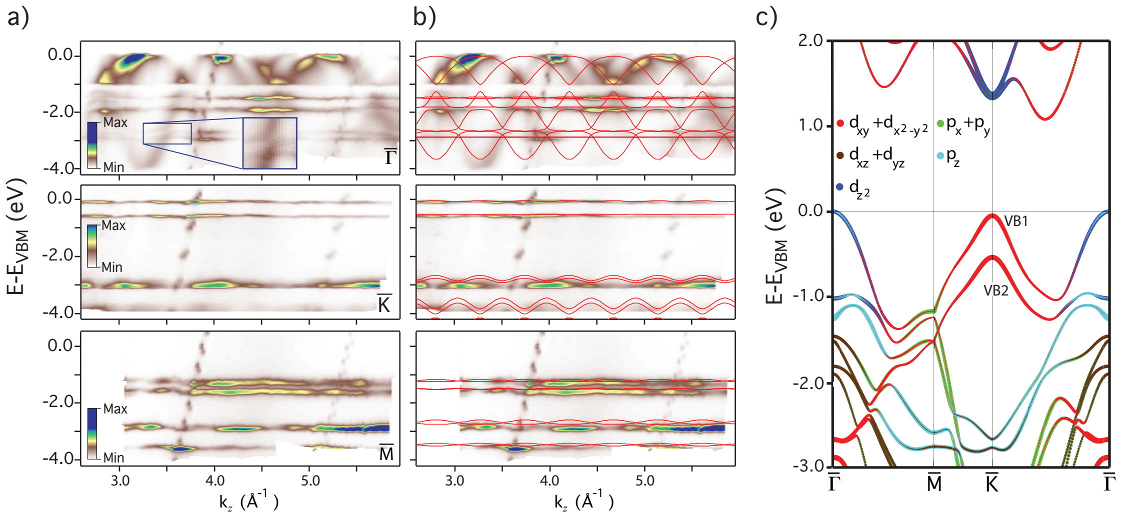

FIGURE 5.6: Photon-energy dependence of bulk WSe$_2$. a) Out-of-plane dispersion at high-symmetry points confirms quasi-2D states at $\overline{\mathrm{K}}$ and $\overline{\mathrm{M}}$, while a mixture of 3D and quasi-2D states exist at $\overline{\Gamma}$. Inset: hybridisation gaps between 3D and 2D states are clearly resolved. b) Comparison to DFT calculations shows excellent agreement with measured dispersions. c) Orbital projection of band structure calculations (at a single value of k_z) indicate the majority of states at $\overline{\mathrm{K}}$ and $\overline{\mathrm{M}}$ are from in-plane orbitals, while states near the zone centre extend in all directions.

both k_z and the in-plane direction, as observed through iso-energy contours and photon energy dependent measurements, indicates states with 3D wavefunctions that extend throughout the bulk crystal. Thus, even though ARPES is a surface sensitive technique, it is capable of measuring bulk electronic structure as the 3D Bloch states are still defined up to the surface. The clear observation of quasi-2D electronic states around the zone edges and 3D states near the zone centre are characteristic of the bulk electronic structure as suggested by the DFT calculations.

Projecting the orbital character onto the DFT calculations reveals a rich orbital texture of the band structure, Fig. 5.6c. One can easily assign the features at $\overline{\mathrm{K}}$ and $\overline{\mathrm{M}}$ as arising from predominantly planar d_{xy}+$d_{x^2-y^2}$ and p_x+p_y orbital character, respectively. The combination of relatively small overlap of these orbitals in the z direction and suppressed interlayer hopping due to spin-orbit coupling [61] results in almost negligible dispersion along k_z, while their extended nature in-plane ensures significant dispersion throughout the surface Brillouin zone. On-the-other-hand, the states around $\overline{\Gamma}$ are derived from orbitals with significant extension in both the in-plane and out-of-plane directions, producing considerable in-plane and k_z dispersion. One also notes the presence of hybridisation gaps, for example between two- and three- dimensional states along the Γ-A line, indicating the strong atomic spin-orbit interaction in this compound. The strength of the spin-orbit interaction is also reflected in the large splitting of $\sim$0.5 eV of the top of the bands at $\overline{\mathrm{K}}$, discussed earlier. In monolayers, the spin-orbit coupling that splits these bands breaks the spin-degeneracy which in turn produces the spin-valley locking, as already mentioned. However, because the bulk structure has a centre of inversion, the bands at $\overline{\mathrm{K}}$ are expected to be spin-degenerate.

5.3 Spin Texture Measured in a Bulk TMDC

In addition to traditional ARPES measurements, spin-resolved measurements were performed on bulk WSe_2, at MAX-Lab, Sweden, with an ability to resolve spin-polarisations in the out-of-plane direction and the in-plane component aligned along the analyser slit.

5.3.1 Observation of spin-polarisation in bulk WSe_2

Despite the preservation of time-reversal and inversion-symmetry in this material, spin-resolved measurements reveal a strong spin-polarisation in the out-of-plane direction for the upper valence band states at $\overline{\mathrm{K}}$ points, Fig. 5.7a-c. Repeating these measurements at $\overline{\mathrm{K}'}$ reveals a spin-polarisation with the opposite sign, as required by time-reversal symmetry, as seen in Fig. 5.7d-f. However, because spin-detectors are not perfectly efficient, typically the raw data is represented in

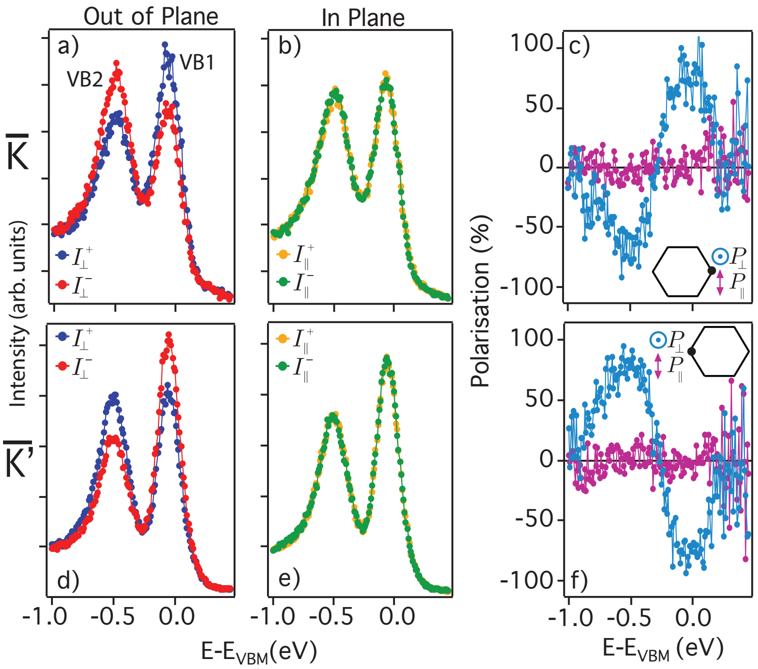

FIGURE 5.7: Unexpected spin-polarisation at zone corners in bulk WSe_2. a) Out-of-plane ($I_\perp$) and b) in-plane ($I_\parallel$) components of the spin at $\overline{\mathrm{K}}$ reveal c) a strong, purely out-of-plane spin-polarisation ($P_\perp$). d-f) Similar measurements at $\overline{\mathrm{K}'}$ show a reversal of this spin-polarisation, as required by time-reversal symmetry.

a "real-spin" method such that:

$$\begin{aligned} I_i^{\uparrow} &= I_i^{tot}(1+P_i)/2 \\ I_i^{\downarrow} &= I_i^{tot}(1-P_i)/2 \\ I_i^{tot} &= (I_i^{+}+I_i^{-}), \end{aligned} \tag{5.1}$$

where $I^{\pm}$ is the raw spin data and $i = \perp, \|$ and P is the spin-polarisation given by:

$$P_i = \frac{1}{S}\frac{I_+ - I_-}{I_+ + I_-}. \tag{5.2}$$

The "real-spin" for the EDCs taken at the $\overline{\mathrm{K}}$ and $\overline{\mathrm{K}'}$ are depicted in Fig. 5.8b, which clearly shows the high degree of spin-polarisation of the valence bands and changing of sign for a given band at the corresponding time-reversal points. By fitting the energy distribution curves of the raw- and real-spin EDCs using a Shirley background and two Lorentz functions, the spin-polarisation can be

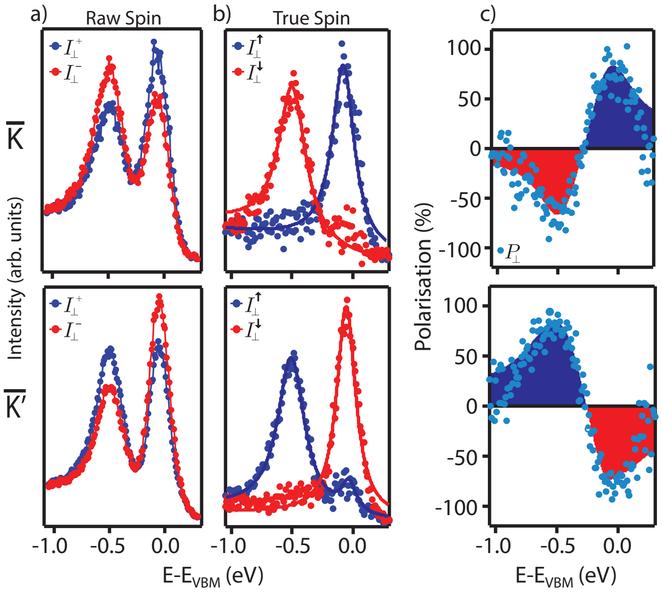

FIGURE 5.8: From raw-spin to real-spin. a) EDCs of the out-of-plane raw-spin data taken at $\overline{\mathrm{K}}/\overline{\mathrm{K}'}$ shows a small asymmetry for the different spin channels due to the inefficiency of the spin-detectors. However, plotting the b) real-spin clearly shows the out-of-plane spin-polarisation of the valence bands. Fitting the peaks using a Shirley background and Lorentz functions, shown as bold lines, allows one to calculate the spin-polarisation, as plotted in c).

extracted and is deduced to exceed 90% in the out-of-plane direction, with no in-plane component, within experimental error. For this analysis, the relative inefficiency of the Mott-spin detector required the use of a Sherman function of S=0.17, which was previously calibrated by beamline scientists [62]; hence the relatively low asymmetry in the raw-data spectra of oppositely aligned spin distributions. In a separate study by Suzuki *et al.* [63], similar measurements were performed on the 3R-MoS_2, which lacks a centre of inversion and therefore one would naively expect to find spin-polarisations perpendicular to the sample surface; however, it is stressed that, here, the bulk crystal structure preserves both time-reversal and inversion symmetry and therefore the electronic states should be spin-degenerate at all points in the Brillouin zone, in apparent contradiction to the spin-ARPES measurements.

By rotating the sample relative to normal emission, as performed for the iso-energy contours, further spin-ARPES measurements along the $\overline{K}$-$\overline{\Gamma}$-$\overline{K'}$ line, displayed in Fig. 5.9, reveal a continuous, monotonic attenuation of the out-of-plane spin-polarisation as one moves along the upper valence bands from $\overline{K}$ to $\overline{\Gamma}$ and eventually a reversal of the spin-polarisation when approaching $\overline{K'}$. In addition to the out-of-plane component, a small in-plane spin-polarisation develops midway between $\overline{K}$ and $\overline{\Gamma}$. Although this in-plane component has not been fully explored, it could be a bulk electronic property [64] or it could arise from relaxations at the sample-vacuum surface that distort the in-plane dipole in the surface layer to project slightly out of the plane, which could give rise to in-plane canting of the spin. One should note, that despite the large size of domains, i.e. larger than the probing beam spot, the presence of rotated domains required extreme care to be taken to avoid illumination of two such domains which would result in the simultaneous measurement of both $\overline{K}$ and $\overline{K'}$. Such simultaneous measurement, similar to photoluminescence experiments which lack k-resolution, would result in observing opposing spin asymmetries and therefore a cancellation of the measured spin-polarisation. In addition to this precaution, measurements were performed

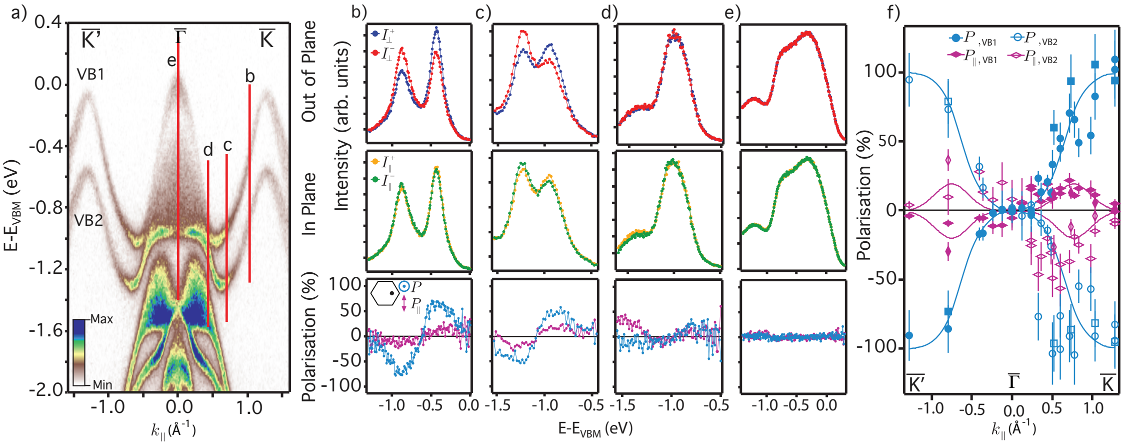

FIGURE 5.9: Spin-polarisation across Brillouin zone. a) ARPES measurement ($h\nu$=125eV, T=30K) along the $\overline{K'}$-$\overline{\Gamma}$-$\overline{K'}$ direction. Red lines indicate the position of b-e) raw spin-ARPES data ($h\nu$=25eV, T=300K). Additional measurements reveal that f) the out-of-plane ($P_{\perp}$) spin-polarisation diminishes as one moves from the zone corner to zone centre, with a small in-plane ($P_{\parallel}$) component developing mid-way along the line. Solid lines are guides-to-eye.

on multiple samples and in a wide array of sample orientations, including azimuthal and polar rotation, to ensure the reversal of spin-polarisation signal for equivalent time-reversal pairs across the zone and at neighbouring zone corners, allowing for a range of geometric factors to be accounted for.

The angle-resolved photoemission measurements of the previous section confirmed the observation of bulk electronic structure of this centrosymmetric material, while the reversal of spin-polarisation at opposite points in k-space indicates that time-reversal symmetry is preserved. Nonetheless, these spin-ARPES measurements clearly reveal a complex k-space spin texture, despite the fact that the combination of time-reversal and inversion symmetry require spin-degeneracy at all points in the Brillouin zone.

5.3.2 Spin-Valley-Layer Locking

The preservation of time-reversal symmetry indicates that no net magnetic moment exists and that the origin of the observed spin-polarisation is of a non-magnetic nature. As demonstrated earlier by the photon energy dependent ARPES measurements, Fig. 5.6, the electronic states that form the upper valence bands at

$\overline{\mathrm{K}}/\overline{\mathrm{K}}'$ have negligible k_z dispersion due to the small out-of-plane extent of the d_{xy} and $d_{x^2-y^2}$ orbitals that suppresses interlayer hopping between successive layers.

The quasi-2D nature exhibited by these states implies that these electrons have their wavefunctions localised to a single Se-W-Se layer. In fact, calculations reveal that the wavefunction for an electron with spin-up in the upper valence band, VB1, at the zone corners is almost entirely localised to the upper W-plane, while the spin-down is localised to the W-plane of the next layer, Fig. 5.10b. Conversely, at the zone centre the spin-up and spin-down wavefunctions are distributed across both layers equally. In other words, the measured out-of-plane spin-polarisation at the zone corners is attributed to a local breaking of inversion symmetry whereby these electronic states experience the 2D nature of the individual layer which does not possess a centre of inversion, whereas around the zone centre, the electronic states experience the full 3D nature of the crystal structure and thus become spin-degenerate as the two-layer unit cell restores inversion symmetry.

The effects of such local inversion-symmetry breaking were recently predicted theoretically and extends not just to the 2H-TMDCs, but also any material where

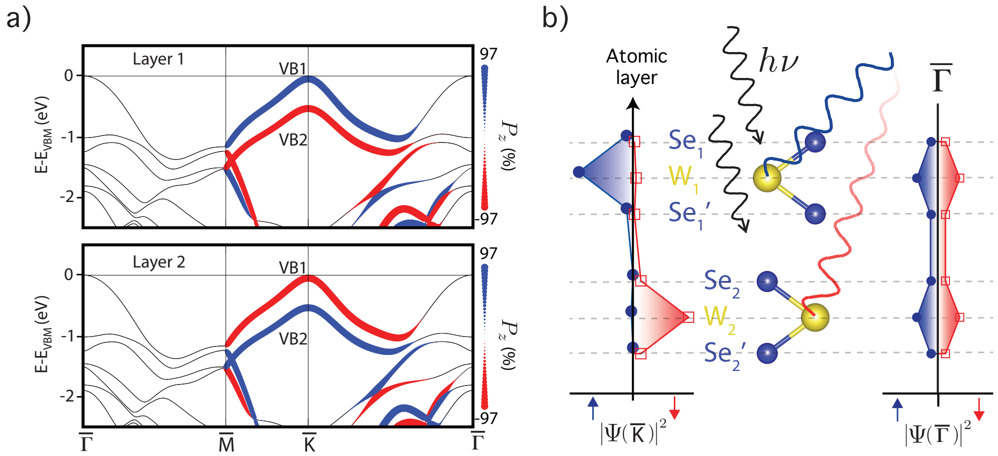

FIGURE 5.10: Spin-valley-layer locking in inversion-symmetric TMDCs. a) Projection of bulk band structure onto individual layers of the unit cell reveals a strong out-of-plane spin-polarisation of electronic states near Brillouin zone boundaries, which reverses between layers. b) Electronic wavefunctions at the zone corners are localised to individual layers for a given spin, while an even distribution exists at the zone centre.

the constituent components lack the inversion symmetry of the unit cell [65]. Indeed, projecting the bulk band structure onto the individual layers, Fig. 5.10a, reveals strong out-of-plane spin-polaristion for the electronic states at the zone corners and edges. Therefore in addition to the spin-valley coupling that occurs at the zone corners for the monolayer, additional locking of the spin to layer degree of freedom manifests itself in the bulk system.

5.3.3 Real- and k-Space Spin-Textures

Thus far, the previous discussion has mainly focused on the surface layer as the emitted photoelectrons will predominantly originate from the uppermost layer; however, it is emphasised that in addition to the reversal of spin-polarisation across the Brillouin zone, as required by time-reversal symmetry, the spin is reversed between layers for a given k, Fig. 5.11a. This is the result of the 180° rotation of subsequent layers in the unit cell which reverses the direction of the net in-plane dipole. Therefore, if one looks at the unit cell as a whole, the population of spin-up and spin-down states are equal, as the centre of inversion is maintained

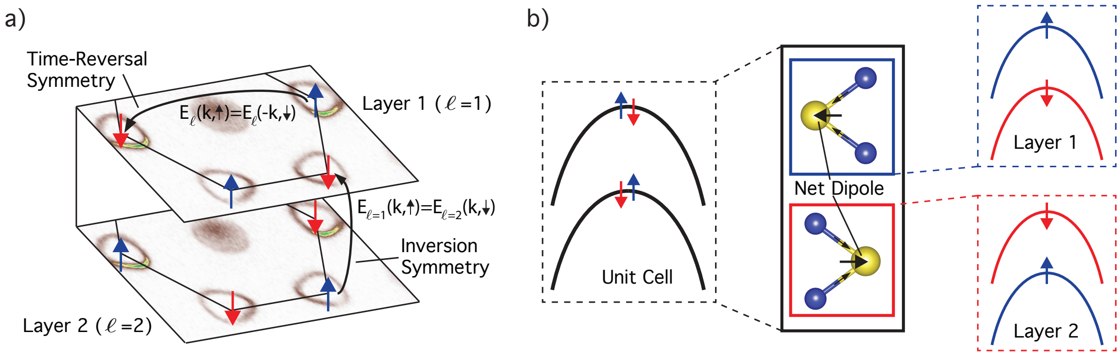

FIGURE 5.11: Local inversion symmetry breaking. a) The out-of-plane spin-polarisation at $\overline{\mathrm{K}}$ reverses direction across the Brillouin zone, preserving time-reversal symmetry, and between layers, preserving inversion-symmetry. b) Therefore, by summing over the unit cell all states are spin-degenerate, but due to a local breaking of inversion symmetry by the individual layers, spin-polarisations perpendicular to the sample surface exist in each layer. The 180° rotation between successive layers reverses the direction of the in-plane dipole and, therefore, the out-of-plane spin-polarisation.

and therefore no net moment occurs for a given k; however, opposite-but-equal spin-polarisations manifest themselves in the individual layers, Fig. 5.11b.

In addition to the out-of-plane spin-polarisation at $\overline{\mathrm{K}}/\overline{\mathrm{K}'}$, the layer-projected band structure presented in Fig. 5.10a suggests a strong out-of-plane spin-polarisation along the zone edges. Indeed, projecting the individual band structures corresponding to the upper valence bands at $\overline{\mathrm{K}}$ onto the two layers of the unit cells, Fig. 5.12a, reveals both a complex real- and k-space spin-texture, as illustrated by the segregation of the zone into two sets of 3 equivalent slices. Each of these sets, which extends out from $\overline{\Gamma}$ to neighbouring $\overline{\mathrm{M}}$ points, encompassing either a $\overline{\mathrm{K}}$ or $\overline{\mathrm{K}'}$, have opposite spin-polarisations which reverses across the zone and between adjacent sections. Additionally, the spin-polarisations is reversed between layers and when moving between the upper and lower valence bands. This real- and k-space spin texture could be ideal for spintronic devices as backscattering, which lowers conductivity, from k to $-k$ requires either a spin-flip (VB1$_u$($\overline{\mathrm{K}}$) →VB1$_u$($\overline{\mathrm{K}'}$)), hopping between layers (VB1$_u$($\overline{\mathrm{K}}$) →VB1$_l$($\overline{\mathrm{K}'}$)) or interband transitions (VB1$_u$($\overline{\mathrm{K}}$) →VB2$_u$($\overline{\mathrm{K}'}$)). Thus all of these processes are suppressed due to energy costs and thus backscattering should be significantly reduced.

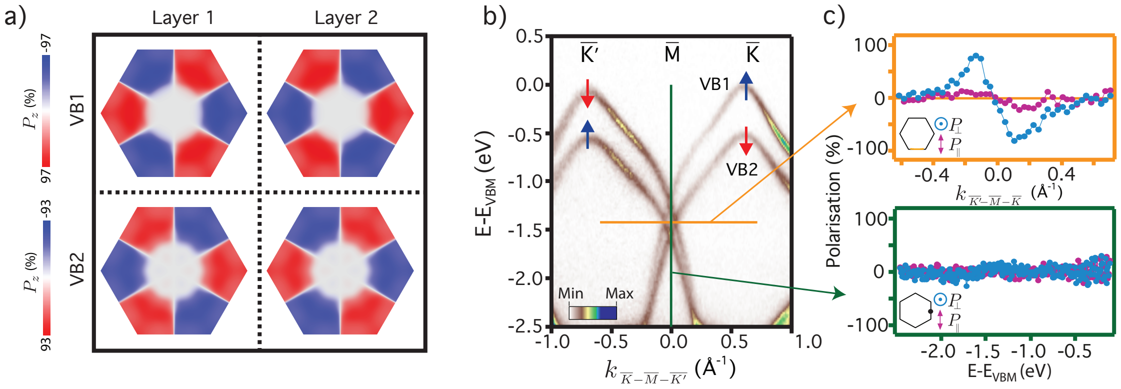

FIGURE 5.12: Real- and k-space spin texture. a) Layer projected band structure for upper (VB1) and lower (VB2) valence bands reveals real- and k-space spin texture throughout the Brillouin zone. b) ARPES measurement ($h\nu$ = 125eV, T=30K) along the $\overline{\mathrm{K}'}$-$\overline{\mathrm{M}}$-$\overline{\mathrm{K}}$ line shows the crossing of bands with spin-polarisations out of the plane. c) A momentum distribution curve (MDC, upper panel) through the middle of the band crossings reveals a preservation of the spin-polarisations that reverses sign across $\overline{\mathrm{M}}$ whereas an EDC (lower panel) at $\overline{\mathrm{M}}$ reveals spin-degeneracy.

One also notices that in addition to a lack of spin-polarisation near the 3D states at the zone centre, a lack of out-of-plane spin-polarisation occurs along the entirety of the $\overline{\Gamma}$-$\overline{\mathrm{M}}$ line. Whereas moving across the zone (i.e. along the $\overline{\mathrm{K}}'$-$\overline{\Gamma}$-$\overline{\mathrm{K}}$ line) the out-of-plane spin-polarisation smoothly diminishes to zero at the zone centre, after which it reverses sign, as observed by the measurments in Fig. 5.9, an abrupt switching of this spin-polarisation occurs along the zone edge (i.e. $\overline{\mathrm{K}}'$-$\overline{\mathrm{M}}$-$\overline{\mathrm{K}}$). The region around $\overline{\Gamma}$ is characterised by the 3D extension of orbitals that provide significant interlayer hopping and, as a result, spin-degeneracy due to the distribution of the spin-up and spin-down wavefunctions across both layers. Conversely, along the zone edge, the crossing of spin-polarised bands with opposite signs, Fig. 5.12b, from neighbouring sections along the $\overline{\Gamma}$-$\overline{\mathrm{M}}$ direction, results in a cancellation of the out-of-plane components. Spin-resolved measurements confirm no out-of-plane spin-polarisation within experimental error in either of the band crossings exactly at $\overline{\mathrm{M}}$; however, measurements along the $\overline{\mathrm{K}}'$-$\overline{\mathrm{M}}$-$\overline{\mathrm{K}}$ verify strong spin-polarisation out of the plane with opposite sign either side of $\overline{\mathrm{M}}$ as one would expect from a crossing of bands with the same spin-polarisation, as shown by the MDC in Fig. 5.12c. The lack of out-of-plane spin-polarisation along the $\overline{\Gamma}$-$\overline{\mathrm{M}}$ direction is the result of the combination of time-reversal symmetry and three-fold rotational symmetry, and is depicted by the DFT calculations previously mentioned, Fig. 5.10a, which predict strong out-of-plane polarisation along the $\overline{\mathrm{K}}$-$\overline{\mathrm{M}}$ line that disappears along the $\overline{\Gamma}$-$\overline{\mathrm{M}}$ line.

5.3.3.1 Quantum Interference Effects

Like surface states, which are localised to the 2D surface-vacuum interface, the electronic states near the Brillouin zone boundary are localised within each W-plane. Because ARPES is a surface-sensitive technique, the majority of the measured photoelectrons originate from the surface layer, with additional attenuated contributions from subsequent layers. Therefore, the combination of the surface sensitivity and the localisation of the states at the Brillouin zone boundary to individual layers allows spin-resolved measurements to probe the spin-polarisation of the surface layer. However, the measured spin-polarisation signal is not entirely free of contributions from subsequent layers and these can give rise to quantum interference effects, similar to the interference patterns seen in Bragg scattering experiments.

To predict the measured out-of-plane spin-polarisation, focusing on the upper valence band at $\overline{\text{K}}$, one starts with a simple bilayer Hamiltonian as developed by Xiao *et al.* [66] such that:

$$H(\mathbf{q}) = \begin{vmatrix} \Delta & at(\tau_z q_x + iq_y) & 0 & 0 \\ at(\tau_z q_x - iq_y) & -\tau_z s_z \lambda & 0 & t_\perp \\ 0 & 0 & \Delta & at(\tau_z q_x - iq_y) \\ 0 & t_\perp & at(\tau_z q_x + iq_y) & \tau_z s_z \lambda \end{vmatrix} \tag{5.3}$$

where $\mathbf{q}$ is the relative wavevector with respect to K points, Δ is the monolayer band gap, a is the lattice constant, $\tau_z = \pm 1$ is the valley index of the bilayer bands, s_z is the Pauli matrix for spin in the z-direction and $t_\perp$ is the nearest-neighbor intra-layer hopping, but due to the symmetry of the d_{z^2} orbitals the interlayer hopping for electrons is zero at K points and therefore is neglected. λ is the spin-valley coupling for holes in monolayers. In a minimal model, as in Ref. [61], the eigenstates of Eq. 5.3 are a spin doublet which for the upper valence band at $\overline{\text{K}}$ can be written as:

$$\begin{aligned} |VB1\rangle =& \frac{\cos\alpha}{\sqrt{2}} \left[\left(\left| d^l_{x^2-y^2} \right\rangle + i \left| d^l_{xy} \right\rangle \right) \otimes |\uparrow\rangle + \left(\left| d^u_{x^2-y^2} \right\rangle - i \left| d^u_{xy} \right\rangle \right) \otimes |\downarrow\rangle \right] \\ &+ \frac{\sin\alpha}{\sqrt{2}} \left[\left(\left| d^u_{x^2-y^2} \right\rangle - i \left| d^u_{xy} \right\rangle \right) \otimes |\uparrow\rangle + \left(\left| d^l_{x^2-y^2} \right\rangle + i \left| d^l_{xy} \right\rangle \right) \otimes |\downarrow\rangle \right] \\ =& \sum_{i,\sigma} c^\sigma_i \phi_{i,\sigma} \end{aligned} \tag{5.4}$$

where $i = u, l$ is the layer index for the upper and lower layer of the unit cell, respectively, and σ is the spin index, with:

$$\begin{aligned} c_u^{\uparrow} &= \frac{\sin\alpha}{\sqrt{2}} = c_l^{\downarrow} \\ c_u^{\downarrow} &= \frac{\cos\alpha}{\sqrt{2}} = c_l^{\uparrow} \\ \phi_{u,\sigma} &= \left|d^u_{x^2-y^2}\right\rangle - i\left|d^u_{xy}\right\rangle \\ \phi_{l,\sigma} &= \left|d^l_{x^2-y^2}\right\rangle + i\left|d^l_{xy}\right\rangle \end{aligned} \tag{5.5}$$

Using this simple construction, one can calculate the photoelectron spin-polarisation, as demonstrated in Refs. [67] and [68], where the photoelectron final state is assumed to be a plane wave and thus the photoemission matrix element can be written as:

$$\begin{aligned} M_{VB1} &= \left\langle e^{i\vec{\mathbf{k}}\cdot\vec{\mathbf{r}}} \middle| \vec{\mathrm{A}}\cdot\vec{\mathrm{p}} \middle| VB1 \right\rangle = \sum_{i,\sigma} c_i^{\sigma} m_i \\ m_i &= \left\langle e^{i\vec{\mathbf{k}}\cdot\vec{\mathbf{r}}} \middle| \vec{\mathrm{A}}\cdot\vec{\mathrm{p}} \middle| \phi_i \right\rangle . \end{aligned} \tag{5.6}$$

The effects of layer-dependent phase and exponential attenuation of photoelectrons emitted from subsequent layers in the crystal can be incorporated using:

$$\begin{aligned} m_i &= e^{-ik_z z_i} e^{-z_i/(2\lambda\cos\theta)} \left\langle e^{i\vec{\mathbf{k}}_{\parallel}\cdot\vec{\mathbf{r}}_{\parallel}} \middle| \vec{\mathrm{A}}\cdot\vec{\mathrm{p}} \middle| \phi_i \right\rangle \\ k_z &= \sqrt{\frac{2m_e}{\hbar^2}(h\nu - E_B) - k_{\parallel}^2}, \end{aligned} \tag{5.7}$$

where θ is the photoelectron emission angle for $\overline{\mathrm{K}}$, λ is the inelastic mean free path and z_i is the layer spacing of W planes perpendicular to the sample surface. As with the Mott-polarimeter, the out-of-plane photoelectron spin-polarisation is given by:

$$P_z = \frac{I_{\uparrow} - I_{\downarrow}}{I_{\uparrow} + I_{\downarrow}} \tag{5.8}$$

except the Sherman function can be neglected (i.e. S=1) and where:

$$I = \left| \sum_i c_i^{\sigma} m_i \right|^2 . \tag{5.9}$$

By combining these last two equations, one can write the spin-polarisation as:

$$P_z = \frac{\sum_i \left(c_i^{\uparrow *} c_i^{\uparrow} - c_i^{\downarrow *} c_i^{\downarrow} \right) |m_i|^2 + \sum_{i \neq i'} \left(c_i^{\uparrow *} c_{i'}^{\uparrow} - c_i^{\downarrow *} c_{i'}^{\downarrow} \right) m_i m_{i'}}{\sum_i \left(c_i^{\uparrow *} c_i^{\uparrow} + c_i^{\downarrow *} c_i^{\downarrow} \right) |m_i|^2 + \sum_{i \neq i'} \left(c_i^{\uparrow *} c_{i'}^{\uparrow} + c_i^{\downarrow *} c_{i'}^{\downarrow} \right) m_i m_{i'}} . \tag{5.10}$$

Here the latter terms give rise to the interference between layers, which for a two-layer system constructed using Eq. 5.5 and assuming $\left\langle e^{i\vec{\mathbf{k}}_\parallel \cdot \vec{\mathbf{r}}_\parallel} \middle| \vec{A} \cdot \vec{\mathrm{p}} \middle| \phi_u \right\rangle = \left\langle e^{i\vec{\mathbf{k}}_\parallel \cdot \vec{\mathbf{r}}_\parallel} \middle| \vec{\mathrm{A}} \cdot \vec{\mathrm{p}} \middle| \phi_l \right\rangle$ simplifies to:

$$P_z = \frac{(\sin^2\alpha - \cos^2\alpha)(1 - e^{-c/(2\lambda\cos\theta)})}{1 + e^{-c/(2\lambda\cos\theta)} + 4\sin\alpha\cos\alpha\cos(\frac{k_z c}{2}) e^{-c/(4\lambda\cos\theta)}} . \tag{5.11}$$

Although this expression initially appears complex, there are several simple things to note. Firstly, is the oscillatory dependence of the measured photoelectron spin-polarisation on the photon energy given by the $\cos(\frac{k_z c}{2})$ term. Thus, by repeating spin-resolved measurements at various photon energies (similar to building the k_z-dispersion maps), one should observe a periodic attenuation/amplification of the magnitude of the measured spin-polarisation. Secondly, one should not only observe periodic fluctuations in the magnitude of the observed spin-polarisation, but also in the total spectral intensity (i.e. the summed intensity of spin-up and spin-down spectra) given by the same quantum interference effects.

To further validate the conclusion that the observed spin-polarisation is the result of locally broken inversion symmetry by the individual layers that constitute the unit cell, a 20-layer bulk-like model was developed using Eq. 5.10. The inelastic mean free paths were calculated from the TPP-2M predictive formula [69], although consistent results were also found using a fixed value of 5 Ångström, and assuming a photon energy dependence of $\left\langle e^{i\vec{\mathbf{k}}_\parallel \cdot \vec{\mathbf{r}}_\parallel} \middle| \vec{\mathrm{A}} \cdot \vec{\mathrm{p}} \middle| \phi_i \right\rangle$ given by the W 5d photoionisation cross section as calculated by Yeh and Lindau [70].

This model was compared to spin-resolved photon energy dependent ARPES measurements, presented in Fig. 5.13a, where very good agreement is found between the predicted and observed maximum spin-polarisation as well as the subsequent drop in measured spin-polarisation which reaches a minimum between $h\nu = 35$eV and $h\nu = 40$eV. Additionally, there is a significant quantitative agreement at higher photon energies, and qualitative agreement at low photon energies, between the calculated and observed total spectral intensity, Fig. 5.13b, as measured by spin-integrated ARPES at Diamond Light Source. The agreement of the model to experimental results provides sufficient confidence in assigning the out-of-plane spin-polarisation as a direct result of the locking of electronic spin to the layer-pseudospin, made possible by the local breaking of inversion symmetry, in addition to the locking of the valley degree of freedom.

As has been seen, despite a centre of inversion in the unit cell, the individual layers of WSe$_2$, and many other TMDCs, locally break inversion symmetry, which, when combined with the net electric dipole moment in each layer, produces layer- and k-dependent spin-polarisations perpendicular to the sample surface. Whereas, ARPES is a surface sensitive technique and therefore capable of directly measuring this spin-polarisation, bulk probes, like the photoluminescence

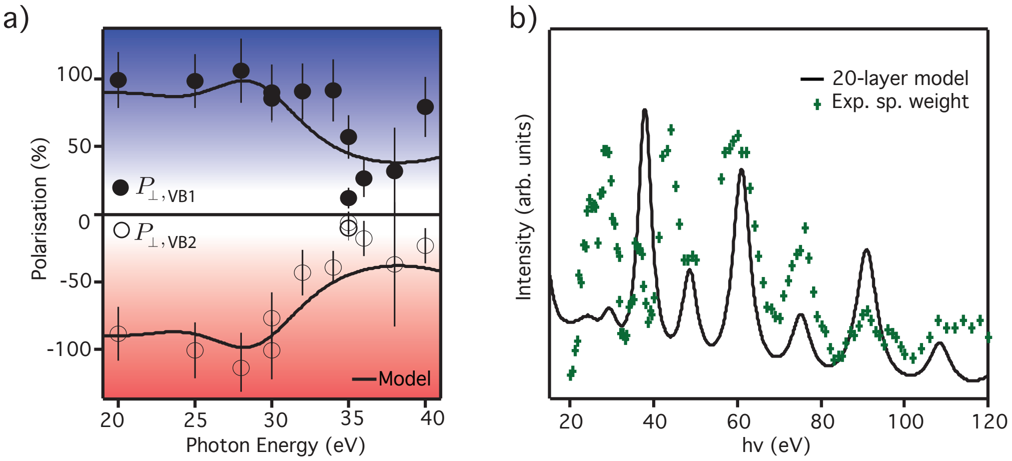

FIGURE 5.13: Depth-dependent attenuation of intensity in ARPES preferentially probes the surface layer, but quantum interference effects between neighbouring layers a) attenuates/amplifies measured spin-polarisation and b) spectral weight of valence bands at $\overline{\mathrm{K}}$.

studies performed on mono- and few-layer TMDCs, will not detect these hidden spin-polarisations because they average over the whole unit cell. Further measurements by Bawden *et al.* [64] on a metallic sister compound 2H-$NbSe_2$ revealed that the strength to which interlayer hopping is suppressed plays a large role in the 3D spin texture. Following on from this work, spin-ARPES measurements on MoS_2 by Razzoli *et al.* [71] showed that the spin-polarised electronic states can be selected using circularly polarised pumping light, while time-resoled ARPES measurements have observed spin-, valley- and layer-polarised excited state populations, also using circularly polarised pumping light [72], adding further support to the locking of spin to the valley- and layer-pseudospins.

Chapter 6

Negative Electronic Compressibility of WSe_2

In the previous chapter the effects of local inversion symmetry breaking on the band structure of bulk WSe_2 were explored. Because the unit cell of bulk 2H-WSe_2 is constructed from two monolayers, which individuallly lack a centre of inversion that is restored by a 180° rotation between successive layers, a hidden spin-polarisation resides in quasi-2D states that are confined to individual layers. This locks the spin to the layer-pseudospin, which is also coupled to the valley-pseudospin. However, all states are required to be spin-degenerate when summed over the entire unit cell. Here, an investigation on the effects of lifting the layer degeneracy of these states by breaking global inversion symmetry is presented [73].

6.1 Breaking of Spin-Layer Degeneracy by Chemical Gating

Semiconducting materials, like silicon and GaAs, underpin most electronic devices for one main reason: their ability to controllably impede the flow of electrical current. Related to this ability is the width of the material's band gap, arguably the most important feature of a semiconductor. If the band gap is too large, such as in insulating materials, it becomes difficult to induce free carriers in the system; too small and thermal occupation of conduction states occurs, giving birth to undesired currents. With a suitably sized band gap, charge carriers can be controllably created in a number of ways, including doping and external potentials. One method for manipulating carrier populations is via charge accumulation in the near surface region of samples. As will be shown, conventional near-surface charge accumulation induces substantial reconstruction of the band structure in semiconducting materials and for WSe_2 it provides a method for controllably lifting the layer-degeneracy of the spin-polarised valence bands investigated in the previous chapter.

6.1.1 Poisson-Schrödinger Solutions for Charge Accumulation at Surfaces

In certain materials, sample preparation, such as the cleavage of single crystals, can result in a charged vacuum-interface due to the off-stoichiometry of the surface layer or from the presence of surface states. The charged surface gives rise to an electric field, which is screened by the rearrangement of electrons in the near-surface region over a length scale approximately equal to the Thomas-Fermi screening length perpendicular to the sample surface. In the case of InAs and InN, unoccupied donor surface states result in a downward bending of electronic bands relative to the Fermi level, leading to an accumulation of electrons at the surface [74]. The band-bending potential is so great that the conduction band states are pulled below the Fermi level and become quantised into discrete levels due to the near-surface potential well, Fig. 6.1a. Because the potential is only in the direction perpendicular to the surface, the quantisation only occurs in this direction and a 2D electron gas is formed as the in-plane motion of carriers is unperturbed. The quantisation of the conduction bands in the band-bending potential well introduces a finite energy offset between the bottom of the well and the resultant conduction band minimum.

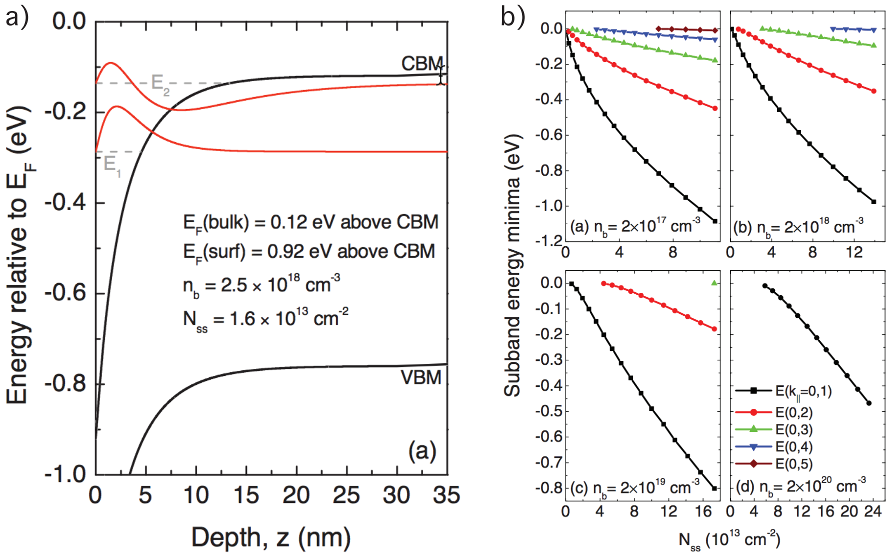

FIGURE 6.1: Poisson-Schrödinger solutions in the modified Thomas-Fermi approximation for InN. a) Charge accumulation at the surface of InN creates a downward band-bending potential into the bulk. The potential well induces the quantisation of the conduction bands into two states with energy E_1 and E_2. b) The binding energy of the conduction band minimum of these quantum well states increases with surface state concentration and decreases with bulk carrier concentration. Adapted from Ref. [74].

Several approaches have been developed to calculate the extent of the band-bending potential, the re-distribution of charge in the near surface region and the in-plane dispersion of the quantised subbands. These methods utilise a self-consistent solution of the Poisson and Schrödinger (PS) equations to describe the effective one-electron potential at the semiconductor surface [75]. An alternative method was developed by Paasch and Übensee [76] within a modified Thomas-Fermi approximation (MTFA) where an infinite potential step at the surface is assumed and the local density of states is modified to approximate the quantum-mechanical reflection at this barrier. While this method is not a self-consistent solution, it was shown to give very accurate results at considerably smaller computational expense. In this formalism, described in detail in Ref. [74] and reproduced briefly here, the one-electron potential, $V(z)$, normal to the sample surface must satisfy Poisson's equation [77]:

$$\frac{d^2V}{dz^2} = -\frac{e}{\epsilon(0)\epsilon_0}\left[N_D^+ - N_A^- - n(z) + p(z)\right], \tag{6.1}$$

where $\epsilon(0)$ is the static dielectric constant, N_D^+ (N_A^-) is the bulk donor (acceptor) density, and $n(z)[p(z)]$ is the electron (hole) density. Charge neutrality requires that no band bending is present in the bulk (i.e. $V(z) \rightarrow 0$ as $z \rightarrow \infty$) and that at the surface (z=0):

$$\frac{dV}{dz} = \frac{e}{\epsilon(0)\epsilon_0} N_{SS}, \tag{6.2}$$

where N_{SS} is the surface state density or an extrinsically induced charge. The carrier density of the conduction and valence bands, respectively, are calculated using:

$$\begin{aligned} n(z) &= \int_0^{\infty} g_c(E) f_{FD}(E) f(z) dE, \\ p(z) &= \sum_i \int_{E_{V_i}}^{-\infty} g_{V_i}(E) \left[1 - f_{FD}(E)\right] f(z) dE, \end{aligned} \tag{6.3}$$

where i denotes one of a number of valence bands, $g_c(E)$ $[g_{V_i}(E)]$ is the density of states for the conduction (i^{th} valence) band, f_{FD} is the Fermi-Dirac function including the potential dependence:

$$f_{FD}(E) = \left(1 + e^{\beta[E - E_F + V(z)]}\right)^{-1}, \tag{6.4}$$

where E_F is the Fermi energy and $\beta^{-1} = k_B T$, and $f(z)$ is the MTFA factor to account for the potential barrier at the surface [78] given by:

$$f(z) = 1 - \text{sinc}\left[\frac{2z}{L}\left(\frac{E}{k_B T}\right)^{1/2}\left(1 + \frac{E}{E_g}\right)^{1/2}\right], \tag{6.5}$$

where L is the thermal length $L = \hbar/(2m_0^* k_B T)^{1/2}$ for nondegenerate and $L = 1/k_F$ for degenerate semiconductors.

With the one-electron band-bending potential solved, one can numerically solve the Schrödinger equation via a Fourier-series representation [79, 80] in terms of envelope functions $\Psi(\mathbf{r}_\parallel, z)$, where $\mathbf{r}_\parallel$ and z are the parallel and normal components of the position vector, respectively, because of the broken translational symmetry in the z direction. Thus the Schrödinger equation is given by:

$$[E_c(-i\nabla) + V(z)]\,\Psi(\mathbf{r}_\parallel, z) = E\Psi(\mathbf{r}_\parallel, z), \tag{6.6}$$

where the eigenfunction for a subband j and a given parallel wave vector $\mathbf{k}_\parallel$ is:

$$\Psi_{\mathbf{k}_\parallel,j}(\mathbf{r}_\parallel, z) = \frac{1}{\sqrt{A}} e^{i\mathbf{k}_\parallel\cdot\mathbf{r}_\parallel} \psi_{\mathbf{k}_\parallel,j}(z), \tag{6.7}$$

with A being the normalisation factor and $\psi_{\mathbf{k}_\parallel,j}(z)$ is the component of the eigenfunction normal to the surface for a given subband and parallel wavevector. Assuming that the wave function is zero at the surface (i.e. does not extend into the vacuum) and decays to zero some distance l into the bulk, $\psi_{\mathbf{k}_\parallel,j}(z)$ can be written as:

$$\psi_{\mathbf{k}_\parallel,j}(z) = \sum_{\nu=1}^{\infty} \sqrt{\frac{2}{l}} a_\nu^{\mathbf{k}_\parallel,j} \sin\left(\frac{\nu\pi}{l}z\right). \tag{6.8}$$

This allows one to rewrite Eq. 6.6 in the matrix representation, such that:

$$\mathbf{M}^{\mathbf{k}_\parallel}\mathbf{a}^{\mathbf{k}_\parallel} = E^{\mathbf{k}_\parallel}\mathbf{a}^{\mathbf{k}_\parallel}, \tag{6.9}$$

and the matrix elements are given by:

$$|\mathbf{M}|_{\nu\nu'} = E_c(k_\nu)\delta_{\nu\nu'} + \frac{2}{l}\int_0^l dz V(z) \sin\left(\frac{\nu\pi}{l}z\right) \sin\left(\frac{\nu'\pi}{l}z\right), \tag{6.10}$$

where $k_\nu = \sqrt{k_\parallel^2 + (\nu\pi/l)^2}$ and $\delta_{\nu\nu'}$ is the Kronecker delta function. The subband energies and wave functions normal to the surface can therefore be determined from the eigenvalues and eigenfunctions of **M**, respectively.

These calculations were performed by King *et al.* [74] for InN where it was found that the increase in bulk carrier concentration reduced the effects of the band-bending potential. As shown in Fig. 6.1b, increasing the bulk carrier concentration, and thus the effective screening, shifted the conduction band minima of the quantised subbands towards the Fermi level and, if this shift was sufficiently large, prevented higher order subbands from forming. It was also shown that by increasing the surface state carrier concentration, the subbands are shifted to higher binding energy as the strength of the surface potential is increased. One method for increasing the bulk carrier concentration is through bulk doping as the Fermi level shifts to maintain charge neutrality while the charge accumulation at the surface can be altered through the application of an external field, such as the electrical gating performed in transistors.

6.1.2 Band-Bending Potential via Chemical Gating

Understanding the effects of such electric field gating is vital for any material that is to be used in spin- or valley-tronic devices. Furthermore, applying an electrostatic potential across a TMDC sample has been proposed as a method to break

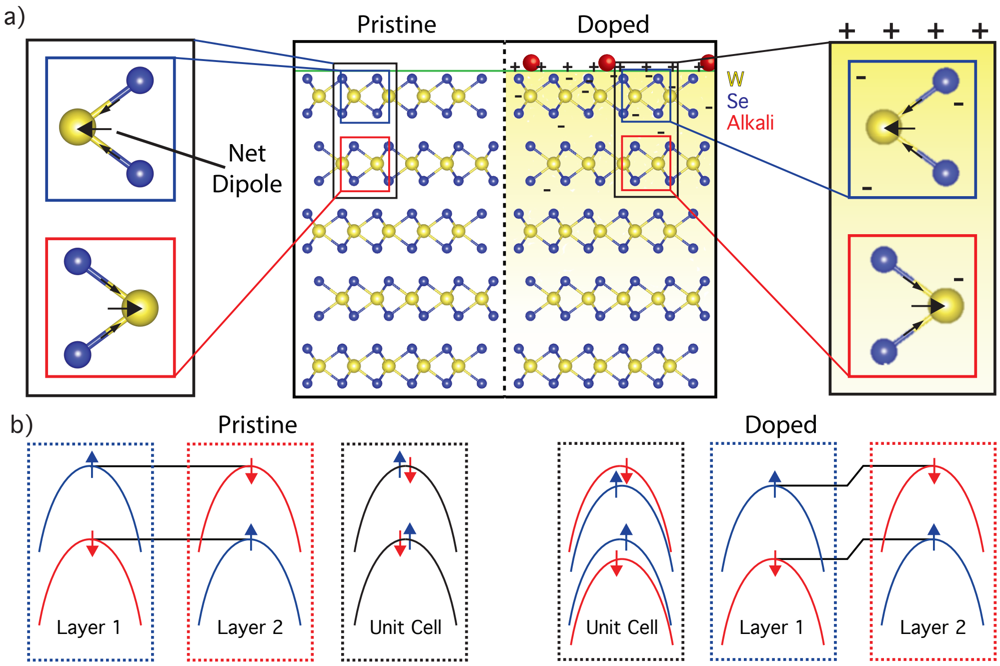

FIGURE 6.2: Breaking the layer-degeneracy via chemical gating. a) The unit cell of WSe_2 is inversion symmetric, although the constituent layers lack a centre of inversion. The deposition of alkali metals onto the sample surface creates an electrostatic band-bending potential which is attenuated as it penetrates into the bulk of the material. b) Schematic of the layer-dependent and unit-cell summed valence bands at $\overline{\mathrm{K}}$ revealing the spin-degeneracy in pristine WSe_2 and spin-splitting in the surface doped case.

the layer-degeneracy as the depth-dependent profile of the potential shifts the layer-localised spin-polarised bands by varying amounts, depicted in Fig. 6.2, as suggested by a study using ionic-liquid gating [81]. Unfortunately, electric fields are not easily compatible with ARPES measurements as the external fields can distort the trajectories of the photoemitted electrons before reaching the analyser lens elements. However, an analogous route to electrically gating bulk WSe_2 crystals is through the deposition of sub-monolayer coverage of alkali metals at the clean sample surface, using a properly outgassed SAES getter source. Due to the electronegativity of the alkali metal, the deposited atoms act as electron donors, creating a charge accumulation layer at the sample surface that induces an electrostatic potential, which penetrates into the bulk of the sample. This potential should be dependent on the alkali concentration, allowing for tuneable increases in potential strength, although reduction is not possible as the desorption of the alkali metal is technically challenging. This method of 'chemical' gating not only mimics the field-effect doping by creating an electrostatic band-bending potential similar to those established by a voltage applied to a traditional electrical gate, like those in transistors, but leaves the surface accessible to detailed ARPES investigations.

6.1.3 Formation of a 2D Electron Gas

It was previously shown that in bulk WSe_2 the valence band maximum (VBM) resides at the zone centre, while an almost degenerate band sits at $\overline{K}$ with a spin-split band at higher binding energy, Fig. 6.3a. The deposition of a small amount of alkali metals (Rb or K) onto the in-situ cleaved surface results in multiple reconstructions of the band structure, as seen in Fig. 6.3b. The induced band-bending potential pulls the conduction band below the Fermi level at a point midway between $\overline{\Gamma}$ and $\overline{K}$, denoted $\overline{T}$. In addition to this electron pocket, the conduction band at $\overline{K}$ is also pulled below the Fermi level; however, due to the indirect band gap nature that places the conduction band minimum at $\overline{T}$ in the pristine bulk

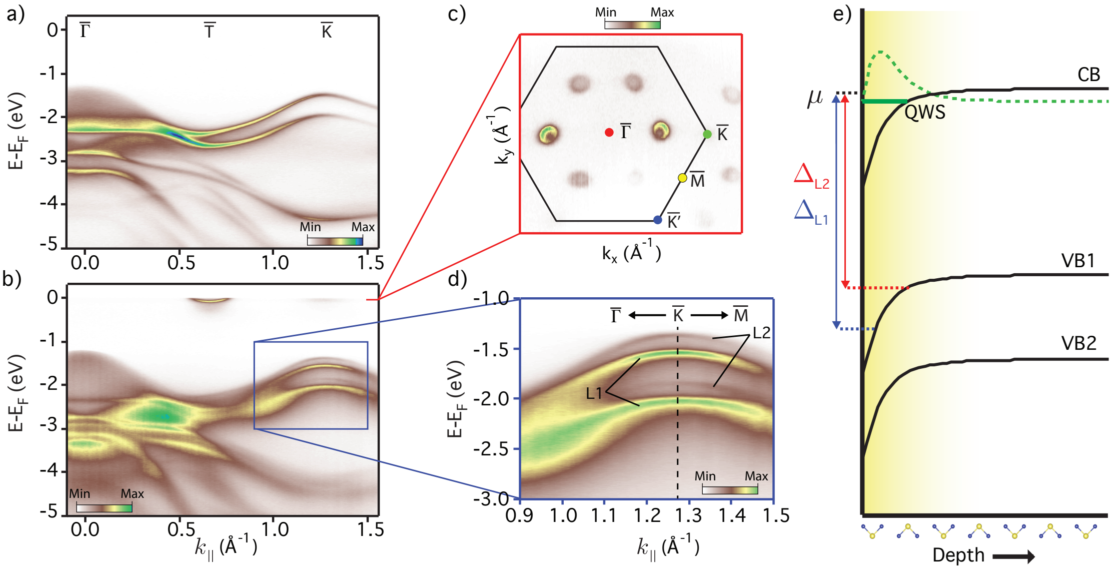

FIGURE 6.3: Band structure reconstruction via alkali metal deposition. ARPES measurements of a) bulk-cleaved WSe$_2$ ($h\nu$ = 75eV) and b) surface Rb-dosed WSe$_2$ ($h\nu$ = 49eV) reveal multiple reconstructions of the bulk electronic structure. c) Iso-energy contours ($h\nu$ = 75eV) reveal the states which cross the Fermi level form six circular electronic pockets midway between $\overline{\Gamma}$ and $\overline{\mathrm{K}}$, as well as smaller pockets at $\overline{\mathrm{K}}$. Additionally, the near-surface electrostatic potential variation that drives the conduction band below the Fermi level also induces a strong spin-splitting between layer 1 (L1) and layer 2 (L2) localised valence band states at $\overline{\mathrm{K}}$. e) Schematic of the depth-dependent electrostatic potential which breaks the layer degeneracy of the valence bands and induces the quantum well states.

material, the spectral weight at $\overline{\mathrm{K}}$ sits closer to the Fermi level and a smaller electron pocket is formed. Taking several measurements while rotating the sample, Fig. 6.3c, the in-plane dispersion of the states at the Fermi level reveals six circular electron pockets at each of the $\overline{\mathrm{T}}$ points with smaller pockets at $\overline{\mathrm{K}}/\overline{\mathrm{K}'}$ points in the Brillouin zone, as one would expect from bulk band structure calculations [60].

Along with the appearance of states that cross the Fermi level, the two valence band states at $\overline{\mathrm{K}}$ split into four well-resolved bands, as seen in Fig. 6.3d. The appearance of a second set of bands is a direct consequence of breaking the layer-degeneracy of the electronic structure. As suggested by the right-hand side of Fig. 6.2b, the layer closest to the surface will experience the strongest electrostatic potential and therefore is shifted to higher binding energies relative to the bulk valence bands, while the subsequent layer experiences a relatively smaller shift due to the attenuation of the band-bending potential as it penetrates into the sample. From the previous chapter, it was established that each of these bands has a spin-polarisation perpendicular to the sample surface with a reversal of sign between layers, as well as between the upper and lower bands. Therefore, breaking the layer-degeneracy is equivalent to inducing a spin-splitting between the layer 1 (L1) and layer 2 (L2) valence bands, as depicted in Fig. 6.2b.

As discussed earlier, in the typical band-bending picture, one expects a shift of band features to higher binding energy, as depicted in Fig. 6.3e, which results in quantum well states (QWS) due to confinement effects of the conduction bands. These QWS should have minimal extension into the bulk as dictated by the depth profile of the potential and therefore negligible dispersion perpendicular to the surface. Photon energy dependent measurements, performed at Diamond Light Source's I05 beamline, reveal the out-of-plane dispersion of both the electron pockets at $\overline{\Gamma}$ and $\overline{\mathrm{K}}$. k_z-dependent momentum distribution curves (MDCs) taken at the Fermi level confirm the 2D nature of the electron gas at $\overline{\Gamma}$, as shown by the fixed value of k_F as the photon energy is varied, Fig. 6.4a. The lack of k_z-dependence is also exhibited by the fixed energy of the conduction band minimum, as seen by the energy distribution curve (EDC) k_z-map taken at $\overline{\Gamma}$ in Fig. 6.4b.

Such k_z-dependent EDCs taken at $\overline{\mathrm{K}}$ also reveal a constant spin-splitting of the valence bands for all k_z and a constant binding energy for the additional, small electron pocket, Fig. 6.4c. As previously mentioned, due to the relatively small electron escape depth, ARPES is a surface-sensitive technique in which the spectral weight originates from the near surface layers with minor additional contributions from the subsequent layers, which are suppressed by inelastic scattering events. From the relative intensity of the valence bands at $\overline{\mathrm{K}}$, one is able to assign the valence band at higher binding energy to the first layer for both the upper and lower valence band, while the additional set of bands is attributed to the second layer, as labelled in Fig. 6.3d. The shift to higher binding energy for the

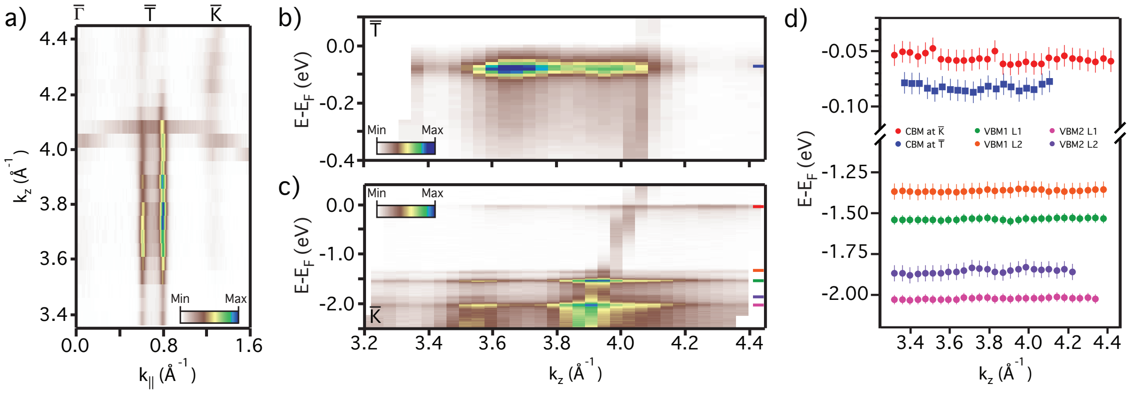

FIGURE 6.4: Photon-energy dependent measurements of Rb-dosed WSe_2. a) k_z dependent measurements taken at the Fermi level, along the $\overline{\Gamma}$-$\overline{\mathrm{K}}$ line reveal no change in k_F as a function of k_z, nor b) any dispersion of the conduction band minimum at $\overline{\mathrm{T}}$. The lack of dispersion in the out-of-plane direction is indicative of a 2D electron gas (2DEG). Similar behaviour is seen in c) the small electron pocket at $\overline{\mathrm{K}}$, as well as the spin-split valence band states at higher binding energies. d) The k_z dependence of the conduction and valence band extrema in b) and c) are extracted, determined from fitting energy distribution curves, confirming the two-dimensional nature of these states. For all measurements presented here, a free-electron final state model was employed, with an inner potential of 13 eV.

near-surface layer matches the qualitative picture expected from typical band-bending theory, as a result of the stronger electrostatic potential experienced by the near surface layer relative to the second layer.

Although, the two-dimensional nature of the conduction and valence band states is similar to the behaviour embodied in the valence band states at $\overline{\mathrm{K}}$ in pristine WSe_2, Fig. 6.4d, confirming the lack of the dispersion in the out-of-plane direction, one should note that the origins of the 2D nature are different between the valence and conduction bands. The spin-split valence band states at $\overline{\mathrm{K}}$ originate from planar $d_{x^2-y^2}$ and d_{xy} orbitals that suppress interlayer hopping, a property that is inherited from the bulk, and therefore even without the application of external potentials these would therefore be two-dimensional. On the other hand, the conduction band states gain their two-dimensionality from the confinement of the carrier's wavefunction in the quantum well created by the near-surface band-bending potential. Therefore, with increased probing depth and improved resolving power, one would expect to see additional spin-split valence bands at $\overline{\mathrm{K}}$

from subsequent layers which experience the ever-weakening potential as it penetrates into the bulk, until eventually the bands are essentially degenerate again as $V(z \to \infty) = 0$. At these photon energies the electron escape depth is <1nm and so only the first two layers are accessible. However, such increased probing ability would reveal no additional information regarding the electron pockets as the wave function is confined entirely to the near-surface region. Nonetheless, these measurements suggest that the deposition of alkali metals provides a convenient method for inducing both a 2D electron gas (2DEG) in the near-surface region and to break the layer-degeneracy, thereby lifting the spin-degeneracy of the electronic states at $\overline{\mathrm{K}}$.

6.1.4 Tuneable Splitting of Valence Bands

The strength of the band-bending potential is intimately tied to the concentration of alkali metal deposited at the cleaved surface of the bulk WSe_2, as suggested by calculations discussed in Sec. 6.1.1. The additional surface coverage increases the band-bending potential, pulling the conduction band further below the Fermi level and increasing the strength of the quantum well that gives rise to the electron gas. Indeed, by increasing the amount of alkali metal on the surface, an increase in the binding energy of the conduction band minimum and the magnitude of k_F for the electron pocket at $\overline{\mathrm{T}}$ is observed, Fig. 6.5a. Iso-energy contours at the Fermi level around these pockets confirm the increasing size of the 2DEG with increased surface dosing and its approximate isotropic in-plane dispersion. From measured Fermi surface maps (Fig. 6.5b-d insets) and MDCs near E_F across the centre of the electron pockets, the 2D Luttinger volume is extracted and used to calculate the carrier concentration according to:

$$N = \frac{g_v k_F^2}{2\pi} \tag{6.11}$$

where g_v=6 and the spin-multiplicity is taken to be g_s=2.

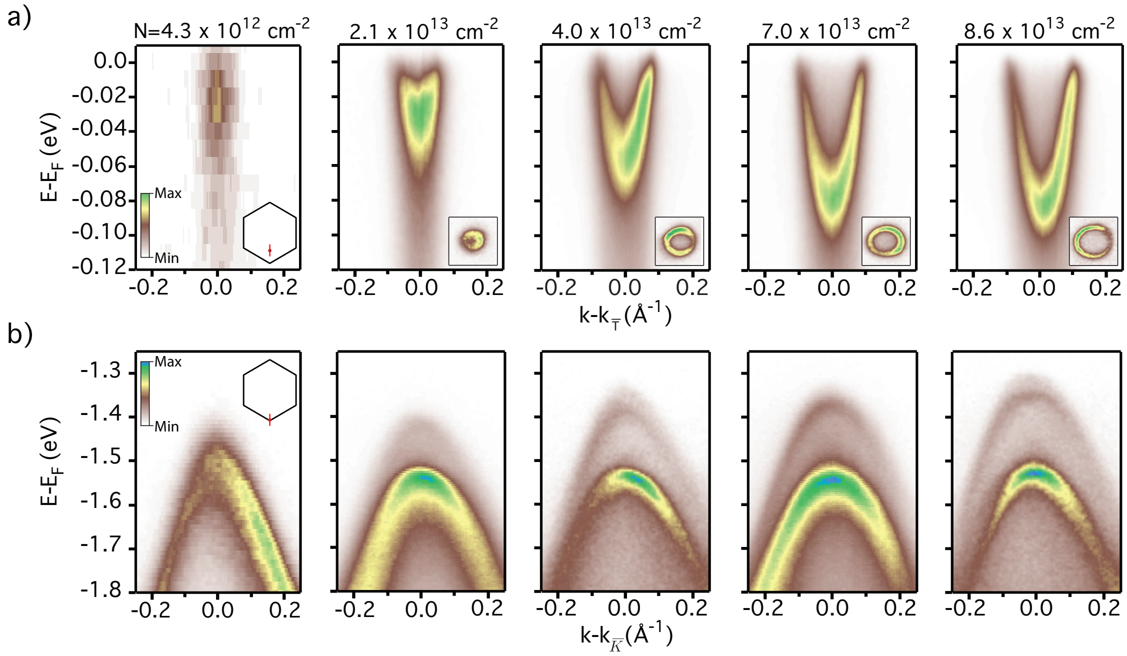

FIGURE 6.5: Tuneable spin-splitting of valence band states. a) ARPES measurements at $\overline{\Gamma}$, aligned along the $\overline{\Gamma}$-$\overline{K}$ direction as indicated by the inset, reveals the dispersion of the 2DEG with increased concentration of the alkali metals deposited on the bulk-cleaved surface. The associated Fermi surface evolution is shown over $k_{x,y} = k_{\overline{T}} \pm 0.17^{-1}$. b) Increased surface dosing also induces a density-dependent spin-splitting of the lowest binding energy valence bands at $\overline{K}$.

Due to the sharp attenuation of this potential into the bulk, the band-bending effects are felt most strongly in the surface layer, with minor effects experienced by the second layer. Because the potential induces a rigid shift of the upper valence bands at $\overline{K}$ for each layer, any difference in the strength of the potential causes a splitting of the bands. By increasing the strength of the potential, one increases the relative difference of the potential experienced by each layer, as depicted in Fig. 6.6, and therefore increases the size of the splitting, Fig. 6.5b. Thus one can use the electrostatic potential to not only break the layer degeneracy, which is akin to inducing a spin-splitting of the valence bands because each has a layer-dependent out-of-plane spin-polarisation, but one can also control the degree of spin-splitting by altering the strength of the electrostatic potential.

From fitting EDCs, the carrier density dependence of the spin-splitting at $\overline{K}$, as well as the binding energy extrema of the electron pocket at $\overline{\Gamma}$, shown in Fig. 6.7a,b respectively, can be extracted. Analysis of this shows that the splitting of

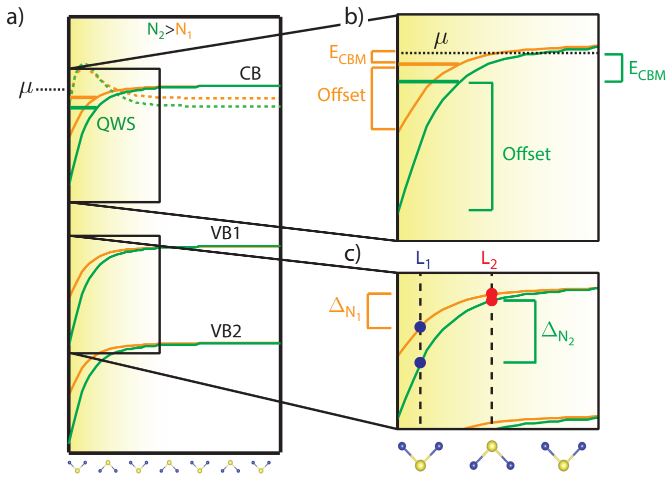

FIGURE 6.6: Alkali concentration dependent electrostatic potential. a) Deposited alkali metals induce electrostatic potential that creates a 2DEG at sample surface and rigid shift of valence bands (orange curves). Increasing the concentration of the alkali metal, increases the strength of the potential, increasing the band-bending effects (green curves) which induces a larger 2DEG such that $N_2 > N_1$. b) The increased potential pushes the conduction band further below the Fermi level, increasing the binding energy of the conduction band minimum, but also the size of the offset between the CBM and the bottom of the potential well. c) The relative strength of the potential felt by subsequent layers results in a splitting of the valence bands that is increased with increased alkali deposition.

the layer 1 and layer 2 valence bands is far larger than the shift in the conduction band minimum, as expected from the rigid shift of the valence band states compared to the confinement of the conduction band within the quantum well where a finite energy offset between the minimum energy of the well and conduction band minimum is introduced. Here, a spin-splitting of up to ∼175 meV is achieved, equivalent to a Zeeman splitting from an external magnetic field of >1000 Tesla [81].

6.2 Doping Dependent Many-Body Effects

Although the downward shift of the conduction bands and the relative shift of the valence bands between layer 1 and layer 2 is consistent with a typical band-bending picture, the ARPES measurements displayed in Fig. 6.5b reveal one inconsistency with this simple picture. Over the range of 2DEG densities spanned by these measurements, band-bending calculations suggest that the valence band

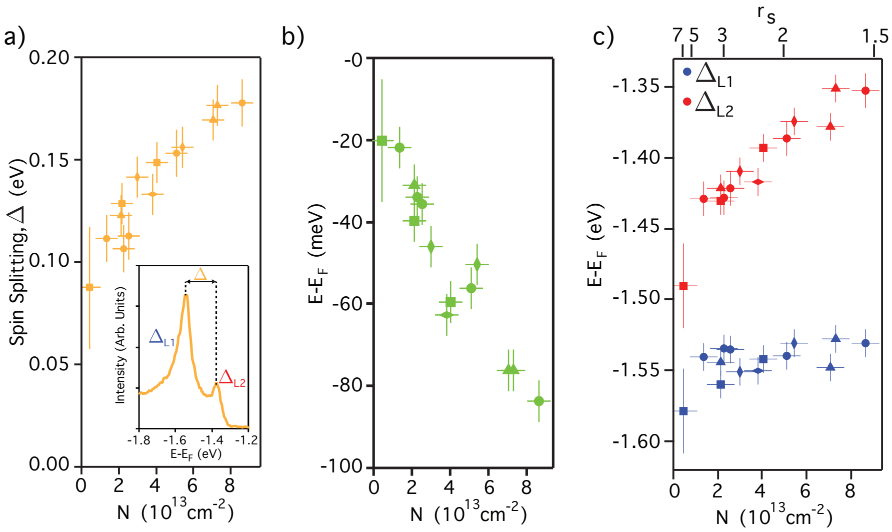

FIGURE 6.7: Carrier concentration dependent shifts of band structure features. a) Extracted density dependence of the spin-splitting, Δ, determined from fitting energy distribution curves (EDCs) at $\overline{\mathrm{K}}$ (inset), where different symbols represent different samples. b) Extracted density dependence of conduction band minimum at $\overline{\mathrm{T}}$, using similar methods, reveals significantly reduced shifts in band extrema. c) Shifting of valence bands to lower binding energies, determined from EDCs like the inset of a), counter-intuitive to traditional band-bending picture.

states originating from the first W layer should increase in binding energy, ΔL1, by more than 200 meV; however, a counterintuitive reduction in the binding energy of ∼50 meV is observed for ΔL1. Additionally, a decrease of almost 150 meV for the valence band states localised on the second W layer, ΔL2, is found, Fig. 6.7c. Such shifts would naively be attributed to conventional semiconductor space-charge regions. However, this explanation would not only imply opposite band-bending for the conduction and valence bands at the surface that is unphysical, but would also be inconsistent with the experimental identification of the relative ordering of L1- and L2-derived valence band states at $\overline{\mathrm{K}}$. Similar arguments rule out surface-photovoltage effects as the origin of the valence-band shifts.

Instead, the reduction in binding energies of the valence band states is attributed to a lowering of the chemical potential in the near surface region due to electron-electron interactions. As illustrated in Fig. 6.8a, if one ignores interactions, the typical band-bending picture for surface charge accumulation is produced. However, inclusion of electron-electron interactions results in a lowering

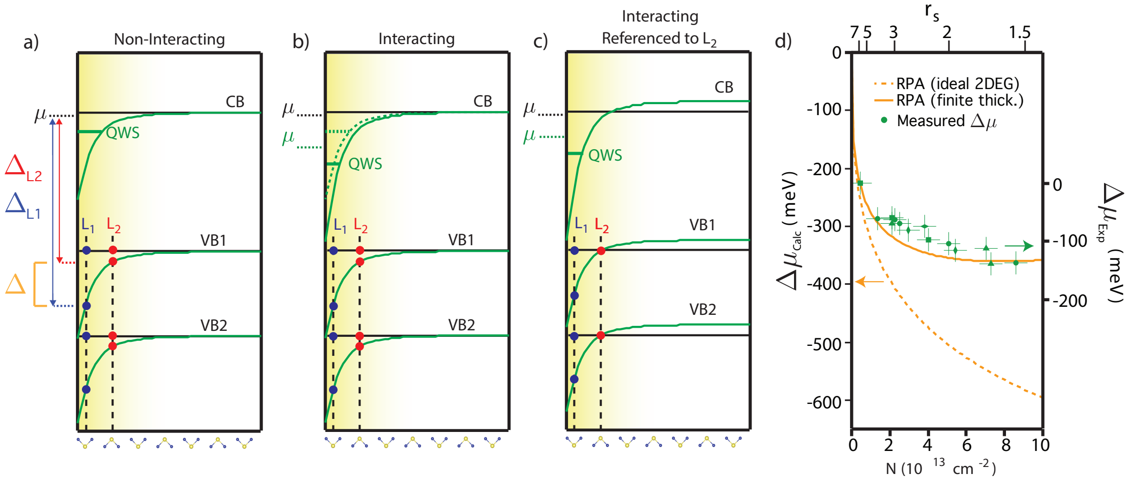

FIGURE 6.8: Estimating the chemical potential shift. a) Cartoon of the non-interacting band-bending picture that drives the conduction band below the Fermi level and rigidly shifts the valence bands in the near surface layers, where the black and green curves represent pristine and surface-dosed WSe_2. b) A reduction of the chemical potential is observed due to electron-electron interactions that can be estimated when c) the binding energy of the conduction band state is referenced to the layer 2 valence bands, which are only weakly effected by the band-bending potential. d) This reveals considerable reduction of the chemical potential, which can be quantitatively explained by RPA calculations including electron-electron interactions in an electron gas of finite thickness.

of the chemical potential and with it the QWS, Fig. 6.8b. Because the strength of the band-bending potential on the second W layer is relatively weak compared to that on the first W layer, the layer 2 valence band states can be used as a reference level to extract a lower limit on the shift of the chemical potential, depicted in Fig. 6.8c. Thus, by referencing the layer 1 valence bands, conduction band minimum and Fermi level relative to the layer 2 valence bands, one finds that the chemical potential monotonically reduces with increased carrier density as shown in Fig. 6.8d, $\kappa = (1/N^2)(\partial\mu/\partial N) < 0$, in a process known as negative electronic compressibility (NEC). This phenomenon is the result of electron-electron interactions that reduce the electronic self-energy as the carrier density is increased, counter to the behaviour in a non-interacting picture.

Typically, semiconductors are considered weakly interacting systems; however, here direct spectroscopic evidence of NEC, which is inherently an effect of many-body interactions, is observed. Furthermore, one finds that $(\partial\mu/\partial N) < 0$ up to the highest measured electron densities of almost 10^{14} cm^{-2}. To put this in context, NEC in GaAs/AlGaAs 2DEGs is observed only at electron densities almost three orders of magnitude lower [82], whereas in graphene, NEC is only found once the kinetic energy is suppressed by the application of a magnetic field [83]. In a previous study by Larentis *et al.* [84] on a gated graphene-MoS_2 heterostructure, transport measurements suggested the chemical potential of the MoS_2 flake could be reduced upon filling of the MoS_2 conduction states, implying the presence of negative electronic compressibility. In that study, calculations of the self-energy in the random phase approximation (RPA) revealed that the exchange and correlation energies dominate the kinetic energy, reducing the chemical potential in MoS_2. As such, the theory of these RPA self-energy calculations will now be reviewed and extended to the case of surface-doped WSe_2.

6.2.1 Self-Energy Calculations in the Random Phase Approximation

In a non-interacting picture, the chemical potential can be calculated in a straightforward manner from the density of states at the Fermi level; however, when interactions are included, one must calculate the electronic exchange and correlation energies as a result of electron-electron interactions. Through calculation of the carrier density dependence of the self-energy, the chemical potential can be determined according to:

$$\mu_{tot} = \frac{\partial(\varepsilon_{tot}N)}{\partial N}, \tag{6.12}$$

where $\varepsilon_{tot} = \varepsilon_{non} + \varepsilon_{exc} + \varepsilon_{corr}$ is the total self-energy, which is the sum of the non-interacting, exchange and correlation energies, respectively.

In the 3D free-electron gas picture, one can visualise doping electrons into the system as adding successive shells to the Fermi sphere, as seen in Ch. II. Because of the Pauli exclusion principle, doping the system increases the energy at which subsequent electrons are added, pushing the chemical potential upwards. This picture is modified in the case of surface doping where electrons are added in concentric rings due to the reduced dimensionality of the 2D electron gas and thus the energy required to add the Nth electron in a non-interacting picture is given by:

$$\varepsilon_{non}(N) = \frac{\hbar^2 \pi N}{g_v g_s m^*}, \tag{6.13}$$

where N is the carrier density, $g_v = 6$ is the valley degeneracy, $g_s = 2$ is the spin-degeneracy and $m^* = 0.555m_e$ is the in-plane effective mass of the carriers. Eq. 6.13 produces the well-known result that in a non-interacting 2D electron gas the energy per electron (i.e. $\partial\varepsilon/\partial N$) is constant and there is a linear increase in the chemical potential with increased carrier density (i.e. $\partial(\varepsilon N)/\partial N$).

If, however, electron-electron interactions are included, the chemical potential for the 2DEG becomes less straightforward to calculate. To this end, one can calculate the exchange and correlation energies in the random phase approximation (RPA). The exchange energy arises from the ability of two or more electrons with parallel spins to exchange their positions in degenerate orbitals, while the correlation energy is related to the degree in which the motion of one electron is affected by the presence of all the other electrons. In this formalism, it is assumed that electrons respond only to the total electric potential, which is the sum of any external potentials and a screening potential, the former of which is assumed to oscillate at a single frequency, w. This method produces a dynamic response function, $\epsilon(\mathbf{k}, w)$, from which it is assumed that the contributions from the total electric potential are averaged out such that only the potential at wave vector $\mathbf{k}$ contributes to the self-energy [85]. This averaging modifies the dynamic response function, producing the Lindhard dielectric function [11, 86].

In the dilute doping limit, the Fermi wavevector is relatively small compared to the intervalley wavevector, i.e. the wavevector scattering an electron from one electron pocket into another. Therefore, relative to intravalley scattering, intervalley electron-electron scattering will be strongly suppressed. As a result, the

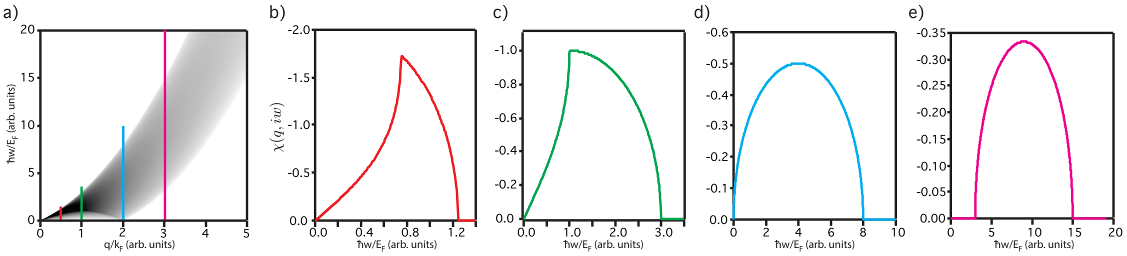

FIGURE 6.9: Polarisability of a dielectric medium. a) The 2D Lindhard dielectric function along the imaginary axis, $\chi(q, iw)$, plotted with dimensionless wavevector, $\overline{q} = q/k_F$ and frequency, $\overline{w} = \hbar w/E_F$. b-e) Line-profiles at $\overline{q}$ =0.5, 1.0, 2.0, 3.0, corresponding to the lines in a), revealing the reduction of $\chi(q, iw)$ with increased $\overline{q}$ and alteration of line-shape, including the well-known 'shark-fin' shape at $\overline{q} < 1$.

valley-pseudospin represents a degeneracy factor in the exchange and correlation interactions, as does the spin degree of freedom. The exchange energy per electron is therefore given by [84]:

$$\varepsilon_{exc} = -\frac{16}{3\pi(g_v g_s)^{1/2}}\left(\frac{R_y^*}{r_s}\right) \tag{6.14}$$

where $R_y^* = R_y m^*/\epsilon_{tot}^2$ is the reduced Rydberg constant, $r_s = m^*/(\epsilon_{tot} a_B (\pi N)^{1/2})$ is the dimensionless interparticle separation parameter, a_B is the Bohr radius and $\epsilon_{tot} = ((\epsilon^{\parallel}_{WSe_2}\epsilon^{\perp}_{WSe_2})^{1/2} + 1)/2$. The latter of these is the total dielectric constant, determined by averaging the bulk properties with the vacuum to account for the penetration of the field lines into vacuum as the 2DEG should be constrained to the near-surface region.

The correlation energy per electron can be calculated by integrating over the dimensionless wavevector, $\overline{q}$, and frequency, $\overline{w}$, such that [84]:

$$\begin{aligned}\varepsilon_{corr} = \frac{4}{g_v^2 g_s^2}\left(\frac{R_y^*}{\pi r_s^2}\right)\int \overline{q}\, \mathrm{d}\overline{q} \int \mathrm{d}\overline{w}\left(r_s \frac{(g_v g_s)^{3/2}}{2\overline{q}}\chi(q, iw)\right.\\ \left.+ \ln\left(1 - r_s \frac{(g_v g_s)^{3/2}}{2\overline{q}}\chi(q, iw)\right)\right),\end{aligned} \tag{6.15}$$

where $\chi(q, iw)$ is the 2D Lindhard dielectric function along the imaginary axis, plotted in Fig. 6.9a, given by [87]:

$$\chi(q, iw) = -\frac{1}{\overline{q}}\left[\Theta(1-\nu_-^2)\sqrt{1-\nu_-^2} - \Theta(1-\nu_+^2)\sqrt{1-\nu_+^2}\right], \tag{6.16}$$

where $\Theta(x > 0) = 1$ is the heavyside step function and the dimensionless wavevector, $\overline{q}$, and frequency, ω, are given by:

$$\begin{aligned} \overline{q} &\equiv \frac{q}{k_F} \\ \nu_\pm &\equiv \frac{w}{q\nu_F} \pm \frac{q}{2k_F}, \end{aligned} \tag{6.17}$$

with k_F being the Fermi wavevector and $\nu_F = \hbar k_{F\sigma}/m^*$ is the Fermi velocity.

Calculating the non-interacting and exchange energies is computationally inexpensive in comparison to the numerical integration required for the calculation of the correlation energy, which was performed by determining the integrand for a 2D grid of ($\overline{q}$,$\overline{w}$) pairs, as plotted in Fig. 6.10b, and using trapazoidal integration to find the area within the grid. Due to the discrete step size of the grid, convergence of the 2D integrals was tested for both Δq and Δw, as shown in Fig. 6.10c,d, resulting in integration fluctuations smaller than 0.1meV. In addition to the convergence tests on the grid size, the limits of the integrals over q and w were tested, resulting in self-energies with less than 1meV uncertainty, below experimental uncertainties for the measurements presented, Fig. 6.10b. Because the integrand is 0 except in a narrow region of the allowable excitations, the area of integration was divided into smaller regions to reduce the computational expense, as shown in Fig. 6.10a.

Using this method, one can calculate the different contributions to the energy required to add an electron to the system at any given carrier density. Doing so, one finds that while the non-interacting energy is always positive, the exchange and correlation energies reduce the energy at which subsequent electrons are added to the conduction band. In fact, RPA calculations reveal that

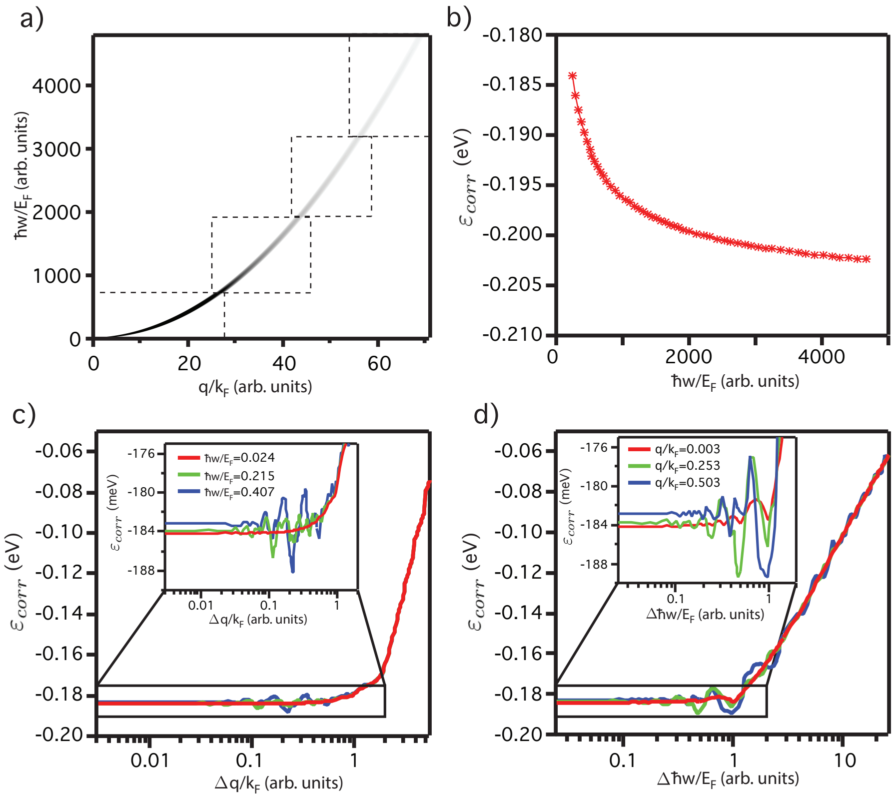

FIGURE 6.10: Calculating correlation energies in the random phase approximation. a) Numerical integration over the dimensionless wavevector and frequency requires construction of multiple grids (outlined in dashed boxes) of ($\overline{q}$,$\overline{w}$) pairs to reduce computational expense. b) Tests for the convergence of the integrated area reveal that $> 95\%$ of the correlation energy is accounted for by integrating over the first two sections. c) Convergence tests of the finite wavevector step size, $\Delta q/k_F$, at three values of $\hbar w/E_F$ reveal sufficient convergence using a grid step size of $\Delta q/k_F \leq 0.1$. d) Similar convergence tests for $\Delta \hbar w/E_F$ show sufficient convergence for $\Delta \hbar w/E_F < 0.2$.

the interacting contributions are sufficient to overcome the increase from the kinetic energy term for carrier densities spanned by the ARPES measurements, and thus the chemical potential monotonically reduces with increased carrier density (i.e. $\partial(\varepsilon_{tot}N)/\partial N < 0$), qualitatively reproducing the reduction of the chemical potential observed experimentally, $\Delta\mu_{exp}$, shown in Fig. 6.8d. However, one should note that these calculations represent the chemical potential for an ideal 2DEG (i.e. zero extension into the bulk) and therefore a form factor $f(q)$ with $\epsilon^*_{tot}(q) = \epsilon_{tot}/f(q)$ is included to account for the finite-thickness of the electron

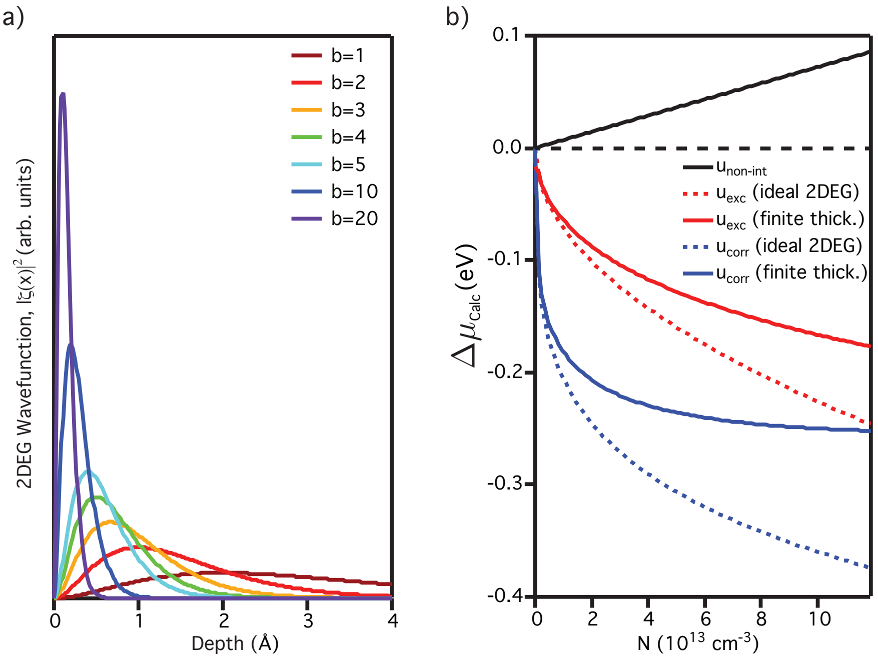

FIGURE 6.11: Inclusion of finite thickness into RPA calculations. a) Depth profile of the 2D wavefunction into the sample as a result of the triangular well form factor $f(q)$ for various values of b. b) Modification of the exchange and correlation energies after inclusion of form factor with $\epsilon^*_{tot}(q) = \epsilon_{tot}/f(q)$ resulting in significant reduction of the contribution of the exchange and correlation to the change of the chemical potential.

gas. This form factor is given by:

$$f(q) = \frac{8 + 9x + 3x^2}{8(1+x)^3} + \frac{\epsilon_{tot} - \epsilon_{vac}}{\epsilon_{tot} + \epsilon_{vac}} \frac{1}{(1+x)^6}, \tag{6.18}$$

where $x = q/b$ and b is taken to be 3Å^{-1} to give a 2DEG localised over approximately 5Å. Such form factors are described by a wave function of the form $\zeta(z) = 2b^{3/2} z e^{-bz}$, where z is the spatial extent into the bulk. Inclusion of the finite thickness effects of the 2DEG greatly reduces the effects of both the exchange and correlation energies to the change in the chemical potential, Fig. 6.11b, which results in excellent quantitative agreement with observed measurements, even to the highest carrier concentrations, Fig. 6.8d.

The observation of such persistent NEC here indicates a powerful role of many-body interactions, whereby exchange and correlation energies dominate the kinetic energy over a remarkably large carrier-density range. This is attributed to a combination of factors. The six-valley 2DEG at $\overline{\mathrm{T}}$ and relatively high effective mass ensures that the kinetic energy stays low even for rather high electron densities. Moreover, the high effective mass, together with low dielectric constants of both WSe$_2$ and the vacuum-interface, enhance the exchange and correlation energies, which allows them to dominate the kinetic energy for a wider range of carrier densities.

6.2.2 Reduction in Band Gap

One striking consequence of NEC in WSe$_2$ is the reduction of the indirect band gap as a function of carrier density. In a non-interacting picture, the band-bending potential at the surface would conventionally cause a downward shift of the valence bands originating in the near-surface layers relative to the Fermi level and the quantisation of the conduction band in the narrow potential well. From band-bending calculations, illustrated in Fig. 6.11a, it is estimated from the RPA calculations that the 2DEG wavefunction is localised near the sample surface and extends less than half a unit cell into the bulk, while the states at $\overline{\mathrm{K}}$ were previously seen to reside entirely in individual W-planes. Thus, one can restrict discussions of the indirect bandgap to transitions from the layer 1 upper valence band to the QWS, as transitions from the layer 2 valence bands would require additional energy to perform the interlayer hopping necessary to reach an available final state.

The quantisation of the conduction band in the potential well introduces a finite offset between the minimum of the quantum well state and the bottom of the well. Because of the energy offset inherent to the QWS, in the non-interacting picture, the energy difference between the valence band maximum at $\overline{\mathrm{K}}$ for layer 1 and the minimum of the QWS (i.e. the layer 1 indirect bandgap) should always increase with increased surface coverage of alkali metal. Instead, in the presence of strong electron-electron interactions, as the band-bending potential pulls the conduction band further below the Fermi level and the carrier density of the 2DEG is increased, the effects of NEC grow and thereby the chemical potential is lowered, which reduces the binding energy of the valence bands relative to the Fermi level. If the reduction in the chemical potential is greater than the incremental increase in the CBM/potential-well offset, the valence bands will shift up enough to overcome the enlargement of the bandgap expected in the non-interacting picture.

To disentangle the non-interacting effects of the band-bending potential and the subsequent many-body effects that result in NEC, density functional theory calculations were performed by Dr. Saeed Bahramy for bulk WSe_2 using the Perdew-Burke-Ernzerhof exchange-correlation potential modified by the Becke-Johnson potential as implemented in the WIEN2K programme, fully taking into account relativistic effects, including the spin-orbit interaction [17]. The Brillouin zone was sampled by a 12 x 12 x 6 k-mesh. The tight-binding supercell calculations were performed by downfolding these calculations using maximally localised Wannier functions [88], with W $5d$ & $5s$ and Se $5p$ & $5s$ orbitals as the basis states. To account for the surface sensitivity of the ARPES measurements, the spectral weight calculated for each WSe_2 layer was multiplied by an exponential decay function e^{-z/λ_e}, where z is the distance from the surface and $\lambda_e = 5\text{Å}$ is the inelastic mean free path of the photoelectrons. Such calculations, shown in Fig. 6.12a, qualitatively reproduce the band structure of pristine WSe_2 and the observed out-of-plane spin-polarisation of the states at $\overline{\text{K}}$, due to the spin-valley-layer locking discussed in the previous chapter.

These calculations were extended through inclusion of band bending as an on-site potential term [89], as calculated using the PS-MTFA method described in Sec. 6.1.1. These predict the formation of a QWS and downward shift of the valence bands, as well as the spin-splitting of the valence bands from the lifting of the layer-degeneracy and increase in the layer 1 and layer 2 indirect bandgaps, ξ_{L1} and ξ_{L2}, respectively, Fig. 6.12b. Finally, inclusion of additional potential contributions for the conduction bands from many-body exchange and correlation effects were incorporated, Fig. 6.12c, with renormalisation of the chemical potential

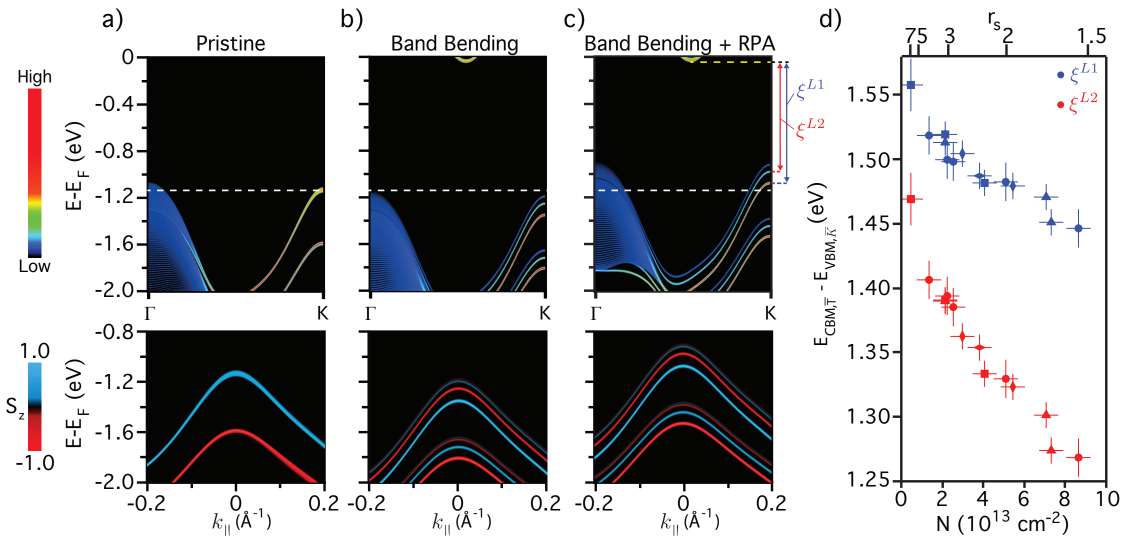

FIGURE 6.12: Modification of the indirect band gap. Surface-projected tight-binding supercell calculations of the electronic structure (top) and out-of-plane spin projection, S_z, of the valence bands at $\overline{\mathrm{K}}$ (bottom) of a) pristine bulk WSe_2 and b) chemically gated WSe_2, including band bending but not the effects of electron interactions. This reveals the creation of a 2DEG and spin splitting of the valence bands. c) Including an exchange and correlation potential derived from the finite-thickness RPA calculations leads to an upward shift of the near-surface valence bands relative to the chemical potential which induces a shrinkage of the layer-dependent quasiparticle bandgap, $\xi_{L1,L2}$, extracted experimentally in d). White dashed lines represent the binding energy of the upper valence bands at $\overline{\mathrm{K}}$ for pristine bulk WSe_2, included as an energy reference in b) and c). The yellow dashed line in c) marks the energy of the 2DEG conduction-band minimum.

to maintain the same layer-dependent charge density as for the non-interacting system. These latter calculations qualitatively match the ARPES measurements on surface-dosed WSe_2 and predict the reduction in ξ_{L1} and ξ_{L2}. Indeed, analysis of the layer-dependent indirect band gaps, extracted from EDCs of the conduction band at $\overline{\Gamma}$ and valence bands at $\overline{\mathrm{K}}$ reveals that, over this range of carrier densities, there is a ~200meV reduction to ξ_{L2} and over 100meV shrinkage of ξ_{L1}, Fig. 6.12d. The reduction of the bandgap has subsequently been suggested to occur from optically excited carrier concentrations in time-resolved ARPES measurements [90] and through doping [91] of monolayer MoS_2, as well as in measurements of monolayer $MoSe_2$ where a significantly smaller bandgap was observed for heavily electron-doped samples [65] compared with undoped samples [92]. Therefore, it is expected that the findings of persistent negative electronic compressibility just discussed are likely to hold for all TMDCs and establishes this family of materials as strongly interacting systems.

Constructed of monolayer sheets, weakly held together by van der Waals interactions, these materials exhibit many novel phenomena directly related to their reduced dimensionality, as demonstrated by the experimental observations of the last two chapters. It has been shown that as a result of this reduced dimensionality, states that are localised to individual layers experience a monolayer-like environment that gives birth to a hidden out-of-spin spin-polarisation in the out-of-plane direction which is forbidden by conventional symmetry arguments. Furthermore, it was seen that by controlling the formation of a 2D electron gas at the sample surface, drastic reconstruction of the band structure can be induced with counter-intuitive shifts as a result of many-body interactions. The dominance of these many-body interactions to carrier concentrations orders of magnitude larger than in typical semiconductors is attributed to relatively heavy electron masses, the multi-valley nature of the electron pockets that form, and the relatively low dielectric constants of WSe_2 in conjunction with the surface-vacuum interface. All of these are likely to be intimately tied to the 2D nature of these materials, as suggested by the drastic reduction of the NEC effects when a finite thickness was included in the RPA calculations. In the next two chapters, experimental evidence will be presented for similar many-body interactions, but in a fully 3D material, Gd-doped EuO.

Chapter 7

Growth of Europium (II) Oxide, EuO, by MBE

Paramount to the function of spintronic devices is a material in which electronic spins can be manipulated for the transfer of information. However, this is not the only element necessary for the function of devices such as the spin-transistor envisioned by Datta and Das in 1990 [2]; the injection of a highly spin-polarised current into the semiconducting material must also be achieved, as well as an ability to "read" the spins after they have passed through the interim medium. These processes have produced significant issues as the injection of highly spin-polarised electrons into a semiconducting material requires the source and drain materials to be half-metals, such as metallic Fe, with spin-polarised conduction bands, but semiconductor-metal interfaces have been shown to produce strong reductions in the purity of the spin-current, making injection and reading inefficient. However, one material, europium (II) oxide, provides a possible solution to this issue due to its properties as a ferromagnetic semiconductor. Initial attempts to integrate EuO with silicon, the basis for many existing electronic devices, resulted in considerable spin-flip scattering due to the presence of interstitial phases at the EuO/Si interface [93], although more recent developments in the growth process have achieved abrupt interfaces necessary to preserve the highly spin-polarised current upon injection [94]. Here, an overview will be given of the basic properties of EuO and the growth recipe developed in the mu-MBE system attached to the I05-endstation at Diamond Light Source. Through in-situ transfer, these samples were then measured by ARPES, which forms the results of the following two chapters.

7.1 Background Information

The whole family of europium mono-chalcogenides (EuX, X=Se,S,O,Te) embody a large array of interesting magnetic and electrical phenomenon [95]. Since its discovery in solid solution with SrO [96] and subsequent isolation in the 1960's, europium monoxide, EuO, has been shown to host a wide range of phenomenon including the giant magneto-optic Kerr [97] and Faraday effects [98, 99] and the anomalous Hall effect [100]. However, it is the interesting interplay between EuO's magnetic and electrical properties that are the focus of the discussion here.

7.1.1 Ferromagnetic Transition

In stoichiometric EuO, each Eu $4f$ orbital is half-filled, which if one ignores magnetic effects, has 7 unaligned electrons, while the O $2p$ derived states at higher

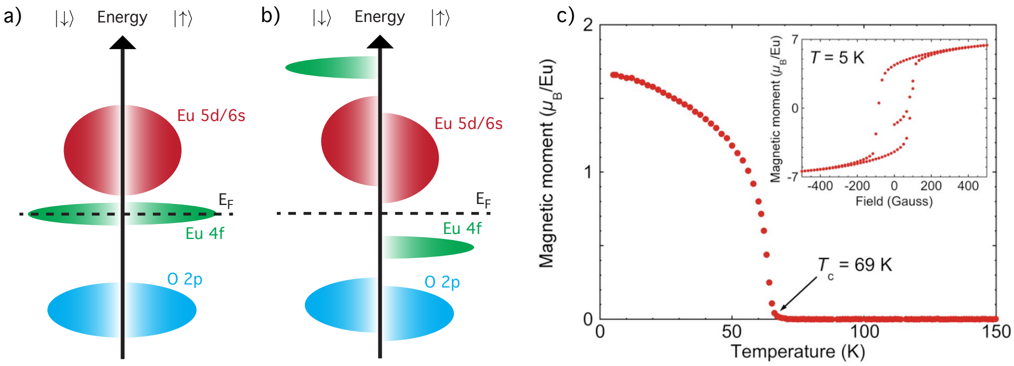

FIGURE 7.1: Magnetic origin of EuO. a) Ignoring magnetic effects, the half-filled Eu $4f$ band and fully-filled O $2p$ bands have equal spin-up and spin-down populations, while the Eu $5d$ orbitals remain empty. b) If magnetic effects are included, the 7 unpaired $4f$ electrons align, causing an exchange splitting of the O $2p$ valence and Eu $5d$ conduction states. c) Temperature dependence of the magnetic moment of undoped EuO, revealing the onset of ferromagnetism at T_C=69K, reproduced from Ref. [101]. (inset) Magnetic hysteresis loop, taken at 5K, shows the ferromagnetic behaviour with saturation magnetisation of $7\mu_B$ per Eu atom.

binding energy are completely filled, visualised in Fig. 7.1a. "Turning-on" magnetism, the 7 unpaired $4f$ electrons at each Eu^{2+} lattice site align their spin states according to Hund's rule, resulting in a large magnetic moment on each cation, Fig. 7.1b, when cooled below the Curie temperature, determined to be T_C=69K for stoichiometric EuO [102], Fig. 7.1c. The alignment of the Eu $4f$ electrons induces an exchange splitting of the O $2p$ valence bands and Eu $5d$ conduction bands. Due to the highly-localised nature of the Eu $4f$ electrons, crystal field effects are suppressed and spin-orbit coupling is relatively strong. This gives rise to a net spin moment of $S = 7/2$ per Eu atom and a saturation magnetisation in the low temperature phase of $7\mu_B$ for every Eu atom. While smaller than gadolinium [103] and dysprosium [104], EuO hosts the third highest magnetisation of all known ferromagnets, even higher than pure europium, due to an increase in the density of Eu in EuO compared to pure Eu [105, 106].

Because of the highly localised nature of the Eu $4f$ orbitals and relatively high effective screening, the individual magnetic moments are considered almost completely localised to the Eu lattices sites. While it was originally thought that EuO was an ideal embodiment of a Heisenberg ferromagnet, as evidenced by its temperature-dependent magnetisation curve which is a near-perfect Brillouin function [101], recent angle-resolved photoemission measurements have revealed momentum dependence of the Eu $4f$ band structure, providing evidence for the hybridisation of adjacent $4f$ orbitals [107]. Additionally, temperature-dependent ARPES measurements have revealed shifts of the Eu $4f$ and O $2p$ bands that have been attributed to the hybridisation of the Eu $4f$-O $2p$ and Eu $4f$-$5d$ orbitals via the momentum-dependent superexchange and indirect exchange interactions, respectively [107]. These measurements suggest that many-body interactions play a vital role in the electronic structure of EuO.

7.1.2 Metal-Insulator Transition

Undoped EuO is highly insulating, making photoemission experiments particularly difficult as emission of electrons through the photoelectric effect would result in severe charging effects. However, a transition into a metallic phase, concomitant with the ferromagnetic transition, has been observed in electron doped samples [109]. In samples with oxygen vacancies, which contain two extra electrons per vacancy, an activation energy of $\sim$0.3eV has been measured in the paramagnetic phase, but below the transition temperature the conductivity was seen to increase by approximately 13 orders of magnitude [108], as shown in Fig. 7.2a. It has been postulated that this dual transition to a ferromagnetic metal is the result of the exchange splitting of the Eu 5df conduction band states, which drives the spin-majority band below the Fermi level [110]. Using spin-resolved x-ray absorption spectroscopy, Steeneken *et al.* [111] showed that in the ferromagnetic state, the degeneracy of the majority and minority conduction band is lifted and the bands become separated by approximately 0.6eV. Thus, as EuO becomes magnetically ordered, the spin-majority band shifts downwards 0.3eV, consistent

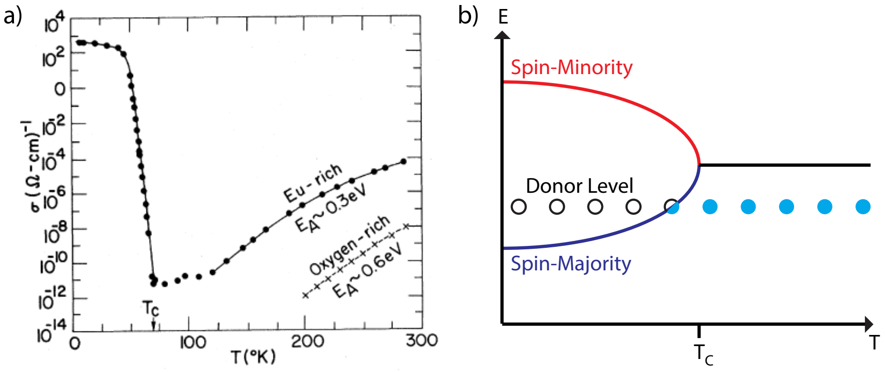

FIGURE 7.2: Oxygen-rich EuO samples are highly insulating, even at relatively high temperatures. a) Introducing oxygen vacancies increases the conductivity by approximately 4 orders of magnitude, in the paramagnetic state, although the samples are still insulating above T_C. As the magnetic transition is approached, the conductivity reduces such that it is immeasurable, but increases over 13 orders of magnitude as ferromagnetic ordering sets in. Reproduced from Ref. [108]. b) Schematic of donor levels that contribute to the metal-insulator transition.

with the (activation) energy needed to make oxygen-deficient samples conductive above T_C, and crosses the Fermi level such that the conduction band and donor levels become degenerate, thereby driving the insulator-metal transition. In the weak-doping limit, only the spin-majority band crosses the Fermi level, producing a spin-polarised conduction band, which is ideal for spin-injection in spintronic devices.

An additional explanation for the simultaneous transitions has been attributed to bound magnetic polarons (BMPs). In systems with magnetic ions, carriers can reduce their energy via the exchange interaction by aligning their spins with that of the nearby magnetic ions, forming free magnetic polarons. In the case of EuO, it is believed that the carriers become bound to impurity sites and are thus referred to as bound magnetic polarons. Experimental evidence for the presence of BMPs in oxygen deficient EuO has been observed and through which T_C can be altered with the application of external magnetic fields [108, 112].

7.1.3 Tuneable T_C through Doping and Film Thickness

The drastic deviation from the insulating behaviour of stoichiometric films has not just been seen in oxygen-deficient samples, but has also been observed by substitutional dopants of the divalent Eu^{2+} ions with La^{3+} [113, 116–118], Gd^{3+} [113, 117–119] or Fe^{3+} [119–122], which are trivalent and thus donate a single electron per dopant. Not only has such substitutional doping been shown to induce the insulator-metal transition concomitant with the ferromagnetic transition, it has also been shown to significantly increase the Curie temperature [113]. Transport and magnetisation measurements on a wide range of $Eu_{1-x}Gd_xO$ samples with varying doping concentrations revealed that the increase in conductivity is always concurrent with the magnetic ordering, shown in Fig. 7.3a,b, further highlighting the intimate interplay of the exchange splitting and the position of the Fermi level. The highest T_C has been recorded for Fe- and La-doping [116,

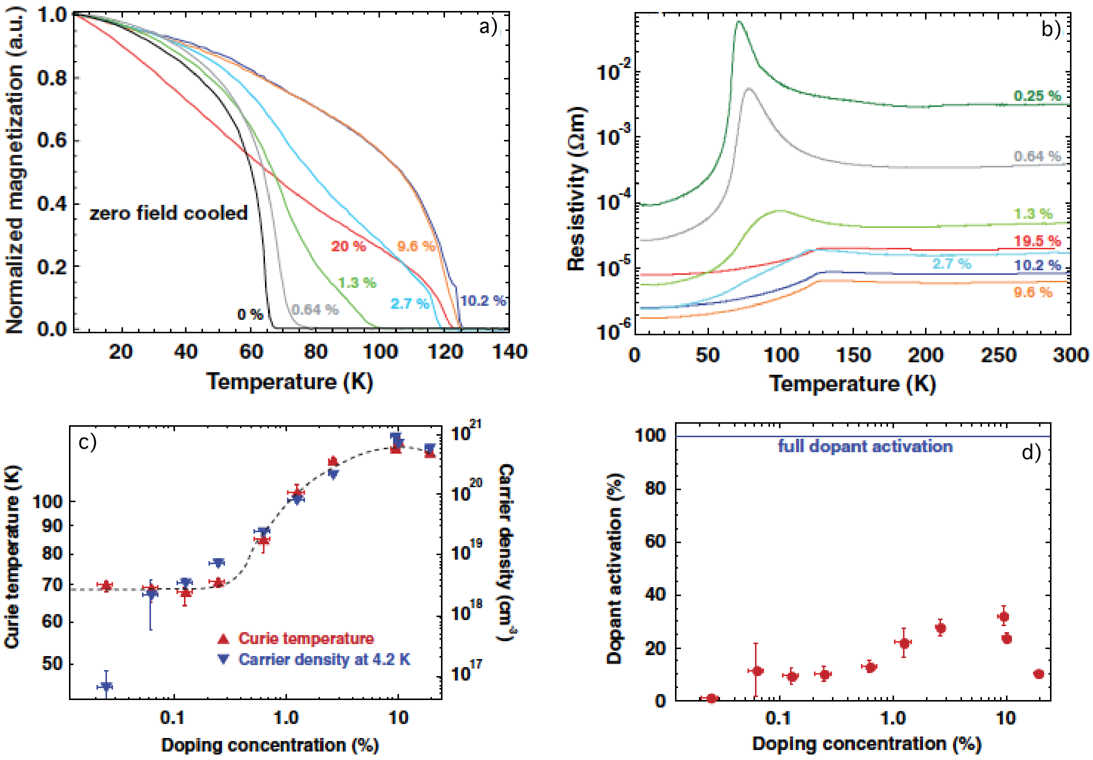

FIGURE 7.3: Magnetic and transport properties of Gd-doped EuO. As the doping concentration is increased, a) the Curie temperature is raised, as measured by the DC SQUID magnetisation vs. temperature curves in zero magnetic field. b) Additionally, temperature dependent transport measurements show that the metal-insulator and ferromagnetic transitions always occur simultaneously. c) The Curie temperature and carrier density saturate at ~130K and ~6x10^{20}cm^{-3}, respectively. Both properties are seen to decrease at doping concentrations above 10%, corresponding to d) a sudden decrease in the dopant activation. Reproduced from Ref. [113].

122] where the transition temperature was increased to 200K; however, subsequent research has struggled to reproduce such drastic increases in Curie temperature and typically the T_C is found to saturate around 120K-130K. Comparison of the Curie temperature and the carrier density as a function of the doping concentration shows how closely tied the two properties are, Fig. 7.3c, and the apparent saturation of T_C as been attributed to a drastic reduction in the dopant activation at high concentrations, Fig. 7.3d. As the doping concentration increases, the likelihood of two dopants being nearest neighbours (ignoring O^{2-} sites) increases and as these clusters of the dopants increase in size and frequency, small domains of gadolinium oxide can form, preventing the Gd^{3+} from donating an electron.

Replacing some of the Eu^{2+} atoms with Gd^{3+}, La^{3+} or Fe^{3+}, or removing O^{2-}

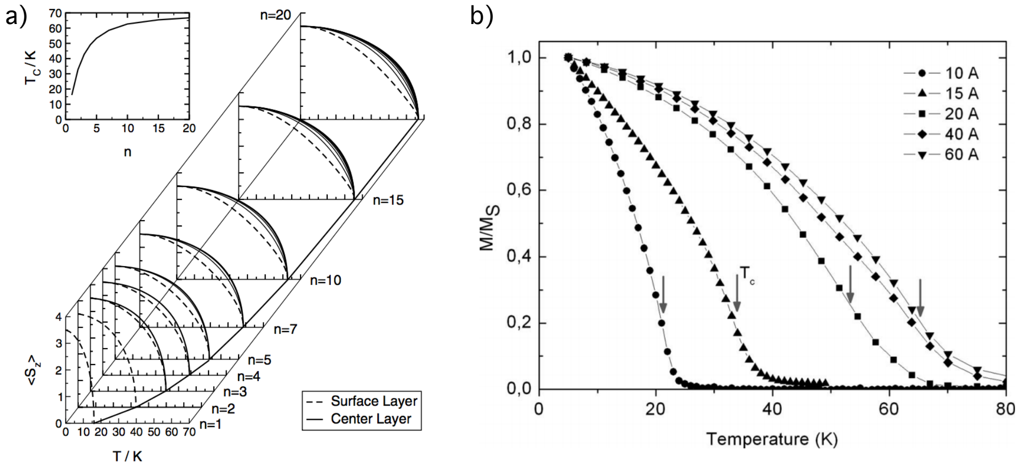

FIGURE 7.4: Thickness dependence of EuO thin films. a) Theoretical calculations predict a significant reduction of T_C as sample thickness is reduced below 20 monolayers. (inset) Curie temperature as a function of number of layers. b) Experimental measurement of temperature dependent magnetisation of ultra-thin films confirms the reduction of T_C as samples are thinned from 12 to 2 monolayers. a) and b) are reproduced from Ref. [114] and Ref. [115], respectively.

ions, is not the only method for altering the T_C. Schiller and Nolting [114] predicted that as sample thickness is reduced below ∼20 monolayers, the T_C is drastically reduced, as shown in Fig. 7.4a. The lowering of T_C has been acreditted to the reduced number of neighbouring Eu sites at the surface and interface layers of the thin films. In the bulk layers of EuO, each Eu^{2+} ion is ferromagnetically coupled to its 12 nearest neighbour (NN) and 6 next-nearest neighbour (NNN) Eu atoms, but on the surface layers of the (001) face, there are only 8 NN and 5 NNN Eu atoms to couple to. Müller *et al.* [115] confirmed this prediction showing that ultra-thin films indeed have a reduced T_C, shown in Fig. 7.4b, except a lower T_C was reported than predicted by Schiller and Nolting, which was attributed to incomplete surface layers and imperfect boundaries.

As will be seen next, the intimate connection between magnetic properties, chemical composition and thickness are useful indicators for the initial stages of Gd-doped EuO thin film growth. Additionally, the change in resistivity of samples above and below T_C with doping allows for ARPES measurements, which require conductive surfaces, to be taken on samples, allowing for one to directly investigate the ferromagnetic and insulator-metal transition.

7.2 Thin Film Growth of $Eu_{1-x}Gd_xO$

While EuO is scientifically interesting and embodies a range of novel phenomena, it is also only a meta-stable form of europium, making it difficult to work with. Exposure to atmospheric conditions results in further oxidation of the europium atoms to form the more stable Eu_3O_4 and Eu_2O_3. Interestingly, these latter materials do not display the same high magnetisation or metal-insulator transition of the monoxide form. Therefore, the preparation and measurement of EuO requires great care to prevent unwanted oxidation and involves either the use of in-situ transfer to measurement chambers or burying samples under a capping layer. As discussed earlier, one such growth system exists at Diamond Light Source and has been developed to grow EuO as part of this PhD project, with in-situ transfer to the HR-ARPES branch of the I05 beamline for measurement using synchrotron radiation. This section discusses the growth of high quality thin films of single-crystal Gd-doped EuO.

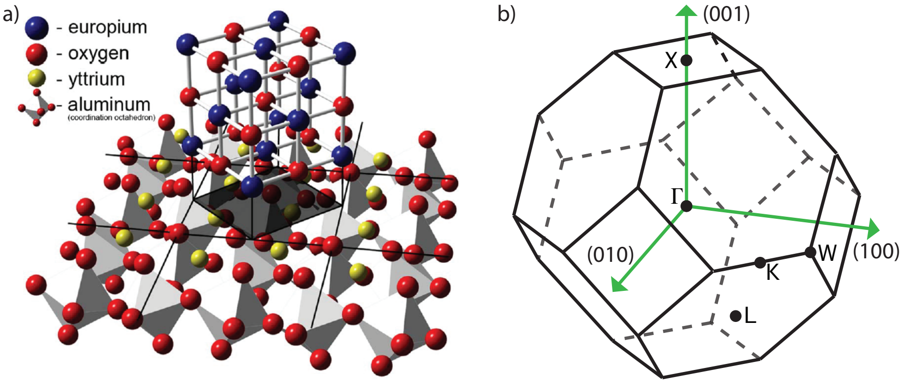

FIGURE 7.5: Crystal structure and Brillouin zone of EuO. a) $YAlO_3$ provides a suitable substrate for the growth of EuO. A rotation of 45° allows two unit cells of EuO to fit within a single $YAlO_3$ unit cell, providing relatively low linear strain, ~2.1% along the $[110]_{EuO} \parallel [\bar{1}10]_{YAlO_3}$ direction. Reproduced from Ref. [101]. b) Corresponding bulk Brillouin zone of EuO with high symmetry points and lattice directions.

7.2.1 Growing in the Adsorption Controlled Regime

Like the other europium monocalcogenides, EuO forms in the rock salt, face-centred cubic (fcc, space group Fm$\overline{3}$m) crystal structure with a lattice constant that varies from a=5.127 Å to 5.144 Å as the sample is cooled below 300K [123]. Growth of EuO thin films has been demonstrated on a wide range of substrates, including Si [93, 124], GaAs [125] and graphene [126, 127], making it an ideal candidate for next generation electronic devices based around current semiconductor production processes. Unfortunately, in the case of Si/EuO heterostructures, preserving a pristine Si interface has proved challenging as there is a propensity for silicon oxides and other interstitial phases to form at the interface which prevent efficient spin-injection into Si [124]. Although atomically sharp interfaces between EuO and Si, without the presence of europium silicides, have been achieved [94], this presents an additional obstacle in preparing high quality films.

On the other hand, substrates such as yttria-stabilised cubic zirconia (YSZ) [128], $LaAlO_3$ [129] and $YAlO_3$ [101] have been shown to release oxygen into the initial layers of deposited Eu, allowing for sharp interfaces with growth of stoichiometric EuO, provided certain precautions are taken to avoid over-oxidation. As shown in Fig. 7.5, with a 45° degree rotation, EuO is well suited for growth on $YAlO_3$ (110) single crystals, which have in-plane lattice constants of 7.431 Å and 7.370 Å along [$\bar{1}$10] and [001], respectively. This provides a relatively small linear lattice mismatch of 2.1% for $[110]_{EuO} \; \| [\bar{1}10]_{YAlO_3}$ and 1.3% for $[\bar{1}10]_{EuO} \; \| [001]_{YAlO_3}$, respectively [130]. Alternatively, growth on YSZ provides almost perfect lattice matching.

One of the interesting aspects of the growth of EuO is that at high substrate temperatures atomic Eu has a low sticking coefficient and desorbs from the surface. Thus, at elevated substrate temperatures, typically reported as anywhere above 350-400°C, similar to the Eu source temperature, only oxidised Eu atoms will remain on the substrate. In this adsorption-controlled regime, the deposition

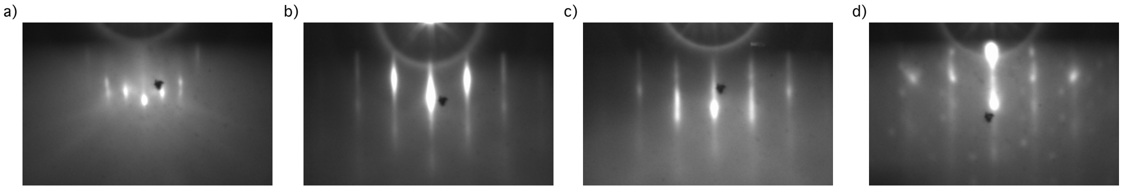

FIGURE 7.6: Effects of O_2 partial pressure on RHEED patterns. a) RHEED pattern of cleaned and annealed (at T=900°C) $YAlO_3$ substrate along the (100) orientation. EuO films measured along the $(1\bar{1}0)$ direction, grown at T=850°C, on top of the $YAlO_3$ substrate with O_2 partial pressures of b) 7, c) 9, and $10\text{x}10^{-9}$mbar with a Eu partial pressure of $1\text{x}10^{-7}$mbar. Extra spots appear in d) between RHEED streaks for over-oxidised europium. Black spot in centre of image is a scratch on the RHEED screen.

rate is entirely regulated by the oxygen partial pressure, whereby stoichiometric EuO is deposited at a greater rate with increased O_2 partial pressure until $P_{O_2} > P_{crit}$ and the surplus flux of O^{2-} ions results in higher oxidation states of Eu atoms. Therefore, by carefully regulating the partial pressure of molecular oxygen, one can balance the Eu^{2+} and O^{2-} fluxes, preventing the formation of higher oxidised states, but also limit oxygen vacancies. Thus, growing EuO in the adsorption-controlled regime becomes a two-dimensional problem with substrate temperature and ratio of Eu and O_2 flux being the variable parameters.

Arguably the most useful tools for analysing the composition and quality of thin films grown by MBE is reflection high-energy electron diffraction (RHEED), as this provides information about the in-plane lattice spacing, film homogeneity and surface roughness in real-time. As demonstrated in Fig. 7.6, as the oxygen partial pressure is increased relative to a fixed Eu flux, the RHEED streaks are largely unchanged, until a critical pressure, P_C, is reached. Above P_C, the appearance of additional spots between the RHEED streaks is observed, indicative of excess oxygen and Eu_2O_3 clusters [128]. With sufficiently high oxygen partial pressure, these additional spots form into complete streaks as the majority of the deposited material is Eu_2O_3. Analysis of the spacing of RHEED streaks for stoichiometric EuO, relative to the streaks for the annealed $YAlO_3$ substrate, reveal a lattice spacing of $a=5.14\pm0.01$ Å, suggesting the films have relaxed to an unstrained in-plane lattice constant, although from the uniformity of the RHEED streaks, this is likely to have occurred at the substrate interface leaving the subsequent layers free of dislocations.

While RHEED can provide rough determination of the oxidation state of films, for fine analysis of the film's composition and thus the boundary between stoichiometric EuO and higher oxidation states, one should analyse the valency of the Eu ions using x-ray photoemission spectroscopy (XPS), Fig. 7.7a. In metallic EuO, the Eu^{2+} $4d$ doublet pair of core levels sit at binding energies of ~129.5 eV and ~134.5 eV, but when over-oxidised into the Eu^{3+} state, these peaks shift to higher energies by approximately 8 eV, as in Fig. 7.7b. One also notes the existence of an additional set of peaks at ~154 eV and ~142.5 eV in stoichiometric EuO which has been attributed to shake-off excitations due to extrinsic plasmon losses [131].

Higher oxidation states can also be seen in XPS by examining the shallow core levels (i.e. binding energies less than 40 eV). In EuO, a large, narrow peak from the Eu^{2+} $4f$ valence band is seen at a binding energy of ~2 eV with a shoulder feature at ~6 eV from the O $2p$ band, as well as the Eu $5p$ and O $2s$ bands at binding energies of ~19 eV and ~23.5 eV, respectively. Upon exposure to an oxygen partial pressure, the strong peak near E_F reduces in intensity and a shift to higher binding energy is seen due to charging effects as the sample becomes more insulating from the formation of Eu_2O_3 and other oxidation states. This reduction in intensity of the Eu^{2+} $4f$ component is concurrent with the appearance of the Eu^{3+} $4f$ peaks in a range of 6 eV to 12 eV. Using a combination of RHEED and XPS measurements, it was established that when grown on clean $YAlO_3$ annealed at 525°C and subsequently cooled to a growth temperature of 425°C, the critical O_2 partial pressure, defining the boundary between growth of EuO and higher oxidation states, is between P_{O_2}=2.4x10^{-8}mbar and 3.5x10^{-8}mbar, as determined from a beam flux monitor, when using an Eu partial pressure of P_{Eu}=2x10^{-7}mbar.

The determination of the critical oxygen pressure for a given Eu flux solves

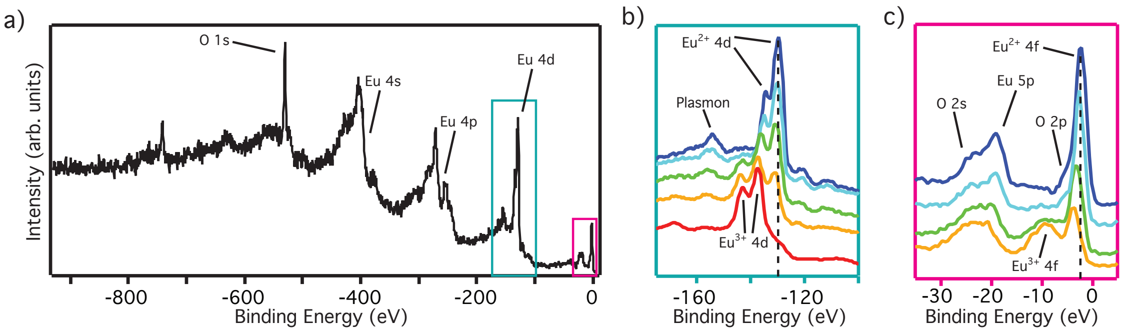

FIGURE 7.7: Effects of O_2 partial pressure on Eu core levels. a) Overview XPS measurement, using Mg Kα ($h\nu = 1153.7$eV), showing the O 1s, Eu 4s, 4p and Eu 4d core levels. b) Expanding the region around the Eu 4d peaks reveals a shift to higher binding energy for higher oxidation states (i.e. $Eu^{2+} \rightarrow Eu^{3+}$) when exposed to increasing O_2 partial pressures, as well as the presence of a plasmon peak at higher binding energies in stoichiometric EuO. c) In the near Fermi level region, the presence of higher oxidation states results in a reduction in the Eu^{2+} $4f$ intensity at 2eV and increase of Eu^{3+} $4f$ intensity between 6eV and 12eV. Charging effects, from the less conductive Eu_2O_3 clusters, results in increased binding energies of the Eu^{2+} $4d$ and Eu^{2+} $4f$ states in b) and c), respectively, as illustrated by the dashed lines.

one of the two parameters needed for growth of stoichiometric EuO in the adsorption controlled regime; however, to ensure the lack of oxygen vacancies, one must also determine the temperature at which Eu atoms will desorb from the sample surface. This temperature constraint is harder to determine using RHEED and XPS as it was demonstrated that for growth on YSZ [128] and $YAlO_3$ substrates, the mobility of oxygen atoms in the substrate allows for the formation of a few layers of EuO, even in the absence of an O_2 partial pressure. Thus one cannot determine the boundaries of the adsorption controlled regime simply by measuring the RHEED pattern or XPS spectra of EuO samples grown at different temperatures as EuO should form at any temperatures, provided that $P_{O_2} < P_{crit}$.

However, an alternative method can be used to determine a suitable growth range by introducing Gd^{3+} dopants. Experiments performed by Mairoser *et al.* [132] on the effects of substrate temperature on the Curie temperature and carrier density of Gd-doped EuO showed that above a threshold temperature, well above the lower-cutoff of the adsorption controlled regime, dopant activation was significantly reduced, leading to little enhancement of the Curie temperature or carrier

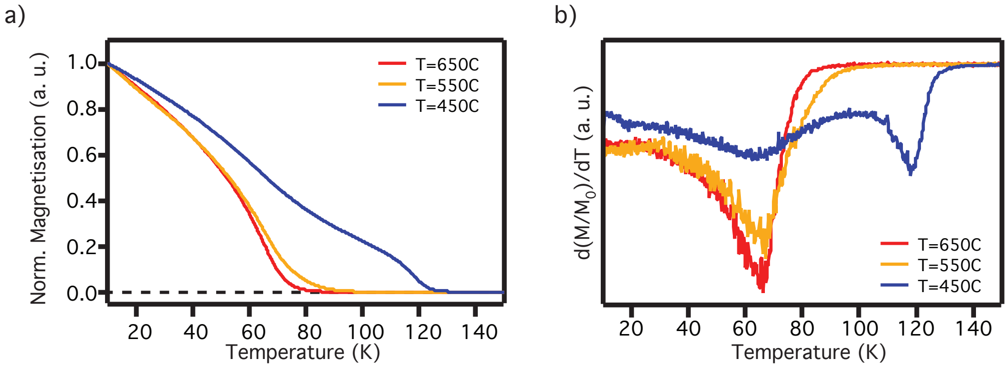

FIGURE 7.8: Effects of substrate temperature on Curie temperature. a) DC SQUID magnetisation vs. temperature (MvT) measurements and b) first-derivative curves (dM/dT), reveal that decreasing the substrate temperature during the growth of Gd-doped EuO results in minor enhancement in T_C for substrate temperatures above 550°C, but a sudden increase in T_C for samples grown at 450°C or below. The inflection point in b) is taken as the sample T_C. Samples were measured with H=200 Oe.

density. By adding a small Gd partial pressure, P_{Gd}=6x10^{-9}mbar, $Eu_{1-x}Gd_xO$ films were grown at various substrate temperatures and capped with a thick layer, ~55nm, of Si to prevent oxidation once removed from vacuum and measured using DC SQUID, displayed in Fig. 7.8. These magnetisation vs. temperature (MvT) curves show qualitative agreement with the trend established by Mairoser *et al.* Thus an upper limit to the growth temperature was established whereby oxygen vacancies are reduced as excess, unoxidised Eu atoms will re-evaporate from the sample surface, but the temperature is low enough for sufficient carrier activation. Due to a small temperature dependence of the critical O_2 pressure, the O_2 partial pressure was chosen to be sufficiently less than the critical value to ensure no higher oxidation states form when varying the substrate temperature. The small addition of Gd, approximately 3% of the Eu partial pressure, should have only minimal effects on the flux ratio of Eu to O_2.

7.2.1.1 Determination of Film Thickness

Having determined an appropriate substrate growth temperature (425°C) and O_2 partial pressure for a given Eu flux (with additional Gd flux for doping purposes), it is also appropriate to estimate the deposition rate of EuO, as well as the subsequent capping layer used to preserve the sample. One could calibrate source fluxes using a quartz crystal microbalance (QCM), which provides element specific deposition rates. However, a beam flux monitor (BFM), was utilised to accurately monitor the O_2 partial pressure incident on the sample surface, which would not have been possible using the QCM. Thus, to determine the deposition rate of Si for the capping layer using a BFM, a $YAlO_3$ substrate was partially covered with Teflon tape and subsequently exposed to a Si partial pressure of $2.5\text{x}10^{-8}$mbar for 30 minutes at room temperature. Removal of the Teflon tape produces a step edge, Fig. 7.9, which when measured using atomic force microscopy (AFM), reveals a deposition rate of ~1.8nm/min. Unfortunately, the discrepancies between atomic Eu and EuO's deposition rate at room temperature and growth temperature do not allow for such masked substrate and AFM tests to be performed for EuO itself, as the heating of Teflon tape is not suitable for

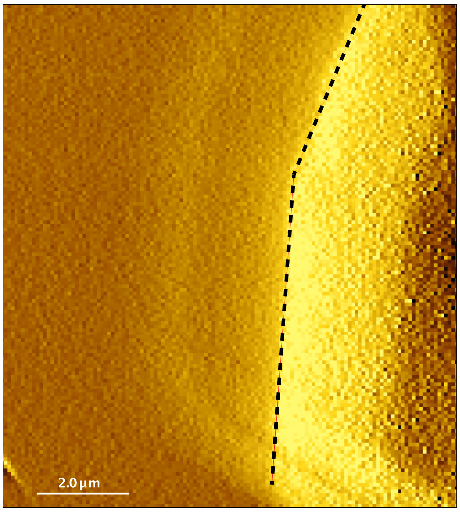

FIGURE 7.9: Masking a portion of a $YAlO_3$ substrate with Teflon tape results in step-edge formation (dashed line) when coated with Si and the mask is removed. Such a step-edge allows for the deposition rate of the capping layer to be determined for a given flux and deposition time.

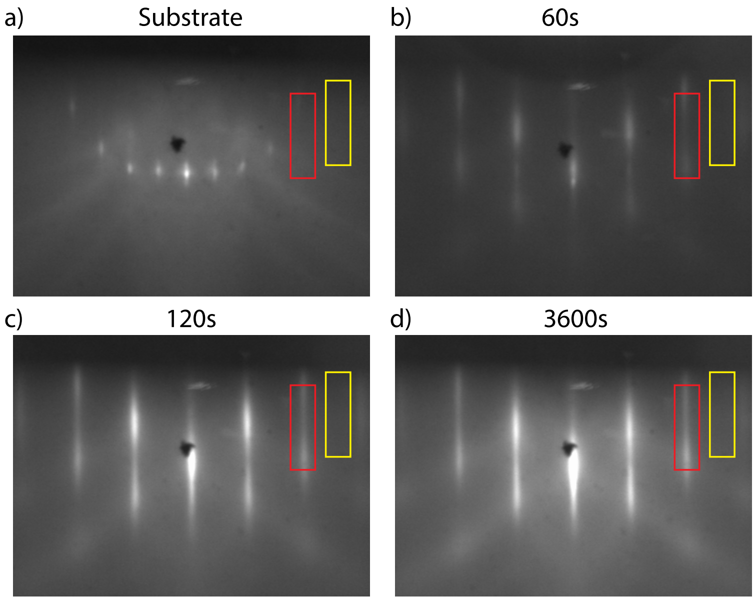

FIGURE 7.10: RHEED pattern for EuO on $YAlO_3$ in initial stages of growth. a) RHEED pattern for substrate annealed at T=525°C and cooled to 425°C. b) Exposure to Eu and O_2 fluxes for 60s reveals a drastic change of the RHEED pattern, consistent with growth of EuO. c) Integrated intensity of the RHEED streak (red region) compared to background intensity (yellow region) peaks at 120s with d) only minor changes in intensity after a full growth cycle (3600s).

UHV purposes. Additionally, exposure to atmosphere would result in alteration of the chemical composition of the deposited film, altering it's thickness and density.

Therefore to determine the deposition rate of EuO, alternative methods were implemented utilising RHEED and XPS. As mentioned in Ch. III, in the initial stages of MBE growth, the pattern of diffraction streaks as measured by RHEED will smoothly change from the underlying substrate pattern to that of the material being grown. With epitaxial growth, the intensity of these streaks will oscillate between peaks and troughs as subsequent full and half layers, respectively, are deposited. Although such RHEED oscillations are not observed here, upon exposure to Eu and O_2 fluxes, a drastic change to the RHEED pattern is observed, Fig. 7.10b, consistent with single-domain EuO and an increase in the RHEED streak integrated intensity is seen to reach a maximum after ~120s of EuO deposition, indicating the growth of a single monolayer (a=5.14Å). Additionally, XPS

Annealing Stage			
Material	Partial Pressure (mbar)	Temp. (°C)	Dep. Time (s)
Substrate ($YAlO_3$)		525	
O_2	$2\text{x}10^{-8}$		1800

Deposition Stage			
Material	Partial Pressure (mbar)	Temp. (°C)	Dep. Time (s)
Substrate ($YAlO_3$)		425	
Eu	$2\text{x}10^{-7}$	530	3600
Gd	$6\text{x}10^{-9}$	1250	Vary for Doping
O_2	$2\text{x}10^{-8}$		3600

Capping Stage			
Material	Partial Pressure (mbar)	Temp. (°C)	Dep. Time (s)
Substrate ($YAlO_3$)		<50	
Si	$2.2\text{x}10^{-8}$	1150	Vary for thickness

TABLE 7.1: Parameters for growth of EuO and $Eu_{1-x}Gd_xO$ thin films, using molecular O_2 source and Si capping.

measurement of ultra-thin (single to few layer) films reveal the disappearance of substrate core level peaks with increased time exposed to such Eu and O_2 partial pressures, consistent with the estimation of a deposition rate of $\sim$2.56Å/min using an escape depth model of 12Å, corresponding to illumination using an Mg Kα x-ray source. For the remainder of this section and the next two chapters, the growth recipe developed for the production of EuO and $Eu_{1-x}Gd_xO$ films, with approximate thickness of 30 to 40 monolayers, is presented in Table 7.1, including the 10nm to 20nm thick Si capping layer used for ex-situ measurement of bulk properties.

7.2.1.2 Field Strength Dependence on Magnetic Properties

The magnetic properties of EuO are best observed through measurement of the temperature dependent magnetisation (MvT) using DC SQUID, as illustrated in Fig. 7.8. Past studies of EuO have reported these measurements depend sensitively on the applied magnetic field. Kimura *et al.* [112] investigated the homogeneity of magnetic domains in undoped EuO under applied field, observing

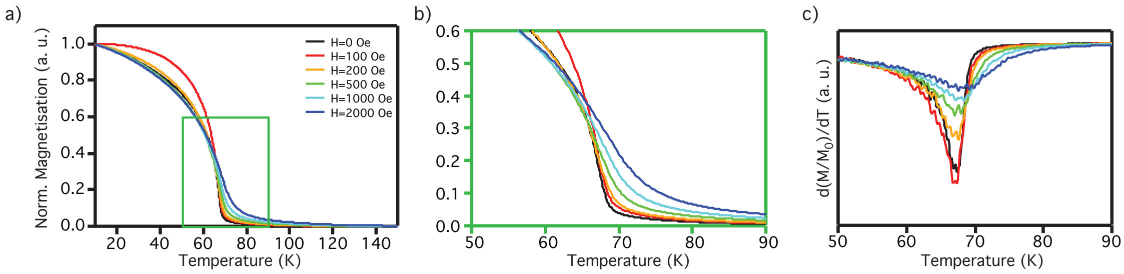

FIGURE 7.11: Effects of external magnetic fields on Curie temperature in undoped EuO. a) MvT curves with increasing strength of applied magnetic field, reveal ferromagnetism that closely follows a Brillouin zone function with H=100 Oe, but is slightly suppressed with larger fields. b) Expansion of the near-T_C temperature range illustrates the elongation of tails above T_C, attributed to the magnetisation of small domains. c) The first-derivative curve shows the broadening of peaks centred at T_C, which shift to higher temperature with increased field strength.

that under an external field of 5T field, the majority of thin film samples could be made ferromagnetic at T=80K, well above the normal Curie temperature, with mixing of paramagnetic and ferromagnetic domains at lower fields.

Thus, in order to accurately determine the onset temperature of the dual ferromagnetic, metal-insulator transition, one should perform MvT SQUID measurements under different applied field strengths. From Fig. 7.11a, one observes that a Brillouin zone function is found for a relatively small field, while larger fields reduce the normalised magnetisation at lower temperatures. The suppression at H=0 Oe is attributed to the remnant field of the magnet, which is in the opposite direction from the applied fields, such that H=100 Oe is closer to a zero applied field. The increase of applied field also has the effect of producing larger tails, likely due to small domains becoming ferromagnetic before the true T_C, Fig. 7.11b, as suggested by Kimura *et al.* [112]. These long tails diminish the sharp peaks in the first derivative (dM/dT) curves, which broaden and shift to higher temperatures with increased applied field, Fig. 7.11c. For the remainder of DC SQUID measurements, an applied field of H=200 Oe is used, unless stated, so as to ensure sufficient field is applied to overcome the remnant field without forcing a significant number of domains to align before the bulk T_C.

7.2.1.3 Effects of Doping on Film Properties

As shown by the MvT measurements on Gd-doped EuO films grown in Fig. 7.12a, controllably increasing the carrier density by electron doping the system allows for ferromagnetic transition temperature to be tuned. These films were grown under similar growth conditions and source partial pressures, except that to regulate the amount of doping, the Gd shutter was closed for a fixed amount of time during 30 second intervals to produce different time-averaged dopant fluxes. Thus if the shutter was open for the full 30s period, a high Gd concentration was achieved, but, by closing the shutter for a fraction of this period, an amount of Gd was deposited proportional to the relative exposure time. This

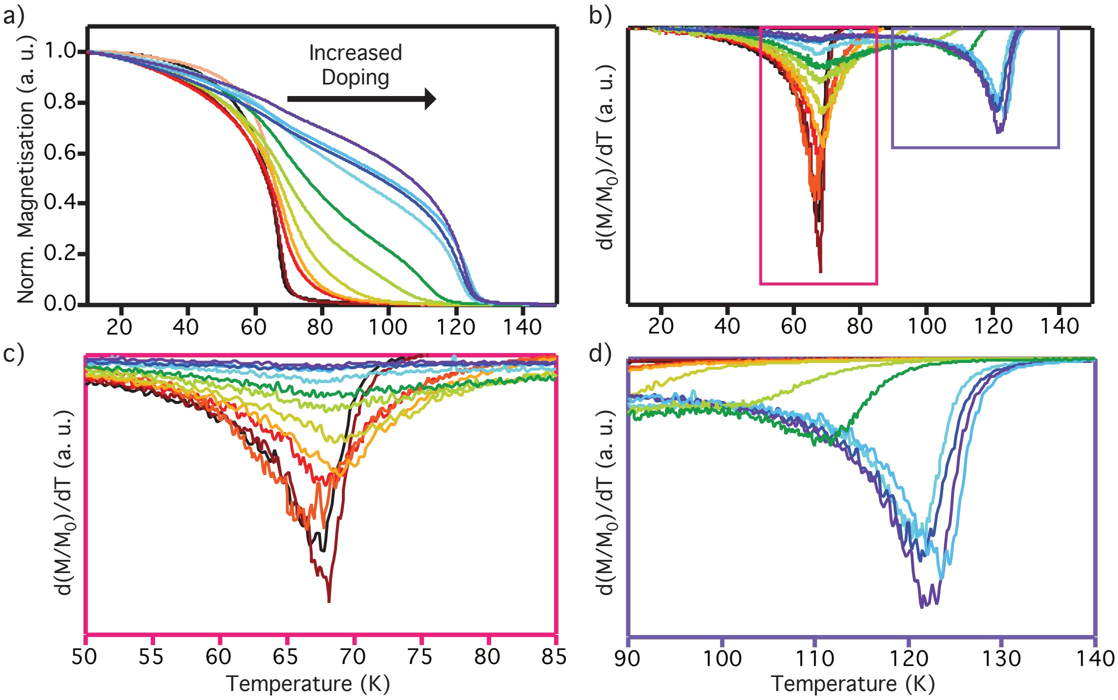

FIGURE 7.12: Effects of Gd concentration on Curie temperature. a) MvT measurements (H=200 Oe) show the enhancement of T_C with increasing doping. b) dM/dT curves reveal inflexion points corresponding to the Curie temperature of the films. c) An expansion around the undoped EuO temperature range depicts the broadening of the low temperature peak and shift to higher temperature with increased Gd concentration. The reduction and shift of this peak is concomitant with d) the increase in height of a shoulder feature at higher temperatures which evolves into a well-resolved peak for higher Gd concentrations. As the T_C saturates, the low temperature peak nearly disappears, consistent with theoretical models.

"doping-by-shuttering" method was suitable for bulk doping of these films because the deposition rate of a single monolayer of EuO under these conditions was determined to be approximately 120s and thus four shuttering cycles are completed within every monolayer. XPS and XAS measurements show no signatures of Gd_2O_3 clusters, implying the Gd atoms indeed act as substitutional dopants without the formation of interstitial phases.

To determine the Gd concentration, one can analyse the relative intensities of the Eu and Gd $M_{5,4}$ absorption edges, corresponding to the $3d \rightarrow 4f$ transition, as measured by x-ray absorption spectroscopy, Fig. 7.13a. With increased Gd concentration, the intensity of the Gd $M_{5,4}$ peaks grow relative to the Eu peaks which are largely unchanged. Not only do the XAS measurements reveal a clear relationship between the length of the Gd shutter opening, but comparison of the Gd concentration and the Curie temperature reveals a clear monotonic relationship between the two, Fig. 7.13b. However, above ~6% Gd concentration an apparent saturation of the Curie temperature occurs, consistent with the determination of reduced dopant activation described by Mairoser *et al.* [113], depicted in Fig. 7.3d.

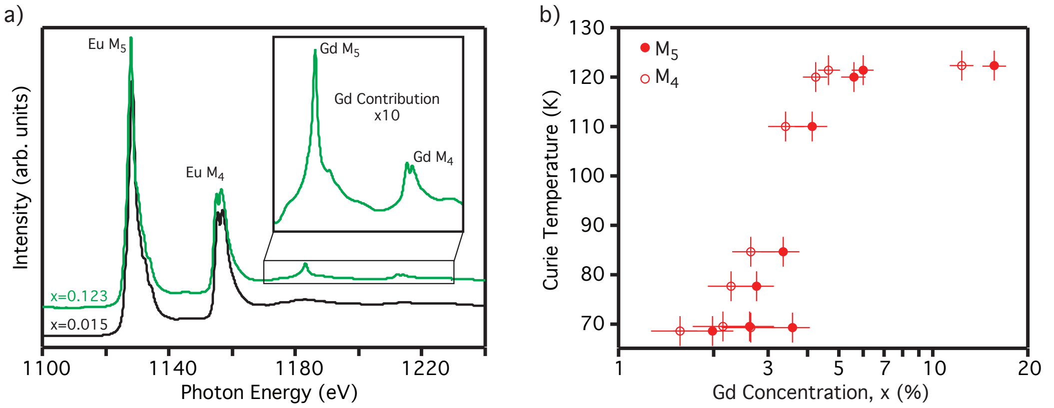

FIGURE 7.13: Determination of Gd concentration using XAS. a) XAS spectrum of lightly doped (x=0.015, black line) and heavily doped (x=0.123, green curve) EuO in the ferromagnetic phase. Comparing the relative intensity of the Eu and Gd $M_{5,4}$ absorption edges, corresponding to the $3d \rightarrow 4f$ transition, allows for the estimation of Gd concentration. b) The increase in Gd concentration, as measured by the M_5 (solid circles) and M_4 (open circles) absorption edges are well correlated to an increase in the Curie temperature, as measured by SQUID.

Nonetheless, it is necessary to question the homogeneity of Gd distribution within the crystal lattice and it's effects on the film's properties. One method to determine the homogeneity of the dopant distribution is through the effects of it's bulk magnetic properties, as depicted by the MvT curves which indicate the onset of magnetism by a peak in the first derivative curves. Miyazaki *et al.* [116] suggested that the appearance of a second peak in the first derivative of the MvT curves was indicative of regions of undoped and La-doped EuO, with a reduction of the lattice constant for the latter regions. However, the presence of two peaks in the dM/dT curves has been seen in several additional studies on samples with substitutional doping and oxygen vacancies [113, 133]. Thus the double peak shape of the dM/dT curves is likely to be endemic to the doping of EuO. Indeed, theoretical models have been developed which predict the presence of a "double-domed" MvT curve for electron-doped EuO [134, 135] in which the low temperature peak is the result of ferromagnetic ordering of the Eu $4f$ moments, while the higher temperature peak has been attributed to either the ordering of the conduction electrons or the enhancement of the $4f$ local moments via the $5d$ conduction electrons due to the $4f$-$5d$ exchange interaction. Alternatively, the enhancement of T_C and additional bump at high temperature has been attributed to the presence of bound magnetic polarons which may provide a route to magnetisation through hybridisation of the conduction band with impurity states [136, 137].

Here, it is seen that without the addition of Gd dopants, the first derivative of the MvT curve reveals a sharp peak at T_C=69K. This is indicative of bulk stoichiometric EuO as below 20 monolayers one would expect a reduced Curie temperature. Addition of a small number of Gd atoms causes the peak near T=69K in the dM/dT curves to become broader and less intense, while also shifting to slightly higher temperatures, indicative of a small enhancement of the Curie temperature, Fig. 7.12b,c. As the Gd concentration increases further, the elongated tail of the dM/dT curve evolves into a second peak at much higher temperatures (>90K),

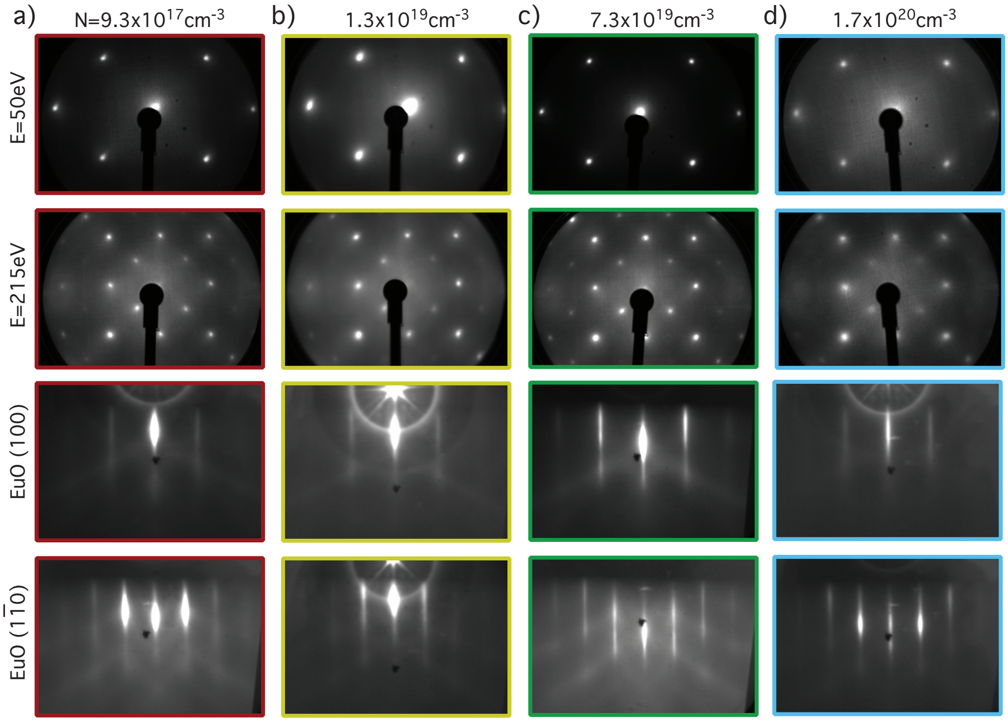

FIGURE 7.14: Effects of Gd concentration on film quality. a) LEED pattern for EuO film with lowest Gd concentration at E=50eV (top panel) and E=215eV (second panel) revealing cubic structure with sharp diffraction spots, indicating high quality growth. Corresponding RHEED images along the (100) (third panel) and (1$\bar{1}$0) (bottom panel), displaying Kikuchi lines, suggestive of pristine surface layers. b-d) Same as in a) except with increasing Gd concentration as indicated by carrier densities. Film quality is largely unchanged with increased doping, over almost 3 decades of carrier concentration, the determination of which is discussed later. Colour borders correspond to magnetisation vs. temperature curves in Fig. 7.12.

while the low temperature peak reduces in intensity, as shown by Fig. 7.12d. Further increases to the Gd concentration results in the almost complete disappearance of the inflexion point at T=69K, while the peak at ∼120K becomes narrower and more intense, eventually saturating at T_C=124K. The appearance of the second peak and subsequent shift to higher temperatures concomitant with the reduction of the low temperature peak is qualitatively matched by the theoretical calculations of Takahashi [135], which predicts the appearance of the "double-domed" magnetisation curve. Therefore, sufficient evidence has been provided that the bulk magnetic properties of these films are representative of thick (>20 monolayers) $Eu_{1-x}Gd_xO$, free of significant Eu^{3+} impurities.

Techniques such as LEED and RHEED can also be used to determine the effects of doping on the film quality by analysing the structural homogeneity, as the inclusion of dopants can introduce impurity sites which increase inelastic scattering and reduce the crystallinity of the film, broadening the features of the diffraction patterns. As seen in Fig. 7.14a, for films with very low doping, the LEED patterns at both low and high energy have sharp diffraction spots in the expected cubic structure. One notes that the inclusion of light doping is necessary to make the samples sufficiently conductive at room temperature to prevent charging effects similar to those in ARPES. Increasing the doping concentration has little effect on the sharpness of LEED spots, Fig. 7.14b-c, except at extremely high concentrations, Fig. 7.14d, which is likely the result of over-doping that leads to small amounts of impurity scattering. The size of the LEED spot is several times larger than that of synchrotron beam spot and therefore the observation of single domain EuO in LEED implies the films are suitable for ARPES. Further evidence for the homogeneity of the doping and general high quality of the films is observed in the RHEED pattern along the (100) and $(1\bar{1}0)$ directions. Across the whole range of doping concentrations, sharp streaks are observed with the addition of Kikuchi lines from extra surface diffraction. Only slight broadening of the line widths is observed for the highest doped films. Thus, through a combination of RHEED, LEED, XPS, XAS and SQUID, it has been demonstrated that the mu-MBE system on the I05-endstation is capable of growing high quality, bulk $Eu_{1-x}Gd_xO$ thin films, opening the prospect to study their electronic structure as presented in the next two chapters.

Chapter 8

ARPES of Bulk Doped EuO using Synchrotron Radiation

Along with the in-situ characterisation of Gd-doped EuO thin films using the techniques just discussed, the unique setup at Diamond's I05-beamline allows for the investigation of the material's electronic structure using high-resolution ARPES. Previous experiments that combine MBE and ARPES to study EuO have utilised synchrotron radiation to investigate the dispersion of the valence bands in undoped films [107, 138] and a He-lamp source to examine the behaviour of the conduction band in lightly doped films in the ferro- and paramagnetic phases [139, 140]. The former of these revealed small in-plane and out-of-plane dispersion of the Eu $4f$ valence bands, previously thought to be completely localised as in a Heisenberg ferromagnet. It was also seen that the increase in temperature resulted in significant shifting of the Eu $4f$ and O $2p$ bands, which was attributed to the hybridisation between Eu $4f$ and O $2p$ majority-spin bands in the ferromagnetic phase. The He-lamp based experiment supported the temperature dependent shifts of the valence bands in Gd-doped EuO, in addition to measuring the Fermi surface in both phases. Due to the limitations of a He-lamp, only a single plane in the k_z direction can be measured, leaving questions about the evolution of the 3D electronic structure across this transition. Here, ARPES measurements of the full electronic structure of Gd-doped EuO are presented, including the orbital texture and temperature dependence of the Fermi surface.

8.1 3D Electronic Structure in the Ferromagnetic Phase

The advantage of using synchrotron radiation for investigating the electronic structure of materials is the ability to alter the region in k-space that one is probing by changing the photon energy, which changes k_z, and sample orientation, altering $k_\parallel$. An additional advantage of the I05-beamline is the ability to also change the polarisation of the probing light, allowing one to disentangle the orbital origins of the electronic states through photoemission selection rules.

8.1.1 Photon energy dependence

Unlike the transition metal dichalcogenides seen earlier, which are formed by sheets loosely bound together by van der Waals forces and host 2D states localised to individual layers, the crystal lattice of EuO is formed by strong ionic bonds into the cubic rocksalt structure and thus one naively expects it to exhibit significant in-plane and out-of-plane dispersion due to the 3D nature of the crystal structure. Indeed, previous ARPES measurements have revealed considerable

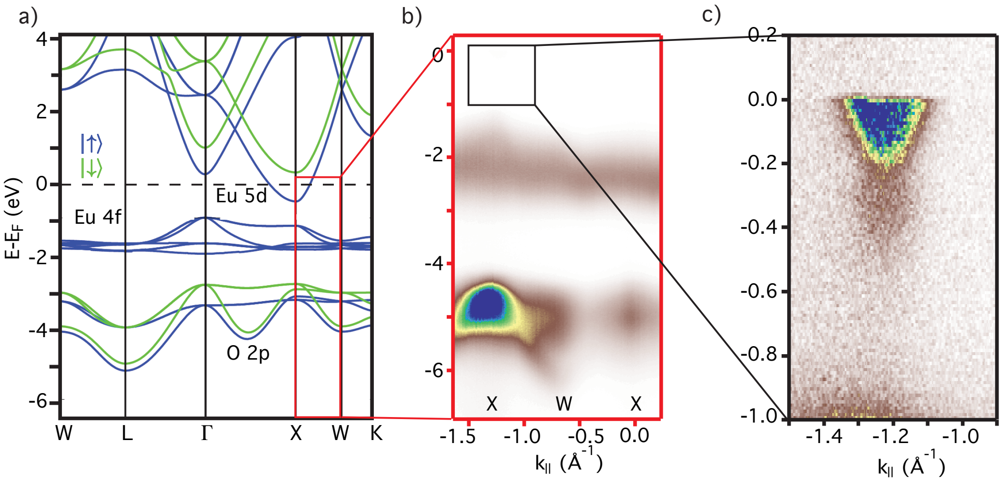

FIGURE 8.1: Electronic structure of Gd-doped EuO. a) DFT calculations of band structure of $Eu_{1-x}Gd_xO$, predicting spin-polarised elliptical electron pockets at X-points. b) ARPES measurement ($h\nu$=48eV) directed along the X-W-X line shows good agreement with DFT, revealing dispersive O $2p$ bands with a minimum at W and maxima at X, as well as the relatively dispersion-less Eu $4f$ band. c) Enlargement and increased contrast of the near Fermi level region around the neighbouring zone X-point confirms the presence of an electron pocket.

dispersion of the O $2p$ bands [138]. However, the Eu $4f$ bands are almost completely localised to the Eu^{2+} lattice sites, with relatively small overlap between neighbouring sites, leading to reduced dimensionality and only minor 3D dispersion is observable, relative to the O $2p$ states, as drawn schematically in Fig. 7.1b. On the other hand, as with the O $2p$ bands, the Eu $5d$ bands are expected to have significant in-plane and out-of-plane dispersion as predicted by DFT calculations shown in Fig. 8.1a. Apart from an underestimation of the binding energies, these calculations qualitatively reproduce the band dispersion of the O $2p$ bands in the observed ARPES measurements where band maxima are seen at X and a minima is seen at W. One also observes in Fig. 8.1b the relatively dispersion-less Eu $4f$ band at a binding energy of approximately -2.25eV, although some dispersion is observed around X as expected by DFT calculations.

As indicated in Fig. 8.1a, upon electron doping of the system the Fermi level is rigidly shifted upwards such that the exchange-split spin-majority band crosses the Fermi level. This presents a range of doping concentrations in which the electron pocket should be completely spin polarised, i.e. Fermi level below the spin-minority conduction band minimum, making the material a ferromagnetic half-metal in the low temperature phase. Expansion of the near Fermi level region around the X-point of the neighbouring zone reveals the presence of an electron pocket, Fig. 8.1c. Previous studies of the Eu $5d$ bands have estimated the exchange splitting to be $\Delta \mathrm{E}_{exc}$=600 meV and therefore one concludes that, here, the doping is sufficiently low to achieve half-metal character as the conduction band minimum sits at a binding energy of $\sim$200 meV. As indicated by the DFT calculations, the conduction band should form an elliptical electron pocket centred at the X point, with its short axis, k_F^s, along the X-W line and the long axis, k_F^l, directed towards the zone centre, Γ. One of these elliptical electron pockets should form on each of the square faces of the Brillouin zone, as illustrated in Fig. 8.2b.

This configuration presents two high symmetry planes of interest: 1) the k_z=0

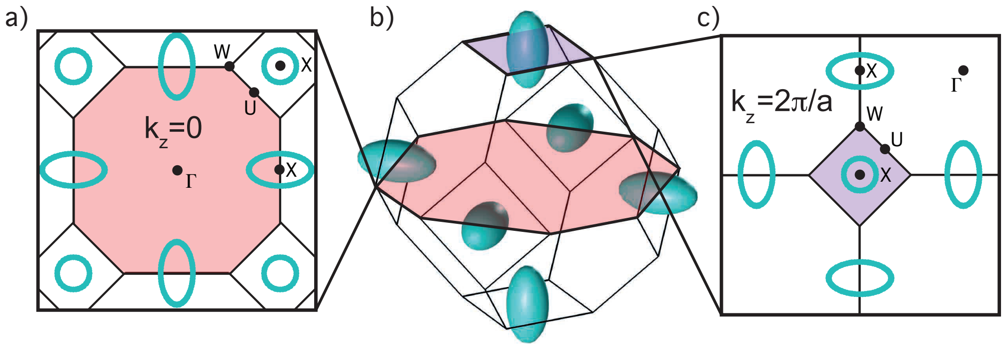

FIGURE 8.2: Calculated Fermi surface of Gd-doped EuO. The DFT calculated Fermi surface of $\mathrm{Eu}_{1-x}\mathrm{Gd}_x\mathrm{O}$, produced by Dr. Matthew Watson, b) consists of 6 elliptical electron pockets, each centred on the X-points, with their short axes, k_F^s, residing in the square face of the Brillouin zone and the long axis, k_F^l, aligned along Γ-X. Isoenergy contours at a) k_z=0 (Γ-plane) reveal the long axis of the elliptical pockets aligned along k_x=0 and k_y=0, while at c) $k_z = \pm 2\pi/a$ (X-plane) the pockets rotate such that the long axes are directed towards the neighbouring zone centres. The appearance of a circular pocket around $k_\parallel$=0 is also observed in the X-plane, but not the Γ-plane, where circular pockets are observed at (k_x,k_y)=($\pm 2\pi/a$,$\pm 2\pi/a$).

plane which cuts through the centre of the first Brillouin zone, which will be referred to as the Γ-plane, as illustrated by the distorted octagon in Fig. 8.2a and 2) the k_z=$2\pi/a$ plane, which will be referred to as the X-planes as $k_\parallel$=0 is an X-point, Fig. 8.2c. Because each adjacent Brillouin zone is shifted by (Δk_x,Δk_y,Δk_z)= ($2\pi/a$,$2\pi/a$,$2\pi/a$), a horizontal cut centred on the Γ-plane of the first Brillouin zone will include the X-planes of the adjacent zones and, conversely, an equivalent slice centred on the X-plane will contain the Γ-planes of the adjacent zones. Thus by measuring these two high-symmetry planes, one should observe a 90° rotation of the elliptical contours at $(\pm 2\pi/a, 0) = (k_x, k_y) = (0, \pm 2\pi/a)$, while at the zone centre a circular contour should only be observed in the X-plane. Additionally, measurement of the electronic structure along the k_x=0 or k_y=0 and k_x=k_y directions at varying k_z should reveal the evolution of the out-of-plane dispersion around the Γ- and X-points of the first and neighbouring Brillouin zones, confirming the full 3D Fermi surface.

Indeed, by changing the photon energy of the probing light source, the out-of-plane dispersion along these two orientations is measured, as shown in Fig. 8.3, where the free electron final state model was used to convert between $h\nu$ and

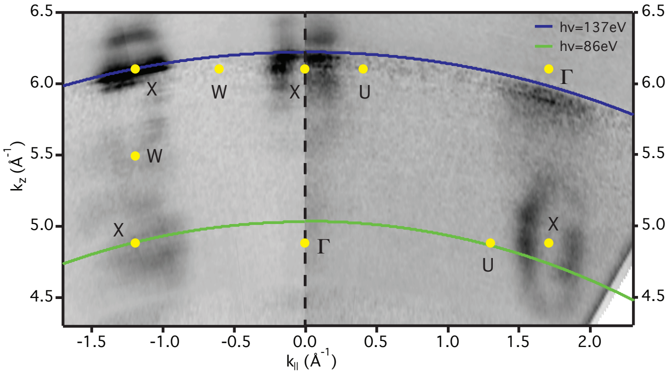

FIGURE 8.3: Photon energy dependent measurements along the k_y=0 (left) and k_x=k_y (right) orientations. Overlaid are the high-symmetry points (yellow dots) along these directions and the constant photon energy slices traced at $h\nu = 86eV$ (green) and $h\nu = 137eV$ (blue).

k_z, with an inner potential, V$_0$=15.0 eV, consistent with Ref. [138]. The appearance and disappearance of electronic states at the zone centre and $k_{\|}$=1.75Å^{-1}, along the Γ-U-X direction, i.e. $k_x = k_y$, indicates the switch between an X-plane (k_z=6.2Å^{-1}) and a Γ-plane (k_z=4.9Å^{-1}). One also notes the increase in k_F of the state at $k_{\|} = 2\pi/a$ at low k_z along the $k_y = 0$ direction, consistent with the rotation of the elliptical pocket between X- and Γ-planes. The appearance of spectral weight at intermediate values of k_z is attributed to finite resolution in k_z, resulting in additional broadening of electronic features in the out-of-plane direction. Although confinement effects from the limited thickness of samples, which are expected to produce a 2DEG in ultra thin films similar to those seen in WSe$_2$, cannot be completely discounted, these effects are expected to be negligible given the evolution of the in-plane dispersion, to be discussed next, which shows no signatures of quantum size effects and the bulk-like magnetic properties of these films. Additionally, a surface state that crosses the Fermi level has been suggested which could explain the intensity where no electron pockets are expected [114, 127].

From the k_z maps, the relevant photon energies to probe the in-plane dispersion of the conduction band states in the two high symmetry planes can be determined. However, due to conservation of momentum, increasing the in-plane momentum results in a compensating reduction in the out-of-plane momentum, for fixed photon energies. Thus constant energy contours measured at a fixed photon energy result in a "warping" in k_z, as shown by the coloured curves in Fig. 8.3 such that probing a high-symmetry point at large $k_{\|}$ results in measuring slightly off the high-symmetry point at the zone centre or at even higher $k_{\|}$.

The photon energies used to measure the in-plane dispersion of the Fermi surface were chosen to probe the X-points at $k_{\|} = 2\pi/a$, displayed in Fig. 8.4a,c. As expected, when using $h\nu$=86 eV, corresponding to a Γ-plane, one observes elliptical pockets at (k_x,k_y)=(0,±1.226 Å^{-1})=(±1.226 Å^{-1},0) with the k_F^l pointed towards the zone centre. Additionally, due to integration over a finite range of k_z, inherent to ARPES, circular pockets centred at the X-points of the neighbouring zones (square faces) are seen with a k_F comparable to the short axis of the pockets in the first zone. One also notes the lack of features at the zone centre, as predicted by DFT. The Fermi surface centred on a Γ-point differs drastically from one centred on an X-plane ($h\nu$=137eV), as suggested by Fig. 8.2c. The rotation of the elliptical pockets is clearly observed due to the half unit-cell displacement of the

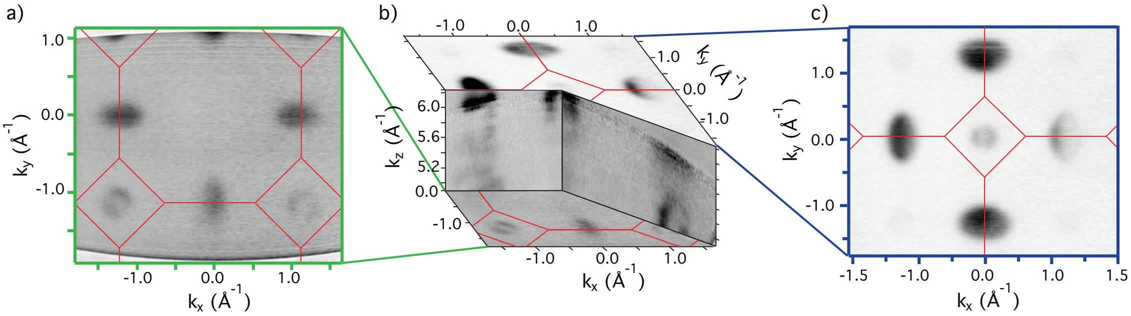

FIGURE 8.4: ARPES measurements of the 3D Fermi surface of Eu$_{1-x}$Gd$_x$O. a) Fermi surface of the Γ-plane ($h\nu$=86eV) shows both the electron pockets at the edges of the first Brillouin zone and those of the neighbouring zones. The former of these pockets rotate 90° in c) the X-plane ($h\nu$=137eV), while the latter shifts to the zone centre. In addition to Fermi surface maps of the two high symmetry planes, b) photon energy dependent measurements along the $k_y = 0$ and $k_x = k_y$ directions reveal the k$_z$ dispersion of the Fermi surface. Along the $k_x = k_y$ direction, the electron pocket at the $k_{\|}$=0 and high k_z disappears with decreasing k_z, while a similar pocket appears at high in-plane momentum. Spectral weight is seen at the zone edge along the $k_y = 0$ direction, with a larger k_F at lower k_z, indicative of a Γ-plane. Measurements are the summed spectral intensity using s- and p-polarised light.

neighbouring Brillouin zones, as well as the appearance of a circular pocket at the centre of the X-plane. The carrier density, N=5.2±0.4 x10^{20}cm^{-3}, of the film can be extracted from the in-plane iso-energy contours by comparison with simulations of the spectral intensity accounting for k_z broadening, which will be described in the next chapter where a detailed study of the carrier density dependent evolution of the band structure is presented. Combining the k_z maps and the iso-energy contours allows for the full 3D Fermi surface of Gd-doped EuO to be constructed for the first time, as shown in Fig. 8.4b, confirming the bulk nature of these films.

8.1.2 Orbital Determination of Conduction Band States

Not only can one measure the full 3D Fermi surface, but by probing the films using light with the electric field component parallel (perpendicular) to the scattering plane, corresponding to linearly p-polarised (s-polarised) light, as illustrated in Fig. 8.5a, one can disentangle the orbital origins of the electronic structure. The single-electron photoemission matrix element, $\left|M_{f,i}^{\mathbf{k}}\right|^2 \propto |\langle\phi_f^{\mathbf{k}}|\mathbf{A}\cdot\mathbf{p}|\phi_i^{\mathbf{k}}\rangle|^2$, from Eq. 3.3, suggests that spectral intensity should only be measured when the probing light interacts with the atomic orbitals such that the photoemission matrix element is non-zero, i.e. integrand of the overlap integral must be even.

For the idealised case, the incoming light source and the detector lie within the scattering plane. Because odd-parity final states would be zero on the scattering plane, and therefore on the detector, the final states must have even parity. Once photoemited into the vacuum, the electronic wavefunction is assumed to be a free electron described by $e^{i\mathbf{kr}}$ with momentum in the scattering plane and even-symmetry across the scattering plane [141]. Thus for the photoemission matrix element to be non-zero, the product $\mathbf{A}\cdot\mathbf{p}|\phi_i^{\mathbf{k}}\rangle$ must be even and therefore one can use light with even symmetry (i.e. p-polarised) to probe orbitals with even-parity across the scattering plane, while photoemission processes using s-polarised light should only be allowed for orbitals with odd-parity. The conduction bands of EuO are predominantly derived from the Eu $5d$ orbitals, which are believed to

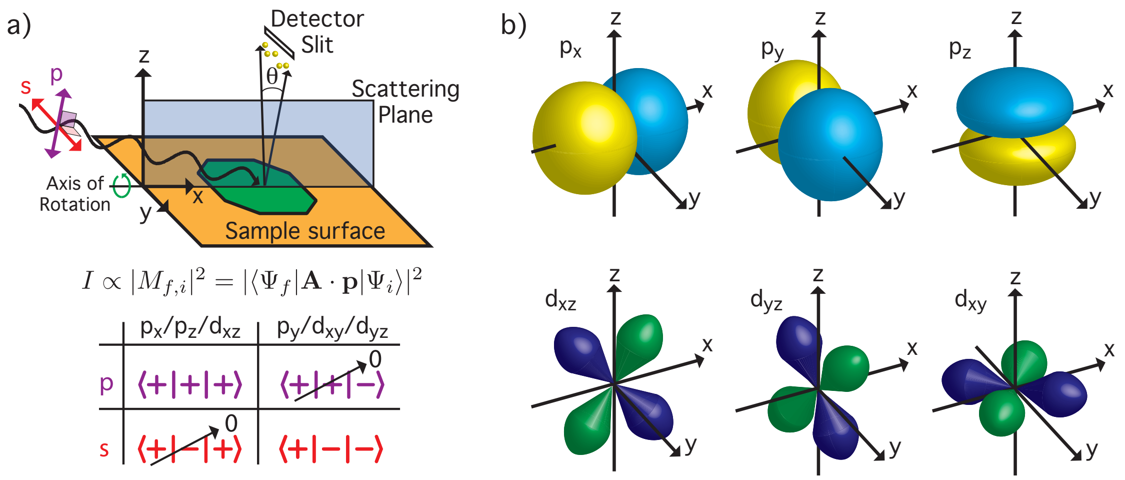

FIGURE 8.5: Forbidden photoemission processes under linearly polarised light. a) Only photoemission processes with a non-zero matrix element from the spectral function are allowed. Light incident on the sample surface photoemits electrons into a vacuum as a free electron with an symmetric final state wave. By using p-polarised (s-polarised) light, which is symmetric (anti-symmetric) with respect to the scattering plane, the orbital origin of the Fermi surface, which is of b) predominantly Eu $5d$ origin with small O $2p$ orbital contribution, can be disentangled, as the allowed/forbidden processes are determined by the symmetry of the initial state wavefunction. A summary of the allowed processes under (s-) p-polarised light is provided in a).

hybridise with the O $2p$ orbitals. From Fig. 8.5b, one can see that the wavefunctions of initial states originating from O p_x/p_z and Eu d_{xz} orbitals are symmetric about the scattering plane, whereas initial states with O p_y and Eu d_{yz}/d_{xy} character have odd symmetry. A summary of the allowed processes, along with the symmetry arguments, is depicted in Fig. 8.5a.

Unfortunately, the true experimental geometry deviates from the ideal case. In order to measure the in-plane Fermi surface, as in Fig. 8.4a,c, the sample must be rotated such that the light source and detector are no longer within the scattering plane, which causes a deviation from the symmetry arguments that forbid certain photoemission processes. Nonetheless, these selection rules can be used as a rough approximation for the determination of the orbital character of the Fermi surface. Indeed, illumination under s-polarised light, Fig. 8.6a, reveals suppressed spectral intensity for the elliptical pockets with their long-axis directed parallel to the k_y-axis in both the Γ- and X-plane Fermi surfaces, while

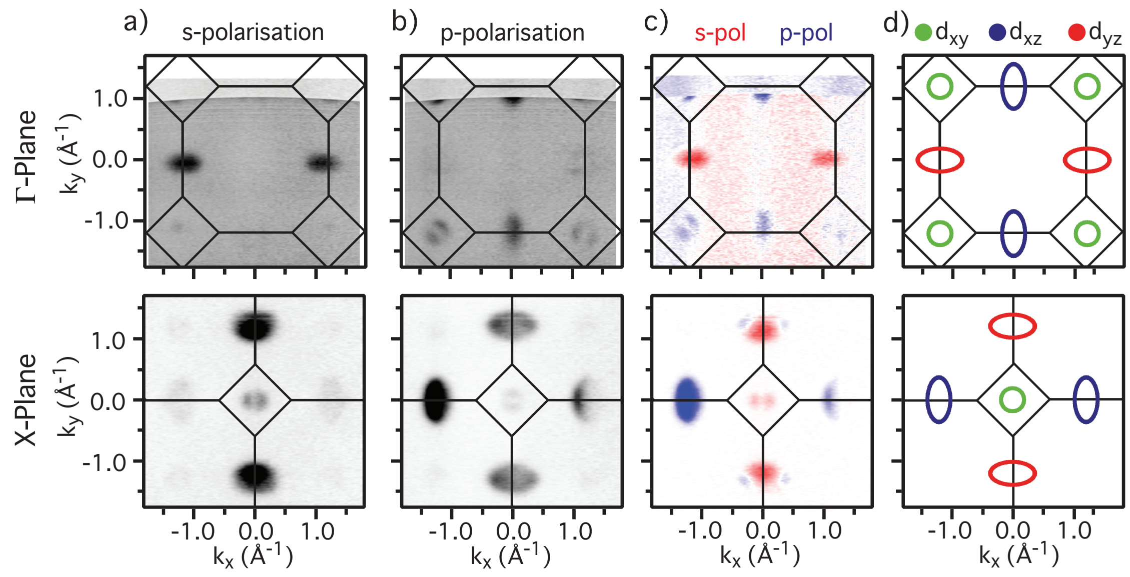

FIGURE 8.6: Linear dichroism of the Femi surface of $Eu_{1-x}Gd_xO$. Orbital texture of isoenergy contours at the Γ-plane (top panel) and X-plane (bottom plane) under a) s- and b) p-polarised light. c) The corresponding linear dichroism (I_p-I_s) reveals strong polarisation dependence of the conduction band states which qualitatively match the selection rules as demonstrated by d) DFT calculations projected onto the Eu d-derived states.

p-polarised light, Fig. 8.6b, reveals those pockets whose long-axis are rotated 90° degress. The degree of suppression of spectral intensity is highlighted by linear dichorism plots, Fig. 8.6c, where one can clearly see the switch in intensity of the iso-energy contours when illuminated by s- and p-polarised light.

Consistent with expectations from a tight-binding picture, orbitally-projected DFT calculations, shown in Fig. 8.6d, predict that, in the Γ-plane the electron pockets along the k_y-axis are of d_{xz} origin, while those along the k_y=0 line are of d_{yz} character. These calculations also reveal that, along with a rotation of the elliptical pockets, the orbital nature of these pockets switch when compared to the X-plane Fermi surface. In addition to the out-of-plane Eu-derived 5d orbitals, evidence for the in-plane Eu 5d_{xy} orbitals that contribute to the circular pockets (i.e. long axis aligned along k_z) is seen near the zone centre in the X-plane under s-polarisation. This qualitatively matches the experimental polarisation dependent measurements very well, as does the switch in intensity at the zone edges between the two planes.

One notes that there are additional signs of the circular pockets in the neighbouring zones of the Γ-centred plane, under p-polarised light. This apparent violation of the selection rules can be attributed to the high angular rotation that causes significant mixing of the s- and p-polarised vectors and final state effects that cause a breakdown of the selection rules. Nonetheless, despite the experimental geometry resulting in imperfect selection rules, one observes the suppression of forbidden photoemission processes relative to the allowed transitions for the majority of states, under both s- and p-polarised light, allowing for the orbital texture of the conduction band states to be disentangled.

8.2 Moving Through T$_C$

Thus far, the present investigation of the electronic structure of $\mathrm{Eu}_{1-x}\mathrm{Gd}_x\mathrm{O}$ has focused on the conduction bands in the ferromagnetic state, well below T$_C$; however, historically, the majority of the research performed on this material has centred around the evolution of the ferromagnetic transition itself. In the remainder of this chapter, the reconstruction of the electronic states across the dual ferromagnetic, metal-insulator transitions will be examined, focusing on the exchange splitting of the Eu $5d$ states.

8.2.1 Exchange Splitting of Conduction Band States

In the low temperature phase, the exchange splitting of the conduction band pushes the spin majority band below the Fermi level in n-doped samples. Therefore, by increasing the temperature, a measurable decrease in the size of the electron pocket should be observed, which, one would naively expect, to be related to the magnetic moment of the Eu $4f$ atoms that drive the ferromagnetism, Fig. 8.7. Indeed, measurement of the conduction band along the short axis of the electron pocket (i.e. along W-X-W line in Fermi surfaces of Fig. 8.6, bottom row) for a film

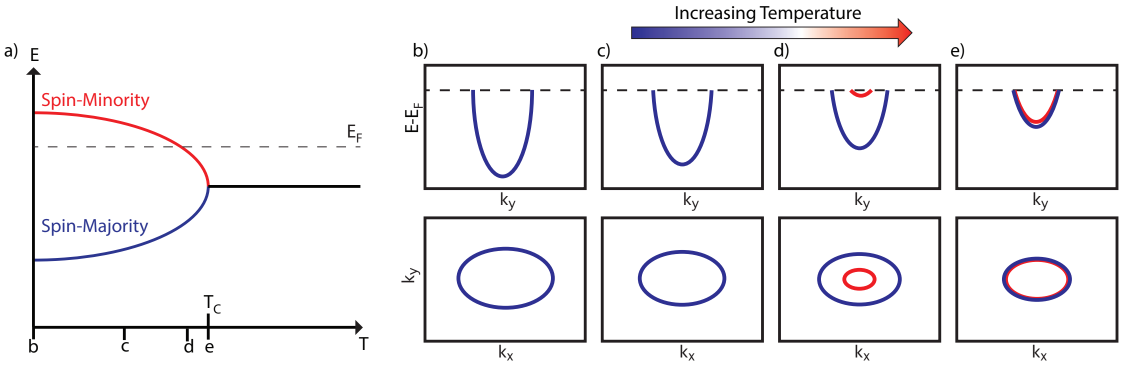

FIGURE 8.7: Cartoon schematic of the temperature dependent reconstruction of the conduction band across the ferromagnetic transition. a) Schematic of the spin-majority and spin-minority conduction band minima as a function of temperature, relative to the Fermi level in a heavily electron doped EuO sample. b) At T=0K, the full extent of the exchange splitting is achieved, such that only the spin-majority band is below the Fermi level. c) Increasing the temperature reduces the size of the exchange splitting, decreasing the size of the spin-majority electron pocket. d) At sufficiently high temperatures, but below T_C the spin-minority band shifts below the Fermi level, until e) the exchange splitting collapses almost completely and thus the electron pocket is not spin-degenerate due to local moment effects.

with a high carrier density, N=5.9±0.4 x10^{20} cm^{-3}, and T_C=123K, shows a significant reduction in the size of the conduction band in the paramagnetic phase (T=160K) compared to the low temperature phase (21K), as shown Fig. 8.8a-c. Energy distribution curves (EDCs) taken through the centre of the electron pocket, displayed in Fig. 8.8d, show that at low temperatures the conduction band has almost even intensity up to 500meV below the Fermi level. This is likely due to k_z-broadening and impurity scattering and not additional spectral weight from the spin-minority band. Even at this high level of doping, the exchange splitting of the conduction band, believed to be $\sim$600 meV, should place the spin-minority band above the Fermi level. Upon heating to T=100K, a slight upward shift of the band is observed and a peak of intensity is seen near the Fermi level, both of which are the result of a reduction of the exchange splitting that causes the spin-minority band to be pulled below the Fermi level while also shifting the spin-majority band upwards, as depicted in Fig. 8.7d. Finally, above the Curie temperature (T=160K) a single broad peak of intensity is observed with significantly reduced binding energy.

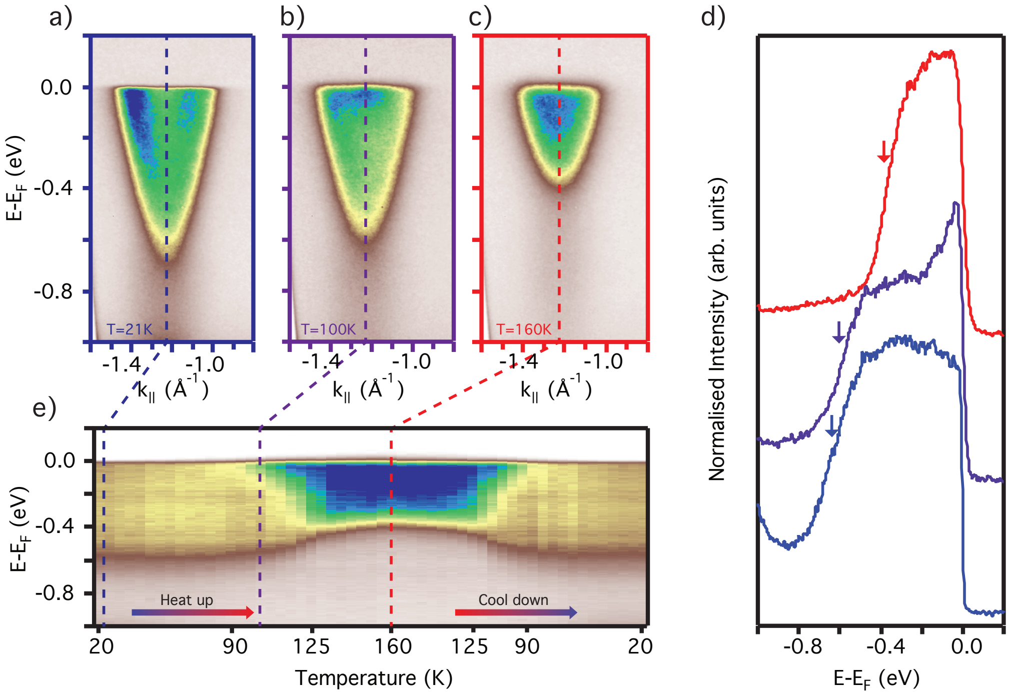

FIGURE 8.8: Temperature dependence of the conduction band energy distribution across the ferromagnetic transition, T$_C$=123K. a) ARPES measurement ($h\nu$=48eV) in the ferromagnetic (T=21K), b) transitional (T=100K), c) paramagnetic (T=160K) phases of doped EuO. Dashed vertical lines correspond to EDCs through $k_{\|}$=-1.23 Å^{-1}, shown in d). Similar EDCs taken at several temperatures show e) little change in the intensity profile of the conduction bands below 90K, but a significant upward shift of the spin-majority band bottom and downward shift of the spin-minority band as it crosses the Fermi level. Above T=140K minimal reconstruction of the conduction band is observed and upon cooling the reversal of the shifts is seen as the exchange splitting drives the spin majority and minority bands apart.

EDCs such as these can be used to construct a temperature dependent map showing the shift of the conduction bands as a function of temperature, as illustrated in Fig. 8.8e. Upon heating from 20K to ~90K, relatively little change to the intensity profile is observed. However, between 90K and 140K, a sudden change of the conduction band is observed as the spin-majority band shifts to lower binding energy. Concomitant with this is the appearance of spectral weight near the Fermi level, indicative of the spin-minority band moving below the Fermi level as the exchange splitting is reduced. Surprisingly, the upward shift of the spin-majority band bottom and downward shift of the minority-spin band is observed to continue well above T$_C$. As the sample is cooled through T$_C$, the reversal of the conduction band shifts is observed as the exchange splitting is increased, pushing

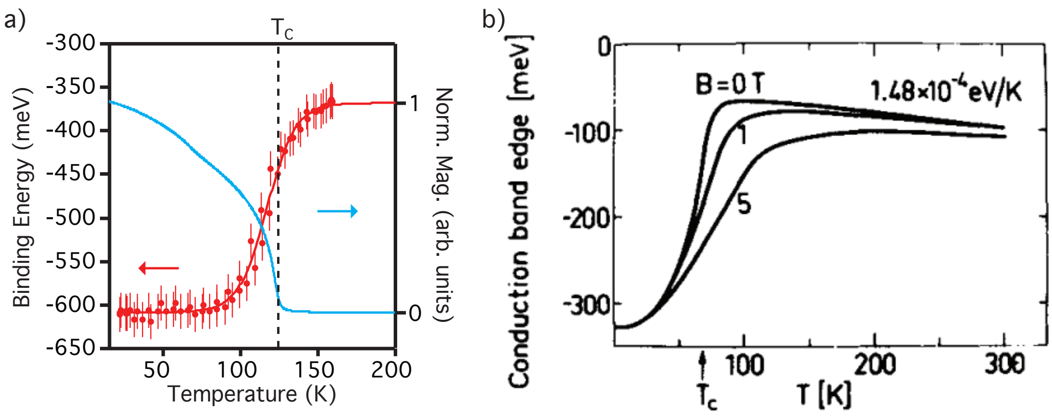

FIGURE 8.9: Redshift of the conduction band bottom. a) Binding energy of the half-maximum intensity of the rising edge of the conduction band minimum (red) reveals a sudden upward shift of the band edge by ΔE=244±20 meV, with significant shift occurring above T_C as shown by temperature dependent magnetisation SQUID measurements (blue). b) The redshift of undoped EuO has been theoretically predicted, adopted from Ref. [142], and quantitatively matches the temperature dependence of highly Gd-doped EuO, when adjustments are made for binding energy and Curie temperature.

the spin-minority band back above the Fermi level. Unfortunately, because of the broad nature of these features, determining the true binding energy of either the majority or minority spin band bottom is difficult.

However, one can estimate the overall shift of the band bottom by examining the half-maximum intensity of the leading edge, as indicated by the arrows in Fig. 8.8d, as a function of temperature. As shown in Fig. 8.9a, the rising edge of the conduction band remains at constant binding energy up to ~80K, at which point a sudden shift to lower binding energy is observed. This upward movement continues well past T_C=123K, with shifts being observed even at 160K. Additionally, by fitting a Gaussian profile to the rising edge, one finds that the intensity profile becomes steeper with increased temperature, ruling out thermal broadening effects as an explanation for the shift of the position of half-maximum intensity of the rising edge. The shift of the band edge qualitatively matches the overall appearance of the temperature dependent map in Fig. 8.8e, suggesting that the band edge is a suitable proxy for the behaviour of the spin-majority band minimum.

The redshift of the conduction band edge has been observed by optical absorption spectroscopy measurements. These indirect measurements of the conduction band minimum revealed an upward shift of 260meV of the Eu $4f \rightarrow 5d$ transition with increased temperature for undoped EuO, which was attributed to the collapse of the exchange splitting. Theoretical calculations by Wachter [142] predict an upward shift of the conduction band edge with increased temperature and, interestingly, the conduction band minimum to continue moving upwards above T$_C$, depicted in Fig. 8.9b. Subsequently, a downward shift of the band minimum is predicted, typical behaviour for semiconductors due to lattice dilation and phonon effects. These calculations show considerable agreement with the optical absorption measurements on undoped EuO and, if a rigid shift in binding energy and Curie temperature is applied to account for doping effects, with the shift of the rising edge observed here. By fitting a hyperbolic tangent function to the temperature dependent edge shift, as a rough approximation to the calculations performed by Wachter, one finds that the low-to-high temperature shift is ΔE=244±20eV, consistent with the red shift observed in optical absorption measurements. However, the size of the exchange splitting is believed to total 600meV, suggesting that the shift of the conduction band bottom is insufficient to completely close the energy gap between the majority and minority spin bands.

In addition to the EDCs through the band centre, a similar temperature dependent map using MDCs taken at the Fermi level can be used to reveal the evolution of the minority-spin band as it shifts below the Fermi level during the ferromagnetic transition, as illustrated in Fig. 8.10a. Below T=90K, MDCs show two peaks of intensity equally spaced around the X-point ($k_{\|}$=-1.23 Å^{-1}) corresponding to the branches of the majority-spin band. However, between 90K and ~120K, an additional feature appears at $k_{\|}$=-1.23 Å^{-1} and gains intensity relative to the side peaks, Fig. 8.10b, which is attributed to the spin-minority band passing below the Fermi level. The appearance of the spin-minority band is clearly evident from

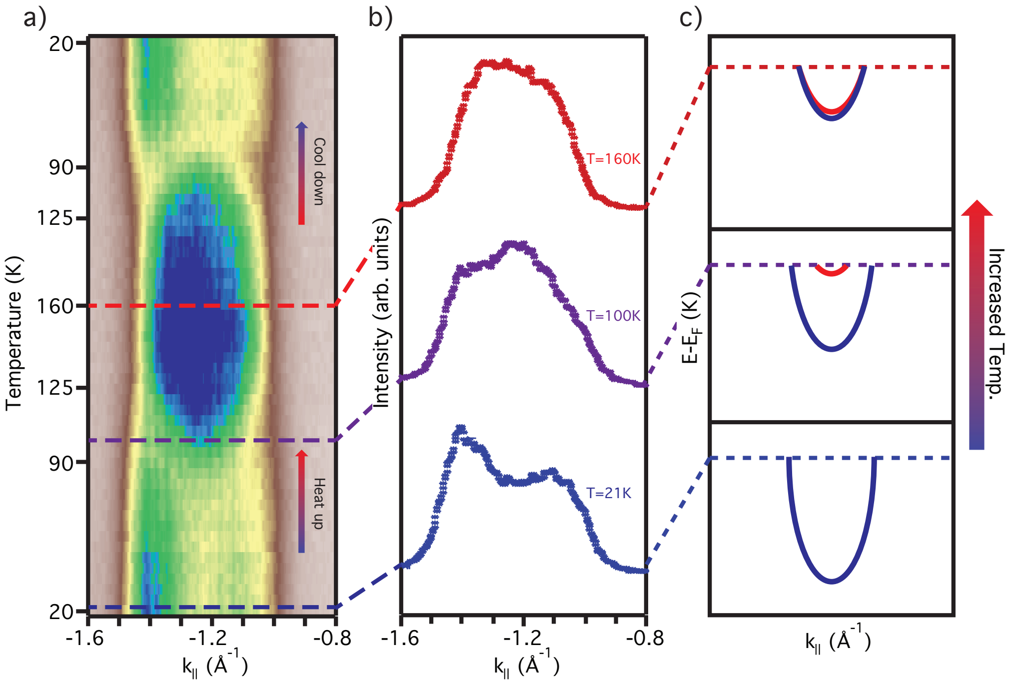

FIGURE 8.10: Temperature dependence of the conduction band momentum distribution across the ferromagnetic transition. a) Temperature dependent maps of momentum distribution curves at the Fermi level shows the appearance of the minority-spin band crossing the Fermi level at T=90K. This band continues to shift downward up to ∼140K, as shown by the widening of the high intensity region centred at $k_{\parallel}$=-1.23Å^{-1}. b) Individual MDCs suggest a single band crossing the Fermi level at low temperature, but as the sample is heated, the spin-minority band crosses the Fermi level. c) Cartoon schematic of the band evolution with increased temperature.

the temperature dependent map in Fig. 8.10a, where above T=90K an oval shape appears, centred at $k_{\parallel}$=-1.23Å^{-1}. As T$_C$ is approached the width of the feature centred at $k_{\parallel}$=-1.23Å^{-1} increases, while the overall width of the electronic pocket reduces, consistent with the shift of the spin-minority band downwards and the spin-majority band upwards towards the Fermi level. The width of the central oval feature continues to increase up until T≈140K, as the spin-minority band shifts further below the Fermi level.

These measurements suggest that, although the onset of magnetic ordering is not instantaneous, as evidenced by magnetisation vs. temperature measurements shown in the middle panel of Fig. 8.10a, it is neither a slow process with the exchange splitting increasing down to T=0K. Rather, the separation of the majority- and minority-spin bands reaches a maximum at a finite temperature below T$_C$, but well above T=0K, which qualitatively matches the picture suggested by the SQUID measurements. Additionally, the EDC and MDC temperature dependent maps, suggest that at and slightly above the Curie temperature, a finite exchange splitting occurs in the Eu $5d$ conduction band states. Raman scattering studies of the metal-insulator transition of $\mathrm{Eu}_{1-x}\mathrm{Gd}_x\mathrm{O}$ have suggested the presence of magnetic polarons (BMPs) that survive well above T_C. It is believed that near the ferromagnetic transition the formation of BMPs allows for the system's energy to be lowered as the conduction electrons locally align with the Eu $4f$ moments, giving rise to a local exchange splitting of the Eu $5d$ states above T_C [108, 112]. Furthermore, it has been suggested that finite exchange splitting of the conduction band states near T_C is necessary to facilitate the metal-insulator transition [143]. As will be seen in the next chapter, the presence of many-body interactions is not only restricted to the near-T_C temperature range, but they are embodied well below the temperature of ferromagnetic ordering.

Chapter 9

Signatures Plasmonic and Phononic Polarons in Gd-doped EuO

Up until this point, the investigation of the electronic structure of electron doped EuO presented here has focused on samples with relatively large Gd concentration (>10%) as determined by XAS. As was demonstrated in the previous chapter, the high level of doping resulted in sufficient filling of the Eu $5d$ conduction band such that in the ferromagnetic state the Fermi level sat just below the minimum of the spin-minority band. One naively expects the filling of the conduction band to be a straightforward process, in which the Fermi level is rigidly shifted upwards, but as will be shown in this chapter, signatures of many-body effects are evident upon reducing the carrier concentration of the films, via control of the Gd concentration, indicative of the correlated nature of EuO.

9.1 Controllable Band Filling

Of paramount importance for integration of any material into an electronic device is an understanding of the materials response to a change in the carrier density. As was seen in Ch. 6, chemical gating, akin to the electric gating used in transistors, resulted in significant reconstruction of the band structure as carriers were added to the system. Here, instead of altering the carrier concentration of the EuO films via deposition of alkali metals, the bulk properties of the films

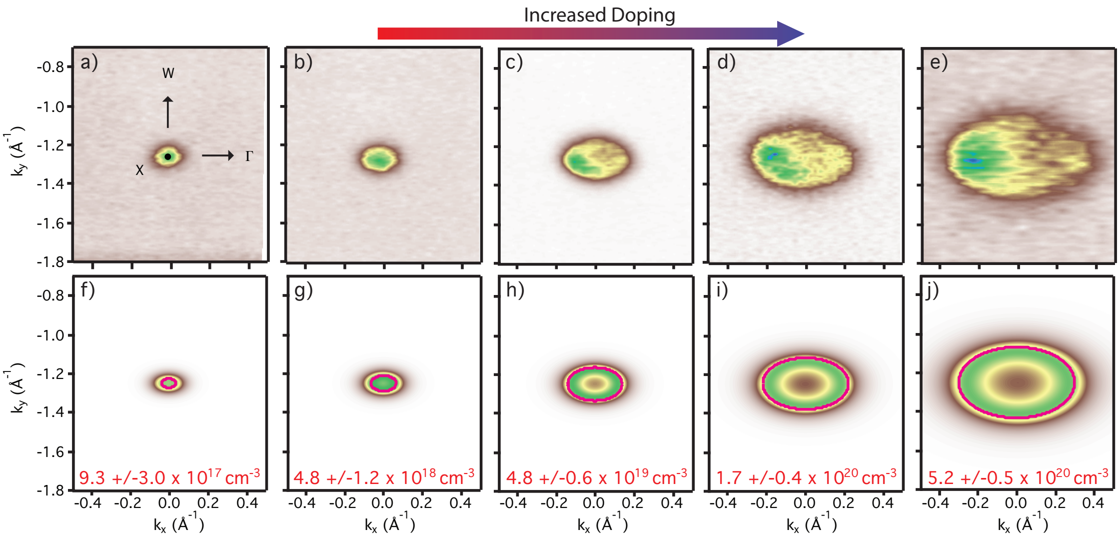

FIGURE 9.1: Tuning the Eu 5d band filling. a-e) ARPES ($h\nu$=137eV) iso-energy contours at the Fermi level reveal the increase in band filling with increased Gd doping. f-j) Spectral function simulations incorporating k_z broadening allow for the calculation of carrier density. Pink ellipses denote the iso-energy contour taken at k_z=0 with $\sum''(E, \mathbf{k}) = 0$.

can be altered during growth by controlling the concentration of the trivalent dopants. As expected, reducing the concentration of Gd^{3+} ions from >10% to ~2% results in a significant reduction of the Luttinger volume enclosed by the Fermi surface, as shown by the iso-energy contours taken at the Fermi level, Fig. 9.1a-e.

Unfortunately, due to the 3D nature of the elliptical electron pockets, determination of the carrier density from ARPES is more complicated than in 2D materials or 2DEGs, like those observed earlier in WSe$_2$. Due to broadening from impurity scattering and integration over a range of out-of-plane momenta, intrinsic to ARPES, a broad feature is observed in each of the angular dependent maps instead of well-resolved sharp bands. While one could use the standard method of calculating the carrier density from the Luttinger volume, given by:

$$N = g_v * g_s \frac{k_F^l k_F^s k_F^s}{6\pi^2}, \tag{9.1}$$

where $g_{v,s}$ is the valley/spin multiplicity, respectively and $k_F^{s,l}$ are the Fermi wavevector along the short and long axis, respectively, the determination of accurate $k_F^{s,l}$ introduces significant error. In order to precisely determine the carrier density, here, the in-plane dispersion at the Fermi level for a given value of N is simulated. To do this, one starts with the spectral function given by:

$$A(\mathbf{k}, E) = \frac{1}{\pi} \frac{\sum''(E, \mathbf{k})}{\left[E - E_0(\mathbf{k}) - \sum'(E, \mathbf{k})\right]^2 + \left[\sum''(E, \mathbf{k})\right]^2}, \tag{9.2}$$

where $\sum'(E, \mathbf{k})/\sum''(E, \mathbf{k})$ are the real and imaginary parts of the self-energy, respectively. Apart from intensity variations due to matrix elements, which can vary due to final state effects and interaction of the photons with the atomic orbitals, the latter of which was discussed in previous chapter, ARPES measurements directly probe the spectral function. Thus by calculating the in-plane spectral function for several values of k_z, for a given carrier density, one can sum each k_z slice to simulate the iso-energy contour for a 3D electron pocket.

Because the constant energy contours are taken at the Fermi level, E is set to zero. By assuming that the only relevant part of the self-energy term is that which gives rise to elastic impurity scattering, i.e. $\sum'(E, \mathbf{k})$=0 and $\sum''(E, \mathbf{k})$=const.=ϵ, the measured intensity can be rewritten as:

$$I(k_x, k_y) \propto \left(\sum_{k_z} \frac{I(k_z)}{E_0(k_x, k_y)^2 + \epsilon^2} \right) \otimes G(k_x, k_y) \tag{9.3}$$

where $G(k_x, k_y)$ is a 2D Gaussian function with full-width half-maximum (FWHM) equal to 0.01/Å and 0.02/Å at $h\nu$=137eV, to account for the experimental resolution along the k_y and k_x axes, respectively, and the sum over k_z accounts for the out-of-plane momentum broadening with an attenuation factor given by [22]:

$$I(k_z) = \frac{1}{2\pi\lambda} \frac{1}{(k_z - k_{z,0})^2 + (1/2\lambda)^2} \tag{9.4}$$

where λ is the inelastic mean free path as determined by the TPP-2M algorithm

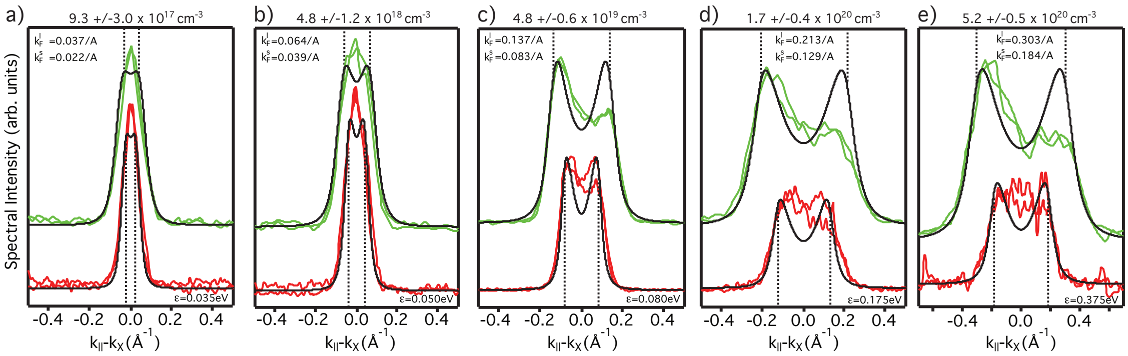

FIGURE 9.2: Comparison of measured and simulated momentum energy distribution curves. a-e) MDCs aligned along the short (red curves) and long (green curves) axes of the constant energy Fermi surface maps for increasing carrier concentrations. MDCs of simulated Fermi surfaces (black curves) provide excellent agreement with measured dispersions. Dashed black lines indicate Fermi wavevectors for the short and long axes.

[69] and $k_{z,0}$ is the out-of-plane momentum corresponding to the probing photon energy.

Thus by calculating the intensity for a range of k_z values, one can sum the individual iso-energy contours to simulate the measured spectral function for the 3D elliptical pockets, Fig. 9.1f-j. Comparison of momentum energy distribution curves, shown in Fig. 9.2, reveals excellent agreement between simulations and experimentally measured energy contours across the whole range of carrier densities. Due to the k_z broadening, the peak of intensity shifts towards $k_{x,y}$=0 and would result in an underestimation of N by $\sim$40% if the peak intensity was used for $k_F^{s,l}$. One should also note that the inclusion of the ϵ term corresponds to a broadening of the spectral intensity that increases with higher Gd concentration attributed to an increase in impurity sites caused by the enhanced number of dopants, which is also evidenced by the slight reduction in quality of LEED images for heavily doped films.

Accurate determination of the carrier density also allows one to compare it to the Gd concentration and Curie temperature, determined from XAS and SQUID measurements, respectively, discussed earlier. As depicted in Fig. 9.3, a clear

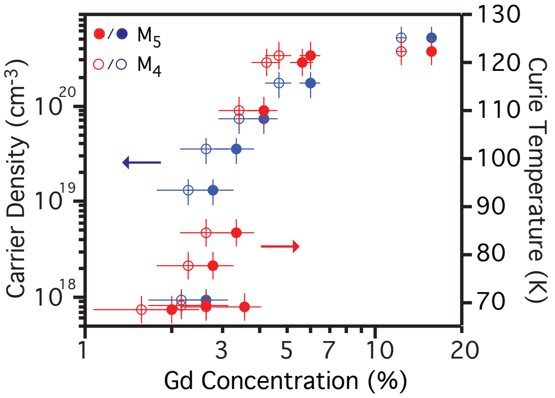

FIGURE 9.3: Comparison of carrier density, Curie temperature and Gd concentration. Curie temperature (red) and carrier density (blue), as determined by SQUID and ARPES measurements, respectively, as a function of Gd concentration determined from XAS measurements. A monotonic trend is observed with possible saturation of carrier density and Curie temperature at Gd concentrations in excess of 10%.

trend exists between the Curie temperature and the carrier density, as the concentration of Gd^{3+} ions is increased, consistent with previous measurements. This additional comparison supports the observation of a possible saturation in both Curie temperature and carrier density as the Gd concentration exceeds ∼10%, suggestive that as the spin-minority band approaches the Fermi level in the ferromagnetic phase, the increase in the density of states prevents further enhancement of the carrier density, which is intimately tied to the Curie temperature.

9.2 Replica Features near the Conduction Band Minimum

Just as one expects an enlargement of the Fermi surface with increased carrier density, one naively expects the conduction band minimum to rigidly shift to higher binding energy as the electron concentration increases. Taking ARPES measurements through the centre of the electron pocket, along the W-X-W line of the Brillouin zone (i.e. $k_x = 0$ in Fig. 9.1), one can analyse the effects of the carrier concentration on the electronic structure near the Fermi level, Fig. 9.4a. Indeed, a monotonic increase in the conduction band minimum with increased

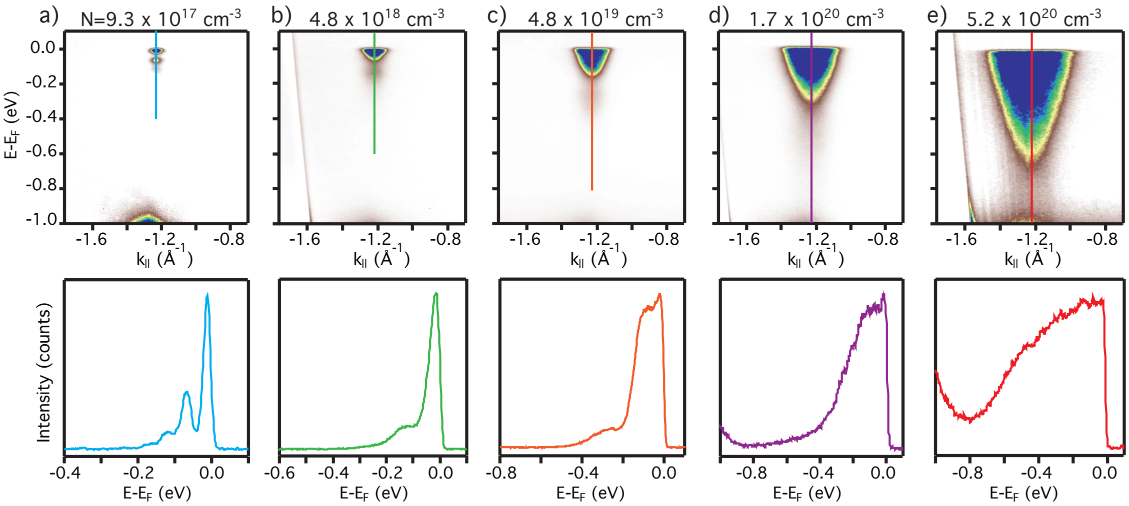

FIGURE 9.4: Satellite features in the conduction band states. a) ARPES measurement ($h\nu$=48eV) of the conduction band state (top) and the energy distribution curve (bottom) corresponding to the coloured line in the panel above. b-e) Same as a) but with increasing carrier concentration. Additional satellite features are observed below the quasiparticle band at higher binding energies.

carrier density is observed, consistent with a rigid upward shift of the Fermi level. However, upon closer examination, additional spectral features are evident at higher binding energies. As evidenced by the energy distribution curves through the centre of the electron pocket, a clear "peak-dip-hump" profile is observed due to the presence of satellite features below the minimum of the quasiparticle band. The appearance of these additional features will be the focus of the remaining discussion of the band structure of n-doped EuO presented here.

9.2.1 Signatures of Phononic Polarons

In the lowest doped sample (N=9.3 x 10^{17} cm^{-3}) measured here, there are three clear satellite peaks in addition to the more intense quasiparticle band near E$_F$. Upon fitting the EDC through the band centre with one Lorentz function for each of the satellites and quasiparticle band, one finds that the peak positions of the satellite features are almost perfectly equally spaced, i.e. $\Delta_1 = \Delta_2 = \Delta_3 = 56 \pm 3$ meV in Fig. 9.5a. The appearance of the additional features at equal increments

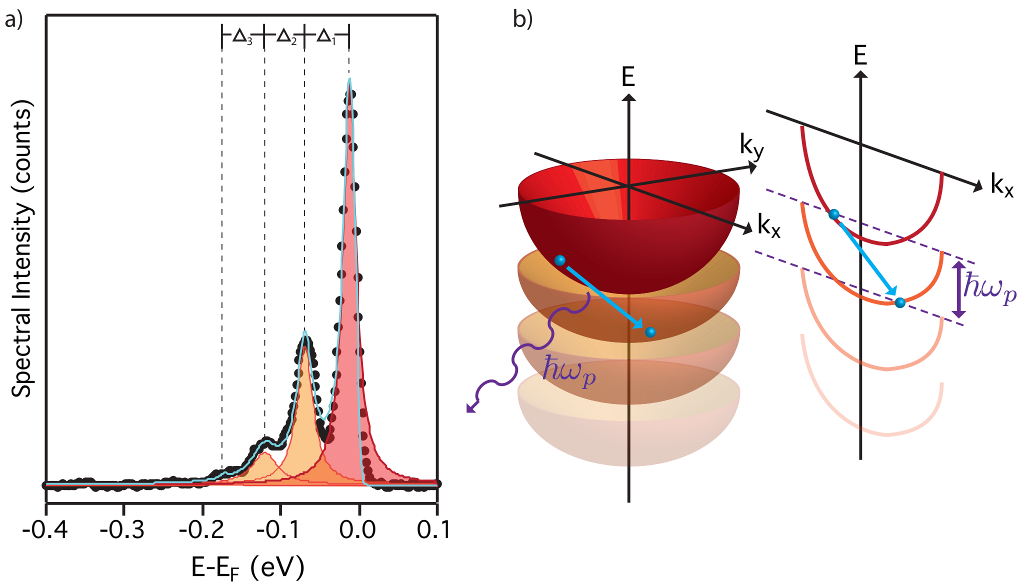

FIGURE 9.5: Fitting the satellite features in EuO. a) Four Lorentz functions are used to fit the lowest doped (N= 9.3 x 10^{17} cm^{-3}) sample, corresponding to the quasiparticle band (red curve) and three additional satellite features (orange curves). The spacing of the peaks Δ_i are seen to be approximately equal, suggestive of b) shake-off excitations from long-range coupling to a phononic mode that produce replica band features. b) has been adapted from Ref. [144].

in energy is reminiscent of signatures of polarons in a range of other oxide systems, such as ZnO surfaces [144], TiO_2 anatase [145] and the interfacial regions of $SrTiO_3$ [146–148].

In each of these systems, ARPES measurements reveal additional satellite features below the conduction band minimum of a 2D electron pocket, producing long tails and the "peak-dip-hump" profile of the energy distribution curve. These satellite features of the conduction bands are attributed to "shake-off" excitations in which a single non-dispersive bosonic mode couples together electrons of momentum **k** and **k**+**q** producing replica bands at successively higher binding energies, depicted in Fig. 9.5b, each separated by integer multiples of the bosonic mode energy [144]. In these studies the replica bands are attributed to electron-phonon coupling as they preserve the original band dispersion, indicative of small **q** processes, characteristic of Fröhlich polarons. These excitations can be visualised as an electron dressed in a polarisation cloud that is dragged around by the electron as it moves through the lattice [148].

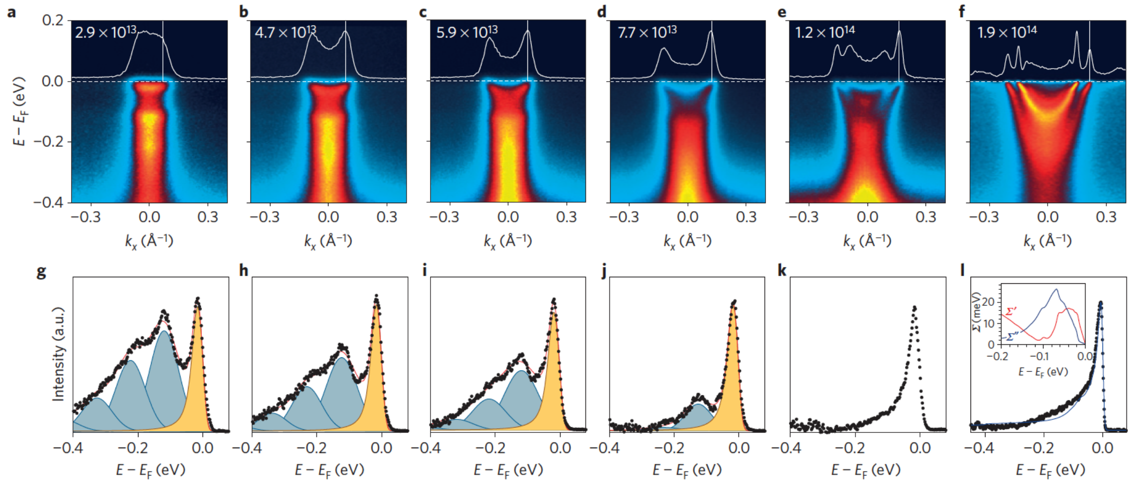

FIGURE 9.6: Evolution of shake-off excitations in $SrTiO_3$ (001) with carrier density. a-f) ARPES measurements of 2D electron liquid with increasing carrier concentration. g-l) Energy distribution curves taken at $k = k_f$ with fitting of quasiparticle (yellow) and phonon loss satellites (blue) overlaid, revealing constant spacing in binding energy of replica features. Reproduced from Ref. [148].

In $SrTiO_3$ and TiO_2 anatase, replica bands are observed across a wide range of carrier densities with constant energy spacings corresponding to the relevant longitudinal optical phonon mode, as illustrated in Fig. 9.6 for $SrTiO_3$. Being a property of the crystal structure, the phonon mode energy is largely independent of the carrier density and thus the energetic spacing of the satellite features is seen to remain fixed. Although the spacing remains constant, the intensity of the satellite features relative to the quasiparticle intensity, i.e. quasiparticle residue given by $Z = 1 - \alpha/2$ where α is a dimensionless coupling constant [149], is reduced, i.e. Z increases, with increasing carrier concentration, as the phonons are more effectively screened by the electrons [148, 150]. The breakdown of the single-polaron model as the polarons lose coherence and disassociate into an electron liquid weakly coupled to the phonons is not only signalled by the loss of spectral weight in the replica bands but also by the emergence of kinks in the quasiparticle band near the Fermi level [145], a well-known signature of weakly-coupled electron-phonon interactions. Additionally, in $SrTiO_3$ a significant mass renormalisation is observed at low carrier densities due to polaron formation, but this effect is reduced as the phonons become screened by the electrons when the two have comparable energy scales (i.e. $E_{CBM} \approx \hbar\omega_{ph}$) [151].

9.2.2 Carrier Density Dependence of Satellite Features

As mentioned earlier, at a carrier concentration of N=9.3x10^{17} cm^{-3}, the shoulder features observed in Gd-doped EuO can be fit using Lorentz functions with an average spacing of ΔE=56±3 meV, on the order of the longitudinal optical phonon mode. However, at even slightly higher carrier densities, EDCs no longer have multiple, well-defined satellite features, although the characteristic peak-dip-hump profile is still present to some degree, as demonstrated in Fig. 9.4b,c. Nonetheless, one notes that as the carrier concentration is increased, the relative intensity of the satellite features is reduced, indicative of the screening of electron-phonon interactions, consistent with the behaviour exhibited by $SrTiO_3$ [148]. The even spacing of the shoulder features at very low carrier densities, the increase in quasiparticle residue, i.e. reduction in satellite intensity, at higher carrier densities, and kinks in the conduction band near the Fermi level are all highly suggestive of electron-phonon coupling in EuO. To fully understand the origins of the satellite features and the kink in the spectral intensity, numerical simulations were performed, similar to those used to determine the carrier density.

By setting k_x=0 instead of E=0 in Eq. 9.3 and incorporating k_z integration as before, one can calculate the energy vs. momentum dispersion along the W-X-W direction. In order to account for the formation of Fröhlich polarons, replicas of the conduction bands are included with a relative shift to higher binding energies equal to ΔE=56meV and attenuation of intensity, λ^i, where i is the replica index. As shown in Fig. 9.7a, a single bare band, with effective mass m^*=0.55m_e, and three replica features, with intensity attentuation equal to $\lambda = 0.35$, is sufficient to reproduce the experimentally observed spectral function for the sample grown with the lowest carrier density. This value of λ corresponds to a quasiparticle residue of $Z \approx 0.55$, as estimated by the relative integrated intensity of the quasiparticle and satellite peaks.

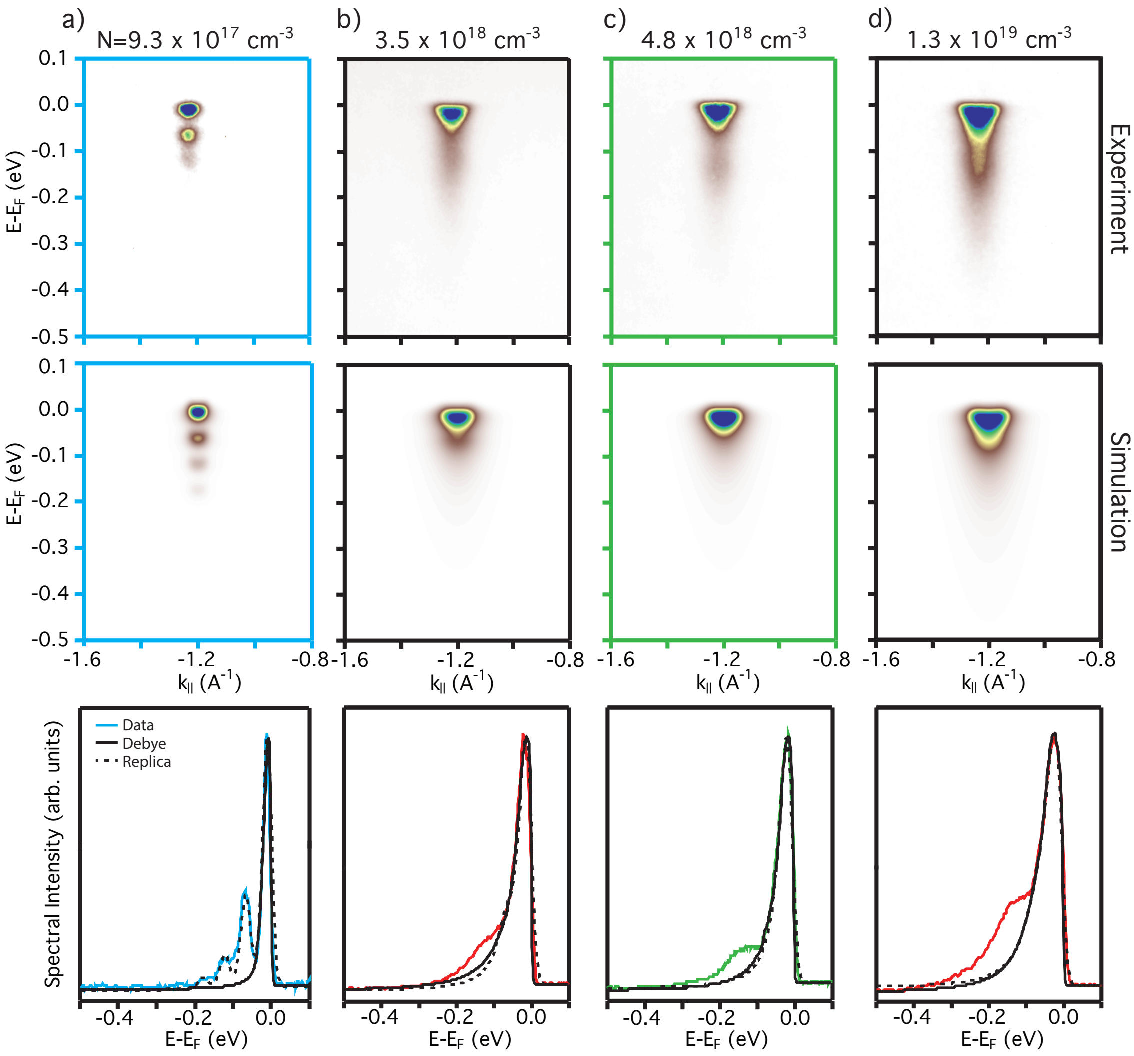

FIGURE 9.7: Simulating electron-phonon coupling in the low carrier density regime. a) ARPES measurement ($h\nu$=48eV, top panel) of Eu$_{1-x}$Gd$_x$O with N=9.3x10^{17} cm^{-3} and the calculated spectral function using a bare-band model with three additive replica features (middle panel). EDCs of the measured band dispersion (coloured line) and calculated spectral function using a bare-band replica (three replicas, dashed line) and Debye (solid line) model. b-d) As as in a), for increasing carrier density but with one replica feature. Both models reproduce the quasiparticle peak and shoulder feature, but not the additional satellite feature at higher binding energy.

Increasing the carrier density, one achieves good agreement between the experimental and simulated spectral function in the near Fermi level region, Fig. 9.7b-d, up until N≈1.3x10^{19}cm^{-3}, by a combination of: 1) monotonically reducing the effective mass, m^*, from 0.55m_e to 0.45m_e; 2) increasing the intensity attenuation of the phonon replica feature, i.e. $\lambda \rightarrow 0.1$; and 3) increasing the impurity scattering term (i.e. the constant imaginary part of the self-energy), as

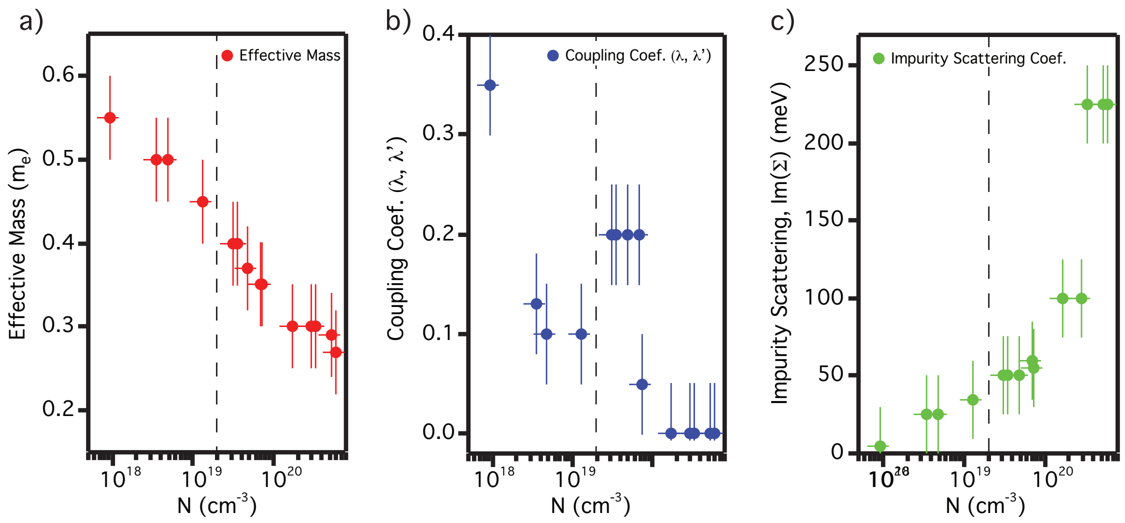

FIGURE 9.8: Model parameters for energy dispersion simulations incorporating electron-phonon coupling. Carrier density dependence of a) effective mass, b) electron-phonon coupling coefficient (λ or λ') and c) imaginary part of the self-energy. The dashed line denotes the approximate break-down of the bare band replica model. Note: the coupling coefficient in b) changes from λ to λ' across the dashed lines to reflect the change in model.

illustrated in Fig. 9.8. The increase of the effective mass at low carrier densities by a factor of up to ~1.8 compared to the theoretical value of $m^* \approx 0.3m_e$, as predicted by DFT, is indicative of a mass renormalisation, similar to that observed in $SrTiO_3$ [148], as is the reduction in coupling strength, suggestive of electrons screening the phonon interactions. Additionally, the increase in impurity scattering is consistent with the trend established in the Fermi surface simulations used to estimate N. However, as will be discussed later, this bare band replica model is incapable of reproducing the satellite feature at higher binding energies, well above the energy of the longitudinal optical phonon mode.

As the carrier density is increased beyond ~1.3x10^{19}cm^{-3}, the binding energy of the bare band bottom increases such that it is approximately equal to that of the phonon mode energy and a drastic reconstruction of the band structure is observed as the phonons are screened by the electrons. Whereas at lower carrier densities the quasiparticle band produces a sharp peak just below the Fermi level, at elevated N a broad band is observed, as shown in Fig. 9.9a. Additionally, kinks in the conduction band dispersion are seen near k_F, indicative of the

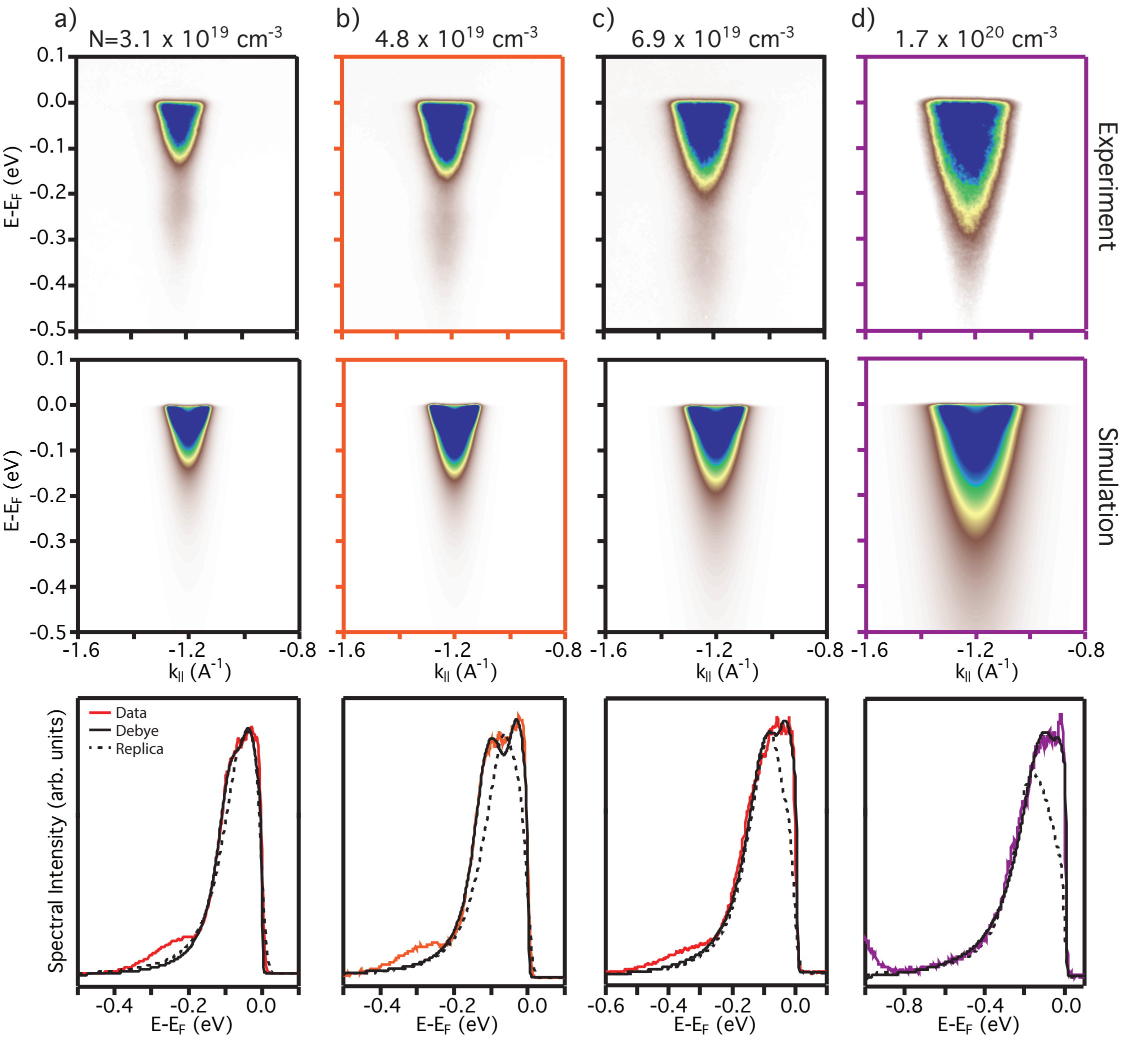

FIGURE 9.9: Simulating electron-phonon coupling in the regime of weak electron-phonon coupling. a) ARPES measurement ($h\nu$=48eV, top panel) of $\mathrm{Eu}_{1-x}\mathrm{Gd}_x\mathrm{O}$ with N=3.1x10^{19} cm^{-3} and calculated spectral function using the Debye model for electron-phonon coupling (middle). Energy distribution curves of the measured band dispersion (coloured line) and calculated spectral function using the bare-band replica (dashed line) and Debye (black line) model. b-d) Same as in a), but with increased carrier density. EDCs illustrate the breakdown of the bare-band replica model as phonons become screened by the increased electron concentration.

break-down of the phononic polaron model and emergence of a regime of much weaker electron-phonon coupling. The simplistic model of a replicated bare band is therefore insufficient to reproduce the observed spectral intensity at higher carrier densities and an alternative model is required. In order to account for the broad band observed at higher carrier densities, electron-phonon coupling is implemented in the Debye model, such that in Eq. 9.2 the real and imaginary parts of the self-energy are given by:

$$\sum\nolimits'_{e-ph}(E,\mathbf{k}) = -\lambda'\frac{\hbar\omega_D}{3}\left[\frac{E}{\hbar\omega_D} + \left(\frac{E}{\hbar\omega_D}\right)^3 \ln\left|1 - \left(\frac{\hbar\omega_D}{E}\right)^2\right| + \ln\left|\frac{1+\frac{E}{\hbar\omega_D}}{1-\frac{E}{\hbar\omega_D}}\right|\right]$$

and

$$\sum\nolimits''_{e-ph}(E,\mathbf{k}) = \begin{cases} \frac{\pi}{3}\lambda'\frac{|E|^3}{(\hbar\omega_D)^2} \text{ for } |E| \leq \hbar\omega_D \\ \frac{\pi}{3}\lambda'\hbar\omega_D \text{ for } |E| > \hbar\omega_D \end{cases} \tag{9.5}$$

respectively, where λ' is the electron-phonon coupling coefficient and ω_D is the Debye frequency, which is set to the phonon mode frequency, ω_{ph}. Additionally, impurity scattering is retained in the form a constant contribution to the imaginary part of the self-energy. Using this alternative model, one not only finds good agreement for the observed quasiparticle peak at intermediate carrier densities, but also in the high carrier density regime, up until N≈2.9x10^{20}cm^{-3}. Kinks in the conduction band states are observed across this range of elevated carrier densities and, due to the incorporation of k_z broadening in the simulation, these kinks form a peak of intensity near the Fermi level that mimics a shallow band, consistent with the ARPES measurements.

However, an additional satellite feature at higher binding energies, much larger than the energy associated with the longitudinal optical phonon mode energy, is observed across all carrier densities that neither the bare band replica nor the Debye model for electron-phonon coupling are able to reproduce. Additionally, one sees that this feature shifts to higher binding energy with increased carrier density. Unlike the phonon mode energy, which is independent of carrier density, the monotonic increase in binding energy implies that this feature is derived from coupling to a different bosonic mode that has a carrier density dependence, i.e. the plasmon mode [152, 153]. In an analogue of phononic polarons, these "plasmonic" polarons can be visualised as an electron dressed in the collective sea of electrons that are dragged around as the electron moves through the crystal lattice.

By subtracting the calculated spectral functions from the EDCs as measured by ARPES, depicted in Fig. 9.10a, the spectral weight from the plasmon loss feature can be separated out and fit with a Lorentz function to determine the peak position and thus the energy shift. As expected this feature continues to shift to higher binding energies, Fig. 9.10b, while the intensity of the feature reduces with increased carrier density, Fig. 9.10c. The peak positions of the features at higher binding energies can be described by the plasmon energy given by:

$$\hbar\omega_{pl} = \sqrt{\frac{Ne^2}{\epsilon^* m^*}} \tag{9.6}$$

where m^*=0.3m_e is the effective mass at high N and $\epsilon^* = 4.5\epsilon_0$ is the effective dielectric constant. One notes that at high carrier densities, good agreement is achieved between the plasmon energy and the extracted peak positions, but in the low/intermediate regime the agreement breaks down. This could be a result of possible "mode-mixing" between the phonon and plasmon modes when their energies are comparable [154]. Eventually, a high enough carrier density

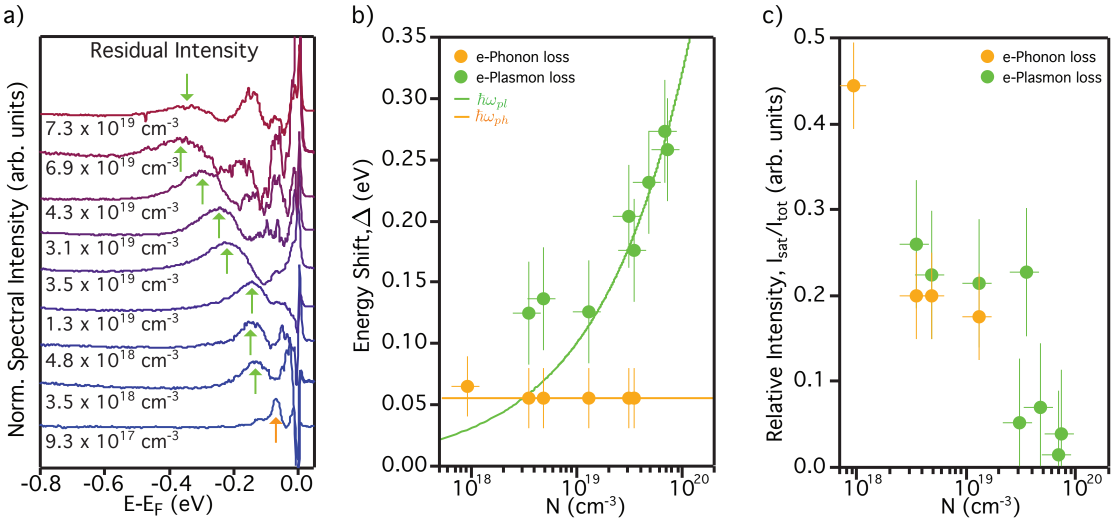

FIGURE 9.10: Carrier dependence of the plasmonic and phononic polaron peaks. a) Residual spectral intensity attributed to loss features associated with electron-plasmon coupling, determined by the difference in the measured and simulated spectral function using the Debye model with electron-phonon coupling. Arrows depict b) peak positions and c) corresponding relative integrated intensity of the peaks associated with plasmon and phonon loss features in a).

($N\approx 1.7\text{x}10^{20}\text{cm}^{-3}$) is reached such that no signatures of plasmonic polaron formation are observed, i.e. no satellites at high binding energies, but the weak electron-phonon coupling is maintained, as evidenced by the kink features near the Fermi level. Therefore, these measurements and supporting simulations suggest that as N is increased and $E_{CBM} \geq \hbar\omega_{ph}$, the system shifts from a regime of "phononic" polarons and "plasmonic" polarons, to a regime of weaker electron-phonon coupling where only plasmonic polaron formation is observed. Eventually, a possible third regime is reached in which only signatures of weak electron-phonon coupling are seen.

9.2.3 *Ab Initio* Calculation of Spectral Function

Through a collaboration with Dr. Feliciano Giustino, his group was able to develop a fully *ab initio* method for calculating the spectral function of the 3D elliptical electron pockets, that includes both electron-phonon and electron-plasmon coupling. This model builds on previous work by Giustino *et al.* in which electron-phonon interactions in polar semiconductors were calculated in the Fröhlich model [155] using fully localised Wannier functions [156, 157] and where the effects of electron-plasmon interactions on the spectral function were calculated [152, 153, 158] in the GW plus cumulant approximation [159, 160]. Very recently, these two methods were combined into a single formulation to predict a carrier density dependence of the loss features observed in the spectral function of TiO_2 anatase which arises purely from electron-phonon coupling but becomes screened when the plasmon mode energy is comparable to the LO phonon mode energy [150]. Here, the model is extended to include k_z broadening by calculating the spectral function for a number of k_z values for a given value of N and summing each with a Lorentzian weight according to Eq. 9.4. Additional broadening has been included with a 2D Gaussian profile to account for the energy and momentum resolution of the experimental setup.

Using this method, the spectral function for electron-doped EuO with carrier densities representative of the samples measured in ARPES were calculated, illustrated in the top row of Fig. 9.11. Furthermore, the spectral intensity was decomposed into the electron band and the loss features associated with electron-phonon and electron-plasmon coupling, as seen in the bottom row of Fig. 9.11. From this, one can see that the model is capable of reproducing several elements of the observed spectral intensity: 1) multiple satellite features are observed for the lowest carrier density in excellent agreement with the lowest N sample; 2) the increase in carrier density results in an increase in the energy shift of the plasmon loss feature but not the phonon-derived peak; 3) the quasiparticle residue,

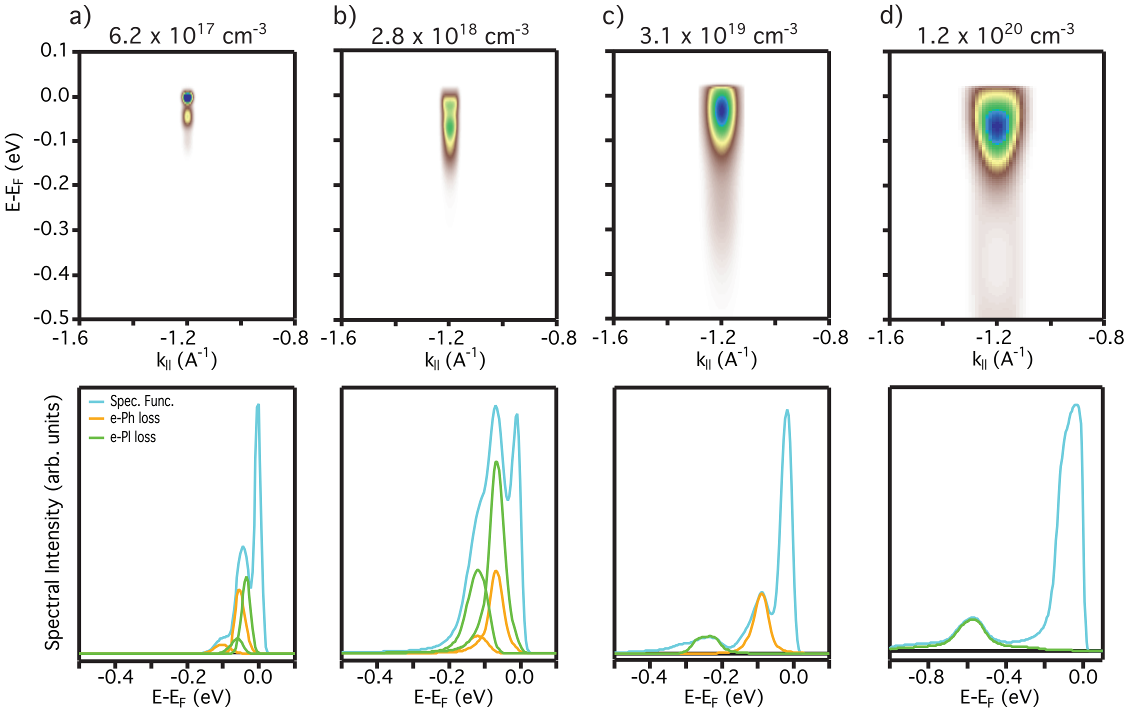

FIGURE 9.11: Calculation of the spectral function for $Eu_{1-x}Gd_xO$. a) *Ab-initio* calculation of the spectral function and decomposition of EDC through band centre, for lightly doped (N=6.2x10^{17} cm^{-3}) EuO, predicting the appearance of multiple replica bands corresponding to the formation of phononic and plasmonic polarons. Bottom panel: decomposition of the theoretical energy distribution curve revealing the phonon and plasmon loss features. b-c) As the carrier density is increased, the plasmon frequency increases and the associated replica bands are shifted to higher binding energies, while the phonon loss features are shifted by a constant energy. d) At high carrier density, the electrons screen the phonons sufficiently to suppress the satellite features associated with electron-phonon coupling.

Z, increases with increased N; and 4) at large N the electron-phonon interaction is screened, resulting in a broad electron band and disappearance of the phonon loss satellite feature, 9.11d. Although the intensity of the plasmonic and phononic polaron peaks relative to the electron peak do not reproduce the measured spectrum as well as the simulated dispersions described in the previous section, these features can be affected by additional factors that have not been accounted for in the calculation, such as sample quality, which could reduce the coupling to the different bosonic modes.

Nonetheless, these *ab initio* calculations do predict a carrier density dependent mass renormalisation, consistent with the data and previous simulations. More importantly, these calculations accurately reproduce the size of the energy shift of satellite features to higher binding energies observed in the ARPES measurements, validating the nature of the two different sets of satellite features: those which are independent of carrier density, i.e. phononic polarons, and those which shift to higher binding energies as the carrier density is increased, i.e. plasmonic polarons. Furthermore, the model predicts the cross-over from the regime of strong electron-phonon coupling (i.e. phononic polaron formation) to the electron-liquid-like regime where phonons are effectively screened by the electrons.

In this chapter, an investigation of the carrier density dependence of the electronic structure has been presented. It was seen that the conduction electrons, introduced via Gd^{3+} dopants, couple to two bosonic modes: phonons and plasmons. While the phonon frequency is independent of the carrier density, and thus replicas of the quasiparticle band were seen to shift by a constant amount, by increasing the carrier density, evidence was provided for electron-plasmon coupling that gives rise to additional satellite features that depend on the plasmon frequency. Just as in WSe_2, where the screening of the electron-electron interactions reduces the exchange and correlation energies such that $E_{exc+corr} \approx E_{kin}$ at high carrier densities and the effects of negative electronic compressibility were reduced, as the number of carriers is increased in EuO, the phonons become more efficiently screened and the system moves into a regime of weaker electron interactions.

9.3 Future Work on EuO

An ability to grow ultra-thin samples would open up several avenues for future research focused on EuO. By reducing the dimensionality of the system, the ability of the electrons to screen the phonons should be significantly reduced as a larger proportion of field lines penetrate vacuum. Changing the screening environment could possibly extend the regime of the phononic polaron formation to higher carrier densities, as well as altering the strength of the electron-plasmon interactions which also depend strongly on screening and dimensionality. Additionally, monolayer and few layer samples should have negligible k_z dispersion as the carrier wavefunctions are restricted by the quantum well that forms between the insulating substrate and vacuum, much like the 2DEG that formed at the surface of the alkali doped samples of WSe_2. Thus, by reducing the system to a 2D sheet, one would expect ARPES measurements to reveal sharp bands and, hopefully, clearly resolved satellite features.

As mentioned in Ch. 7, reducing the thickness of the films below 20 atomic layers also suppresses the magnetic transition in stoichiometric EuO, decreasing the Curie temperature. Naively, one expects this to create a competing effect with the addition of trivalent dopants, which raises the Curie temperature in bulk films. By directly measuring the electronic structure with ARPES, one can analyse the interplay between carrier density and thickness in the temperature dependent band reconstruction across the dual ferromagnetic and metal-insulator transition.

The ability to grow EuO films and finely tune a wide-range of characteristics, such as thickness and carrier density, would also hopefully provide a sufficient blueprint for the growth of similar binary oxides, which would expand the possibilities for measuring the electronic structure of interfaces and heterostructures. Due to the high mobility of O^{2-} ions in $SrTiO_3$ and high reactivity of atomic Eu, deposition of the latter on a $SrTiO_3$ substrate is believed to extract sufficient oxygen from the substrate to form stoichiometric EuO, resulting in the formation of a 2DEG in the interfacial layer of the then oxygen-deficient $SrTiO_3$ substrate [161]. Such methods provide an alternative recipe for the growth of monolayer EuO while leaving the interfacial 2DEG accessible to measurement by ARPES. It has also been predicted that the strain induced by the lattice mismatch of SmO thin films grown on bulk EuO results in topologically non-trivial phases in the flat Sm $4f$ bands [162]. Thus if growth recipes for EuO can be adapted to SmO, which also has the same rock-salt structure, a method for realising the quantum anomalous Hall effect in a strongly correlated system could be achieved. Thus further investigation into the electronic structure of bulk and ultra-thin EuO is necessary for understanding the underlying behaviour of the material in configurations and environments similar to those in proposed spintronic devices.

Chapter 10

Conclusions and Future Outlook

This concludes the experimental study of the electronic structure of WSe_2 and Gd-doped EuO. Using the powerful technique of angle-resolved photoemission spectroscopy (ARPES) combined with a tuneable light source delivered by synchrotron radiation, the electronic band structures of single-crystal and thin film samples were directly probed. Presented in this thesis was a discussion of original research centred around spin-split valence band states of WSe_2 and conduction band states in EuO. Despite having different crystal structures, symmetries and dimensionality, both WSe_2 and EuO were seen to show signatures of many-body effects due to electron interactions: electron-electron interactions in WSe_2 and electron-bosonic mode coupling in Gd-doped EuO.

Previous theoretical and experimental studies of monolayer transition metal dichalcogenides observed a locking of the spin and valley-pseudospin, due to a combination of spin-orbit coupling and broken inversion symmetry, that produces a spin-splitting of the valence band states around the Brillouin zone corners. Restoration of inversion symmetry in the bulk unit cell of the 2H structures should result in spin-degeneracy throughout the Brillouin zone, as confirmed by bulk-sensitive photoluminescence experiments. However, through a combination of spin- and angle-resolved photoemission spectroscopy measurements on bulk 2H-WSe_2 it was shown here that the valence band states at $\overline{\mathrm{K}}$ retain an out-of-plane spin-polarisation which reverses sign at the time-reversal conjugate point, $\overline{\mathrm{K}'}$. Photon-energy dependent measurements revealed that these electronic states have negligible dispersion in the out-of-plane direction, confining the electronic wavefunctions to the 2D environment of the individual Se-W-Se sheets. Thus the local breaking of inversion symmetry by the individual layers of the unit cells allows for a "hidden" spin-polarisation to exist for these states within each layer, locking the spin to the valley- and layer-pseudospins. Because of the surface-sensitivity of ARPES, these measurements predominantly probe the uppermost layer, allowing for the hidden spin-polarisation to be directly measured. This hidden spin-polarisation extends around the Brillouin zone and towards the centre, where it eventually disappears due to the 3D states near $\overline{\Gamma}$ which experience the full symmetry of the unit cell.

Unfortunately, the out-of-plane spin-polarisation will indeed remain "hidden" to bulk-sensitive techniques as the symmetry of the unit cell requires spin-degeneracy when summed over both layers, which is enforced by the reversal of spin-polarisation between layers for a given state. However, by breaking global inversion symmetry, one breaks the layer-degeneracy, and therefore the spin-degeneracy, of the valence bands. A chemical analogue to the electrical gating performed in transistors was adapted to induce a depth-dependent electrostatic potential while leaving the sample surface exposed to probing with ARPES. The deposition of alkali metals was shown to induce a drastic reconstruction of the band structure as the downward band-bending potential pulls the conduction band below the Fermi level in the near-surface region, in addition to a layer dependent shift of the valence bands. Because the electrostatic potential is greatly attenuated as it penetrates the bulk of the material, the valence bands at $\overline{\mathrm{K}}$ in the uppermost layer experience the greatest shift, with a reduced effect in subsequent layers that is akin to a tuneable spin-splitting. Although the valence bands were seen to split as expected, a counterintuitive reduction in the binding energy of both bands was observed. Attributed to a combination of the high effective mass and low dielectric constant, the exchange and correlation energies from electron-electron interactions dominate the electronic kinetic energy. This causes a reduction of the chemical potential as additional carriers are added to the system, in a process known as negative electronic compressibility, that reduces the binding energy of the valence band states. This phenomena is expected to hold for the entire family of materials, establishing the TMDCs as strongly interacting materials.

Although one would naively not expect many similarities between WSe_2 and EuO, a surprising number have been presented. While the breaking of inversion-symmetry gives rise to spin-polarised states in WSe_2, it is broken time-reversal symmetry, from the half-filled Eu $4f$ orbitals, that produce spin-split states in EuO. Here, an investigation of the bulk electronic structure of EuO thin films grown by molecular beam epitaxy was presented, focusing on the conduction bands, made accessible by the substitutional doping of Gd^{3+} for Eu^{2+}. An overview of the recipe developed to grow high quality EuO films was demonstrated, in addition to the effects on the bulk magnetic properties seen by varying the Gd concentration.

Using a sample with high Gd concentration (>10%), angular-dependent ARPES measurements at different photon energies, corresponding to two high symmetry planes, revealed the rotation of the in-plane dispersion of the elliptical electron pockets. Combined with photon energy dependent measurements, which probe the out-of-plane dispersion, the full Fermi surface of doped EuO was measured for the first time, confirming the 3D nature of the conduction band states consistent with DFT calculations. Further measurements suggest a distinct orbital texture that was unveiled using s- and p-polarised light, which couple to different orbitals through symmetry selection rules. Finally, temperature dependent measurements were exploited to analyse the reconstruction of the band structure through the dual ferromagnetic, metal-insulator transition. It was shown that for sufficiently doped samples, the collapse of the exchange splitting can be examined as the spin-minority band shifts below the Fermi level while the spin-majority band moves upwards. Surprisingly, the temperature-dependent shift of the conduction band is seen to continue above the sample's Curie temperature, suggestive of finite spin-splitting above T_C.

Last of all, an investigation of the effects of increased carrier density on the band structure, specifically the Eu $5d$ conduction bands, was presented. Here, observation of additional features below the conduction band minimum were observed for a wide range of carrier densities. These were attributed to replicas of the conduction band that arise from electrons coupling strongly to a bosonic mode. Similar satellite features have been seen in polar oxide systems as a result of electron-phonon coupling that gives rise to Fröhlich polarons. However, simulations of the conduction band dispersions of $Eu_{1-x}Gd_xO$ with varying concentrations of Gd, incorporating only electron-phonon coupling, cannot fully reproduce the energy distribution observed by ARPES. Unaccounted for by these simulations is an additional feature at increasingly higher binding energies, as N is increased, that arises from electron-plasmon coupling, i.e. formation of plasmonic polarons. It was shown that two different regimes exist in the system: 1) at low carrier densities, the system is characterised by the appearance of both phononic and plasmonic polarons; and 2) at high carrier densities, the phononic-polaron model breaks down as the electrons screen the phonons, but plasmonic-polaron formation is maintained. These measurements and simulations were supported by *ab-initio* calculations of the spectral function, by collaborators at the University of Oxford, which incorporated both electron-phonon and electron-plasmon coupling.

These four separate, but interconnected investigations open up a large range of future studies into the electronic structure of TMDCs and EuO. The observation of negative electronic compressibility in WSe_2 should persist across the family of materials. Thus further understanding on how different screening environments (i.e. exposed surfaces vs. heterostructures) and material properties (i.e.thickness, effective mass and dielectric constant) alter this effect is required before incorporation of these devices into any electronic device. An ability to tune the material properties of EuO across a wide range of phase space (i.e. strain,

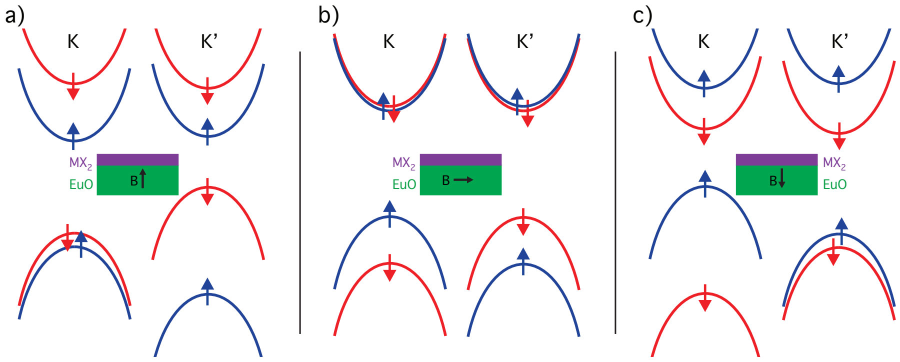

FIGURE 10.1: Integration of EuO and TMDCs for manipulation of spin-polarised states. a) In the low temperature phase, orientation of the magnetic moments of EuO perpendicular to the TMDC interface breaks time-reversal symmetry and lifts the layer degeneracy of the valence band states at $\overline{\mathrm{K}}$. b) Removal of the out-of-plane magnetic field, either by increased temperature or orientating the magnetic moments in-plane, re-establishes TRS and the layer-degeneracy. c) Reversing the orientation of the fields in a) reverses the magnetic effects and induces the opposite spin-splitting of the conduction and valence bands.

carrier density, thickness, etc.) provides alternative routes to exploring the many-body effects presented in this material.

One of the most exciting areas to explore is the integration of these two interesting materials into a single heterostructure. As well as breaking layer-degeneracy as shown here, another way to remove the spin-degeneracy in WSe$_2$ is by breaking time-reversal symmetry. Although traditional fields of a few Tesla have been unable to achieve large spin-splittings, $\sim$0.1-0.2 meV/T [163–167], it is believed that proximity coupling to a ferromagnetic substrate could be capable of inducing a large spin-splitting of the states around $\overline{\mathrm{K}}$, equivalent to hundreds or even thousands of Tesla [168–171]. Such a heterostructure could have useful spintronic properties as spin-split valence band states (and to a lesser extent, conduction band states) could be controlled by either temperature or orientation of the underlying EuO magnetic domains, depicted in Fig. 10.1, allowing for spin-polarised currents to be excited in the TMDC layer [172]. Such a heterostructure could be fabricated with oxide and chalcognide MBE systems, linked in-situ, and studied via ARPES to directly probe the spin-split valence bands, offering just one possible future investigation for a suitably equipped MBE/ARPES system.

— THE END —

Bibliography

1. Theis, T. & Solomon, P. It's Time to Reinvent the Transistor! *Science* **327,** 1600 (2010).
2. Datta, S. & Das, B. Electronic analog of the electro-optic modulator. *Appl. Phys. Lett.* **56,** 665 (1990).
3. Koo, H. *et al.*. Control of Spin Precession in a Spin-Injected Field Effect Transistor. *Science* **325,** 1515 (2009).
4. Gong, K. *et al.* Electric Control of Spin in Monolayer WSe_2 Field Effect Transistors. *Nanotech* **25,** 435201 (2014).
5. Yan, W. *et al.* A Two-Dimensional Spin Field-Effect Switch. *Nat. Comms.* **7,** 13372 (2016).
6. Luo, Y. *et al.*. Opto-Valleytronic Spin Injection in Monolayer MoS_2/Few-Layer Graphene Hybrid Spin Valves. *DOI: 10.1021/acs.nanolett.7b01393* (2017).
7. Podzorov, V. & Gershenson, M. *et al.*. High-Mobility Field-Effect Transistors Based on Transition Metal Dichalcogenides. *Appl. Phys. Lett.* **84,** 3301 (2004).
8. Shen, T., Penumatch, A. & Appenzeller, J. Strain Engineering for Transition Metal Dichalcogenides Based Field Effect Transistors. *ACS Nano* **10,** 4712 (2016).
9. Li, Y. *et al.* Anti-Ambipolar Field-Effect Transistors Based on Few-Layer 2D Transition Metal Dichalcogenides. *ACS Appl. Mater. Inter.* **8,** 15574 (2016).
10. Marder, M. *Condensed Matter Physics* (Wiley, 2010).
11. Ashcroft, N. & Mermin, N. *Solid State Physics* (Holt Reinhard and Winston, 1976).

12. Rogers, A. *Essentials of Optoelectronics with Applications* (CRC Press, 1997).
13. Ibach, H. & Lüth, H. *Solid-State Physics: An Introduction to Principles of Materials Science* 4th ed. (Springer-Verlag, 2009).
14. Simon, S. *The Oxford Solid State Basics* (Oxford University Press, 2013).
15. Yu, P. & Cardona, M. *Fundamentals of Semiconductors: Physics and Materials Properties* 4th ed. (Springer Verlag, 2010).
16. Tsuneda, T. *Density Functional Theory in Quantum Chemistry* (Springer Japan, 2014).
17. Blaha, P. *et al. WIEN2K, An Augmented Plane Wave + Local Orbitals Program for Calculating Crystal Properties* Karlheinz Schwarz, Techn. Universität Wien, Austria, 2001.
18. Perdew, J. Density Functional Theory and the Band Gap Problem. *Int. J. Quant. Chem.: Quant. Chem. Symp* **19,** 497 (1986).
19. Krupin, O. *Dichroism and Rashba effect at magnetic crystal surfaces of rare-earth metals* PhD thesis (Freie Universität, Berlin, 2004).
20. Hüfner., S. *Photoelectron Spectroscopy* 3rd ed. (Springer, Berlin, 2010).
21. Damascelli, A. Probing the Electronic Structure of Complex Systems by ARPES. *Phys. Scrip.* **T109,** 61 (2004).
22. Wadati, H. *et al.* Angle-Resolved Photoemission Spectroscopy of Perovskite-Type Transition-Metal Oxides and Their Analyses Using Tight-Binding Band Structure. *Phase Transitions* **79,** 617 (2006).
23. Gay, T. & Dunning, F. Mott Electron Polarimetry. *Rev. Sci. Instrum.* **63,** 1635 (1992).
24. Mott, N. The Scattering of Fast Electrons by Atomic Nuclei. *Proc. R. Soc. A* **124,** 425 (1929).
25. Mott, N. The Polarisation of Electrons by Double Scattering. *Proc. R. Soc. A* **135,** 429 (1932).

26. Jozwiak, C. *et al.* A High-Efficiency Spin-Resolved Photemission Spectrometer Combining Time-of-Flight Spectroscopy with Exchange-Scattering Polarimetry. *Rev. Sci. Instrum.* **81,** 053904 (2010).
27. Herman, M. & Sitter, H. *Molecular Beam Epitaxy: Fundamentals and Current Status* (Springer-Verlag, 1989).
28. Ichimiya, A. & Cohen, P. *Reflection High-Energy Electron Diffraction* (Cambridge University Press, 2011).
29. Bashouti, M. *et al.* A Non-Oxidative Approach Towards Hybrid Silicon Nanowire-Based Solar Cell Heterojunctions. *Hybrid Materials* **1,** 1 (2014).
30. Zhang, Y. *et al.* The Isotype ZnO/SiC Heterojunction Prepared by Molecular Beam Epitaxy– A Chemical Inert Interface with Significant Band Discontinuities. *Sci. Rep.* **6,** 23106 (2016).
31. `http://www.diamond.ac.uk/Beamlines/Surfaces-and-Interfaces/I05/layout.html`. 2017.
32. Hoesch, M. *et al.* A facility for the analysis of the electronic structures of solids and their surfaces by synchrotron radiation photoelectron spectroscopy. *Rev. of Sci. Instr.* **88,** 013106 (2017).
33. Baker, A. *et al.*. An ultra-compact, high-throughput molecular beam epitaxy growth system. *Rev. of Sci. Intsr.* **86,** 043901 (2015).
34. Geim, A. K. & Novoselov, K. S. The rise of graphene. *Nature Mat.* **6,** 183 (2007).
35. Katsnelson, M., Novoselov, K. & Geim, A. Chiral tunnelling and the Klein paradox in graphene. *Nature Phys.* **2,** 620 (2006).
36. Huard, B. *et al.* Transport measurements across a tunable potential barrier in graphene. *Phys. Rev. Lett.* **98,** 236803 (2007).
37. Novoselov, K. *et al.* Two-dimensional gas of massless Dirac fermions in graphene. *Nature* **438,** 197 (2005).

38. Zhang, Y., Tan, Y., Stormer, H. & Kim, P. Experimental observation of the quantum Hall effect and Berry's phase in graphene. *Nature* **438,** 201 (2005).
39. *et al*, K. N. Unconventional quantum Hall effect and Berry's phase of 2 pi in bilayer graphene. *Nature Phys.* **2,** 177 (2006).
40. McCann, E. & Fal'ko, V. Landau-level degeneracy and quantum hall effect in a graphite bilayer. *Phys. Rev. Lett.* **96,** 086805 (2006).
41. Ohta, T. *et al.* Controlling the electronic structure of bilayer graphene. *Science* **313,** 951 (2006).
42. *et al*, S. Z. Substrate-induced bandgap opening in epitaxial graphene. *Nature Mater.* **6,** 770 (2007).
43. McCann, E. Asymmetry gap in the electronic band structure of bilayer graphene. *Phys. Rev. B* **74,** 161403 (2006).
44. Chhowalla, M. *et al.* The chemistry of two-dimensional layered transition metal dichalcogenide nanosheets. *Nature Chem.* **5,** 263 (2013).
45. Morpurgo, A. F. Gate Control of Spin-Valley Coupling. *Nature Phys.* **9,** 532 (2013).
46. Sakamoto, K. *et al.* Valley spin polarization by using the extraordinary Rashba effect on silicon. *Nature Comms.* **4,** 2073 (2013).
47. Zeng, H. *et al.* Valley polarization in MoS_2 monolayers by optical pumping. *Nature Nano.* **7,** 490 (2012).
48. Mak, K., He, K., Shan, J. & Heinz, T. Control of valley polarization in monolayer MoS_2 by optical helicity. *Nature Nano.* **7,** 494 (2012).
49. Cao, T. *et al.* Valley-selective Circular Dichroism of Monolayer Molybdenum Disulphide. *Nature Commun.* **3,** 887 (2012).
50. Zeng, H. *et al.* Optical Signature of Symmetry Variations and Spin-Valley Coupling in Atomically Thin Tungsten Dichalcogenides. *Sci. Rep.* **3,** 1608 (2013).

51. T., C. & Lambrecht, W. Quasiparticle band structure calculation of monolayer, bilayer, and bulk MoS_2. *Phys. Rev. B* **85,** 205302 (2012).

52. Yun, W. *et al.*. Thickness and strain effects on electronic structures of transition metal dichalcogenides: 2H-MX_2 semiconductors (M = Mo, W; X = S, Se, Te). *Phys. Rev. B* **85,** 033305 (2012).

53. Zhang, Y. *et al.* Direct observation of the transition from indirect to direct bandgap in atomically thin epitaxial $MoSe_2$. *Nature Nano.* **9,** 111 (2013).

54. Zhao, W. *et al.* Evolution of Electronic Structure in Atomically Thin Sheets of WS_2 and WSe_2. *ACS Nano.* **7,** 791 (2013).

55. Wang, W. *et al.*. Electronics and Optoelectronics of Two-Dimensional Transition Metal Dichalcogenides. *Nature Nano.* **7,** 699 (2012).

56. Jin, W. *et al.* Direct Measurements of the Thickness-Dependent Electronic Band Structure of MoS_2 Using Angle-Resolved Photoemission Spectroscopy. *Phys. Rev. Lett.* **111,** 10681 (2013).

57. Kadantsev, E. & Hawrylak, P. Electronic Structure of a Single MoS_2 Monolayer. *Solid State Commun.* **152,** 909 (2012).

58. Coehoorn, R. *et al.* Electronic Structure of $MoSe_2$, MoS_2, and WSe_2. I. Band-Structure Calculations and Photoelectron Spectroscopy. *Phys. Rev. B* **35,** 6195 (1987).

59. Coehoorn, R. *et al.* Electronic Structure of $MoSe_2$, MoS_2, and WSe_2. II.The Nature of the Optical Band Gaps. *Phys. Rev. B* **35,** 6195 (1987).

60. Riley, J. *et al.*. Direct Observation of Spin-Polarized Bulk Bands in an Inversion-Symmetric Semiconductor. *Nature Phys.* **10,** 835 (2014).

61. Gong, Z. *et al.* Magnetoelectric Effects and Valley-Controlled Spin Quantum Gates in Transition Metal Dichalcogenide Bilayers. *Nature Commun.* **4,** 2053 (2013).

62. Berntsen, M. *et al.*. A Spin- and Angle-Resolving Photelectron Spectrometer. *Rev. Sci. Instrum.* **81,** 035104 (2010).

63. Suzuki, R. *et al.* Valley-Dependent Spin Polarization in Bulk MoS_2 with Broken Inversion Symmetry. *Nature Nano.* **9,** 611 (2014).

64. Bawden, L. *et al.* Spin-valley locking in the normal state of a transition-metal dichalcogenide superconductor. *Nature Comms.* **7,** 11711 (2016).

65. Zhang, X. *et al.* Hidden Spin Polarization in Inversion-Symmetric Bulk Crystals. *Nature Phys.* **10,** 387393 (2014).

66. Xiao, D. *et al.* Coupled Spin and Valley Physics in Monolayers of MoS_2 and Other Group-VI Dichalcogenides. *Phys. Rev. Lett.* **108,** 196802 (2012).

67. Zhu, Z.-H. *et al.* Layer-by-Layer Entangled Spin-Orbital Texture of the Topological Surface State in Bi_2Se_3. *Phys. Rev. Lett.* **110,** 216401 (2013).

68. Zhu, Z.-H. *et al.* Photoelectron Spin-Polarization Control in the Topological Insulator Bi_2Se_3. *Phys. Rev. Lett.* **112,** 076802 (2014).

69. Tanuma, S., Powell, C. & Penn, D. Calculation of Electron Inelastic Mean Free Paths (IMFPs) VII. Reliability of the TPP-2M IMFP Predictive Equation. *Surf. Interf. Anal.* **21,** 165 (1994).

70. Yeh, J. & Landau, I. Atomic subshell photoionization cross sections and asymmetry parameters: $1 \leq Z \leq 103$. *Atomic Data and Nuclear Data Tables* **32,** 1 (1985).

71. Razzoli, E. *et al.* Selective Probing of Hidden Spin-Polarized States in Inversion-Symmetric Bulk MoS_2. *Phys. Rev. Lett.* **118,** 086402 (2017).

72. Bertoni, R. *et al.* Generation and Evolution of Spin-, Valley-, and Layer-Polarized Excited carrier in Inversion-Symmetric WSe_2. *Phys. Rev. Lett.* **117,** 277201 (2016).

73. Riley, J. *et al.*. Negative Electronic Compressibility and Tunable Spin Splitting in WSe_2. *Nature Nano.* **10,** 1043 (2015).

74. King, P., Veal, T. & McConville, C. Nonparabolic Coupled Poisson-Schrö,dinger Solutions for Quantized Electron Accumulation Layers: Band Bending, Charge Profile, and Subbands at InN Surfaces. *Phys. Rev. B* **77,** 125305 (2008).

75. Baraff, G. & Appelbaum, J. Effect of Electric and Magnetic Fields on the Self-Consistent Potential at the Surface of a Degenerate Semiconductor. *Phys. Rev. B* **5,** 475 (1972).

76. Paasch, G. & Übensee, H. A Modified Local Density Approximation. Electron Density in Inversion Layers. *Phys. Status Solidi B* **113,** 165 (1982).

77. Monch, W. *Semiconductor Surfaces and Interfaces* (Spring Berlin, 2001).

78. Zöllner, J.-P. *et al.* A Novel Self-Consistent Theory of the Electronic Structure of Inversion Layers in InSb MIS Structures. *Phys. Status Solidi B* **134,** 837 (1986).

79. Streight, S. & Mills, D. Influence of Surface Charge on Free-Carrier Density profiles in GaAs Films: Application to Second-Harmonic Generation by Free Carriers. *Phys. Rev. B* **37,** 965 (1988).

80. Abe, S., Inaoka, T. & Hasegawa, M. Evolution of Electron States at a Narrow-Gap Semiconductor Surface in an Accumulation-Layer Formation Process. *Phys. Rev. B* **66,** 205309 (2002).

81. Yuan, H. *et al.* Zeeman-Type Spin Splitting Controlled by an Electric Field. *Nature Phys.* **9,** 563 (2013).

82. Eisenstein, J., Pfeiffer, L. & West, K. Negative Compressibility of Interacting Two-Dimensional Electron and Quasiparticle Gases. *Phys. Rev. Lett.* **68,** 674 (1992).

83. Yu, G. *et al.*. Interaction Phenomena in Graphene Seen Through Quantum Capacitance. *Proc. Natl. Acad. Sci. USA* **110,** 3282 (2013).

84. Larentis, S. *et al.* Band Offset and Negative Compressibility in Graphene-MoS_2 Heterostructures. *Nano. Lett.* **14,** 2039 (2014).

85. Ehrenreich, H. & Cohen, M. Self-Consistent Field Approach to the Many-Electron Problem. *Phys. Rev.* **115,** 786 (1959).

86. Lindhard, J. On the Properties of a Gas of Charged Particles. *K. Dan. Vidensk. Selsk., Mat. Fys. Medd.* **28,** 8 (1954).

87. Giuliani, G. & Vignale, G. *Quantum Theory of the Electron Liquid* (Cambridge University Press: New York, 2005).

88. Souza, I. *et al.* Maximally Localized Wannier Functions for Entangled Energy Bands. *Phys. Rev. B* **65,** 035109 (2001).

89. King, P. *et al.*. Quasiparticle Dynamics and Spin-Orbital Texture of the $SrTiO_3$ Two-Dimensional Electron Gas. *Nature Comm.* **5,** 3414 (2014).

90. Ulstrup, S. *et al.* Ultrafast Band Structure Control of a Two-Dimensional Heterostructure. *ACS Nano* **10,** 6315 (2016).

91. Liang, Y. & Yang, L. Carrier Plasmon Induced Nonlinear Band Gap Renormalization in Two-Dimensional Semiconductors. *Phys. Rev. Lett.* **114,** 063001 (2014).

92. Ugeda, M. *et al.*. Giant Bandgap Renormalization and Excitonic Effects in a Monolayer Transition Metal Dichalcogenide Semiconductor. *Nature Mat.* **13,** 1091 (2014).

93. Mundy, J. *et al.*. Hetero-Epitaxial EuO Interfaces Studied by Analytic Electron Microscopy. *Appl. Phys. Lett.* **104,** 091601 (2014).

94. Averyanoc, D. *et al.*. Atomic-Scale Engineering of Abrupt Interface for Direct Spin Contact of Ferromagnetic Semiconductor with Silicon. *Sci. Rep.* **6,** 22841 (2016).

95. Wachter, P. Europium Chalcogenides: EuO, EuS, EuSe and EuTe. *Handbook on the Physics and Chemistry of Rare Earths* **2,** 507 (1979).

96. Brauer, G. Uber Europium(II)-Oxyd. *Angew. Chem.* **65,** 261 (1953).

97. Suits, J. & Lee, K. Giant magneto-Optical Kerr Effect in EuO. *J. Appl. Phys.* **42,** 3258 (1971).

98. Ahn, K. & Shafer, M. Relationship Between Stoichiometry and Properties of EuO Films. *J. Appl. Phys.* **41,** 1260 (1970).

99. Huang, C.-C. & Ho, J. Faraday Rotation Near the Curie Point of EuO. *Phys. Rev. B* **12,** 5255 (1975).

100. Yamasaki, T. *et al.* Observation of Anomalous Hall Effect in EuO Epitaxial Thin Films Grown by a Pulse Laser Deposition. *Appl. Phys. Lett.* **98,** 082116 (2011).

101. Ulbricht, R. *et al.*. Adsorption-Controlled Growth of EuO by Molecular-Beam epitaxy. *Appl. Phys. Lett.* **93,** 2105 (2008).

102. Matthias, B., Bozorth, R. & Van Vleck, J. Ferromagnetic Interaction in EuO. *Phys. Rev. Lett.* **7,** 160 (1961).

103. Elliott, J., Legvold, S. & Spedding, F. Some Magnetic Properties of Gadolinium Metal. *Phys. Rev.* **91,** 28 (1953).

104. Liu, S. *et al.*. Interpretation of Magnetic Properties of Dysprosium. *Phys. Rev.* **116,** 1464 (1959).

105. McMasters, O. D., Gschneidner, K. A., Kaldis, E. & Sampietro, G. High-temperature enthalpies and standard Gibbs free energies of formation of the europium chalcogenides: EuO, EuS, EuSe, and EuTe. *J. Chem. Thermodyn.* **6,** 845 (1974).

106. *Europium: Elemental Information* `http://www.rsc.org/periodic-table/element/63/europium`. Accessed: 14/06/17.

107. Miyazaki, H. *et al.* Direct Observation of Momentum-Dependent Exchange Interaction in a Heisenberg Ferromagnet. *Phys. Rev. Lett.* **102,** 227203 (2009).

108. Torrance, J., Shafer, M. & McGuire, T. Bound Magnetic Polarons and the Insulator-Metal Transition in EuO. *Phys. Rev. Lett.* **29,** 1168 (1972).

109. Oliver, M., Dimmock, J. & Reed, T. Temperature and Magnetic Field Dependence of the Conductivity of EuO. *J. Res. Dev.* **14,** 276 (1970).

110. Oliver, M. *et al.* Pressure Dependence of the Electrical Resistivity of EuO. *Phys. Rev. Lett.* **24,** 1064 (1970).

111. Steeneken, P. *et al.*. Exchange Splitting and Charge Carrier Spin Polarization in EuO. *Phys. Rev. Lett.* **88,** 047201 (2002).

112. Kimura, S.-I. *et al.* Electronic Inhomogeneity EuO: Possibility of Magnetic Polaron States. *Phys. Rev. B* **78,** 052409 (2008).

113. Mairoser, T. *et al.* Influence of Chemical Doping on the Magnetic Properties of EuO. *Phys. Rev. B* **87,** 014416 (2013).

114. Schiller, R. & Nolting, W. Prediciton of a Surface State and a Related Surface Insulator-Metal Transition for the (100) Surface of Stochiometric EuO. *Phys. Rev. Lett.* **86,** 3847 (2001).

115. Müller, M., Miao, G.-X. & Moodera, J. Thickness Dependence of Ferromagnetic- and Metal-Insulator Transition in Thin EuO films. *J. Appl. Phys.* **105,** 07C917 (2009).

116. Miyazaki, H. *et al.* La-doped EuO: A Rare Earth Ferromagnetic Semiconductor with the Highest Curie Temperature. *Appl. Phys. Lett.* **96,** 232503 (2010).

117. Shafer, M. *et al.* Studies of Curie-Point Increases in EuO. *J. Appl. Phys.* **39,** 588 (1968).

118. Ahn, K. *et al.*. Magnetic and Magneto-optic Properties of EuO Films Doped with Trivalent Rare-Earth Oxide. *J. Appl. Phys.* **39,** 5061 (2003).

119. Ahn, K. EuO Films Doped with Fe and Gd. *J. Appl. Phys.* **43,** 231 (1972).

120. Kikuda, S. *et al.* Magnetic Properties of EuO Thin Films Doped with Transition Metal. *IEEE Transl. J. Magn. Jpn.* **2,** 434 (1987).

121. Ahn, K. Y. Increase of Curie Temperature in EuO Films by Fe Doping. *Appl. Phys. Lett.* **17,** 347 (1970).

122. McGuire, T. *et al.* Magnetic and Magneto-Optical Properties of Fe-Doped EuO Films. *J. Appl. Phys.* **42,** 1775 (1971).

123. Lévy, F. Effets magnétostrictifs spontanés de quelques composés des terres rares. *Physik Kondens. Materie* **10,** 71 (1969).

124. Lettieri, J. *et al.* Epitaxial Growth and Magnetic Properties of EuO On (001) Si by Molecular-Beam Epitaxy. *Appl. Phys. Lett.* **83,** 975 (2003).

125. Swartz, A. *et al.*. Epitaxial EuO Thin Films on GaAs. *Appl. Phys. Lett.* **97,** 112509 (2010).

126. Swartz, A. *et al.*. Integrating MBE Materials with Graphene to Induce Novel Spin-Based Phenomena. *J. Vac. Sci. Tech. B* **31,** 04D105 (2013).

127. Klinkhammer, J. *et al.* Spin-Polarized Surface State in EuO(100). *Phys. Rev. Lett.* **112,** 016803 (2014).

128. Sutarto, R. *et al.* Epitaxial and Layer-by-Layer Growth of EuO Thin Films on Yttria-Stabilized Cubic Zirconia (001) using MBE Distillation. *Phys. Rev. B* **79,** 205318 (2009).

129. Caspers, C. *Magnetic Oxide Heterostructures: EuO on Cubic Oxides and on Silicon* PhD thesis (Universität Duisburg-Essen, 2013).

130. Mairoser, T. *et al.* High-quality EuO Thin Films the Easy Way via Topotactic Transformation. *Nat. Comms.* **6,** 7716 (2015).

131. Caspers, C. *et al.* Electronic Structure of EuO Spin Filter Tunnel Contacts Directly on Silicon. *Phys. Status Solidi RRL* **1,** 1 (2001).

132. Mairoser, T. *et al.* Influence of Substrate Temeprature on the Curie Temperature and Charge Carrier Density of Epitaxial Gd-doped EuO films. *Appl. Phys. Lett.* **98,** 102110 (2011).

133. Liu, P. *et al.* Ce-doped EuO: Magnetic Properties and the Indirect Band Gap. *J. Appl. Phys.* **109,** 07C311 (2011).

134. Arnold, M. & Kroha, J. Simultaneous Ferromagnetic Metal-Semicondutor Transition in Electron-Doped EuO. *Phys. Rev. Lett.* **100,** 046404 (2008).

135. Takahashi, M. Origin of Anomalous Magnetization Curve of Electron-Doped EuO. *J. Phys. Soc. Jap.* **80,** 075001 (2001).

136. Liu, P. & Tang, J. A Magnetic Polaron Model for the Enhanced Curie Temperature of EuO$_{1-x}$. *J. Phys.: Condens. Matter* **25,** 125802 (2013).

137. Rho, H. *et al.* Evolution of Magnetic Polarons and Spin-Carrier Interactions through the Metal-Insulator Transition in Eu$_{1-x}$Gd$_x$O. *Phys. Rev. Lett.* **88,** 127401 (2002).

138. Miyazaki, H. *et al.* Three-Dimensional Angle-Resolved Photoemission Spectra of EuO Thin Films. *J. Elec. Spc. and Rel. Ph.* **191,** 7 (2013).

139. Shai, D. *et al.*. Temperature Dependence of the Electronic Structure and Fermi-Surface Reconstruction of Eu$_{1-x}$Gd$_x$O through the Ferromagnetic Metal-Insulator Transition. *Phys. Rev. Lett.* **108,** 267003 (2012).

140. Shai, D. *et al.*. Observation of Semilocalized Dispersive States in the Strongly Correlated Electron-Doped Ferromagnet Eu$_{1-x}$Gd$_x$O. *Phys. Rev. B* **94,** 195102 (2016).

141. Damascelli, A., Hussain, Z. & Shen, Z.-X. Angle-resolved Photoemission Studies of the Cuprate Superconductors. *Revs. Mod. Phys.* **75,** 473 (2003).

142. Wachter, P. The Optical Electrical and Magnetic Properties of the Europium Chalcogenides and the Rare Earth pnictides. *Crit Rev. Solid State Sci.* **3,** 189 (1972).

143. Stollenwerk, T. & Kroha, J. Theory of Curie Temperature Enhancement in Electron-Doped EuO. *Phys. Rev. B* **92,** 205119 (2015).

144. Yukawa, R. *et al.* Phonon-Dressed Two-Dimensional Carriers on the ZnO Surface. *Phys. Rev. B* **94,** 65313 (2016).

145. Moser, S. *et al.* Tunable Polaronic Conduction in Anatase TiO_2. *Phys. Rev. Lett.* **110,** 196403 (2013).

146. Lee, J. *et al.*. Interfacial Mode Coupling as the Origin of the Enhancement of T_c in FeSe Films on $SrTiO_3$. *Nature* **515,** 245 (2014).

147. Cancellieri, C. *et al.* Polaronic Metal State at the $LaAlO_3/SrTiO_3$ Interface. *Nature Comms.* **7,** 10386 (2015).

148. Wang, Z. *et al.* Tailoring the Nature and Strength of Electron-Phonon Interactions in the $SrTiO_3$ (001) 2D Electron Liquid. *Nature Mat.* **15,** 835 (2016).

149. Lee, T. *et al.*. The Motion of Slow Electrons in a Polar Crystal. *Phys. Rev.* **90,** 297 (1953).

150. Verdi, C., Caruso, F. & Giustino, F. Origin of the Crossover from Polarons to Fermi Liquids in Transition Metal Oxides. *Nat. Comms.* **8,** 15769 (2017).

151. Giustino, F. Electron-phonon interactions from first principles. *Rev. Mod. Phys.* **89,** 15003 (2017).

152. Caruso, F. & giustino, F. Spectral Fingerprints of Electron-Plasmon Coupling. *Phys. Rev. B* **92,** 045123 (2015).

153. Caruso, F. & giustino, F. Theory of Electron-Plasmon Coupling in Semiconductors. *Phys. Rev. B* **94,** 115208 (2016).

154. Hwang, E., Sensarma, R. & Sarma, S. Plasmon-phonon coupling in graphene. *Phys. Rev. B* **82,** 195406 (2010).

155. Fröhlich, H. Electrons in Lattice Fields. *Adv. Phys.* **3,** 325 (1954).

156. Giustino, F., Cohen, M. & Louie, S. Electron-Phonon Interaction using Wannier Functions. *Phys. Rev. B* **76,** 165108 (2007).

157. Verdi, C. & Giustino, F. Verdi, C. and Giustino, F.Fröhlich Electron-Phonon Vertex from First Principles. *Phys. Rev. Lett.* **115,** 76401 (2015).

158. Verdi, C. & Giustino, F. The GW plus Cumulant Method and Plasmonic Polarons: Application to the Homogeneous Electron Gas. *Eur. Phys. J. B* **89,** 238 (2016).

159. Hedin, L. New Method for Calculating the One-Particle Green's Function with Application to the Electron-Gas Problem. *Phys. Rev.* **39,** A96 (1965).

160. Langreth, D. Singularities in the X-Ray Spectra of Metals. *Phys. Rev. B* **1,** 471 (1969).

161. Posadas, A. *et al.*. Scavenging of Oxygen from $SrTiO_3$ During Oide Thin Film Deposition and the Formation of Interfacial 2DEGs. *J. Appl. Phys.* **121,** 105302 (2017).

162. Kasinathan, D. *et al.* SmO Thin Films: A Flexible Route to Correlated Flat Bands with Nontrivial Topology. *Phys. Rev. B* **91,** 195127 (2015).

163. Srivastava, A. *et al.* Valley Zeeman Effect in Elementary Optical Excitations of Monolayer WSe_2. *Nat. Phys.* **11,** 141 (2014).

164. MacNeill, D. *et al.* Breaking of Valley Degeneracy by Magnetic Field in Monolayer $MoSe_2$. *Phys. Rev. Lett.* **114,** 037401 (2015).

165. Stier, A. *et al.*. Exciton Diamagnetic Shifts and Valley Zeeman Effects in Monolayer WS_2 and MoS_2 to 65 Tesla. *Nat. Comms.* **7,** 10643 (2016).

166. Plechinger, G. *et al.* Excitonic Valley Effects in Monolayer WS_2 under High Magnetic Fields. *Nano Lett.* **16,** 7899 (2016).

167. Arora, A. *et al.* Valley Zeeman Splitting and Valley Polarization of Neutral and Charged Excitons in Monolayer $MoTe_2$ at High Magnetic Fields. *Nano Lett.* **16,** 3624 (2016).

168. Wang, Z. *et al.* Proximity-induced ferromagnetism in graphene revealed by the anomalous Hall effect. *Phys. Rev. Lett.* **114,** 016603 (2015).

169. Katmis, F. *et al.* A high-temperature ferromagnetic topological insulating phase by proximity coupling. *Nature* **553,** 513 (2016).

170. Lazic, P., Belashchenko, K. D. & Zutic, I. Effective gating and tunable magnetic proximity effects in two-dimensional heterostructure. *Phys. Rev. B* **93,** 241401 (2016).

171. Scharf, B. *et al.* Magnetic Proximity Effects in Transition-Metal Dichalcogenides: Converting Excitons. *arXiv:1704.07984* (2017).

172. Qi, J. *et al.* Giant and Tunable Valley Degeneracy Splitting in $MoTe_2$. *Phys. Rev. B* **92,** 121403.